ANIMAL MODELS FOR PHARMACOLOGICAL INVESTIGATION OF TREATMENTS AND DIAGNOSTICS FOR DISEASES

EDITED BY: Natália Martins Feitosa, Ives Charlie-Silva and Rafael Henrique Nóbrega

PUBLISHED IN: Frontiers in Cell and Developmental Biology

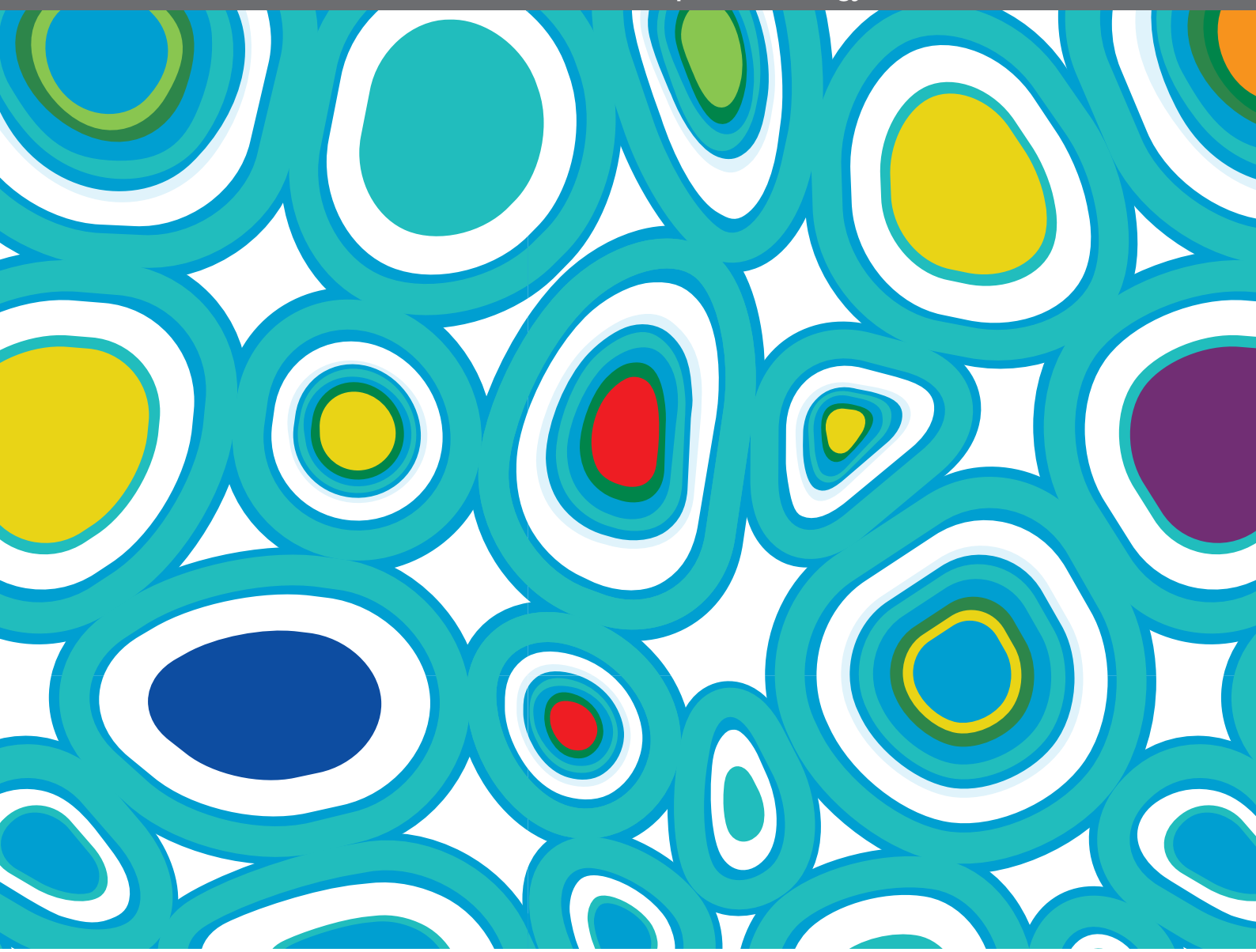

frontiers Research Topics

ISSN 1664-8714
ISBN 978-2-83250-519-9
DOI 10.3389/978-2-83250-519-9

About Frontiers

Frontiers is more than just an open-access publisher of scholarly articles: it is a pioneering approach to the world of academia, radically improving the way scholarly research is managed. The grand vision of Frontiers is a world where all people have an equal opportunity to seek, share and generate knowledge. Frontiers provides immediate and permanent online open access to all its publications, but this alone is not enough to realize our grand goals.

Frontiers Journal Series

The Frontiers Journal Series is a multi-tier and interdisciplinary set of open-access, online journals, promising a paradigm shift from the current review, selection and dissemination processes in academic publishing. All Frontiers journals are driven by researchers for researchers; therefore, they constitute a service to the scholarly community. At the same time, the Frontiers Journal Series operates on a revolutionary invention, the tiered publishing system, initially addressing specific communities of scholars, and gradually climbing up to broader public understanding, thus serving the interests of the lay society, too.

Dedication to Quality

Each Frontiers article is a landmark of the highest quality, thanks to genuinely collaborative interactions between authors and review editors, who include some of the world's best academicians. Research must be certified by peers before entering a stream of knowledge that may eventually reach the public - and shape society; therefore, Frontiers only applies the most rigorous and unbiased reviews.
Frontiers revolutionizes research publishing by freely delivering the most outstanding research, evaluated with no bias from both the academic and social point of view. By applying the most advanced information technologies, Frontiers is catapulting scholarly publishing into a new generation.

What are Frontiers Research Topics?

Frontiers Research Topics are very popular trademarks of the Frontiers Journals Series: they are collections of at least ten articles, all centered on a particular subject. With their unique mix of varied contributions from Original Research to Review Articles, Frontiers Research Topics unify the most influential researchers, the latest key findings and historical advances in a hot research area! Find out more on how to host your own Frontiers Research Topic or contribute to one as an author by contacting the Frontiers Editorial Office: frontiersin.org/about/contact

ANIMAL MODELS FOR PHARMACOLOGICAL INVESTIGATION OF TREATMENTS AND DIAGNOSTICS FOR DISEASES

Topic Editors:
Natália Martins Feitosa, Federal University of Rio de Janeiro, Brazil
Ives Charlie-Silva, University of São Paulo, Brazil
Rafael Henrique Nóbrega, São Paulo State University, Brazil

Citation: Feitosa, N. M., Charlie-Silva, I., Nóbrega, R. H., eds. (2022). Animal Models for Pharmacological Investigation of Treatments and Diagnostics for Diseases. Lausanne: Frontiers Media SA. doi: 10.3389/978-2-83250-519-9

Table of Contents

frontiers | Frontiers in Cell and Developmental Biology

TYPE Editorial
PUBLISHED 03 October 2022
DOI 10.3389/fcell.2022.1023512

OPEN ACCESS

EDITED AND REVIEWED BY
Ramani Ramchandran,
Medical College of Wisconsin,
United States

*CORRESPONDENCE
Natália Martins Feitosa,
nataliafeitosa@gmail.com

SPECIALTY SECTION
This article was submitted to Molecular and Cellular Pathology, a section of the journal Frontiers in Cell and Developmental Biology

RECEIVED 19 August 2022
ACCEPTED 31 August 2022
PUBLISHED 03 October 2022

CITATION
Feitosa NM and Nóbrega RH (2022), Editorial: Animal models for pharmacological investigation of treatments and diagnostics for diseases. *Front. Cell Dev. Biol.* 10:1023512. doi: 10.3389/fcell.2022.1023512

Editorial: Animal models for pharmacological investigation of treatments and diagnostics for diseases

Natália Martins Feitosa[1]* and Rafael Henrique Nóbrega[2]

[1]Integrated Laboratory of Translational Biosciences (LIBT), Institute of Biodiversity and Sustainability (NUPEM), Federal University of Rio de Janeiro, Macaé, Rio de Janeiro, Brazil, [2]Reproductive and Molecular Biology Group, Department of Structural and Functional Biology, Institute of Biosciences, São Paulo State University (UNESP), Botucatu, Brazil

KEYWORDS

animal models, metabolism, endocrine system, reproduction, disease model, neuroprotective, drug therapy, new targets

Editorial on the Research Topic
Animal models for pharmacological investigation of treatments and diagnostics for diseases

In the last decades, interdisciplinary science has been shaping modern science to understand life, health, and disease (Erskine et al., 2013; Zhang et al., 2017; Mazzocchi, 2019). Along this path, animal models played a fundamental role in building knowledge from basic to applied science and diseases (Robinson et al., 2019; Mukherjee et al., 2022) including more recently in SARS-CoV-2 studies (Caldera-Crespo et al., 2022). *In vitro* and *in silico* studies are undoubtedly relevant, however, animal models in research are still essential and their use has been largely accepted in the scientific community. These debates led to the ethical improvement of animal welfare rules in many countries, which avoids unnecessary use of animals and animal cruelty (review Robinson et al., 2019). Therefore, much of the pharmacological investigation and other fields of science benefit from animal models.

In this Research Topic, mostly murine and fish models were used to introduce new studies to understand not only diseases but normal development and homeostasis (Figure 1). In the case of fish models, Ladisa et al. presented the goldfish as a great model to study energy attribution related to reproduction and growth, through metabolomics. More specifically, they demonstrated that changes in metabolism may affect the development and growth of gonads in oviparous fish. Gonadotropin Inhibitory Hormone (GnIH) would play a role in this regulation, including lipid yield as preparation for egg production. Although goldfish is a seasonal response animal, GnIH signaling might be a conserved pathway among vertebrates. Increased GnIH levels in mice for example affect adiposity and reproduction (review Bédécarrats et al., 2022). In the light of hormone crosstalk with metabolism and gonad maturation, Rodrigues et al. showed that

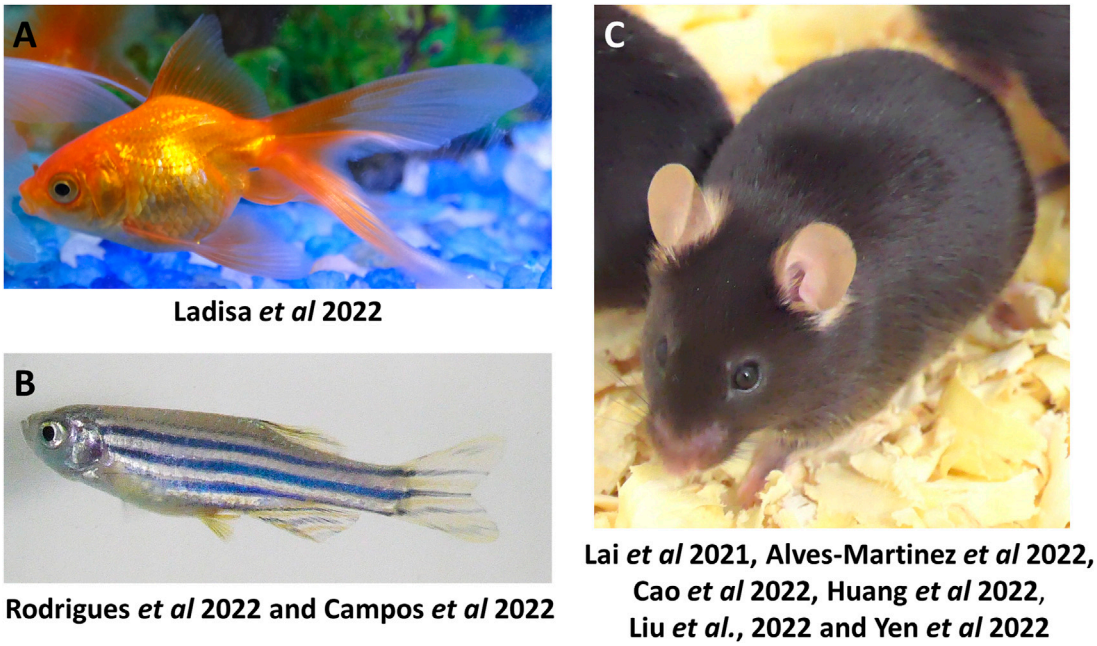

FIGURE 1
Animals used as experimental models in pharmacology research. **(A–C)** Representative pictures of the animal models and the respective research papers related to them. **(A)** goldfish (*Carassius auratus*), **(B)** zebrafish (*Danio rerio*); and **(C)** mouse (*Mus musculus*). A C57BL/6J mouse picture is shown.—In some studies published in this Research Topic, the Balb-c (picture not shown) species was used.

thyroid hormones had an effect on zebrafish spermatogenesis. The impairment of thyroid hormone production and activity through methimazole directly impacted sperm production and genes related to the control of spermatogenesis Ladisa et al. and Rodrigues et al. studies demonstrated that the endocrine system, reproduction, and metabolism are intimately related. The understanding of the connections among those pathways is fundamental to assessing the impact of endocrine disruptors in the organism of vertebrates.

A classic substance for human control of hypercholesterolemia, simvastatin, was revisited for drug safety using zebrafish embryos and chicken cell culture. Campos et al. group used the zebrafish embryos and chicken muscle culture as models to investigate the unwanted side effects of simvastatin on the muscles of human patients. The authors indicated that simvastatin could affect muscle formation and inhibit cell proliferation *in vivo* and *in vitro*. Campos et al. presented their results, provided a small review of the literature, and opened an important discussion on the use of simvastatin in clinics. They highlighted that when dealing with muscle degenerative diseases, simvastatin reduction of cell proliferation in muscle regeneration should be considered.

The genes and proteins do not only act in the normal development and differentiation of organs but can play a protective role in pathological events, such as kidney acute or chronic injury. Acute kidney injury (AKI) is defined as a sudden decay in the capacity of glomerular kidney filtration (Han and Thomas Lee, 2019). AKI can evolve into chronic kidney disease and/or death of the patient and some of the causes include sepsis and renal ischemia-reperfusion injury (IRI) (Murugan and Kellum, 2011; Han and Thomas Lee, 2019). IRI may happen after the interruption of renal blood flow followed by subsequent reperfusion that leads to renal dysfunction (Han and Thomas Lee, 2019). In the literature, it has been described that the severity of the injuries has a sex-related trait. Males were more sensitive to renal IRI than females (Kang et al., 2014). The following studies used mice as the main animal model. Huang et al. studied renal IRI in mice and found a differential expression of androgen receptor (AR) and microRNA-21 (miR-21) expression. The AR and miR-21 could inhibit the expression of caspase-induced apoptosis and were more greatly expressed in females than males, and show a protective effect on renal IRI. The role of AR has been extensively studied in the literature related to sex differentiation and male maturation, but the role in other organs such as kidney still need elucidation. In chronic diseases such as diabetic nephropathy (DN), differently from AKI, rarely present histological changes, the parenchyma of the glomerulus is compromised and leads to the disorder's progression (Akchurin, 2019). Cao et al. revealed that high glucose (HG) increased oxidative stress and podocyte cell death through increased activity of cyclin-dependent kinase 5 (CDK5). This enzyme has multiple functions in cell homeostasis including

survival. The authors found that TFP5, a specific inhibitor of CDK5, was able to decrease inflammatory cytokines and oxidative stress protecting the kidney of the diabetic mice model. These data, together with cell culture and RNAseq analyses, emphasized two other Sirt1 and nerve growth factor (NGF) players that could prevent DN progression. Therefore, Cao et al. pointed out the importance of CDK5-NGF/Sirt1 regulating axis in DN and suggested the TFP5 for drug therapy.

Other research groups used an omic approach to investigate new target genes related to the metabolism of parasite infection (Liu et al.) or apnea-induced cardiac injury (Lai et al.). Both groups studied the pathogenesis of public health interest diseases and used mice as a model organism. Liu et al. focused on the liver transcriptomic maps of mice infected with the parasite that causes echinococcosis. This disorder can also be passed from dogs and foxes to humans by food and water intake contaminated with the parasite eggs (Kotwa et al., 2019). Liu et al. suggested several potential lncRNA-mRNA-miRNA axes during *Echinococcus multilocularis* infection that might be important for understanding the disease mechanisms. Long-non coding RNAs (lnRNAs), micro-RNAs (miRNAs), and ncRNAs reportedly play important roles in regulating chromatin remodeling, participating in mRNA transcription, modulating cell differentiation, apoptosis among other functions (Mercer et al., 2009; O'Brien et al., 2018). Lai et al. studied a new class of non-coding RNA, the circular-RNAs (cicRNAs) in the mice model with obstructive sleep apnea (OSA). OSA is a disorder that affects millions of people worldwide and is an important risk factor for cardiac morbidities (Lebkuchen et al., 2021). In this publication, they performed microarray and qPCR analyses, which showed two differentially expressed circRNAs and a circ-miRNA-mRNA regulation network, suggesting that these findings could unveil the pathophysiological mechanisms on OSA-associated cardiovascular disease. Both the studies of Liu et al. and Lai et al. reaffirm the importance of interdisciplinary work to elicit possible new therapeutic targets for diagnostic and treatment of diseases.

Interestingly, nutrients in the human diet such as caffeine and kefir have value in the possible treatment of disorders. Alves-Martinez et al. studied the benefits and the neuroprotective effect of caffeine in germinal matrix-intraventricular hemorrhage (GM-IVH) in mice. GM-IVH is a disease that is most frequently found intracranially in preterm infants. The authors presented multiple results suggesting that caffeine diminished brain complications related to GM-IVH. Furthermore, Yen et al. analyzed the properties of Kefir peptides (KP) on a mice model that mimics hemophilia. Hemophilic patients experience osteoporosis as a prevalent comorbidity. KP treatment could ameliorate the inflammatory levels of IL-6 and osteoclastogenesis. Their results suggest the use of KP as a complementary therapy for osteoporosis in hemophilic patients.

In summary, each study add knowledge about signaling pathways that protect or enhance the severity of diseases, leading to a more accurate choice of new targets for diagnostics and future therapies.

Author contributions

All authors listed have made a substantial, direct, and intellectual contribution to the work and approved it for publication.

Funding

This work was supported by the Conselho Nacional de Desenvolvimento Científico e Tecnológico (CNPq, funding number 431352/2018-6 for NM) and Fundação de Amparo a Pesquisa do Estado de São Paulo (FAPESP, funding number 2021/13545-1 for NM and RN).

Acknowledgments

We would like to thank Prof Sérgio Luis Felisbino and Ana Luiza Romano Gabriel from the Extracelular matrix laboratory (LabMEC) Department of Morphology, Institute of Biosciences, São Paulo State University (UNESP), Botucatu, for permission to take photos of C57BL/6J mice.

Conflict of interest

The authors declare that the research was conducted in the absence of any commercial or financial relationships that could be construed as a potential conflict of interest.

Publisher's note

References

Akchurin, O. M., Cao, S. L., Luo, H. Y., Gao, Y. C., Lan, X. M., Liu, S. Y., Li, B., et al. (2019). Chronic kidney disease and dietary measures to improve outcomes. *Pediatr. Clin. N. Am.* 66, 247. doi:10.1016/j.pcl.2018.09.007

Bédécarrats, G. Y., Hanlon, C., and Tsutsui, K. (2022). Gonadotropin inhibitory hormone and its receptor: Potential key to the integration and coordination of metabolic status and reproduction. *Front. Endocrinol.* 12, 781543. doi:10.3389/fendo.2021.781543

Caldera-Crespo, L. A., Paidas, M. J., Roy, S., Schulman, C. I., Kenyon, N. S., Daunert, S., et al. (2022). Experimental models of COVID-19. *Front. Cell. Infect. Microbiol.* 11, 792584. doi:10.3389/fcimb.2021.792584

Erskine, K. E., Griffith, E., Degroat, N., Stolerman, M., Silverstein, L. B., Hidayatallah, N., et al. (2013). An interdisciplinary approach to personalized medicine: Case studies from a cardiogenetics clinic. *Per. Med.* 10, 73–80. doi:10.2217/pme.12.108

Han, S. J., and Thomas Lee, H. (2019). Mechanisms and therapeutic targets of ischemic acute kidney injury. *Kidney Res. Clin. Pract.* 38 (4), 427–440. doi:10.23876/j.krcp.19.062

Kang, K. P., Lee, J. E., Lee, A. S., Jung, Y. J., Kim, D., Lee, S., et al. (2014). Effect of gender differences on the regulation of renal ischemia-reperfusion-induced inflammation in mice. *Mol. Med. Rep.* 9 (6), 2061–2068. doi:10.3892/mmr.2014.2089

Kotwa, J. D., Isaksson, M., Jardine, C. M., Campbell, G. D., Berke, O., Pearl, D. L., et al. (2019). Echinococcus multilocularis infection, southern ontario, Canada. *Emerg. Infect. Dis.* 25 (2), 265–272. doi:10.3201/eid2502.180299

Lebkuchen, A., Freitas, L. S., Cardozo, K. H. M., and Drager, L. F. (2021). Advances and challenges in pursuing biomarkers for obstructive sleep apnea: Implications for the cardiovascular risk. *Trends cardiovasc. Med.* 31, 242–249. doi:10.1016/j.tcm.2020.04.003

Mazzocchi, F. (2019). Scientific research across and beyond disciplines: Challenges and opportunities of interdisciplinarity. *EMBO Rep.* 20 (6), e47682. doi:10.15252/embr.201947682

Mercer, T. R., Dinger, M. E., and Mattick, J. S. (2009). Long non-coding RNAs: Insights into functions. *Nat. Rev. Genet.* 10, 155–159. doi:10.1038/nrg2521

Mukherjee, P., Roy, S., Ghosh, D., and Nandi, S. K. (2022). Role of animal models in biomedical research: A review. *Lab. Anim. Res.* 38 (1), 18. doi:10.1186/s42826-022-00128-1

Murugan, R., and Kellum, J. A. (2011). Acute kidney injury: What's the prognosis? *Nat. Rev. Nephrol.* 7, 209–217. doi:10.1038/nrneph.2011.13

O'Brien, J., Hayder, H., Zayed, Y., and Peng, C. (2018). Overview of microRNA biogenesis, mechanisms of actions, and circulation. *Front. Endocrinol.* 9, 402. doi:10.3389/fendo.2018.00402

Robinson, N. B., Krieger, K., Khan, F. M., Huffman, W., Chang, M., Naik, A., et al. (2019). The current state of animal models in research: A review. *Int. J. Surg.* 72, 9–13. doi:10.1016/j.ijsu.2019.10.015

Zhang, J., Cunningham, J. J., Brown, J. S., and Gatenby, R. A. (2017). Integrating evolutionary dynamics into treatment of metastatic castrate-resistant prostate cancer. *Nat. Commun.* 8 (1), 1816. doi:10.1038/s41467-017-01968-5

frontiers in Cell and Developmental Biology

ORIGINAL RESEARCH
published: 08 November 2021
doi: 10.3389/fcell.2021.767283

Circular RNA Expression Profiles and Bioinformatic Analysis in Mouse Models of Obstructive Sleep Apnea-Induced Cardiac Injury: Novel Insights Into Pathogenesis

Suxian Lai[1†], Lijun Chen[2†], Pingyun Zhan[3†], Guofu Lin[4], Hai Lin[4], Huibin Huang[2] and Qingshi Chen[2*]*

[1]Department of Neonatology, The First Hospital of Quanzhou Affiliated to Fujian Medical University, Quanzhou, China, [2]Department of Endocrinology and Metabolism, The Second Affiliated Hospital of Fujian Medical University, Quanzhou, China, [3]Department of Cardiology, Haidu Hospital, Quanzhou, China, [4]Department of Respiratory and Critical Care Medicine, The Second Affiliated Hospital of Fujian Medical University, Quanzhou, China

OPEN ACCESS

Edited by:
Rafael Henrique Nóbrega,
São Paulo State University, Brazil

Reviewed by:
Changwei Shao,
Chinese Academy of Fishery Sciences (CAFS), China
Anurag Kumar Singh,
Banaras Hindu University, India

***Correspondence:**
Qingshi Chen
chenqingshi1986@126.com
Huibin Huang
huibinhuang@aliyun.com

[†]These authors have contributed equally to this work

Specialty section:
This article was submitted to Molecular and Cellular Pathology, a section of the journal Frontiers in Cell and Developmental Biology

Received: 30 August 2021
Accepted: 25 October 2021
Published: 08 November 2021

Citation:
Lai S, Chen L, Zhan P, Lin G, Lin H, Huang H and Chen Q (2021) Circular RNA Expression Profiles and Bioinformatic Analysis in Mouse Models of Obstructive Sleep Apnea-Induced Cardiac Injury: Novel Insights Into Pathogenesis. Front. Cell Dev. Biol. 9:767283. doi: 10.3389/fcell.2021.767283

Circular RNAs (circRNAs) participate in the development of various kinds of diseases. However, the function and roles of circRNAs in obstructive sleep apnea (OSA)-induced cardiovascular disease remain poorly understood. Therefore, we sought to explore the circRNA expression profiles and predict their functions in OSA-induced cardiac injury with the use of bioinformatics analysis. The model of OSA was established in mouse treated by chronic intermittent hypoxia (CIH) exposure. Then, we screened the circRNA profile using circRNA microarray. By comparing circRNA expression in three matched pairs of CIH-treated cardiac tissues and controls, differentially expressed circRNAs were identified in the CIH groups. Comparison of the selected circRNAs expression levels was performed between qRT-PCR and microarray. Meanwhile, we employed Gene Ontology (GO) and Kyoto Encyclopedia of Genes and Genomes (KEGG) pathway analyses to predict the functions of these selected circRNAs. Finally, we constructed a circRNA-miRNA-mRNA network based on the target prediction. It was found that a total of 124 circRNAs were differentially expressed in CIH-treated cardiac tissues ($p \leq 0.05$, fold-change ≥ 1.5). Among them, 23 circRNAs were significantly down-regulated, and the other 101 were up-regulated. Then, ten circRNAs were randomly selected to validate the reliability of the microarray results by using qRT-PCR. Next, we conducted the GO and KEGG pathway analysis to explore the parental genes functions of differentially expressed circRNA. Finally, two significantly differentially expressed circRNAs (mmu_circRNA_014309 and mmu_circRNA_21856) were further selected to create a circRNA-miRNA-mRNA regulation network. Our study did first reveal that the differentially expressed circRNAs played a vital role in the pathogenesis of OSA-induced cardiac damage. Thus, our findings bring us closer to unraveling the pathophysiologic mechanisms and eliciting novel therapeutic targets for the treatment of OSA-associated cardiovascular diseases.

Keywords: CircRNAs, obstructive sleep apnea, cardiac injury, chronic intermittent hypoxia, expression profile

INTRODUCTION

Obstructive sleep apnea (OSA) is a complex, multifactorial disorder defined by chronic intermittent hypoxia (CIH), which affected millions of people worldwide. OSA has been established as an important risk factor for cardiovascular mortality and morbidity (Dobrosielski et al., 2017; de Vries et al., 2018; Lebkuchen et al., 2021). OSA contributes to cardiovascular diseases such as myocardial infraction (Porto et al., 2017), cardiac arrhythmias (May et al., 2017), coronary artery disease (Belaidi et al., 2016), and heart failure (Sanderson et al., 2021). Meanwhile, OSA is also associated with various conditions that increase the risk of cardiovascular diseases (CVD) themselves, such as hyperlipidemia (Gunduz et al., 2019) and atherosclerosis (Xue et al., 2017). Thus, a better understanding of OSA-associated cardiovascular disease is urgently needed, which will be helpful for improving the diagnosis and treatment of this disease.

Circular RNAs (circRNAs), a class of newly discovered noncoding RNAs, are reported to be extensively expressed across different species (Cai et al., 2019). Recently, emerging number of studies have focused on the function of circRNAs, indicating that circRNAs can modulate the function of certain miRNA by directly binding at its specific miRNA (Abbaszadeh-Goudarzi et al., 2020; A. ; Huang A. et al., 2020). Dysregulation of circRNAs has been found to be associated with multiple human diseases, including diabetes (Yang et al., 2020). For example, Zhao et al. reported that circRNAs were differentially expressed in type 2 diabetes mellitus (T2DM) and hsa_circ_0054633 may be served as a diagnostic biomarker of T2DM (Zhao et al., 2017). Furthermore, increasing studies have uncovered that some circRNAs exhibit a critical role in cancer development and progression. In non-small cell lung cancer, circNDUFB2 inhibits cancer progression and metastasis via the degradation of IGF2BPs (Li et al., 2021). To date, very little is known about the expression profile and potential role of circRNAs in OSA-induced cardiac injury.

In the current research, we first utilized circRNA microarray to investigate circRNA expression profiles in the mouse model of OSA-induced cardiac injury. Subsequently, we performed GO and KEGG enrichment analyses to annotate the biological functions of the differentially expressed circRNAs. To better understand the pathogenesis of OSA-induced cardiac injury, the functional circRNA-miRNA-mRNA regulatory modules were also constructed. Together, our findings indicated that circRNAs dysregulation may be associated with initiation and progression of OSA-induced cardiac injury and provide more potential biomarkers and new insights for OSA-related cardiovascular disease.

MATERIALS AND METHODS

Animal

Male balb/c mice (17–21g, 6 weeks old) were supplied by Beijing Weitong Lihua Experimental Animal Technology Co., Ltd., Animal experiments were performed in accordance with the NIH Guide for Laboratory Animals. All mice were provided with standard mouse diet and tap water. The Experimental Animal Ethics Committee of the Second Affiliated Hospital of Fujian Medical University approved the animal protocol of this study.

Myocardial CIH Injury Protocol

The animal model of CIH was established as previously described (Chen et al., 2019). Briefly, mice with CIH treatment were placed in the intermittent hypoxia system. The oxygen and nitrogen flow into the chamber was regulated by a gas control system. Ambient oxygen was servo-controlled to create an intermittent hypoxia condition. During a 2-min cycle, nitrogen was delivered to the chamber at a steady rate to reach 6% O_2 for 60 s. After then, compressed air was pumped into the chamber to achieve 21% O_2 for another 60 s. Mice were placed daily in the chamber for 30 cycles per h, 8 h/day for 7 days/week, for eight consecutive weeks. For the control group, mice were housed in the chamber with 21% O_2 during the entire experiment. The oxygen concentration was calculated automatically with the help of an oxygen analyzer. All mice were euthanized at the end of CIH exposure. Their left ventricular tissues were collected.

CircRNA Microarray Hybridization

A NanoDrop ND-1000 was utilized to quantify total RNA from each sample. Based on the Arraystar's standard protocols, the sample preparation and microarray hybridization were conducted. In brief, we first digested total RNAs with Rnase R (Epicentre, Inc.) to eliminate linear RNAs and enrich circular RNAs. Then, with the use of a random priming method (Arraystar Super RNA Labeling Kit), the enriched circular RNAs were amplified and transcribed into fluorescent cRNA. Subsequently, the labeled cRNAs were then hybridized to the Arraystar Mouse circRNA Array V2. At last, the arrays were scanned by the use of the Agilent Scanner G2505C after having washed the slides.

Microarray Data Analysis

The collected array images were analyzed by using Agilent Feature Extraction software (version 11.0.1.1). The R software limma package was further used by us for quantile normalization and subsequent data processing. CircRNAs exhibiting fold changes (FC) $\geq$1.5 and p-values $\leq$0.05 were considered statistically significant. Volcano plots was performed to show all differentially expressed circRNAs between the CIH and control groups. Fold change filtering was conducted to determine the differentially altered circRNAs between the two groups. Hierarchical clustering was also applied to display the distinguishable circRNA-expression patterns among the samples.

Bioinformatic Analyses

Gene Ontology (GO) analysis was carried out to determine functional annotations of differentially expressed circRNAs and their target genes, which mainly included three independent ontologies (cellular component, molecular function and biological process). Moreover, Kyoto Encyclopedia of Genes and Genomes (KEGG) analysis was further performed to clarify the functions and interactions

TABLE 1 | Primers used for qRT-PCR.

Genes	Forward and reverse sequence	Product length (bp)
β-actin	F:5′ GTACCACCATGTACCCAGGC3′ R:5′AACGCAGCTCAGTAACAGTCC3′	247
mmu_circRNA_006185	F:5′GTTACCACAAAGCAGAGAACACT 3′ R:5′GCACATTCTTCATAACATCTGG 3′	65
mmu_circRNA_014309	F:5′GTGAGAGACCTGAGAGGGATAG 3′ R:5′TTCACTAACTTCCTTACGCTAATC 3′	92
mmu_circRNA_014583	F:5′ TATAGCGCCAAGGGAAGCA 3′ R:5′ AGGTCCGGACAGCTGAGTTG 3′	57
mmu_circRNA_21856	F:5′CACTTTTTGGCTACTTTGTGCC 3′ R:5′GTGAAGACACTCACGATGGGG 3′	99
mmu_circRNA_26948	F:5′AGTATAGGCAGCTCTGGGATGA 3′ R:5′ TGCAACGATCAAAGCTGATG 3′	117
mmu_circRNA_35821	F:5′ GCAGAGTCAGAGTTCACCCAC 3′ R:5′ CCCTCACTTATTTCCTCCAAA 3′	85
mmu_circRNA_36076	F:5′ TTTGTATTGACAACTGGAGCG 3′ R:5′CCAAAGTCATAGACCATTGCCT 3′	103
mmu_circRNA_23696	F:5′ CCTAAGTGCCGTACCAGCT 3′ R:5′ TGCAGGTTATTAATGCCTCAT 3′	82
mmu_circRNA_43432	F:5′TCCATAAAGATTATTGAACTCTGA 3′ R:5′GCCTCCTGTAGTGTTGTGAAA 3′	101
mmu_circRNA_32974	F:5′ACAAAGAGGAGGAAGTCGGTC 3′ R:5′ GGTGATTTTCATCGCCAATAAT 3′	82

among these differentially expressed genes. In addition, Fisher's exact test was performed to calculate the *p*-value. Data analysis was based on the KEGG database (https://www.genome.jp/kegg/) and GO database (http://geneontology.org). The *p*-value threshold was <0.05 and the count number >2. The top 10 enrichment GO entries and KEGG pathways of the dysregulated circRNAs were ranked and selected by enrichment score [-log10 (*p*-value)].

Quantitative Real-Time Polymerase Chain Reaction (qRT-PCR)

qRT-PCR was conducted to verify the differential expression level of 10 selected circRNAs. We extracted the total RNA from cardiac tissues by using the TRIzol Reagent (Takara, Dalian, China). All primers were designed to span the distal ends of circRNAs using Primer 5 software (**Table 1**). We utilized the PrimeScript™ RT Reagent Kit (Takara, China) to synthesize cDNA. The qRT-PCR analyses were further carried out with the use of a TB Green™ Premix Ex Taq™ II (Takara, China) and an ABI Q2Real-time PCR system (Applied Biosystems, USA). *β*-actin was served as an internal control. Relative circRNAs expression was calculated by the $2^{-\Delta\Delta Ct}$ method.

Construction of a circRNA-miRNA-mRNA Regulatory Network

The two significant differentially expressed circRNAs were selected to build up a circRNA-miRNA-mRNA network by a software (Arraystar's home-made miRNA target prediction software), which was based on miRanda and TargetScan. What's more, the software that we used should consider the binding capacity of circRNA and microRNA, as well as the capacity and number of microRNA-mRNA binding sites. Finally, we visualized the established competing endogenous RNA (ceRNA) network by use of Cytoscape (Version 3.7.2).

Statistical Methods

All data in this study were from at least three independent repeated experiments. Data were expressed as the means ± standard deviation. Student's t-test was applied for comparisons between the CIH and control groups. Differences were deemed statistically significant at $p < 0.05$.

RESULTS

Overview of CircRNA Expression

We performed circRNA microarray for screening dysregulated circRNAs with six samples (3 samples from the CIH group and 3 from the control group). With a threshold of FC ≥ 1.5 and $p < 0.05$, a total of 124 differentially expressed circRNAs were found in our mouse model of OSA-induced cardiac injury. Among them, 23 circRNAs were significantly downregulated while 101 were obviously upregulated. The box plot demonstrated that the circRNA median of the six samples was not different after quantile normalization (**Figure 1A**). Meanwhile, hierarchical clustering revealed a distinguishable circRNA expression profiling between CIH and control tissues (**Figure 1B**). Furthermore, scatter plot showed the variation of circRNA expression between groups (**Figure 1C**). Volcano plots was also used for visualizing differentially expressed circRNAs (**Figure 1D**).

Classification of the dysregulated circRNAs was listed in the **Figure 2A**. The results found 101 upregulated circRNAs

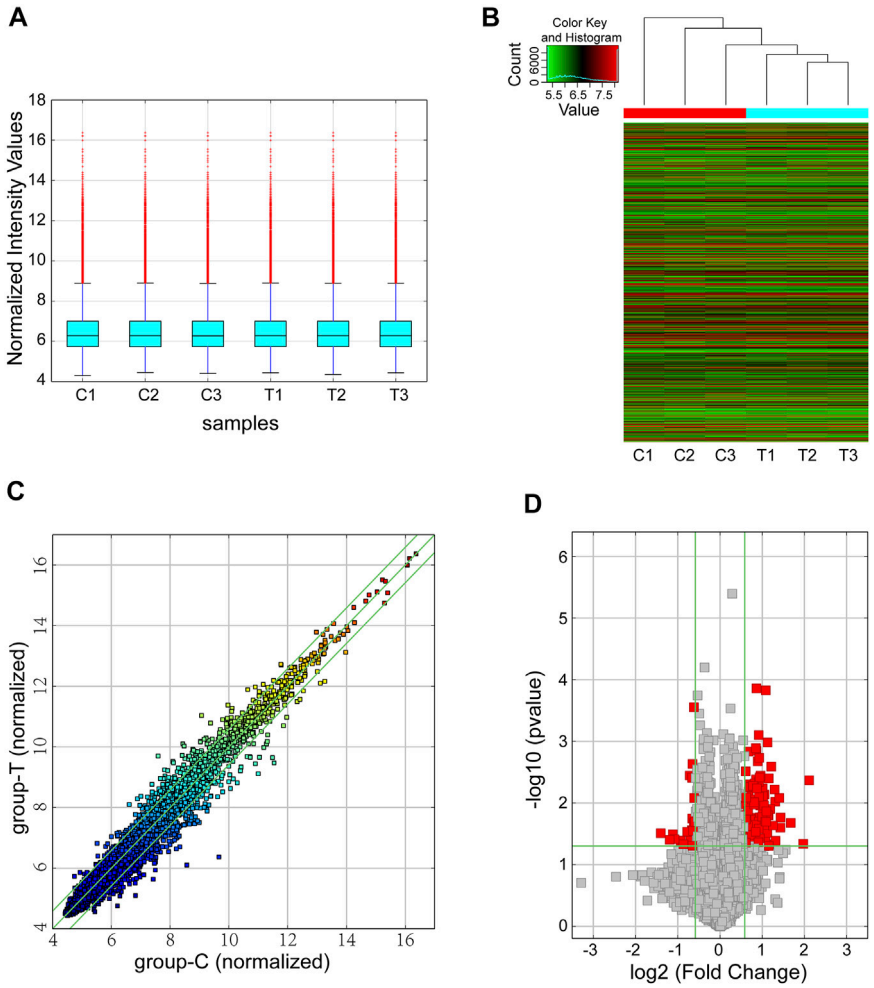

FIGURE 1 | Overview of the microarray signatures. **(A)** The box plot was performed to show the profile distributions of the normalized intensities. **(B)** Hierarchical clustering revealed the differentially expressed circRNAs between the CIH groups and control tissues. **(C)** The scatter plot demonstrated the variation of the differentially expressed circRNAs between the two groups. The green lines represented 1.5-fold changes. circRNAs below or above the green lines indicated >1.5-fold downregulation or upregulation between the two compared groups. **(D)** Differentially expressed circRNAs were displayed by using volcano plot. The vertical green lines represented a 1.5-fold down or up, respectively. The horizontal green line exhibited a *p* value of 0.05 (-log10-scaled). The red squares indicated the dysregulated circRNAs with significant difference. CIH, chronic intermittent hypoxemia.

containing 79 exonic, 6 sense-overlapping, 9 intronic, 2 antisense, and 5 intergenic regions, whereas the 23 downregulated circRNAs comprised 8 sense-overlapping, 10 exonic, 2 intergenic, 0 antisense, and 3 intronic in CIH-tissue samples. In addition, chromosomal distribution analysis revealed that most circRNAs were located at chromosome 4, while few located at the X chromosome and chromosome 13 (**Figure 2B**).

Validation of circRNA Expression

To verify the microarray data, we randomly selected 10 dysregulated circRNAs from the microarray including 5 upregulated circRNAs (mmu_circRNA_006185, 014583, 32974, 23696, and 35821) and 5 downregulated circRNAs (mmu_circRNA_ 014309, 21856, 26948, 43432, and 36076) for further verification by qRT-PCR in samples. A general consistency was demonstrated between the microarray and qRT-PCR results. That is, four selected downregulated circRNAs and four selected upregulated circRNAs were validated (**Figure 3**). Our findings were in agreement with microarray results.

GO and KEGG Analyses

To investigate the role of circRNAs on the expression of target genes, five circRNAs (2 of them were downregulated and 3 were upregulated) were further selected from the validated circRNAs to carry out GO and KEGG pathway analyses. GO analysis annotated genes targeted by the five altered expressed circRNAs, which included multiple biological processes, cellular components and molecular functions (**Figures 4A–C**). The most significant GO functions of mmu_circRNA_014309 and _21856 were related to intracellular organelle, metal ion binding, biological regulation, cation binding, regulation of

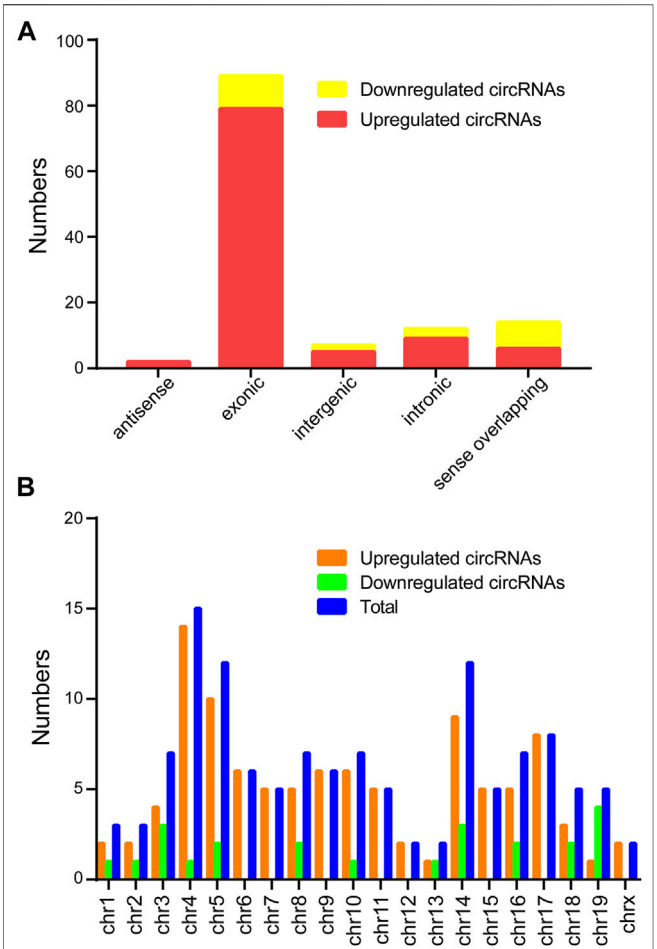

FIGURE 2 | Classification and distribution of the differentially expressed circRNAs. **(A)** Classification of the altered expressed circRNAs was listed. **(B)** The number of altered expressed circRNAs was determined in each chromosome.

biological process, intracellular, regulation of cellular process, cellular anatomical entity, cellular metabolic process, and nitrogen compound metabolic process. Additionally, KEGG pathway analysis suggested that numerous pathways involved in OSA-induced cardiac injury were associated with the dysregulated circRNAs. Our study found that enrichment of multiple key biological functions was engaged with OSA-induced cardiac damage. The results for mmu_circRNA_014309 and _21856 were listed in **Figure 4D**. The host genes of the altered expressed circRNAs were significantly associated with Pentose phosphate pathway, Cushing syndrome, the Hippo signaling pathway, Ferroptosis, and Melanogenesis.

Construction an Interaction Network of ceRNA

In order to explore the ceRNA network, the targets of dysregulated circRNAs and downstream genes were predicted by TargetScan and miRanda. In addition, to elucidate the biofunction of circRNAs took part in OSA-induced cardiac injury, we used Cytoscape software to construct a ceRNA network, based on the underlying effect of two selected circRNAs (mmu_circ_014309 and mmu_circ_21856), and their targeted miRNA and downstream mRNAs. The circRNA-miRNA-mRNA regulatory network was presented in **Figure 5**. The data indicated potential roles for the identified circRNAs as ceRNA ability of altering the expression of target genes. As shown in the picture, a total of 7 miRNAs (miR-326–5p, miR-298–5p, miR-3098–5p, miR-3086–3p, miR-6954–5p, miR-1955–5p, and miR-7088–5p) and corresponding target mRNAs were further predicted to have correlation with mmu_circRNA_21,856 in our current study. Meanwhile, a number of 20 miRNAs (mmu-miR-26b-3p, mmu-miR-26a-2-3p, mmu-miR-7039–3p, mmu-miR-7092–5p, mmu-miR-7067–5p, mmu-miR-7024–3p, mmu-miR-5107–3p, mmu-miR-6966–3p, mmu-miR-6918–5p, mmu-miR-7649–3p, mmu-miR-3473c, mmu-miR-1960, mmu-miR-7232–3p, mmu-miR-7090–5p, mmu-miR-1906, mmu-miR-1839–5p, mmu-miR-7092–5p, mmu-miR-6981–5p, mmu-miR-674–3p, and mmu-miR-7215–3p) and corresponding target mRNAs were further revealed to have correlation with mmu_circ_014309. Our finding provides us with innovative research strategy to uncover the underlying mechanism of mmu_circRNA_21,856 by revealing its associated miRNAs and investigating whether it can regulate its certain associated mRNAs expression.

DISCUSSION

To the best of our knowledge, this study is the first study reporting the specific circRNA expression profiles in the mouse model of OSA-induced cardiac injury. Additionally, we provide some potential targets and pathways of the circRNAs involved in OSA-induced cardiac damage. Our findings offer

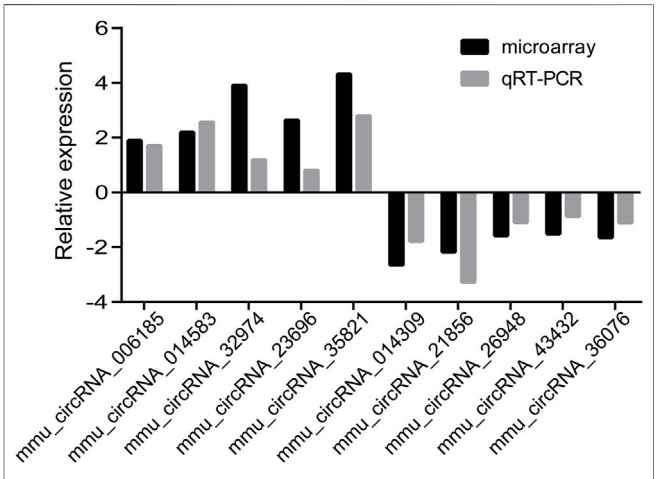

FIGURE 3 | Relative fold changes of 10 randomly selected circRNAs by qRT-PCR and microarray. The downwards indicates downregulation, while upwards indicates upregulation.

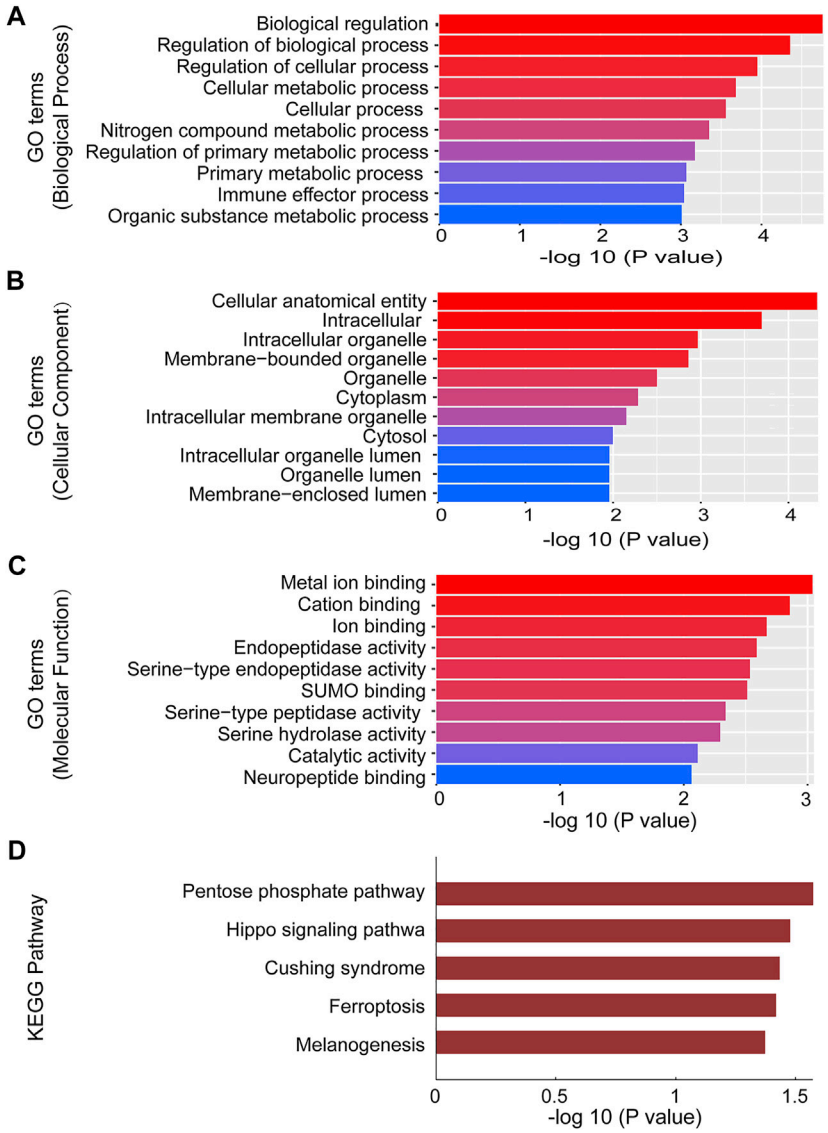

FIGURE 4 | GO and Pathway analysis of mmu_circRNA_014309 and 21856. **(A)** Top 10 GO terms in BP. **(B)** Top 10 GO terms in CC. **(C)** Top 10 GO terms in MF. **(D)** Top 6 enrichment pathways. GO, Gene Ontology; CC, cellular components; BP, biological processes; MF, molecular functions.

valuable clues to find the critical roles of circRNAs in the pathologic process of OSA-related cardiovascular disease.

As a novel heterogeneous class of ncRNAs, circRNAs have gained increased attention owing to their involvement with various forms of disease (Zhong et al., 2018). CircRNAs are abundant, endogenous, stable, conserved, and cell-type specific molecules, which could participate in regulating cell function (Kristensen et al., 2019). Increasing attention has focused on functions for circRNAs in human diseases, such as neurological diseases (W. Han et al., 2018; Chen et al., 2020a), cardiovascular disease (Zhang et al., 2020a; Tang et al., 2021), diabetes mellitus (Zhang et al., 2020b; Zaiou, 2020), and tumorigenesis (Goodall and Wickramasinghe, 2021; G. ; Huang et al., 2020b), especially cardiovascular diseases. For instance, Garikipati et al. found that circRNAs were altered expressed in the mouse model of post myocardial infarction (MI) (Garikipati et al., 2019). Furthermore, Ge et al. first revealed that a total of 185 circRNAs were significantly differentially expressed in the pathological process of ischemia/reperfusion (I/R) induced cardiac injury (Ge et al., 2019). Based on the high-throughput circRNA microarray data, we also found 101 upregulated circRNAs and 23 downregulated circRNAs in the CIH group compared with the control group. However, their roles in OSA-induced cardiac injury remain largely unknown.

To investigate the possible roles of circRNAs on OSA-induced cardiac injury, 124 differentially expressed circRNAs were identified. qRT-PCR of the 10 differentially expressed circRNAs confirmed that 8 of them were statistically significant and concordant with microarray assay results ($p < 0.05$). The main reasons for these discrepancies are: Firstly, owing

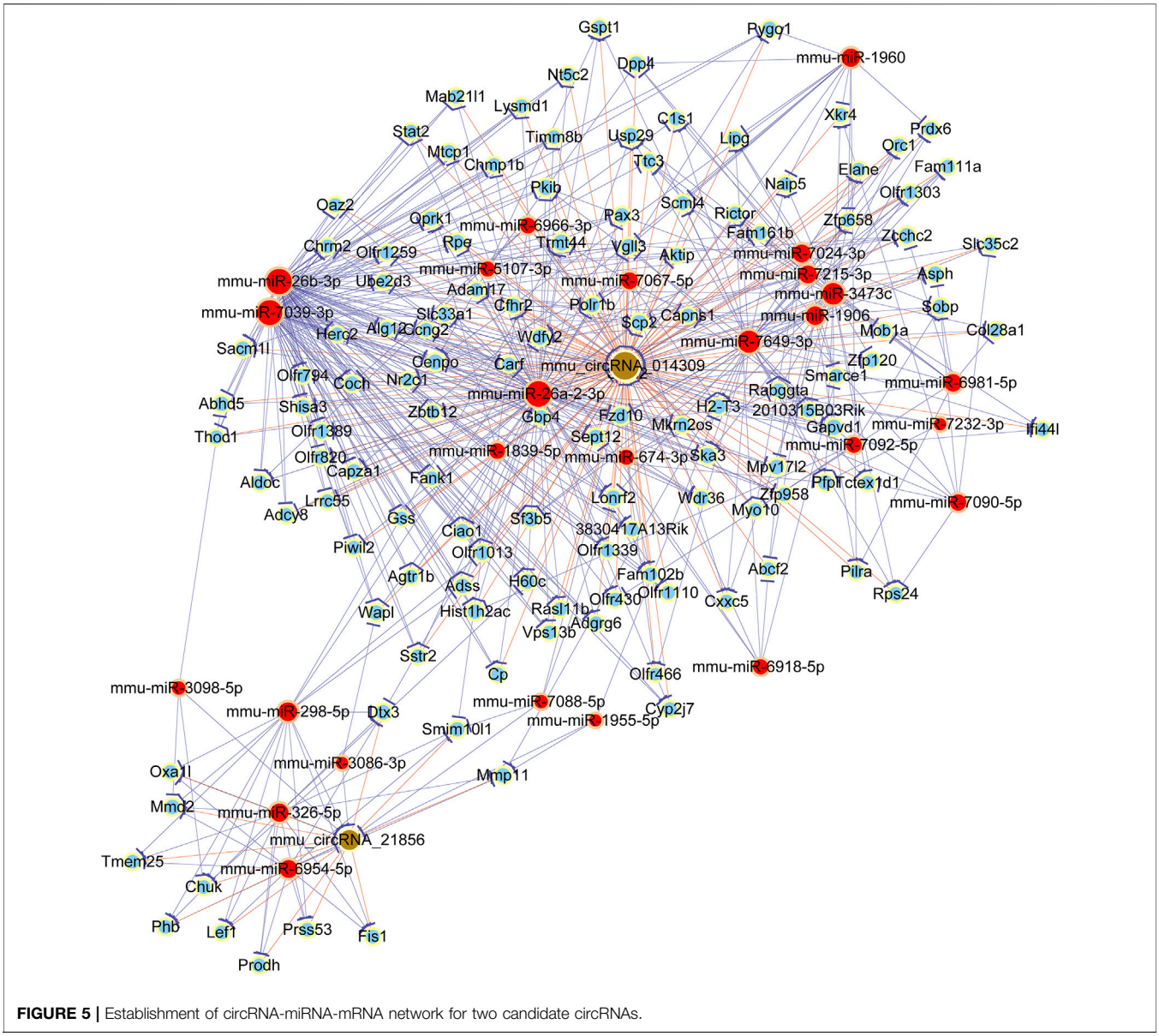

FIGURE 5 | Establishment of circRNA-miRNA-mRNA network for two candidate circRNAs.

to the high cost of circRNA microarray chips, a limited number of samples were performed for screening of circRNAs. Secondly, the microarray chip technology is highly dependent on computational analyses, there is a certain false positive rate. Thirdly, different results are likely to occur due to the inherent differences among mice, such as the degree of pathological alterations. Finally, the difference detected between the two groups may be due to the small sample size used for verification by qRT-PCR.

To unveil new insight into the potential roles of the dysregulated circRNAs in the development of OSA-induced cardiac damage, both GO and pathway analysis were further performed to predict the biological functions and underlying mechanisms of the targeted genes. The most important GO functions were associated with cellular metabolic process, regulation of biological process, biological regulation, cellular anatomical entity, and regulation of cellular process. Meanwhile, to gain more credible biological functions, KEGG pathway analysis was also carried out to identify the significant pathways. It was found that the dysregulated transcripts were related to the Hippo signaling pathway, Cushing syndrome, and Ferroptosis. Furthermore, Chen et al. demonstrated that the Ferroptosis pathway was involved in the animal model of CIH-induced liver injury (Chen et al., 2021; L. D. ; Chen et al., 2020b). Therefore, it was indicated that the Ferroptosis pathway might play an important role in the development of OSA-induced injury. Further investigations are still in urgent need to confirm these findings.

In recent years, a large number of circRNAs have been discovered. Mounting evidence has shown that circRNAs have emerged as a novel special class of endogenous noncoding RNAs. To date, more and more studies have reported strong associations

between circRNAs and cardiovascular disease (Li et al., 2020; Zhang and Wang, 2020; Yu et al., 2021). What is more, circRNAs can regulate parent gene expression or function as miRNA sponges to affect disease initiation and progression. For example, the silence of circHIPK3 could ameliorate MI-induced cardiac dysfunction *via* targeting miR-93–5p and inhibiting the Rac1/PI3K/Akt pathway (Wu et al., 2021). Recently, more studies demonstrated that circRNAs can function mainly as miRNA sponges (Misir et al., 2020). In our study, we first found many differentially expressed circRNAs in the heart tissue after CIH exposure. Meanwhile, we also predicted a putative circRNA/microRNA/mRNA interaction with the use of miRanda and TargetScan software. To our interest, we revealed that mmu_circRNA_21856 can tightly bind to miR-326–5p, which may be a potential sponge of miR-326–5p. Meanwhile, Li et al. reported that miR-326–5p could enhance the angiogenic ability of endothelial progenitor cells (EPCs) and promote functional cardiac repair of EPCs through targeting Wnt1 in an acute MI model (Li et al., 2019). mmu_circRNA_21,856 is likely to represent a novel mediator of OSA-induced cardiac injury. Therefore, we propose a hypothesis that circRNA_21,856 may act as an efficient sponge of miR-326–5p and then influence the downstream mRNAs expression. However, due to the limited available data on functions of miRNAs and circRNAs, more circRNA/microRNA interaction should be further investigated in the future research.

The present study was the first to characterize the circRNA expression profile in the process of OSA-associated cardiovascular diseases. However, several limitations should be acknowledged in this study. Firstly, due to the relatively small sample size the generalizability of the present results is difficult to establish. Secondly, the exact mechanisms of these candidate circRNAs in OSA-induced cardiac injury pathogenesis were not explored in our study. Thus, further studies will be required to investigate the function and regulatory mechanisms of these dysregulated circRNAs. Thirdly, although mice exhibit a high degree in sequence homology with humans, whether these results can also be successfully applied to humans needs further confirmation. Last, a well performed characterization of nullified and/or down-regulated mmu_circ_014,309 and mmu_circ_21856 circRNA mouse, would greatly improve the quality of the manuscript.

In conclusion, our study has provided the first evidence of differentially-expressed circRNAs in the occurrence and development of OSA-induced cardiac injury. We also have made preliminary predictions about the potential functions of these circRNAs by bioinformatics analysis and a ceRNA network. These findings may yield new insight into the underlying mechanisms of OSA-induced cardiac damage, and might present novel molecular targets for treatment of OSA-related cardiovascular disease.

DATA AVAILABILITY STATEMENT

The raw data supporting the conclusions of this article will be made available by the authors, without undue reservation.

ETHICS STATEMENT

The animal study was reviewed and approved by the Experimental Animal Ethics Committee of The Second Affiliated Hospital of Fujian Medical University, China.

AUTHOR CONTRIBUTIONS

QS and HB conceived the study. SX and LJ contributed bioinformatics methods and data analysis. PY, GF, and H provided microarray data and performed experimental validations. SX, LJ, and PY drafted the manuscript. PY, GF, and H contributed animal model. All authors revised the manuscript.

FUNDING

This work was supported by the National Natural Science Foundation of China (grant number: 82000094) and Natural Science Foundation of Fujian Province (grant number: 2020J01203).

ACKNOWLEDGMENTS

We thanked Ling Zheng and Jiayu Lin for their kind help. We thanked KangChen Bio-tech (Shanghai, China) for the microarray work.

REFERENCES:

Abbaszadeh-Goudarzi, K., Radbakhsh, S., Pourhanifeh, M. H., Khanbabaei, H., Davoodvandi, A., Fathizadeh, H., et al. (2020). Circular RNA and Diabetes: Epigenetic Regulator with Diagnostic Role. *Curr. Mol. Med.* 20 (7), 516–526. doi:10.2174/1566524020666200129142106

Belaidi, E., Morand, J., Gras, E., Pépin, J.-L., and Godin-Ribuot, D. (2016). Targeting the ROS-HIF-1-Endothelin Axis as a Therapeutic Approach for the Treatment of Obstructive Sleep Apnea-Related Cardiovascular Complications. *Pharmacol. Ther.* 168, 1–11. doi:10.1016/j.pharmthera.2016.07.010

Cai, H., Li, Y., Niringiyumukiza, J. D., Su, P., and Xiang, W. (2019). Circular RNA Involvement in Aging: An Emerging Player with Great Potential. *Mech. Ageing Develop.* 178, 16–24. doi:10.1016/j.mad.2018.11.002

Chen, L.-D., Huang, Z.-W., Huang, Y.-Z., Huang, J.-F., Zhang, Z.-P., and Lin, X.-J. (2021). Untargeted Metabolomic Profiling of Liver in a Chronic Intermittent Hypoxia Mouse Model. *Front. Physiol.* 12, 701035. doi:10.3389/fphys.2021.701035

Chen, L.-D., Wu, R.-H., Huang, Y.-Z., Chen, M.-X., Zeng, A.-M., Zhuo, G.-F., et al. (2020b). The Role of Ferroptosis in Chronic Intermittent Hypoxia-Induced Liver Injury in Rats. *Sleep Breath* 24 (4), 1767–1773. doi:10.1007/s11325-020-02091-4

Chen, Q., Lin, G., Huang, J., Chen, G., Huang, X., and Lin, Q. (2019). Expression Profile of Long Non-Coding RNAs in Rat Models of OSA-Induced Cardiovascular Disease: New Insight into Pathogenesis. *Sleep Breath* 23 (3), 795–804. doi:10.1007/s11325-018-1753-0

Chen, W., Wang, H., Feng, J., and Chen, L. (2020a). Overexpression of circRNA circUCK2 Attenuates Cell Apoptosis in Cerebral Ischemia-Reperfusion Injury via miR-125b-5p/GDF11 Signaling. *Mol. Ther. - Nucleic Acids* 22, 673–683. doi:10.1016/j.omtn.2020.09.032

de Vries, G. E., Wijkstra, P. J., Houwerzijl, E. J., Kerstjens, H. A. M., and Hoekema, A. (2018). Cardiovascular Effects of Oral Appliance Therapy in Obstructive Sleep Apnea: A Systematic Review and Meta-Analysis. *Sleep Med. Rev.* 40, 55–68. doi:10.1016/j.smrv.2017.10.004

Dobrosielski, D. A., Papandreou, C., Patil, S. P., and Salas-Salvadó, J. (2017). Diet and Exercise in the Management of Obstructive Sleep Apnoea and Cardiovascular Disease Risk. *Eur. Respir. Rev.* 26 (144), 160110. doi:10.1183/16000617.0110-2016

Garikipati, V. N. S., Verma, S. K., Cheng, Z., Liang, D., Truongcao, M. M., Cimini, M., et al. (2019). Circular RNA CircFndc3b Modulates Cardiac Repair after Myocardial Infarction via FUS/VEGF-A Axis. *Nat. Commun.* 10 (1), 4317. doi:10.1038/s41467-019-11777-7

Ge, X., Meng, Q., Zhuang, R., Yuan, D., Liu, J., Lin, F., et al. (2019). Circular RNA Expression Alterations in Extracellular Vesicles Isolated from Murine Heart post Ischemia/reperfusion Injury. *Int. J. Cardiol.* 296, 136–140. doi:10.1016/j.ijcard.2019.08.024

Goodall, G. J., and Wickramasinghe, V. O. (2021). RNA in Cancer. *Nat. Rev. Cancer* 21 (1), 22–36. doi:10.1038/s41568-020-00306-0

Gunduz, C., Basoglu, O. K., Hedner, J., Bonsignore, M. R., Hein, H., Staats, R., et al. (2019). Hyperlipidaemia Prevalence and Cholesterol Control in Obstructive Sleep Apnoea: Data from the European Sleep Apnea Database (ESADA). *J. Intern. Med.* 286 (6), 676–688. doi:10.1111/joim.12952

Han, B., Zhang, Y., Zhang, Y., Bai, Y., Chen, X., Huang, R., et al. (2018). Novel Insight into Circular RNA HECTD1 in Astrocyte Activation via Autophagy by Targeting MIR142-TIPARP: Implications for Cerebral Ischemic Stroke. *Autophagy* 14 (7), 1164–1184. doi:10.1080/15548627.2018.1458173

Huang, A., Zheng, H., Wu, Z., Chen, M., and Huang, Y. (2020a). Circular RNA-Protein Interactions: Functions, Mechanisms, and Identification. *Theranostics* 10 (8), 3503–3517. doi:10.7150/thno.42174

Huang, G., Liang, M., Liu, H., Huang, J., Li, P., Wang, C., et al. (2020b). CircRNA hsa_circRNA_104348 Promotes Hepatocellular Carcinoma Progression through Modulating miR-187-3p/RTKN2 Axis and Activating Wnt/β-Catenin Pathway. *Cell Death Dis* 11 (12), 1065. doi:10.1038/s41419-020-03276-1

Kristensen, L. S., Andersen, M. S., Stagsted, L. V. W., Ebbesen, K. K., Hansen, T. B., and Kjems, J. (2019). The Biogenesis, Biology and Characterization of Circular RNAs. *Nat. Rev. Genet.* 20 (11), 675–691. doi:10.1038/s41576-019-0158-7

Lebkuchen, A., Freitas, L. S., Cardozo, K. H. M., and Drager, L. F. (2021). Advances and Challenges in Pursuing Biomarkers for Obstructive Sleep Apnea: Implications for the Cardiovascular Risk. *Trends Cardiovasc. Med.* 31 (4), 242–249. doi:10.1016/j.tcm.2020.04.003

Li, B., Li, Y., Hu, L., Liu, Y., Zhou, Q., Wang, M., et al. (2020). Role of Circular RNAs in the Pathogenesis of Cardiovascular Disease. *J. Cardiovasc. Trans. Res.* 13 (4), 572–583. doi:10.1007/s12265-019-09912-2

Li, B., Zhu, L., Lu, C., Wang, C., Wang, H., Jin, H., et al. (2021). CircNDUFB2 Inhibits Non-small Cell Lung Cancer Progression via Destabilizing IGF2BPs and Activating Anti-Tumor Immunity. *Nat. Commun.* 12 (1), 295. doi:10.1038/s41467-020-20527-z

Li, X., Xue, X., Sun, Y., Chen, L., Zhao, T., Yang, W., et al. (2019). MicroRNA-326-5p Enhances Therapeutic Potential of Endothelial Progenitor Cells for Myocardial Infarction. *Stem Cel Res. Ther.* 10 (1), 323. doi:10.1186/s13287-019-1413-8

May, A. M., Van Wagoner, D. R., and Mehra, R. (2017). OSA and Cardiac Arrhythmogenesis. *Chest* 151 (1), 225–241. doi:10.1016/j.chest.2016.09.014

Misir, S., Hepokur, C., Aliyazicioglu, Y., and Enguita, F. J. (2020). Circular RNAs Serve as miRNA Sponges in Breast Cancer. *Breast Cancer* 27 (6), 1048–1057. doi:10.1007/s12282-020-01140-w

Porto, F., Sakamoto, Y. S., and Salles, C. (2017). Association between Obstructive Sleep Apnea and Myocardial Infarction: A Systematic Review. *Arq. Bras. Cardiol.* 108 (4), 361–369. doi:10.5935/abc.20170031

Sanderson, J. E., Fang, F., Lu, M., Ma, C. Y., and Wei, Y. X. (2021). Obstructive Sleep Apnoea, Intermittent Hypoxia and Heart Failure with a Preserved Ejection Fraction. *Heart* 107 (3), 190–194. doi:10.1136/heartjnl-2020-317326

Tang, Y., Bao, J., Hu, J., Liu, L., and Xu, D. Y. (2021). Circular RNA in Cardiovascular Disease: Expression, Mechanisms and Clinical Prospects. *J. Cel. Mol. Med.* 25 (4), 1817–1824. doi:10.1111/jcmm.16203

Wu, Y., Wu, M., Yang, J., Li, Y., Peng, W., Wu, M., et al. (2021). Silencing CircHIPK3 Sponges miR-93-5p to Inhibit the Activation of Rac1/PI3K/AKT Pathway and Improves Myocardial Infarction-Induced Cardiac Dysfunction. *Front. Cardiovasc. Med.* 8, 645378. doi:10.3389/fcvm.2021.645378

Xue, J., Zhou, D., Poulsen, O., Imamura, T., Hsiao, Y.-H., Smith, T. H., et al. (2017). Intermittent Hypoxia and Hypercapnia Accelerate Atherosclerosis, Partially via Trimethylamine-Oxide. *Am. J. Respir. Cel Mol Biol* 57 (5), 581–588. doi:10.1165/rcmb.2017-0086OC

Yang, F., Chen, Y., Xue, Z., Lv, Y., Shen, L., Li, K., et al. (2020). High-Throughput Sequencing and Exploration of the lncRNA-circRNA-miRNA-mRNA Network in Type 2 Diabetes Mellitus. *Biomed. Res. Int.* 2020, 8162524. doi:10.1155/2020/8162524

Yu, Z., Huang, Q., Zhang, Q., Wu, H., and Zhong, Z. (2021). CircRNAs Open a new era in the Study of Cardiovascular Disease (Review). *Int. J. Mol. Med.* 47 (1), 49–64. doi:10.3892/ijmm.2020.4792

Zaiou, M. (2020). CircRNAs Signature as Potential Diagnostic and Prognostic Biomarker for Diabetes Mellitus and Related Cardiovascular Complications. *Cells* 9 (3), 659. doi:10.3390/cells9030659

Zhang, C., Han, X., Yang, L., Fu, J., Sun, C., Huang, S., et al. (2020b). Circular RNA circPPM1F Modulates M1 Macrophage Activation and Pancreatic Islet Inflammation in Type 1 Diabetes Mellitus. *Theranostics* 10 (24), 10908–10924. doi:10.7150/thno.48264

Zhang, L., Zhang, Y., Wang, Y., Zhao, Y., Ding, H., and Li, P. (2020a). Circular RNAs: Functions and Clinical Significance in Cardiovascular Disease. *Front. Cel Dev. Biol.* 8, 584051. doi:10.3389/fcell.2020.584051

Zhang, N., and Wang, X. (2020). Circular RNA ITCH Mediates H 2 O 2 -Induced Myocardial Cell Apoptosis by Targeting miR-17-5p via Wnt/β-Catenin Signalling Pathway. *Int. J. Exp. Path* 102 (1), 22–31. doi:10.1111/iep.12367

Zhao, Z., Li, X., Jian, D., Hao, P., Rao, L., and Li, M. (2017). Hsa_circ_0054633 in Peripheral Blood Can Be Used as a Diagnostic Biomarker of Pre-Diabetes and Type 2 Diabetes Mellitus. *Acta Diabetol.* 54 (3), 237–245. doi:10.1007/s00592-016-0943-0

Zhong, Y., Du, Y., Yang, X., Mo, Y., Fan, C., Xiong, F., et al. (2018). Circular RNAs Function as ceRNAs to Regulate and Control Human Cancer Progression. *Mol. Cancer* 17 (1), 79. doi:10.1186/s12943-018-0827-8

Conflict of Interest: The authors declare that the research was conducted in the absence of any commercial or financial relationships that could be construed as a potential conflict of interest.

Publisher's Note: All claims expressed in this article are solely those of the authors and do not necessarily represent those of their affiliated organizations, or those of the publisher, the editors and the reviewers. Any product that may be evaluated in this article, orclaim that may be made by its manufacturer, is not guaranteed or endorsed by the publisher.

frontiers in Cell and Developmental Biology

ORIGINAL RESEARCH
published: 18 February 2022
doi: 10.3389/fcell.2022.794198

Therapeutic Effects of Kefir Peptides on Hemophilia-Induced Osteoporosis in Mice With Deficient Coagulation Factor VIII

*Chih-Ching Yen[1,2†], Yao-Wen Liu[1†], Gary Ro-Lin Chang[1†], Ying-Wei Lan[1], Yung-Tsung Kao[1,3], Shin-Nan Cheng[4], Wei Chen[5] and Chuan-Mu Chen[1,6,7]**

[1]Department of Life Sciences, and Ph.D. Program in Translational Medicine, National Chung Hsing University, Taichung, Taiwan, [2]Department of Internal Medicine, China Medical University Hospita, College of Health Care, China Medical University, Taichung, Taiwan, [3]Ph.D. Program in Tissue Engineering and Regenerative Medicine, National Health Research Institutes and National Chung Hsing University, Taichung, Taiwan, [4]Department of Pediatrics, Department of Medical Research, Tungs' Taichung Metroharbor Hospital, Taichung, Taiwan, [5]Division of Pulmonary and Critical Care Medicine, Chia-Yi Christian Hospital, Chiayi, Taiwan, [6]The iEGG and Animal Biotechnology Center, National Chung Hsing University, Taichung, Taiwan, [7]Rong Hsing Research Center for Translational Medicine, Taichung Veterans General Hospital, Taichung, Taiwan

OPEN ACCESS

Edited by:
Natalia Martins Feitosa,
Federal University of Rio de Janeiro, Brazil

Reviewed by:
Ying Yin,
Medical School of Nanjing University, China
Hongshuai Li,
The University of Iowa, United States

***Correspondence:**
Chuan-Mu Chen
chchen1@dragon.nchu.edu.tw

†These authors have contributed equally to this work

Specialty section:
This article was submitted to Molecular and Cellular Pathology, a section of the journal Frontiers in Cell and Developmental Biology

Received: 13 October 2021
Accepted: 19 January 2022
Published: 18 February 2022

Citation:
Yen C-C, Liu Y-W, Chang GR-L, Lan Y-W, Kao Y-T, Cheng S-N, Chen W and Chen C-M (2022) Therapeutic Effects of Kefir Peptides on Hemophilia-Induced Osteoporosis in Mice With Deficient Coagulation Factor VIII. Front. Cell Dev. Biol. 10:794198. doi: 10.3389/fcell.2022.794198

Osteoporosis is a clinically prevalent comorbidity in patients with hemophilia. A preventive effect of kefir peptides (KPs) on postmenopausal osteoporosis has been proved. The aim of this study was to evaluate the therapeutic effect of KPs for the treatment of osteoporosis in coagulation factor VIII (*FVIII*) gene knockout mice (F8KO), a model of hemophilia A. In this study, male F8KO mice at 20 weeks of age were orally administered different doses of KPs for 8 weeks. The therapeutic effects of KPs were shown in the femoral trabeculae and the 4th lumbar vertebrae, which increased the trabecular bone mineral density (BMD), bone volume (Tb.BV/TV), and trabecular number (Tb.N) and decreased the trabecular separation (Tb.Sp), and they were also observed in the femoral cortical bones, in which the mechanical properties were enhanced in a dose-dependent manner. Characterization of receptor activator of nuclear factor κB ligand (RANKL), osteoprotegerin (OPG), and interleukin 6 (IL-6) demonstrated that the serum RANKL/OPG ratio and IL-6 levels were significantly decreased in the F8KO mice after the KP treatment. Tartrate-resistant acid phosphatase (TRAP) staining of mature osteoclasts indicated that the therapeutic effect of KPs in F8KO mice was associated with the functions of KPs to inhibit RANKL-induced osteoclastogenesis by reducing serum RANKL/OPG ratio and IL-6 secretion. The present study is the first to address the potentials of KPs for the treatment of hemophilia-induced osteoporosis in mice and it also provides useful information for the application of KPs as a complementary therapy for the treatment of osteoporosis in hemophilic patients.

Keywords: hemophilia A, osteoporosis, coagulation factor VIII, kefir peptides, micro-CT, osteoclast

1 INTRODUCTION

Hemophilia is a mostly X-linked genetic disease in which bleeding cannot be stopped normally. The incidence of hemophilia is approximately 1 in 10,000 births, and more than 400,000 estimated patients are affected worldwide based on the World Federation of Hemophilia survey (www.wfh.org). There are two main types of hemophilia: hemophilia A, which is caused by a deficiency of coagulation factor VIII (FVIII) and accounts for 80–85% of the total hemophilia population, and hemophilia B, which is caused by a deficiency of coagulation factor IX (Srivastava et al., 2013). With proper treatment and improved medical management, the mortality rates for hemophilic patients have declined substantially. However, some underestimated comorbidities, such as osteoporosis, arthropathy, and sarcopenia, have made the prognosis of hemophilia more difficult.

Osteoporosis is a systemic bone disorder characterized by low bone mineral density (BMD) and deteriorated bone microarchitecture, and it leads to increased risks of bone fragility and fracture. Many studies have indicated that osteopenia (low BMD) and osteoporosis are prevalent in patients with hemophilia (PWH). In a previous study of young children with hemophilia, Tlacuilo-Parra *et al.* reported that 35% of them were diagnosed with low lumbar spine BMD (Tlacuilo-Parra et al., 2011). In a recent cross-sectional study of adult PWH, Kiper *et al.* reported that 34.8% of patients younger than 50 years had low BMD and 66.6% of patients older than 50 years had osteoporosis (Kiper Unal et al., 2017). In a retrospective study of PWH ≥18 years, Ulivieri *et al.* found that 74 and 54% of the patients exhibited reduced BMD at the femur and the lumbar spine, respectively (Ulivieri et al., 2018). These studies suggested that osteoporosis in PWH is underestimated and that the bone health of PWH should be properly managed because it may aggravate the diseases associated with hemophilia and affect the physical and mental health of patients.

Prophylaxis with factor VIII replacement therapy, regular weight-bearing exercise, adequate calcium and vitamin D supplementation, and fall prevention are usually recommended to promote bone health and prevent low BMD in PWH (Kempton et al., 2015). If pharmacological treatment of osteoporosis in PWH is needed, then the treatment approach is guided by medications to treat osteoporosis in the general population. Most current medications to treat osteoporosis fall into the category of antiresorptives. Bisphosphonates (BPs) (alendronate, ibandronate, etc.) are the first-line antiresorptive agents to prevent and treat osteoporosis in postmenopausal women. However, only one clinical trial using ibandronate has been reported in PWH thus far, and the results demonstrated that ibandronate was well tolerated and that oral administration of monthly 150 mg ibandronate for 12 months led to an increase in lumbar BMD and reduced bone resorption in a cohort of PWH (mean age 43.5 years) (Anagnostis et al., 2013). Teriparatide, a recombinant human parathyroid hormone 1–34, is an expensive, and active anabolic agent to treat patients with severe osteoporosis. Treatment with teriparatide has been shown to stimulate the maturation of circulating osteoblast precursors (D'Amelio et al., 2012) and reduce vertebral fracture risks (Napoli et al., 2018; Díez-Pérez et al., 2019). Long-term use of BPs is associated with an increased risk of osteonecrosis of the jaw (ONJ) (Lee et al., 2013; Chiu et al., 2014), and BP can reside in the bone with an estimated half-life of 10–20 years; however, whether any adverse effects occur has not been clarified (Khan et al., 1997). Furthermore, the incidence of medication-related ONJ in patients with underlying malignant diseases (cancer) taking BPs can reach 15%, whereas this value is only 0.01% in patients with osteoporosis (Mücke et al., 2016). The choice and decision of which medication to use depends mostly on its side effect profile and should be undertaken by consulting with an experienced clinician.

Kefir is a fermented dairy product that can be traced back to ancient Caucasus tribes, and it is produced from complex symbiotic grains that mainly contribute lactic acid bacteria, yeasts, and their metabolic products. Kefir-derived products, such as peptides, polysaccharides, and short-chain fatty acids, are subjects of great interest in Western scientific communities due to their health-promoting properties, including antimicrobial, anticancer, antiallergenic, immunomodulation, lactose and cholesterol metabolism, gastrointestinal health, and wound healing properties (Bourrie et al., 2016; Fiorda et al., 2017; Rosa et al., 2017). Our previous investigations using mouse and rat models of postmenopausal osteoporosis revealed the bone-protective efficacy of kefir peptides (KPs) (Chen et al., 2015). We found that the loss of bone mass was prevented and the skeletal microarchitecture and mechanical properties were improved in ovariectomized mice or rats after 12 weeks of oral administration of KPs at different dosages (164, 328, and 648 mg/kg/day), and the bone-protective extent of KPs displayed a dose-dependent effect and was comparable to that of the first-line antiresorptive agent alendronate (Chen et al., 2015; Tu et al., 2020). In a controlled, parallel, double-blind clinical trial of 65 osteoporosis patients, we demonstrated that the baseline turnover and the 6-month BMD change were significantly improved among the patients receiving KPs (1,600 mg KPs +1,500 mg $CaCO_3$) compared to those receiving the placebo (1,500 mg $CaCO_3$) (Tu et al., 2015).

Based on our previous success in OVX models and clinical trials, the present study used an animal model of *FVIII* knockout (F8KO)-induced hemophilia to evaluate the therapeutic efficacy of KPs in the treatment of osteoporosis in PWH. Initially, we analyzed the femoral bones of the F8KO mice at the age of 20 weeks to confirm the incidence of osteoporosis and then orally administered different doses of KPs for 8 weeks. Microcomputed tomography (μ-CT) for bone microarchitecture (BMD, Tb.BV/TV, Tb.N, and Tb.Sp), nanoindentation for mechanical properties (hardness and elastic modulus), and serum markers for bone remodeling (IL-6, RANKL/OPG ratio) were applied for extensive evaluations.

2 MATERIALS AND METHODS

2.1 Kefir Peptide Preparation

The KPs powder (KEFPEP®) used in this study was provided by Phermpep Biotech. Co., Ltd. (Taichung, Taiwan) as described previously (Chen et al., 2015). The peptide content was determined to be 23.1 g/100 g by the O-phthalaldehyde (OPA) method using triglycine as a standard of calibration (Tu et al., 2015; Chen et al., 2020; Tung et al., 2020).

2.2 Animals and Experimental Design

The experimental procedures and animal handling were approved by the Institutional Animal Care and Use Committee of National Chung Hsing University, Taiwan (IACUC 103–100). A total of 11 male wild-type (WT) mice (C57BL/6J) and 37 male *FVIII* knockout (F8KO) mice (129S4-F8tm1Kaz/J) with FVIII levels of <1% were used in this study. WT and F8KO mice were purchased from BioLASCO Taiwan Co., Ltd. (Taipei, Taiwan) and Jackson Laboratory (Farmington, CT, USA), respectively. During the experimental period, all mice were housed in a room with an individual ventilation cage system (IVC) and maintained at 24–25°C and 50–60% humidity with a 12-h light/dark cycle, and a standard SPF chow diet (#1324–10SPF, Altromin, Germany) and sterile drinking water were provided *ad libitum*.

At the age of 20 weeks, blood was collected from WT and F8KO mice (each $n = 5$) to measure the FVIII activity and coagulation time and then sacrificed first to obtain the femoral bones for histopathological and μ-CT analyses. The other WT mice ($n = 6$) and F8KO mice ($n = 32$) were divided into five groups according to the different treatments: 1) WT (H_2O; $n = 6$), 2) mock (H_2O; $n = 8$), 3) KL (low-dose of KPs, 164 mg/kg body weight per day; $n = 8$), 4) KM (medium-dose of KPs, 328 mg/kg body weight per day; $n = 8$), and 6) KH (high-dose of KPs, 656 mg/kg body weight per day; $n = 8$). KPs were dissolved in H_2O and administered through oral gavage for 8 weeks. Mouse body weight and food intake were recorded every week. At the end of the study, mice were anesthetized by intraperitoneal injection of 2.5% avertin (2,2,2-tribromoethanol; Sigma–Aldrich, St. Louis, MO, USA), blood was collected by orbital sinus sampling, and then the lumbar vertebrae and bilateral femoral bones were removed. The lumbar vertebrae and left femoral bones were immersed in 10% formalin for further characterization, and the right femoral bones were used for the isolation of bone marrow cells.

2.3 Measurement of FVIII Activity and Blood Coagulation Time

Mice were anesthetized and 90 μl of blood was collected and mixed with 10 μl of 3.2% sodium citrate. Citrated blood was added to a Coag Dx Analyzer (IDEXX, Westbrook, Maine, USA) for the activated partial thromboplastin time (aPTT) test. FVIII activity was measured by an FVIII Chromogenic Assay kit (Siemens, Marburg, and Germany) according to the manufacturer's manual instructions.

2.4 Histopathological Analysis

To prepare femur tissue sections for hematoxylin and eosin (H&E) staining, the femur bones were decalcified in Decalcifier I® solution (Leica Microsystems Inc., Buffalo Grove, IL, USA), dehydrated in a series of 50, 60, 70, 80, 90 and 100% ethanol, embedded in paraffin and longitudinally sectioned at 2–3 μm (Chen et al., 2021; Wang et al., 2021). The femur tissue sections were submitted to H&E staining using a Sakura model DRS-60A automatic slide stainer (Tissue-Tex DRS, Sakura, and Japan). The area of trabecular bones in the H&E stain images were quantified using ImageJ software. In addition, TRAP staining was also performed using a Leukocyte Acid phosphatase kit (#387A, Sigma–Aldrich) according to the manufacturer's instructions.

2.5 Microcomputed Tomography

The 4th lumbar vertebrae and left femur bone were used to analyze the trabecular and cortical bone parameters with a high-resolution μ-CT scanner (SkyScan 1,174, SkyScan, Aartselaar, and Belgium). Each sample was scanned at a resolution of 8 μm, rotation step of 0.3°, voltage of 50 kV, amplitude of 800 μA, exposure of 2,500 milliseconds, and reconstruction angular range of 182.7° (Chen et al., 2015). The mineralized bone phase of each resulting image was extracted using a fixed threshold and a low-pass filter to remove noise. A total of 487 two-dimensional (2D) images in each sample (a thickness of 4 mm of lumbar vertebrae or distal femur epiphysis) were reconstructed to obtain its three-dimensional (3D) image. In each 2D image, the trabecular bone was isolated from the cortical bone by manual contouring analysis. From the volume of interest (VOI), the bone mineral density (BMD), bone volume/total volume (BV/TV), trabecular number (Tb.N), trabecular thickness (Tb.Th), and trabecular separation (Tb.Sp) were obtained (Tu et al., 2020).

2.6 Nanoindentation

Nanoindentation was used to evaluate how KPs change the mechanical properties of cortical bones. To prepare the samples for nanoindentation, the bones were embedded in epoxy resin (Struers Inc., Cleveland, OH, USA), and then the surfaces of the embedded bone samples were polished by a milling machine. Nanoindentation was performed using a nanoindenter (Tribolab, Hysitron Inc., Eden Prairie, MN, USA) equipped with a Berkovich diamond indenter (tip radius 50 nm). Each bone was indented from the outer side to the inner side (near the bone marrow), with a total of 10 indents. The parameter settings of the instrument were obtained from our previous studies (Chang et al., 2011; Wang et al., 2013). The mechanical elasticity and hardness of the cortical bones were calculated according to the indentation load-depth curves and the Oliver-Pharr relation.

2.7 Measurements of Serum Bone Markers and Cytokines

The following bone markers and proinflammatory cytokines in mouse serum were measured using commercially available kits

according to the manufacturer's manual instructions: alkaline phosphatase (ALP) (Catalog #K412–500, BioVision, Milpitas, CA, USA), osteocalcin (OC) (Catalog #SEA471Mu, USCN Life Science Inc., Wuhan, China), cross-linked C-telopeptide of type I collagen (CTX1) (Catalog #CEA665Mu, USCN Life Science Inc.), osteoprotegerin (OPG) (Catalog #MOP00, R&D Systems Inc., Minneapolis, MN, USA), receptor activator of nuclear factor κ-B ligand (RANKL) (Catalog #MTR00, R&D Systems Inc.), interleukin-1α (IL-1α) (Catalog #ab113344, Abcam, Cambridge, MA, USA), IL-1β (Catalog #ab108866, Abcam), IL-6 (Catalog #ab100712, Abcam) and tumor necrosis factor-α (TNF-α) (Catalog #ab208348, Abcam). The measurements were conducted by an automated microplate reader (Tu et al., 2021).

2.8 *In vitro* Osteoclast Differentiation

The right femoral bone was used for the isolation of bone marrow cells. Briefly, the removed bones were washed with 70% ethanol for a few seconds and then immersed in Dulbecco's phosphate-buffered saline (D-PBS) (Grand Island, NY, USA). The two ends of the epiphysis were cut off, and the cells were flushed from the bone marrow cavity with α–MEM (Sigma–Aldrich). The marrow content was passed through a 70-μm mash and sequentially suspended in RBC lysis buffer (0.15 M NH_4Cl, 10 mM $NaHCO_3$, 0.1 mM EDTA, pH 7.2–7.4), D-PBS, and complete α–MEM growth media (α-MEM containing 10% fetal bovine serum, 100 U/ml penicillin, 100 mg/ml streptomycin). The cells (8×10^5 cells/cm^2) were inoculated and incubated at 37°C and 5% CO_2 for 24 h. Nonadherent cells were removed, and adherent bone marrow cells were cultured in fresh complete α–MEM growth media supplemented with RANKL (50 ng/ml) and M-CSF (25 ng/ml) for osteoclast differentiation. The cultural media were replaced every 3 days. On the 15th day, the differentiated osteoclasts were assessed by TRAP staining.

In addition, the effect of KPs was also tested in the culture of bone marrow macrophages (BMMs) (Weischenfeldt and Porse, 2008), which were prepared from the femurs of 5-week-old wild-type mice. The marrow contents of femurs were flushed and cultured overnight in complete α–MEM growth media containing M-CSF (25 ng/ml). Nonadherent cells were transferred to new tissue plates to culture stroma-free bone marrow cells. After 3 days, the adherent cells were harvested as BMMs, which were cultured on 96-well culture plates with fresh medium containing M-CSF and RANKL (50 ng/ml) and various concentrations of KPs. The culture medium was refreshed once on the 3rd day. On the 5th day, TRAP staining was performed. The TRAP-positive multinucleated cells (≥3 nuclei) were considered as mature osteoclasts.

2.9 Statistical Analysis

The results are presented as the mean ± SEM (n = 6–8) and were graphed using GraphPad Priam software version 6.0. Statistical analysis was performed using IBM SPSS Statistics software version 20. Group differences were examined based on a one-way ANOVA and Duncan's post hoc test, and significant differences ($p < 0.05$) are indicated by * vs. WT group, # vs. mock group.

3 RESULTS

3.1 F8KO Mice Develop Osteoporosis at the Age of Twenty Weeks

Initially, blood was collected from 5 WT and 5 F8KO mice at the age of 20 weeks to measure the FVIII activity and coagulation time and then sacrificed to obtain the femoral bones for histopathological and μ-CT analyses. As shown in **Figure 1**, FVIII activity was significantly reduced to <1% in the F8KO mice compared with the normal WT mice ($p < 0.001$; **Figure 1A**), and the blood coagulation time of the F8KO mice significantly increased from 102 to 300 sec ($p < 0.01$; **Figure 1B**). Histopathological H&E staining (**Figure 1C**) and femoral μ-CT images (**Figure 1D**) revealed a significant loss of trabecular bone in the F8KO mice compared with the WT mice. The average trabecular BMD of the F8KO mice was 0.239 g/cm^3, thus accounting for a 15.8% reduction compared to the WT mice (0.284 g/cm^3) ($p < 0.001$) (**Figure 1E**). With regard to the changes in the bone microarchitecture, the average bone volume (Tb.BV/TV) was reduced by 56.1% in the F8KO mice (F8KO: 6.28% vs. WT: 14.31%) ($p < 0.001$) **(Figure 1F**), and the average bone number (Tb.N) was reduced by 60% in the F8KO mice (F8KO: 1.4 mm^{-1} vs. WT: 2.9 mm^{-1}) ($p < 0.001$) (**Figure 1G**), and the average bone thickness (Tb.Th) was reduced by 10.2% in the F8KO mice (F8KO: 0.044 mm vs WT: 0.049 mm) ($p < 0.01$) (**Figure 1H**); in contrast, the average bone separation (Tb.Sp) increased 38.8% in the F8KO mice (F8KO: 0.29 mm vs WT: 0.21 mm) ($p < 0.001$) (**Figure 1I**). These data confirmed that the F8KO mice developed osteoporosis at the age of 20 weeks.

3.2 Effects of KP Treatment on Bone Histopathological and Architectural Changes

As shown in **Figure 2A**, histological examination of the femur bones revealed no histopathological changes in the WT group while bone specimens from the F8KO mice without treatment showed significant trabecular bone loss. After 8 weeks of KP treatment, specimens from F8KO mice that received different doses of KP treatment showed significant recovery of trabecular bones and exhibited a comparable morphology with those of normal WT mice. The quantitative data of the areas of trabecular bones in the H&E images from each group were consistent with these findings (**Figure 2A**). In the μ-CT 3D image observation, we also demonstrated that the loss of trabecular bone in the femur of the F8KO mice was successfully recovered after 8 weeks of KP treatment in a dose-dependent manner (**Figure 2B**). These results demonstrated that oral administration of KPs inhibited osteoporosis and recovered the lost bone structure in the F8KO mice.

3.3 Effects of KP Treatment on Bone Mineral Density and Bone Parameters

To investigate whether KPs can improve bone mass and cause changes in the microarchitecture of the distal femur in the F8KO

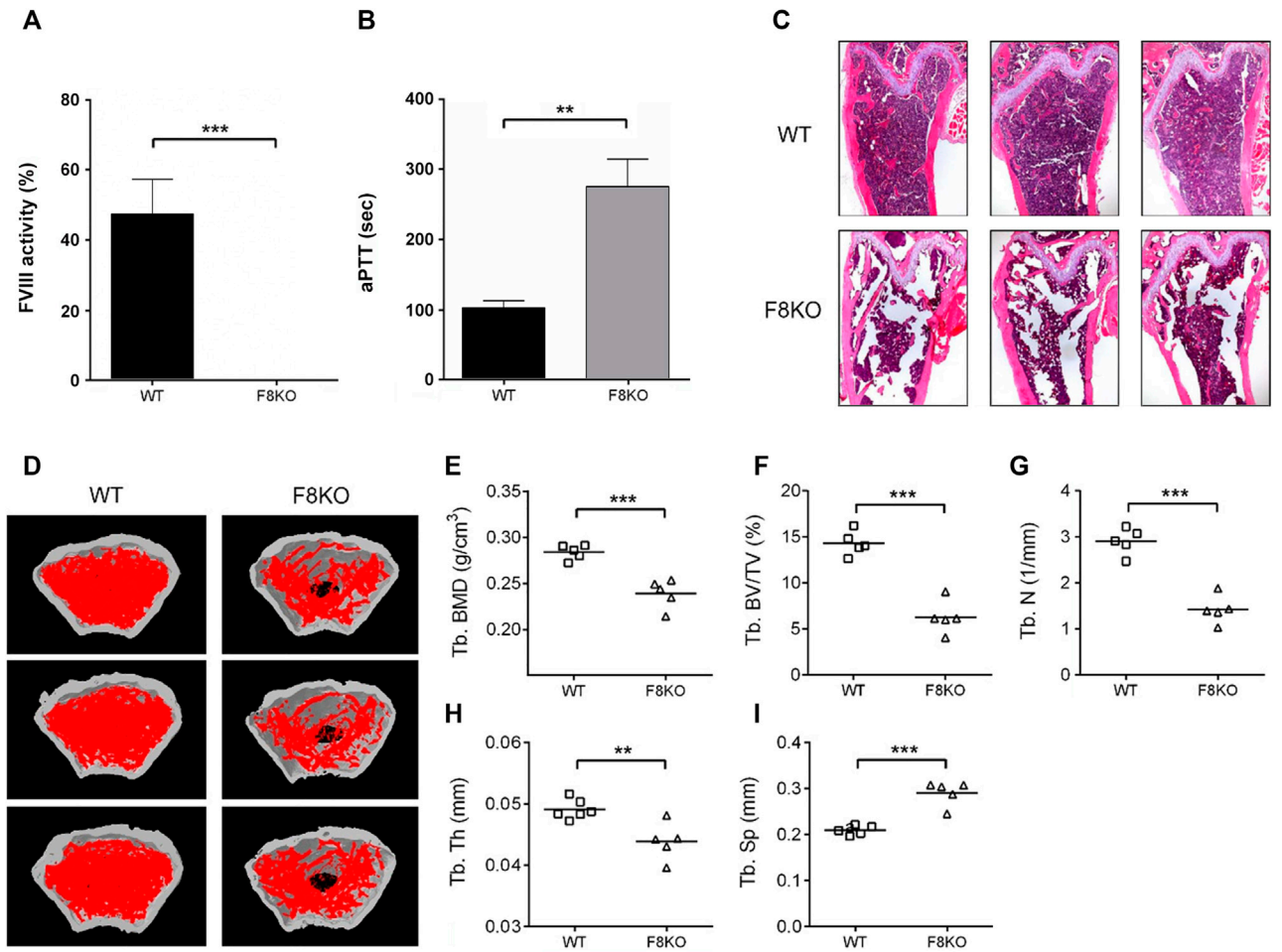

FIGURE 1 | Comparison of blood coagulation activity and femoral structures between *FVIII* knockout mice (F8KO) and C57BL/6J wild-type mice (WT) at 20 weeks of age. **(A)** Blood FVIII activity measurements of male F8KO (n = 5) and WT (n = 5) mice were performed using an FVIII Chromogenic Assay kit. **(B)** Activated partial thromboplastin time (aPTT) tests of male F8KO (n = 5) and WT (n = 5) mice were performed using a Coag Dx Analyzer. **(C)** Hematoxylin and eosin (H&E) staining of femur tissue sections of male F8KO and WT mice for bone histopathological analysis. **(D)** Microcomputed tomography (μ-CT) analysis was performed to characterize femoral architectural structures. Representative images of femur trabecular morphology plotted in red. The quantitative μ-CT results of **(E)** trabecular bone mineral density (Tb.BMD), **(F)** trabecular bone volume/total volume (Tb.BV/TV), **(G)** trabecular number (Tb.N), **(H)** trabecular thickness (Tb.Th), and **(I)** trabecular separation (Tb.Sp) were shown as indicated (**p < 0.01, ***p < 0.001 vs. WT group).

mice, a μ-CT analysis was performed, as shown in **Figure 3A** for the femoral front view and the cross-section of trabecular images. Compared to the WT mice that had dense cancellous bone, the F8KO mice that received mock treatment had relatively less cancellous bone. However, the F8KO mice that received different dosages of KPs exhibited a recovered trabecular bone network, which seemed to be positively correlated with the given dosage of KPs (**Figure 3A**).

The mock group had a markedly reduced trabecular BMD (0.146 g/cm^3) compared with the normal WT group (0.195 g/cm^3). After 8 weeks of treatment with KPs, the trabecular BMD was 0.154 g/cm^3 in the KL group, 0.143 g/cm^3 in the KM group, and 0.183 g/cm^3 in the KH group. The results showed that high-dose KP treatment significantly increased the trabecular BMD of the distal femur by 125% compared to that of the mock group (p < 0.05; **Figure 3B**).

Consistent with **Figure 1**, after 8 weeks of treatment, the trabecular microarchitecture in the mock group showed significant changes in the levels of Tb. BV/TV, Tb.N, Tb.Sp, and Tb.Th (1.19%, 0.27 mm^{-1}, 0.54 mm, and 0.042 mm, respectively) compared with the WT group (4.61%, 1.02 mm^{-1}, 0.30 mm, and 0.045 mm, respectively, p < 0.05 or p < 0.001) (**Figures 3C–F**). Treatment with different doses of KPs in the KL, KM, and KH groups increased the levels of Tb.BV/TV (2.13, 1.99, and 2.82%, respectively, **Figure 3C**) and Tb.N (0.53, 0.47, and 0.67 mm^{-1}, respectively, **Figure 3D**), decreased the levels of Tb.Sp (0.41, 0.44, and 0.36 mm, respectively, **Figure 3E**), and caused slight changes in Tb.Th (0.042, 0.043, and 0.043 mm, respectively, **Figure 3F**). Thus, treatment with KPs restored the F8KO-induced changes in the trabecular microarchitecture, and the changes in the KH group reached statistical significance.

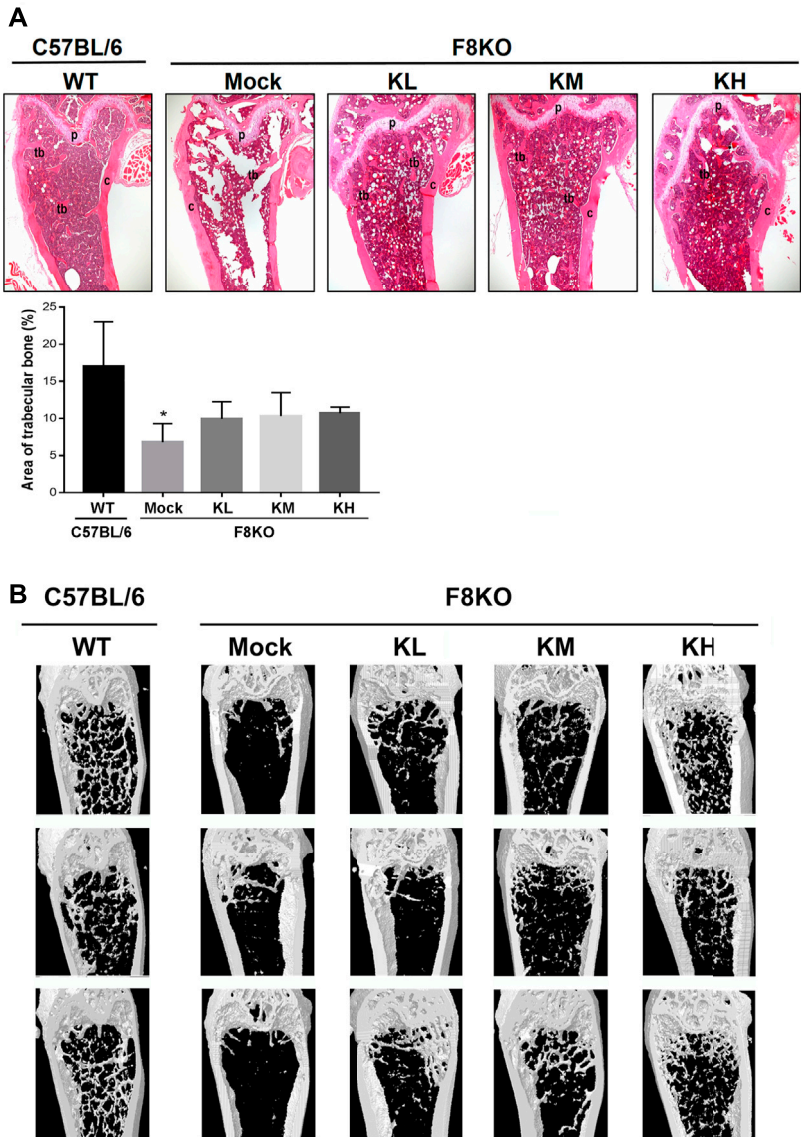

FIGURE 2 | Femur bone histopathological and microarchitectural changes in osteoporotic F8KO mice after kefir peptide (KP) treatment. **(A)** Representative H&E staining images of femur vertical sections of male F8KO mice after treatment with different dosages of KPs for 8 weeks ($n = 8$). C57BL/6J wild-type (WT) mice were used as a normal control. The area of trabecular bone in the H&E images were quantified using ImageJ software as indicated. Tb, trabecular bone; C, cortical bone; P, growth plate. *$p < 0.05$ vs WT group. **(B)** Representative μ-CT 3D images of distal femur vertical sections of male F8KO mice after different dosages of KP treatment for 8 weeks ($n = 8$). The C57BL/6J wild-type (WT) group indicates normal trabecular bone morphology in the distal femur, and the F8KO mock group indicates server trabecular bone loss as a hemophilia-induced osteoporotic mouse. KL: low-dose KP-treated group, 164 mg/kg/day; KM: medium-dose KP-treated group, 328 mg/kg/day; KH: high-dose KP-treated group, 656 mg/kg/day.

3.4 Effects of KP Treatment on the Mechanical Properties of Cortical Bones

Figure 4 shows the change in the mechanical properties of cortical bone in different groups by nanoindentation analysis. Distal femoral bones were embedded in resin, and a diamond indenter was used to indent the polished cortical surfaces from the outer to the inner side (**Figure 4A**). The cortical hardness (**Figure 4B**) and elastic modulus (**Figure 4C**) in the F8KO mice receiving mock treatment were dramatically reduced to 0.52 and 21.8 GPa, respectively, compared to the WT mice (1.00 and 29.8 GPa, respectively, $p < 0.001$). After 8 weeks of treatment with different dosages of KPs, the cortical hardness and elastic moduli in the F8KO mice significantly increased to 0.74/25.2 GPa in the KL group ($p < 0.05$), 0.81/26.8 GPa in the KM group ($p < 0.05$), and 0.89/28.2 in the KH group ($p < 0.01$). Thus, oral administration of KPs significantly improved the mechanical properties of cortical bone in the F8KO mice.

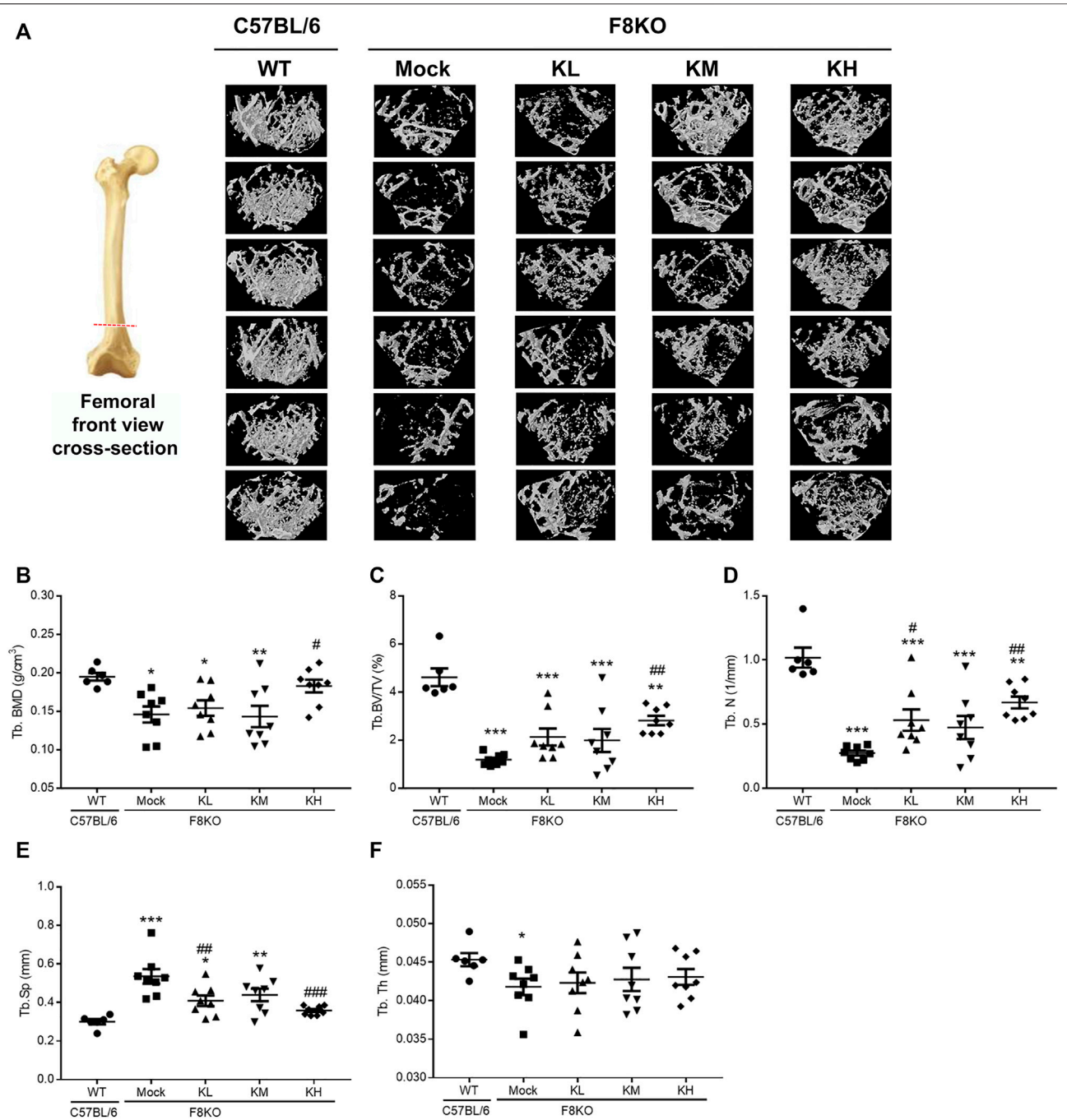

FIGURE 3 | Effects of KP treatment on femoral trabecular bone. F8KO mice at 20 weeks of age were orally administered different dosages of KPs for 8 weeks (n = 8). At the end of treatment, the mice were sacrificed and left femur bones were analyzed by μ-CT to characterize the changes in bone microarchitectural parameters. **(A)** Representative trabecular morphological images of transverse-sectional distal femur bone. The quantitative μ-CT results for **(B)** Tb.BMD, **(C)** Tb.BV/TV, **(D)** Tb.N, **(E)** Tb.Sp, and **(F)** Tb.Th. $^{*}p < 0.05$, $^{**}p < 0.01$, and $^{***}p < 0.001$ vs. WT group; $^{\#}p < 0.05$, $^{\#\#}p < 0.01$, and $^{\#\#\#}p < 0.001$ vs. mock group.

3.5 Effects of KP Treatment on the Lumbar Vertebrae

A μ-CT analysis was performed on the 4th lumbar vertebrae of the mice. As shown in **Supplementary Figure S1A**, the mock F8KO mice had fewer trabeculae than the WT mice. Although not obvious in appearance, the trabeculae were improved in the F8KO mice treated with KPs. Morphometric results showed that the KP treatments did not cause significant change in lumbar Tb.BV/TV ratio (**Supplementary Figure S1B**) but resulted in 4.6, 6.3, and 7.4% increases in lumbar Tb.N (**Supplementary Figure S1C**) and 6.9, 7.9, and 10.1% reductions in lumbar Tb.Sp (**Supplementary Figure S1D**) in

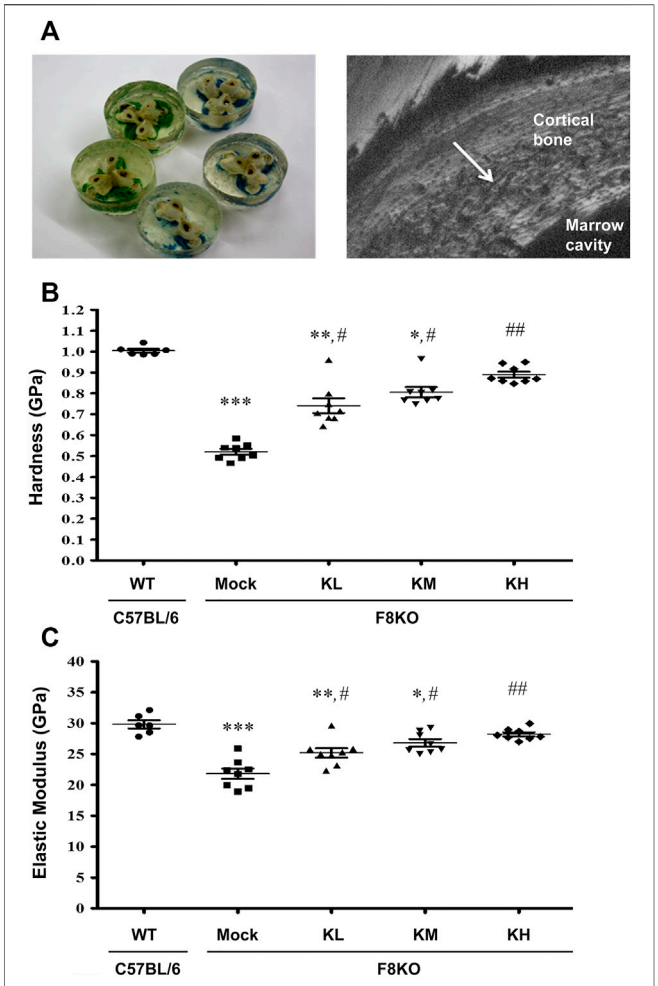

FIGURE 4 | Effects of KP treatment on the mechanical properties of femoral cortical bone. **(A)** Transverse-dissected distal femur bones were embedded in resin (*left*), and a diamond indenter was used to microindent the polished surfaces of the cortical bone from the outer side to the inner side for 10 points by nanoindentation, as shown in a scanning electronic microscopy image (*right*). The quantitative results exhibited the mechanical properties of **(B)** hardness and **(C)** elastic modulus. $^{*}p < 0.05$, $^{**}p < 0.01$, and $^{***}p < 0.001$ vs. WT group; $^{\#}p < 0.05$, $^{\#\#}p < 0.01$ vs. mock group.

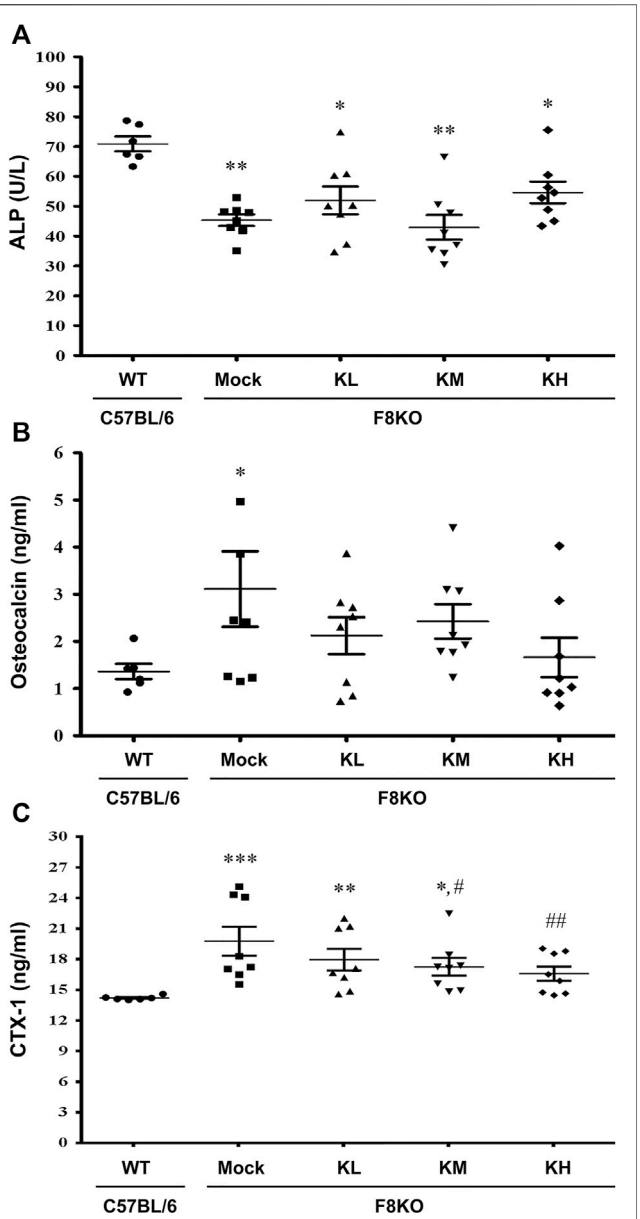

FIGURE 5 | Effects of KP treatment on serum bone turnover markers. F8KO mice at 20 weeks of age were orally administered different dosages of KPs for 8 weeks ($n = 8$). At the end of treatment, mouse blood was collected for bone turnover marker detection. The quantitative data revealed the levels of **(A)** alkaline phosphatase (ALP), **(B)** osteocalcin (OC), and **(C)** C-telopeptide of type I collagen (CTX1) for the KP-treatment groups with different dosages. $^{*}p < 0.05$, $^{**}p < 0.01$, $^{***}p < 0.001$ vs. WT group; $^{\#}p < 0.05$, $^{\#\#}p < 0.01$ vs. mock group.

the KL, KM, and KH groups, respectively, compared to the mock group. The changes with high-dose KP treatment were statistically significant ($p < 0.05$) and comparable to the WT mice.

3.5.1 Effects of KP Treatment on Serum Bone Turnover Markers

Serum biochemical markers of bone formation (ALP and OC) and bone resorption (CTX-1) were analyzed in this study. As shown in **Figure 6**, a significant decrease in ALP ($p < 0.01$) and significant increases in OC ($p < 0.05$) and CTX-1 ($p < 0.001$) were measured in the mock F8KO mice compared to the WT mice. The treatments increased the ALP (**Figure 5A**) and reduced the OC (**Figure 5B**) in the groups of F8KO mice receiving different doses of KPs, although these changes did not reach statistical importance compared to the mock group. CTX-1 in the F8KO mice receiving KPs decreased, but only the treatment with a high dose of KPs led to statistically significance difference compared to the mock group ($p < 0.01$; **Figure 5C**).

3.5.2 Effects of KP Treatment on the Serum RANKL/OPG Ratio

At 20 weeks of age, oral administration of KP or mock (H_2O) treatment was provided to the WT and F8KO mice. As shown in

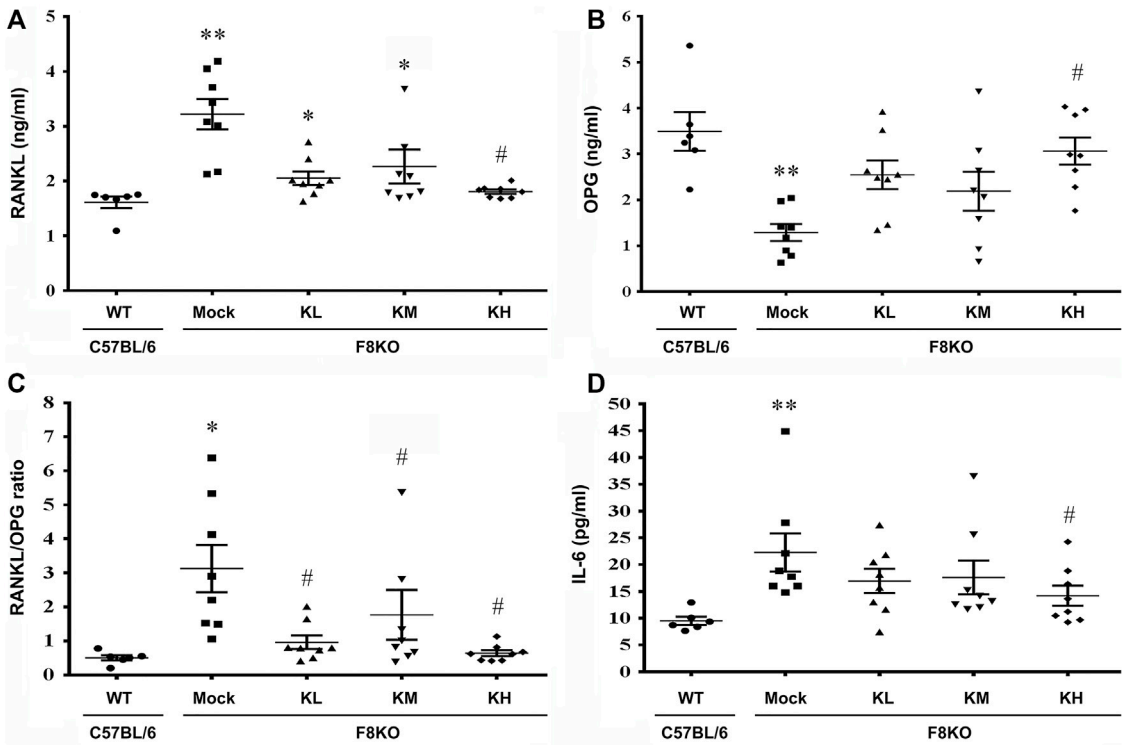

FIGURE 6 | Effects of KP treatment on the serum RANKL/OPG ratio and proinflammatory IL-6 cytokine levels. F8KO mice at 20 weeks of age were orally administered different dosages of KPs for 8 weeks ($n = 8$). At the end of treatment, mouse blood was collected for bone resorption and bone formation marker detection. The quantitative data show the levels of **(A)** receptor activator of nuclear factor κ-B ligand (RANKL), **(B)** osteoprotegerin (OPG), **(C)** RANKL/OPG ratio, and **(D)** interleukin-6 (IL-6) in the KP-treated groups at different dosages. $^{*}p < 0.05$, $^{**}p < 0.01$ vs. WT group; $^{\#}p < 0.05$ vs. mock group.

Figure 6, at the end of treatment, the mock F8KO mice exhibited an increased serum RANKL ($p < 0.01$) along with a decreased serum OPG ($p < 0.01$), which caused a significant increase of the serum RANKL/OPG ratio in the F8KO mice compared to the WT mice ($p < 0.05$). With the KP treatment, the serum RANKL decreased (**Figure 6A**) and OPG increased (**Figure 6B**) in F8KO mice receiving different doses of KPs, and the combined effect led to a significant reduction in the serum RANKL/OPG ratio compared to the mock ($p < 0.05$; **Figure 6C**).

3.5.3 Effects of KP Treatment on Serum Proinflammatory Cytokines

As shown in **Figure 6D**, the serum IL-6 increased significantly in the mock F8KO mice compared to the WT at the end of treatment ($p < 0.01$). Oral administration of KPs reduced the IL-6 level in the F8KO mice, especially for the group with high-dose KP treatment ($p < 0.05$ vs mock, **Figure 6D**). Other proinflammatory cytokines, such as IL-1α, IL-1β, and TNF-α, were also measured, but the changes were not significant (data not shown).

3.5.4 Effects of KP Treatment on Osteoclastogenesis

TRAP staining was performed to examine the contents of mature osteoclasts in the paraffin-embedded femur sections from each group. As shown in **Figures 7A,B**, the TRAP-positive mature osteoclasts were stained in a purple-colored appearance, which were found abundant in the metaphyseal regions of the distal femur sections from the mock F8KO mice, but not apparent in the femur sections from the WT and the KP-treated groups, suggesting that KP treatment caused the inhibition of osteoclastogenesis. We performed *in vitro* osteoclast differentiation using flushed bone marrow cells from each group by stimulating with M-CSF and RANKL. As shown in **Figure 7C**, the TRAP-positive stained areas accounted for approximately 4.24% in the mock group, which represented an increase of 84.2% compared to the WT group (0.69% on average) ($p < 0.01$; **Figure 7D**). With the KP treatments, the TRAP-positive areas were significantly reduced to 2.06% in the KL group ($p < 0.05$), 2.54% in the KM group ($p < 0.05$), and 1.05% in the KH group ($p < 0.01$), which corresponded to 51.6, 40.7, and 73.1% reductions compared to the mock group (**Figure 7D**), respectively, suggesting that oral administration of KPs significantly inhibited osteoclastogenesis. Furthermore, we also performed a similar experiment using primary BMMs to verify the inhibitory effect of KPs on *in vitro* RANKL-induced osteoclastogenesis (**Figure 7E**). As shown in **Figure 7F** for the quantitative data, KPs dose-dependently inhibited the formation of mature osteoclasts from bone marrow cells of macrophage lineage.

4 DISCUSSION

In the present study, the potential therapeutic effects of KPs on hemophilia-induced osteoporosis were investigated in an F8KO

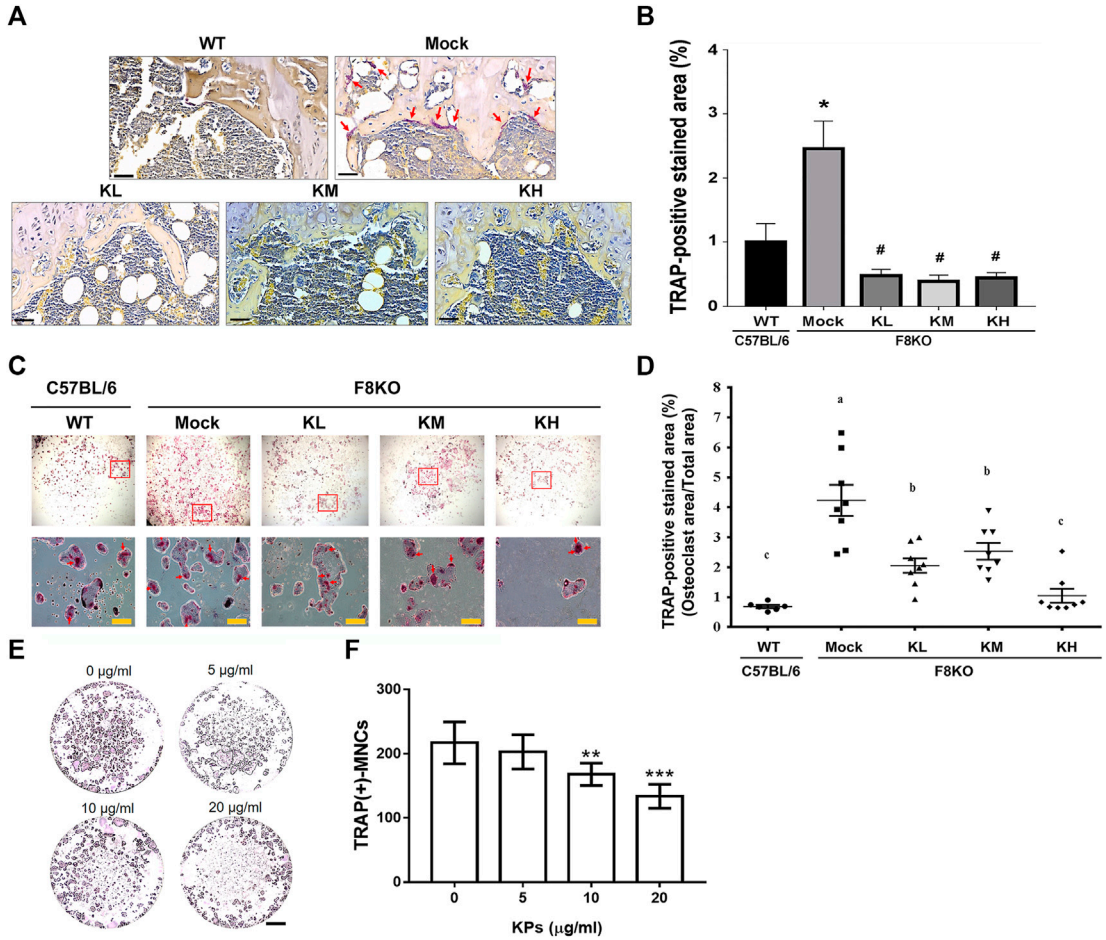

FIGURE 7 | Effects of KP treatment on osteoclast differentiation. **(A)** TRAP staining of the paraffin-embedded femoral tissue sections from each group. The purple-colored TRAP-positive osteoclasts were indicated with red arrows in mock group. Scale bar = 30 μm. **(B)** TRAP-positive stained areas in each group were quantitated and compared using ImageJ software. $^{*}p < 0.05$ vs WT group; $^{\#}p < 0.05$ vs mock group. **(C)** TRAP-staining of mature osteoclasts differentiated from the flushed bone marrow cells with the stimulation of M-CSF and RANKL for 14 days. The multinucleated osteoclasts in squares were magnified and indicated by red arrows. **(D)** TRAP-positive stained areas in each group were quantitated and compared using ImageJ software. $^{*}p < 0.05$, $^{**}p < 0.01$ vs WT group; $^{\#}p < 0.05$, $^{\#\#}p < 0.01$ vs. mock group. **(E)** KP treatment inhibits RANKL-induced osteoclastogenesis in the culture of bone marrow macrophages (BMMs). To stimulate osteoclast differentiation, BMMs were stimulated with M-CSF (25 ng/ml) and RANKL (50 ng/ml) in the presence of various concentrations of KPs. TRAP staining was performed at the 5th day of incubation. **(F)** The TRAP-positive multinucleated cells with the number of nucleus ≥3 were considered as mature osteoclasts. $^{**}p < 0.01$, $^{***}p < 0.001$ vs. 0 μg/ml of KPs; Scale bar = 1 mm.

mouse model. The results revealed that KP treatment restored the femoral trabecular BMD, the trabecular architecture of the femoral bone and the 4th lumbar vertebrae, and the mechanical properties of cortical bone in a dose-dependent manner. In addition, oral administration of KPs inhibited bone resorption by reducing the serum RANKL/OPG ratio and proinflammatory IL-6 levels in the F8KO mice and inhibiting osteoclastogenesis from femoral mesenchymal stem cells in an *in vitro* culture. Therefore, this study suggests that KPs can be used as a complementary or adjuvant therapy for the treatment of osteoporosis resulting from hemophilia.

F8KO mice, which contain only <1% coagulation activity, are an ideal animal model for examining the direct effect of factor VIII deficiency on bone regeneration and are also useful for the assessment of potential anti-osteoporotic therapies in PWH. Previous studies demonstrated that F8KO male mice exhibited lower femoral BMD and cortical thickness than their WT littermates at the age of 18–20 weeks, and these biological changes led to a weakened bone strength to resist fracture (Liel et al., 2012; Recht et al., 2013). Before treatment with KPs, we analyzed the femur bones of the F8KO and WT male mice, and our results confirmed that F8KO mice spontaneously developed osteoporosis at 20 weeks of age (**Figure 1**). Moreover, a recent study compared the bone status of total FVIII gene knockout mice (F8^{TKO}), a new animal model of severe hemophilia, with their WT littermates (Weitzmann et al., 2019). This study also demonstrated that F8^{TKO} mice exhibited significant bone loss at 6 months of age and revealed a sexual dimorphism in the mechanism driving bone loss in male and female F8^{TKO} mice.

Low BMD or osteoporosis and the resultant bone fractures are prevalent age-related comorbidities in PWH, both in adults and

children (Barnes et al., 2004; Wallny et al., 2007; Iorio et al., 2010). A 10-year single institutional retrospective cohort study (n = 382 PWH) exhibited a significantly higher relative risk (RR) of bone fracture in PWH than in the general population ($p < 0.0001$; RR: 10.7, 95% confidence interval (CI): 8.2–14.1) (Gay et al., 2015). Additionally, this retrospective study also indicated that the RR of fracture was positively correlated with the severity of hemophilia, with patients with severe hemophilia showing an increased RR of fracture compared to those with mild or moderate hemophilia ($p < 0.05$). An earlier single institutional cross-sectional study (n = 88) indicated that low BMD became more prevalent with the increasing severity of hemophilia in PWH <50 years, and a large proportion of PWH ≥50 years (no association with the severity of hemophilia) had osteoporosis; thus, adult PWH ≥50 years should receive routine osteoporosis detection (Kempton et al., 2014). Immune tolerance induction (ITI) is routinely used for the treatment of hemophilia with an inhibitor in PWH; however, such a therapeutic regimen has been reported to facilitate the reduction of BMD in patients with an inhibitor (Rezaieyazdi and Mansouritorghabeh, 2020). Few studies have evaluated the effects of anti-osteoporotic treatment in PWH, except ibandronate, a common bisphosphonate used for the treatment of postmenopausal osteoporosis (Anagnostis et al., 2013). This finding urges us to evaluate the effect of KPs on the treatment of hemophilia-induced osteopenia or osteoporosis in an F8KO murine model.

In our previous study, we demonstrated the potential of KPs in the prevention of postmenopausal osteoporosis in ovariectomized (OVX) rats (Chen et al., 2015). To further understand the therapeutic effect of KPs on the treatment of hemophilia-induced osteoporosis, male F8KO mice at 20 weeks of age were orally administered with low-, medium-, and high-dose KPs for 8 weeks. At the end of the experiment, the lost bone mass in the F8KO mice, as indicated by histological and 3D μ-CT images, was partially or completely restored by the KP treatment, especially in the high-dose KP-treated group (**Figures 2**, **3**). The morphological alterations in femoral trabeculae in response to the KP treatment were consistent with the improved BMD and microarchitecture parameters, with the treatment increasing trabecular bone volume (Tb.BV/TV) and trabecular number (Tb.N), and reducing trabecular separation (Tb.Sp). We also examined the effect of KP treatments on the morphological and mechanical changes of the femoral cortical bone. By mid-shaft femur analysis (**Supplementary Figure S2**), we found that the thickest region of the transverse cortical bone increased significantly in all F8KO mice, but the median and the thinnest parts remained indifferent in all mice. In addition, the x-axis width of the transverse cortical bones (x-axis) decreased in all F8KO mice, but the y-axis width of the transverse cortical bones and the lengths of longitudinal cortical bones remained indifferent in all mice. Although KP treatment did not cause significant changes in cortical bones, it significantly improved the mechanical properties of hardness and elastic modulus in femoral cortical bones (**Figure 4**). Furthermore, we also identified anti-osteoporotic effect of KPs on the 4th lumbar vertebra, which exhibited increased Tb.N and decreased Tb.Sp (**Supplementary Figure S1**). These data suggest that KP treatment can enhance bone quality and thus reduce the risk of fracture in F8KO mice or patients with hemophilia.

Biochemical biomarkers of bone turnover can be used to reflect the metabolic status of bone remodeling and provide useful information for therapy monitoring purposes during osteoporosis treatments. These biomarkers are generally divided into two categories representing bone formation and bone resorption. CTX-1 is a biomarker of bone resorption and its serum level is highly correlated with osteoclastic activity. In the present study, we found that CTX-1 elevated in untreated male F8KO mice, suggesting the lack of coagulation Factor VIII promote bone resorption, while the treatment of KPs resists the conversion of serum CTX-1. Moreover, previous study of compared the serum CTX-1 of F8^{TKO} mice with their WT littermate and indicated that CTX-1 elevated significantly only at elder female F8^{TKO} mice but remained unchanged at both young and elder male F8^{TKO} mice (Weitzmann et al., 2019). ALP and OC are two biomarkers of bone formation. Present study exhibited that the untreated F8KO mice (28 weeks old) showed a higher serum OC along with a lower serum ALP than WT mice; however, those mice treated with KPs showed a significant seroconversion of OC and ALP at the end of treatment. ALP and OC have been compared between 20-week-old F8KO and WT mice previously (Recht et al., 2013), but no significant differences have been reported. Different to the present study, all F8KO mice used in previous study were male offspring of WT males and F8KO heterozygote females (Recht et al., 2013). Another earlier study reported that 14-week-old female F8KO mice exhibited decreased OC in the collected bone marrow serum from flushed femur and tibia compared with the WT mice of the same age (Aronovich et al., 2013). These contradictory results may be caused by differences in ages, gender and genetic background of F8KO mice.

To further understand the effects of KPs on the regulation of bone metabolism in the F8KO mice, the serum levels of RANKL and OPG were measured. It has been largely reported that the RANKL/RANK/OPG signaling pathway plays a key role in the control of osteoclastogenesis (Mafi Golchin et al., 2016; Kenkre and Bassett, 2018). RANKL is the ligand of RANK on osteoclast precursors. RANKL/RANK binding induces downstream signaling pathways to regulate the expression of osteoclast genes and to drive further differentiation of osteoclast precursors into mature osteoclasts. OPG, a soluble decoy receptor of RANKL, can inhibit osteoclast differentiation by preventing the binding of RANK to its ligand RANKL. Thus, the circulating RANKL/OPG ratio reflects osteoclast activities during bone metabolism. In this study, we found that the RANKL level increased along with a decrease in OPG, which resulted in a higher RANKL/OPG ratio in the mock F8KO mice than the WT mice, suggesting that increased osteoclastogenesis was activated and that the bone remodeling balance was inclined toward bone resorption in F8KO mice. However, the KP treatment led to decreased RANKL and elevated OPG levels, and the combined effect eventually resulted in a decrease in the RANKL/OPG ratio.

Osteoclastogenesis is also regulated by circulating proinflammatory cytokines, such as TNF-α, IL-1, and IL-6. We did not identify significant alterations in TNF-α and IL-1 levels, although we found that the KP treatment tended to decrease the IL-6 levels in the F8KO mice. IL-6 is secreted by peripheral macrophages and osteoblasts, stimulates osteoclast formation and induces bone resorption (Ishimi et al., 1990). Additionally, we also found that the KP treatment resulted in

decreased TRAP activity in primary osteoclast cultures, as indicated by the decreased TRAP-stained areas shown in **Figure 7**. These data suggested that KP treatment inhibited osteoclastogenesis in F8KO mice and thus resulted in the inhibition of bone resorption. The underlying molecular mechanisms of KPs in regulating the activities of osteoblasts and osteoclasts during bone remodeling require more detailed cellular experiments to understand the full picture.

5 CONCLUSION

In summary, we demonstrated that oral administration of KPs can elicit a therapeutic effect on osteoporosis treatment in hemophilic mice due to FVIII deficiency. The therapeutic effect of KPs is associated with their ability to inhibit osteoclastogenesis and bone resorption by decreasing the serum RANKL/OPG ratio and the secretion of proinflammatory cytokines such as IL-6. Oral administration of KPs is generally safe and more cost-effective than many anti-osteoporotic agents. Therefore, the use of KPs may have potential as a complementary or adjuvant therapy for the long-term management of bone health in patients with hemophilia.

DATA AVAILABILITY STATEMENT

The original contributions presented in the study are included in the article/**Supplementary Material**, further inquiries can be directed to the corresponding author.

ETHICS STATEMENT

The animal study was reviewed and approved by The Institutional Animal Care and Use Committee of National Chung Hsing University, Taiwan (IACUC 103–100).

AUTHOR CONTRIBUTIONS

Conceptualization and resources, C-CY, Y-WL, GR-LC, and C-MC.; methodology, investigation and formal analyses, C-CY, Y-WL, Y-TK, and WC; data curation, WC and C-MC; writing—original draft preparation, Y-WL and GR-LC; writing—reviewing and editing, S-NC and C-MC.; visualization, S-NC and WC; supervision, C-MC.; project administration, GR-LC; and funding acquisition, C-MC. All authors have read and agreed to the final version of the manuscript.

FUNDING

This research was funded by the MOST-107-2313-B-005-042-MY3 Grant from the Ministry of Science and Technology of Taiwan (C-MC) and partially supported by the iEGG and Animal Biotechnology Center from the Feature Areas Research Center Program within the framework of the Higher Education Sprout Project by the Ministry of Education (MOE-110-S-0023-A) in Taiwan (C-MC).

ACKNOWLEDGMENTS

We thank our colleague Dr. Tung-Chou Tsai in the Molecular Embryology & DNA Methylation Laboratory, Department of Life Sciences, National Chung Hsing University, for engaging in discussions, and helping with technical issues. Mr. Y-TK carried out this research with partial funding by the Ph.D. Program in Tissue Engineering and Regenerative Medicine of National Chung Hsing University and National Health Research Institutes.

SUPPLEMENTARY MATERIAL

The Supplementary Material for this article can be found online at: https://www.frontiersin.org/articles/10.3389/fcell.2022.794198/full#supplementary-material

REFERENCES

Anagnostis, P., Vyzantiadis, T. A., Charizopoulou, M., Adamidou, F., Karras, S., Goulis, D. G., et al. (2013). The Effect of Monthly Ibandronate on Bone mineral Density and Bone Turnover Markers in Patients with Haemophilia A and B and Increased Risk for Fracture. *Thromb. Haemost.* 110 (2), 257–263. doi:10.1160/TH13-01-0030

Aronovich, A., Nur, Y., Shezen, E., Rosen, C., Zlotnikov Klionsky, Y., Milman, I., et al. (2013). A Novel Role for Factor VIII and thrombin/PAR1 in Regulating Hematopoiesis and its Interplay with the Bone Structure. *Blood* 122 (15), 2562–2571. doi:10.1182/blood-2012-08-447458

Barnes, C., Wong, P., Egan, B., Speller, T., Cameron, F., Jones, G., et al. (2004). Reduced Bone Density Among Children with Severe Hemophilia. *Pediatrics* 114 (2), e177–e181. doi:10.1542/peds.114.2.e177

Bourrie, B. C. T., Willing, B. P., and Cotter, P. D. (2016). The Microbiota and Health Promoting Characteristics of the Fermented Beverage Kefir. *Front. Microbiol.* 7, 647. doi:10.3389/fmicb.2016.00647

Chang, Y.-T., Chen, C.-M., Tu, M.-Y., Chen, H.-L., Chang, S.-Y., Tsai, T.-C., et al. (2011). Effects of Osteoporosis and Nutrition Supplements on Structures and Nanomechanical Properties of Bone Tissue. *J. Mech. Behav. Biomed. Mater.* 4 (7), 1412–1420. doi:10.1016/j.jmbbm.2011.05.011

Chen, H.-L., Lan, Y.-W., Tu, M.-Y., Tung, Y.-T., Chan, M. N.-Y., Wu, H.-S., et al. (2021). Kefir Peptides Exhibit Antidepressant-like Activity in Mice through the BDNF/TrkB Pathway. *J. Dairy Sci.* 104 (6), 6415–6430. doi:10.3168/jds.2020-19222

Chen, H.-L., Tung, Y.-T., Chuang, C.-H., Tu, M.-Y., Tsai, T.-C., Chang, S.-Y., et al. (2015). Kefir Improves Bone Mass and Microarchitecture in an Ovariectomized Rat Model of Postmenopausal Osteoporosis. *Osteoporos. Int.* 26 (2), 589–599. doi:10.1007/s00198-014-2908-x

Chen, Y.-H., Chen, H.-L., Fan, H.-C., Tung, Y.-T., Kuo, C.-W., Tu, M.-Y., et al. (2020). Anti-inflammatory, Antioxidant, and Antifibrotic Effects of Kefir Peptides on Salt-Induced Renal Vascular Damage and Dysfunction in Aged Stroke-Prone Spontaneously Hypertensive Rats. *Antioxidants* 9 (9), 790. doi:10.3390/antiox9090790

Chiu, W.-Y., Chien, J.-Y., Yang, W.-S., Juang, J.-M. J., Lee, J.-J., and Tsai, K.-S. (2014). The Risk of Osteonecrosis of the Jaws in Taiwanese Osteoporotic Patients Treated with Oral Alendronate or Raloxifene. *J. Clin. Endocrinol. Metab.* 99 (8), 2729–2735. doi:10.1210/jc.2013-4119

D'Amelio, P., Tamone, C., Sassi, F., D'Amico, L., Roato, I., Patanè, S., et al. (2012). Teriparatide Increases the Maturation of Circulating Osteoblast

Precursors. *Osteoporos. Int.* 23 (4), 1245–1253. doi:10.1007/s00198-011-1666-2

Díez-Pérez, A., Marin, F., Eriksen, E. F., Kendler, D. L., Krege, J. H., and Delgado-Rodríguez, M. (2019). Effects of Teriparatide on Hip and Upper Limb Fractures in Patients with Osteoporosis: A Systematic Review and Meta-Analysis. *Bone* 120, 1–8. doi:10.1016/j.bone.2018.09.020

Fiorda, F. A., de Melo Pereira, G. V., Thomaz-Soccol, V., Rakshit, S. K., Pagnoncelli, M. G. B., Vandenberghe, L. P. d. S., et al. (2017). Microbiological, Biochemical, and Functional Aspects of Sugary Kefir Fermentation - a Review. *Food Microbiol.* 66, 86–95. doi:10.1016/j.fm.2017.04.004

Gay, N. D., Lee, S. C., Liel, M. S., Sochacki, P., Recht, M., and Taylor, J. A. (2015). Increased Fracture Rates in People with Haemophilia: A 10-year Single Institution Retrospective Analysis. *Br. J. Haematol.* 170 (4), 584–586. doi:10.1111/bjh.13312

Iorio, A., Fabbriciani, G., Marcucci, M., Brozzetti, M., and Filipponi, P. (2010). Bone mineral Density in Haemophilia Patients. A Meta-Analysis. *Thromb. Haemost.* 103 (3), 596–603. doi:10.1160/TH09-09-0629

Ishimi, Y., Miyaura, C., Jin, C. H., Akatsu, T., Abe, E., Nakamura, Y., et al. (1990). IL-6 Is Produced by Osteoblasts and Induces Bone Resorption. *J. Immunol.* 145 (10), 3297–3303.

Kempton, C. L., Antoniucci, D. M., and Rodriguez-Merchan, E. C. (2015). Bone Health in Persons with Haemophilia. *Haemophilia* 21 (5), 568–577. doi:10.1111/hae.12736

Kempton, C. L., Antun, A., Antoniucci, D. M., Carpenter, W., Ribeiro, M., Stein, S., et al. (2014). Bone Density in Haemophilia: a Single Institutional Cross-Sectional Study. *Haemophilia* 20 (1), 121–128. doi:10.1111/hae.12240

Kenkre, J., and Bassett, J. (2018). The Bone Remodelling Cycle. *Ann. Clin. Biochem.* 55 (3), 308–327. doi:10.1177/0004563218759371

Khan, S. A., Kanis, J. A., Vasikaran, S., Kline, W. F., Matuszewski, B. K., McCloskey, E. V., et al. (1997). Elimination and Biochemical Responses to Intravenous Alendronate in Postmenopausal Osteoporosis. *J. Bone Miner Res.* 12 (10), 1700–1707. doi:10.1359/jbmr.1997.12.10.1700

Kiper Unal, H. D., Comert Ozkan, M., Atilla, F. D., Demirci, Z., Soyer, N., Yildirim Simsir, I., et al. (2017). Evaluation of Bone mineral Density and Related Parameters in Patients with Haemophilia: a Single center Cross-Sectional Study. *Am. J. Blood Res.* 7 (5), 59–66.

Lee, J. K., Kim, K.-W., Choi, J.-Y., Moon, S.-Y., Kim, S.-G., Kim, C.-H., et al. (2013). Bisphosphonates-related Osteonecrosis of the Jaw in Korea: a Preliminary Report. *J. Korean Assoc. Oral Maxillofac. Surg.* 39 (1), 9–13. doi:10.5125/jkaoms.2013.39.1.9

Liel, M. S., Greenberg, D. L., Recht, M., Vanek, C., Klein, R. F., and Taylor, J. A. (2012). Decreased Bone Density and Bone Strength in a Mouse Model of Severe Factor VIII Deficiency. *Br. J. Haematol.* 158 (1), 140–143. doi:10.1111/j.1365-2141.2012.09101.x

Mafi Golchin, M., Heidari, L., Ghaderian, S. M. H., and Akhavan-Niaki, H. (2016). Osteoporosis: A Silent Disease with Complex Genetic Contribution. *J. Genet. Genomics* 43 (2), 49–61. doi:10.1016/j.jgg.2015.12.001

Mücke, T., Krestan, C. R., Mitchell, D. A., Kirschke, J. S., and Wutzl, A. (2016). Bisphosphonate and Medication-Related Osteonecrosis of the Jaw: a Review. *Semin. Musculoskelet. Radiol.* 20 (3), 305–314. doi:10.1055/s-0036-1592367

Napoli, N., LangdahlLangdahl, B. L. B. L., Ljunggren, Ö., Lespessailles, E., Kapetanos, G., Kocjan, T., et al. (2018). Effects of Teriparatide in Patients with Osteoporosis in Clinical Practice: 42-month Results during and after Discontinuation of Treatment from the European Extended Forsteo Observational Study (ExFOS). *Calcif Tissue Int.* 103 (4), 359–371. doi:10.1007/s00223-018-0437-x

Recht, M., Liel, M. S., Turner, R. T., Klein, R. F., and Taylor, J. A. (2013). The Bone Disease Associated with Factor VIII Deficiency in Mice Is Secondary to Increased Bone Resorption. *Haemophilia* 19 (6), 908–912. doi:10.1111/hae.12195

Rezaieyazdi, Z., and Mansouritorghabeh, H. (2020). Clinical Care of Bone Health in Patients on the Immune Tolerance Induction's Protocols with an Immunosuppressive Agent for Inhibitor Eradication in Hemophilia. *Clin. Appl. Thromb. Hemost.* 26, 1076029620913951. doi:10.1177/1076029620913951

Rosa, D. D., Dias, M. M. S., Grześkowiak, Ł. M., Reis, S. A., Conceição, L. L., and Peluzio, M. d. C. G. (2017). Milk Kefir: Nutritional, Microbiological and Health Benefits. *Nutr. Res. Rev.* 30 (1), 82–96. doi:10.1017/s0954422416000275

Srivastava, A., Brewer, A. K., Mauser-Bunschoten, E. P., Key, N. S., Kitchen, S., Llinas, A., et al. (2013). Guidelines for the Management of Hemophilia. *Haemophilia* 19 (1), e1–e47. doi:10.1111/j.1365-2516.2012.02909.x

Tlacuilo-Parra, A., Villela-rodríguez, J., Garibaldi-Covarrubias, R., Soto-Padilla, J., and Orozco-Alcala, J. (2011). Bone Turnover Markers and Bone mineral Density in Children with Haemophilia. *Haemophilia* 17 (4), 657–661. doi:10.1111/j.1365-2516.2010.02439.x

Tu, M.-Y., Chen, H.-L., Tung, Y.-T., Kao, C.-C., Hu, F.-C., and Chen, C.-M. (2015). Short-term Effects of Kefir-Fermented Milk Consumption on Bone mineral Density and Bone Metabolism in a Randomized Clinical Trial of Osteoporotic Patients. *PLoS One* 10 (12), e0144231. doi:10.1371/journal.pone.0144231

Tu, M.-Y., Han, K.-Y., Chang, G. R.-L., Lai, G.-D., Chang, K.-Y., Chen, C.-F., et al. (2020). Kefir Peptides Prevent Estrogen Deficiency-Induced Bone Loss and Modulate the Structure of the Gut Microbiota in Ovariectomized Mice. *Nutrients* 12 (11), 3432. doi:10.3390/nu12113432

Tu, M.-Y., Han, K.-Y., Lan, Y.-W., Chang, K.-Y., Lai, C.-W., Staniczek, T., et al. (2021). Association of TGF-B1 and IL-10 Gene Polymorphisms with Osteoporosis in a Study of Taiwanese Osteoporotic Patients. *Genes* 12 (6), 930. doi:10.3390/genes12060930

Tung, M.-C., Lan, Y.-W., Li, H.-H., Chen, H.-L., Chen, S.-Y., Chen, Y.-H., et al. (2020). Kefir Peptides Alleviate High-Fat Diet-Induced Atherosclerosis by Attenuating Macrophage Accumulation and Oxidative Stress in *ApoE* Knockout Mice. *Sci. Rep.* 10 (1), 8802. doi:10.1038/s41598-020-65782-8

Ulivieri, F. M., Rebagliati, G. A. A., Piodi, L. P., Solimeno, L. P., Pasta, G., Boccalandro, E., et al. (2018). Usefulness of Bone Microarchitectural and Geometric DXA-Derived Parameters in Haemophilic Patients. *Haemophilia* 24 (6), 980–987. doi:10.1111/hae.13611

Wallny, T. A., Scholz, D. T., Oldenburg, J., Nicolay, C., Ezziddin, S., Pennekamp, P. H., et al. (2007). Osteoporosis in Haemophilia ? an Underestimated Comorbidity. *Haemophilia* 13 (1), 79–84. doi:10.1111/j.1365-2516.2006.01405.x

Wang, J.-L., Lan, Y.-W., Tsai, Y.-T., Chen, Y.-C., Staniczek, T., Tsou, Y.-A., et al. (2021). Additive Antiproliferative and Antiangiogenic Effects of Metformin and Pemetrexed in a Non-small-cell Lung Cancer Xenograft Model. *Front. Cel Dev. Biol.* 9, 688062. doi:10.3389/fcell.2021.688062

Wang, Y.-T., Chang, S.-Y., Huang, Y.-C., Tsai, T.-C., Chen, C.-M., and Lim, C. T. (2013). Nanomechanics Insights into the Performance of Healthy and Osteoporotic Bones. *Nano Lett.* 13 (11), 5247–5254. doi:10.1021/nl402719q

Weischenfeldt, J., and Porse, B. (2008). Bone Marrow-Derived Macrophages (BMM): Isolation and Applications. *CSH Protoc.* 2008, pdb.prot5080. doi:10.1101/pdb.prot5080

Weitzmann, M. N., Roser-Page, S., Vikulina, T., Weiss, D., Hao, L., Baldwin, W. H., et al. (2019). Reduced Bone Formation in Males and Increased Bone Resorption in Females Drive Bone Loss in Hemophilia A Mice. *Blood Adv.* 3 (3), 288–300. doi:10.1182/bloodadvances.2018027557

Conflict of Interest: The authors declare that the research was conducted in the absence of any commercial or financial relationships that could be construed as a potential conflict of interest.

Publisher's Note: All claims expressed in this article are solely those of the authors and do not necessarily represent those of their affiliated organizations, or those of the publisher, the editors and the reviewers. Any product that may be evaluated in this article, or claim that may be made by its manufacturer, is not guaranteed or endorsed by the publisher.

frontiers in Cell and Developmental Biology

ORIGINAL RESEARCH
published: 28 February 2022
doi: 10.3389/fcell.2022.834688

Metabolic Changes During Growth and Reproductive Phases in the Liver of Female Goldfish (*Carassius auratus*)

*Claudia Ladisa, Yifei Ma and Hamid R Habibi**

Department of Biological Sciences, University of Calgary, Calgary, AB, Canada

Hormones of the brain-pituitary-peripheral axis regulate metabolism, gonadal maturation, and growth in vertebrates. In fish, reproduction requires a significant energy investment to metabolically support the production of hundreds of eggs and billions of sperms in females and males, respectively. This study used an LC-MS-based metabolomics approach to investigate seasonally-related changes in metabolic profile and energy allocation patterns in female goldfish liver. We measured basal metabolic profile in female goldfish at three phases of the reproductive cycle, including 1) Maximum growth period in postovulatory regressed phase, 2) mid recrudescence in fish with developing follicles, and 3) late recrudescence when the ovary contains mature ovulatory follicles. We also investigated changes in the liver metabolism following acute treatments with GnRH and GnIH, known to be involved in controlling reproduction and growth in goldfish. Chemometrics combined with pathway-driven bioinformatics revealed significant changes in the basal and GnRH/GnIH-induced hepatic metabolic profile, indicating that metabolic energy allocation is regulated to support gonadal development and growth at different reproductive cycles. Overall, the findings support the hypothesis that hormonal control of reproduction involves accompanying metabolic changes to energetically support gonadotropic and somatotropic activities in goldfish and other oviparous vertebrates.

Keywords: seasonal reproductive cycle, targeted metabolomics, LC-MS, chemometrics, growth and reproduction, gonadotropin releasing hormone (GnRH), gonadotropin-inhibitory hormone (GnIH)

OPEN ACCESS

Edited by:
Natalia Martins Feitosa, Federal University of Rio de Janeiro, Brazil

Reviewed by:
Tomohiro Osugi, Suntory Foundation for Life Sciences, Japan
Hiroyasu Kamei, Kanazawa University, Japan

****Correspondence:***
Hamid R Habibi
habibi@ucalgary.ca

Specialty section:
This article was submitted to Molecular and Cellular Pathology, a section of the journal Frontiers in Cell and Developmental Biology

Received: *13 December 2021*
Accepted: *31 January 2022*
Published: *28 February 2022*

Citation:
Ladisa C, Ma Y and Habibi HR (2022) Metabolic Changes During Growth and Reproductive Phases in the Liver of Female Goldfish (Carassius auratus). Front. Cell Dev. Biol. 10:834688. doi: 10.3389/fcell.2022.834688

1 INTRODUCTION

A number of oviparous species, including many fishes, are seasonal breeders and follow cycles of predominantly reproductive and growth phases. Integrated control of reproduction, growth and metabolism is multifactorial, involving neurohormones, the pituitary gonadotropins (LH and FSH), growth hormone (GH), gonadal hormones, and thyroid hormones (Zohar et al., 2009; Yaron, 2011; Habibi et al., 2012; Plant, 2015; Ma et al., 2020a; Ma et al., 2020b; Rajeswari et al., 2020; Somoza et al., 2020; Trudeau and Somoza, 2020). Ovarian follicular development starts with the growth of many small early-stage transparent oocytes accumulating neutral lipids in the ooplasm as lipid droplets (early recrudescence). The growing follicles increase in size progressively by taking up glycolipophosphoproteins termed vitellogenin (Vtg) which is the precursor molecule for the yolk proteins during mid recrudescence (Reading and Sullivan, 2011), and eventually form the preovulatory follicles (late recrudescence). A surge of LH and FSH at the end of the ovarian cycle leads to resumption of meiosis, ovulation and spawning, followed by a regressed gonadal phase, which corresponds to a period of maximum growth (Marchant and Peter, 1986; De Leeuw et al.,

1989). Changes in metabolism accompany seasonal variation in the reproductive cycle to sustain this energy-demanding process specific to the stage of gonadal development or period of growth. Vitellogenesis requires a significant metabolic energy allocation (Schneider, 2004; Fernandez-Fernandez et al., 2006; Shahjahan et al., 2014; Ladisa et al., 2021) to support the production of hundreds of mature eggs filled with lipoprotein-filled yolk (Jalabert, 2005). This is critical in oviparous species since embryonic development and early larval stages depend entirely on energy molecules stored in the egg during the maturation (Reading and Sullivan, 2011). For example, in rainbow trout, ovaries grow from 0.5% to approximately 20% of the bodyweight prior to ovulation, and during gametogenesis, the oocyte diameter increases from less than 1–5 mm (Tyler et al., 1990). At the end of the vitellogenic period, yolk proteins derived from Vtg contribute to 80–90% of the dry mass of a mature egg (Reading and Sullivan, 2011). Estrogens stimulate the production of Vtg in the liver, which is transported through the bloodstream to the ovaries, and processed into yolk proteins in the oocytes (Jalabert, 2005; Lin et al., 2006; Reading and Sullivan, 2011; Mcbride et al., 2015). In the blood, Vtg also functions as a carrier for various molecules, including calcium, magnesium, iron, vitamins, steroids and thyroid hormones (Reading and Sullivan, 2011). It is well established that dramatic changes occur in the liver of fish related to the gonadal maturation and vitellogenesis (Rinchard and Kestemont, 2003). The reproductive cycle begins, in part, with the production of the hypothalamic gonadotropin-releasing hormone (GnRH) in response to environmental and metabolic cues (Zohar et al., 2009; Plant, 2015). GnRH stimulates the synthesis and release of LH and FSH from the anterior pituitary, promoting gonadal hormones and gametogenesis (Zohar et al., 2009; Yaron, 2011). The reproductive process is integrated with the growth response controlled by GH, which is regulated by a complex network of hormonal and nutritional factors, including GnRH ((Chang et al., 2000; Canosa et al., 2007; Chang and Wong, 2009). All vertebrate species have multiple isoforms of GnRH (Lethimonier et al., 2004; Okubo and Nagahama, 2008; Chang and Pemberton, 2018). The two endogenous GnRH isoforms in goldfish, GnRH-II [chicken GnRH-II] and GnRH-III [salmon GnRH] (Peter et al., 1985; Yu et al., 1988; Kim et al., 1995; Chang and Pemberton, 2018), are involved in the control of pituitary gonadotropin and GH production (Peter et al., 1985; Chang et al., 2000; Klausen et al., 2001) and regulation of seasonal reproductive cycle in goldfish (Omeljaniuk et al., 1989; Gamba and Pralong, 2006; Moussavi et al., 2013; Moussavi et al., 2014; Ma et al., 2020a; Ma et al., 2020b). There is now evidence that gonadotropin-inhibitory hormone (GnIH) is also involved in the multifactorial regulation of growth and reproduction, together with GnRH and thyroid hormones (Ma et al., 2020a; Ma et al., 2020b). In birds and mammals, GnIH inhibits the release of gonadotropins (Tsutsui et al., 2000; Ubuka et al., 2006; Kriegsfeld et al., 2010; Pineda et al., 2010; Tsutsui et al., 2013). However, in other vertebrates like fish, GnIH can exert both inhibitory and stimulatory actions on the production of gonadotropins in a seasonally dependent manner (Amano et al., 2006; Moussavi et al., 2012; Moussavi et al., 2013; Ma et al., 2020a; Ma et al., 2020b). In goldfish, the presence of three GnIH variants has been demonstrated (LPXRFa-1, -2, and-3), although only LPXRFa-3 was identified as a mature peptide (Sawada et al., 2002). In several vertebrates, GnRH and GnIH are also involved in the regulation of growth by modulating GH production (Chang and Wong, 2009). Studies conducted on several fish species, including goldfish, have shown the presence of GnRH receptors on somatotroph cells and demonstrated its stimulatory action on the synthesis and release of GH (Melamed et al., 1995; Klausen et al., 2001; Klausen et al., 2002; Bhandari et al., 2003). Additionally, GnIH can influence growth and metabolism by regulating food intake and GH secretion (Clarke, 2014). GnIH orthologs stimulate GH release in frogs (Koda et al., 2002; Ukena et al., 2003), sockeye salmon (Amano et al., 2006) and rat (Johnson et al., 2007). In goldfish, GnIH regulates GH synthesis and release *in vivo* and *in vitro* in a seasonally-dependent manner (Moussavi et al., 2014; Ma et al., 2020a; Ma et al., 2020b). There is evidence that GnRH receptor level changes between reproductive stages. In goldfish, GnRH receptors undergo seasonal variation, and the highest pituitary content is found during the late recrudescence (Habibi et al., 1989). Similarly, treatments with GnIH and GnRH alone or combined influence pituitary GnIH receptor expression in a seasonally dependent manner (Moussavi et al., 2013; Moussavi et al., 2014). Thus, variation in GnRH and GnIH receptor levels is likely to influence the hormone-mediated seasonal changes. Goldfish undergo a distinct seasonal cycle and provide a suitable model organism to study energy allocation associated with reproduction and growth. We used an LC-MS-based metabolomics approach to investigate the hepatic metabolic profile of adult female goldfish during three stages of the reproductive cycle, including maximum growth period in postovulatory regressed phase, mid recrudescence in fish with developing follicles, and late recrudescence when the ovary contains mature ovulatory follicles. We also investigated seasonally related changes in the liver metabolism following acute treatments with GnRH and GnIH, known to be involved in controlling reproduction and growth in goldfish. Most metabolic pathways and cellular regulatory mechanisms are common among vertebrates, and metabolomics data can be interpreted similarly in different species. However, significant differences in metabolic energy allocation exist when comparing oviparous and viviparous species such as fish and humans, respectively, at different stages of reproduction. The present study provides an insight into the metabolic changes accompanying seasonal variation in the reproductive cycle in fish and other seasonally reproducing vertebrates.

2 MATERIALS AND METHODS

2.1 Experimental Animals

In all studies, we used sexually mature (post-pubertal) 4–6 inch (average weigh 34.6 g) goldfish (*Carassius auratus*). Fish were imported by a local supplier (Aquatic Imports, Calgary, AB, Canada) from a fish farm in Pennsylvania (Mercersburg, PA,

TABLE 1 | Injection design of GnRH-III (100 ng/g fish wet weight) and gGnIH (50 ng/g fish) treatments, dissolved in PBS solution. Double injection with PBS (Group 1) served as control group. Intraperitoneal injections were administered at T0 and T12 h followed by samples collection at 24 h post first injection.

Group	T0 h	T12 h
1	PBS	PBS
2	PBS	GnRH
3	GnRH	GnRH
4	PBS	GnIH
5	GnIH	GnIH

United States), where they were reared under the natural daylight and temperature cycles. Each experimental group was assigned 20 fish to ensure that a minimum of six female fish could be used in this study. We used fish at three stages of the annual reproductive cycle, including regressed/maximal growth phase (July-August), mid recrudescence (December- January) and late recrudesce (March-April). At arrival, fish were acclimatized for 4–7 days in a flow through system in 25 L tanks kept under the daylight and temperature corresponding to the environmental conditions. Fish were fed a commercial fish diet once a day to satiation (Nutrafin floating pellets; Hagen, Baie d'Urfé, QC, Canada). A buffered MS-222 solution (tricaine methanesulfonate, 160 mg/L, Sigma Aldrich St Louis, MO, United States) was used to anesthetize the fish before intraperitoneal injection and euthanization following the protocols approved by the University of Calgary animal care committee (protocol #AC19-0161) under the guidelines of the Canadian Council of Animal Care. Ovarian stages were assessed by visual inspection after euthanization before tissue collection. Photographs of ovaries used at different gonadal stages are shown in **Figure 4**. Immediately after collection, liver tissue samples were snap-frozen in liquid nitrogen to arrest the metabolism and stored at −80°C until further analysis.

2.2 Hormones and Injection Treatments

GnRH-III (salmon GnRH) (Pyr-HWSYGWLPG-NH_2) was purchased from Bachem (Torrance, CA, United States). Goldfish GnIH (LPXRFa-3; SGTGLSATLPQRF-NH_2) was synthesized by the University of Calgary Peptide Services (Calgary, AB, Canada). Before injection, hormones were dissolved in phosphate-buffered saline (PBS). GnRH-III, GnIH, and PBS (control) were administered intraperitoneally twice, at 9 am (T-0 h) and 9 pm (T-12 h; **Table 1**). Fish were euthanized, and tissue samples were collected 24 h after the final injection. The control group (Group 1) received a sham injection of PBS at T-0 and T-12 h. The injection protocol was chosen based on previous studies demonstrating that double injection with GnRH or GnIH had a more significant stimulatory effect on GH and LH release in goldfish, compared to single injection indicating that the first injection serves as a primer for tissue response (Klausen et al., 2001; Klausen et al., 2002; Moussavi et al., 2012; Klausen et al., 2014; Ma et al., 2020a; Ma et al., 2020b). Doses of GnRH-III and GnIH were chosen based on previous studies conducted on goldfish (Moussavi et al., 2012; Moussavi et al., 2013; Moussavi et al., 2014; Ma et al., 2020a; Ma et al., 2020b). In particular, GnRH-III: 100 ng/g of fish, and GnIH: 50 ng/g of fish were injected based on the weight of fish in the three experimental seasons.

2.3 Extraction of Metabolites and LC-MS

Several preparation protocols have been developed for the extraction of small molecules from tissue samples, and most involve the addition of organic solvents (Li and Bartlett, 2014). In the present study, we used a water-methanol extraction protocol. This process allowed the extraction of polar metabolites while maintaining the biophysical characteristics of the metabolites present in the sample (Wu et al., 2008; Li and Bartlett, 2014). The metabolites extraction protocol involved homogenizing liver samples in a 50% cold water-methanol solution using a bead-beating homogenizer (TissueLyser II, QIAGEN). Samples (~50 mg) were extracted with methanol [ratio of 1:20 sample (mg): methanol (µl)]. After homogenization, samples were centrifuged at 13,500 rpm for 20 min, and the supernatant was stored at −80°C until further analysis. A Quality control (QC) group was generated by pooling ~20 mg from five random samples, extracted and analyzed in five statistical replicates together with the investigated groups (Vuckovic, 2012). Metabolite extracts were analyzed using Ultra-High-Performance Liquid Chromatography (UHPLC) mass spectrometry (MS) coupled with a Thermo Fisher Scientific Q-Exactive HF mass spectrometer. A hydrophilic interaction liquid chromatography column (Syncronis HILIC, Thermo Fisher) was used to separate the metabolites. High-resolution full-scan MS data were acquired using negative-mode electrospray ionization, and data were analyzed with MAVEN freeware (Melamud et al., 2010) based on retention times and *m/z* of standards in a targeted profiling approach. MAVEN's feature detection algorithm extracts peak groups with retention times and *m/z* matching specified standards (Clasquin et al., 2012). Relative quantification of metabolites is estimated based on the intensity of the analyzed peaks. Area top was used to measure peak intensity, representing the average intensity of the top three points of the peak.

2.4 Statistical Analysis

We used normalization by median, log transformation and Pareto scaling approach described previously (Katajamaa and Orešič, 2007) to eliminate noise and artifact. To reduce the innate complexity of metabolomics data, multivariate analysis and dimensionality reduction tools such as Principal Component Analysis (PCA) and Partial Least Squared—Discriminant Analysis (PLS-DA) were used to identify significant differences in the metabolic profile of the groups investigated. PCA was performed on treatment groups and the QC group to validate the LC-MS analysis's accuracy and identify the presence of outliers (Sangster et al., 2006). Moreover, PLS-DA was performed on the treatment groups to highlight differences in metabolic profiles and identify important metabolites (Lee et al., 2018).

R^2 and Q^2 parameters estimate the "goodness of fit" and "goodness of prediction" for each model, respectively (Triba et al., 2015). PLS-DA models with R^2 and $Q^2 > 0.5$ were deemed good fitting and good predictability, respectively.

TABLE 2 | One-way ANOVA results of all the VIP > 1 metabolites identified for the three PLS-DA models investigating the metabolic changes between reproductive phases (Regressed, Mid and Late). Tukey's post-hoc test was used for multiple comparisons following ANOVA.

VIP metabolites	*p*-value	FDR	Tukey's HSD
Taurine	1.55×10^{-5}	0.00041	Late-Regressed; Late-Mid
Glutamic acid	2.16×10^{-5}	0.00041	Late-Regressed; Late-Mid
GMP	2.36×10^{-5}	0.00041	Mid-Regressed; Late-Mid
Asparagine	3.75×10^{-5}	0.00046	Mid-Regressed; Late-Mid
Uridine	4.44×10^{-5}	0.00046	Mid-Regressed; Late-Mid
Acetylglutamine	0.00011	0.00092	Mid-Regressed; Late-Mid
Ophthalmic acid	0.00019	0.0014	Mid-Regressed; Late-Regressed
Acetoacetic acid	0.00028	0.0017	Late-Regressed; Late-Mid
Uric acid	0.00029	0.0017	Mid-Regressed; Late-Mid
Glucose 1-phosphate	0.0005	0.0026	Late-Regressed; Late-Mid
Adenine	0.0006	0.0026	Mid-Regressed; Late-Mid
Pantothenic acid	0.0008	0.0033	Late-Regressed; Late-Mid
CMP	0.0009	0.0036	Late-Mid
Glutathione	0.0012	0.0044	Late-Regressed; Late-Mid
Glycogen	0.0014	0.0048	Mid-Regressed
Glucose	0.0017	0.0054	Late-Regressed
Inosinic acid	0.0028	0.0081	Mid-Regressed; Late-Mid
Histidine	0.0028	0.0081	Late-Regressed; Late-Mid
Guanosine	0.0058	0.015	Mid-Regressed; Late-Regressed
Adenosine	0.0060	0.015	Mid-Regressed
Fructose	0.0061	0.015	Late-Regressed
Allantoin	0.0078	0.018	Late-Mid
Arginine	0.0081	0.018	Late-Regressed
EAP	0.0088	0.019	Late-Mid
Ornithine	0.011	0.022	Late-Mid
Citrulline	0.011	0.023	Late-Mid
Creatine	0.013	0.024	Late-Regressed; Late-Mid
Aminoadipic acid	0.015	0.028	Mid-Regressed; Late-Mid
AMP	0.016	0.028	Late-Mid
UMP	0.016	0.028	Late-Regressed; Late-Mid
Alanine	0.017	0.029	Late-Regressed; Late-Mid
Valine	0.021	0.032	Late-Regressed
Inosine	0.021	0.032	Mid-Regressed
Tyrosine	0.022	0.032	Late-Regressed
Phenylalanine	0.022	0.032	Late-Regressed
Malonate	0.022	0.032	Late-Mid
Lysine	0.029	0.040	Late-Regressed
Pterin	0.030	0.040	Late-Mid
Leucine	0.030	0.040	Late-Regressed
Ciliatine	0.035	0.045	Late-Regressed

p-*value <0.05 indicates statistically significant differences between groups. False Discovery Rate (FDR) indicates the* p-*value adjusted for multiple comparisons.*

Furthermore, a cross-validation process (CV-ANOVA) based on a 7-fold cross-validation permutation testing method was used to assess the significance of the PLS-DA models. Models with a *p*-value <0.05 were considered significant.

We used Variable Importance in Projection (VIP) > 1 as a variable selection method and threshold to identify significant metabolites in the PLS-DA models. Metabolites with VIP score >1 were selected for each model to generate heatmaps and pathway analysis (MetPA; MetaboAnalyst 4.0). The clustered heatmaps display the relative concentration of metabolites and an overview of the metabolic profile for various treatment groups to visualize changes in metabolite concentrations. Hierarchical clustering was conducted on the rows/variables of the data matrix and the dendrograms cluster metabolites that undergo similar changes in abundance. Finally, differences in the levels of metabolites in various groups were tested by one-way ANOVA, followed by Tukey's post-hoc analyses that identify differences between groups (**Table 2**). To further investigate differences between seasons, we conducted multiple t-tests, and the *p*-values are also shown in **Supplementary Table S5**. The effect of single and double injection with GnRH and GnIH on basal metabolism was also analyzed with ANOVA and multiple t-tests (**Supplementary Tables S6–S13**).

p-value adjusted for multiple comparisons using False Discovery Rate (FDR) < 0.05 indicates a significant difference between groups.

2.5 Pathway Analysis

The concentration levels of the VIP > 1 metabolites identified for every PLS-DA model were used to conduct pathway analysis and determination of metabolic pathways involved in different treatment groups. In the present study, we used the MetPA metabolomics pathway analysis offered by the Metaboanalyst 4.0 platform as an analytical tool (Xia et al., 2010). Pathway

analysis in MetPa combines quantitative enrichment analysis based on the metabolite concentration values and topological analysis that measures the importance of a metabolite in the metabolic pathway. The nodes importance value (pathway impact) is calculated from centrality measures, normalized by the sum of the importance value of metabolites in the pathway (Xia et al., 2010). In this regard, the impact value of zero indicates a relatively low number of connections of one node to others. This suggests that the matched metabolites for a specific pathway have a marginal role concerning the "length" and complexity of the pathway. The global test and Relative-betweenness Centrality were selected as algorithms for the enrichment and topological analysis, respectively (Chong et al., 2019). In the present study, we used the zebrafish (*Danio rerio*) KEGG pathway library as a reference.

3 RESULTS

3.1 Characterization of Fish Hepatic Metabolism at Different Stages of the Seasonal Cycle

Female liver samples collected at different stages of the reproductive cycle were analyzed using LC-MS for relative quantification of metabolites. Samples were analyzed using negative-mode electrospray ionization, and complementary analysis using positive-mode was not carried out in the present study. A targeted metabolomics profiling approach using an *m/z* and retention times standard library led to the identification of 71 metabolites in the aqueous phase of liver extracts. Examples of peak detection and measurements are shown in **Supplementary Figure S1**. Furthermore, the average peak intensity (±SEM) of the VIP > 1 metabolites during the three investigated reproductive stages is provided in **Supplementary Table S1**. In this study, we used both univariate and multivariate statistical and visualization techniques to comprehensively characterize the metabolic profile of different reproductive stages and investigate seasonal variations in metabolism. Chemometrics tools such as PLS-DA and PCA were used to reduce the dimensionality of the dataset and to visualize similarities (cluster formation) and dissimilarities (cluster separation) between the investigated groups. PCA was conducted on the metabolic data obtained from the Control samples collected from female goldfish at three stages of reproduction. The three groups included fish at regressed gonadal phase/somatotropic phase (n = 10), mid recrudescence (n = 10), and late recrudescence (n = 10). We also used a quality control group (QC, n = 5) (**Supplementary Figure S2**). The PCA scatter plot shows a strong cluster formation for the QC group, confirming the reliability of our dataset and the absence of outliers as all samples fall within the 95% confidence area. We performed PLS-DA on the dataset to further explore the shift seen in the PCA analysis. In the supervised multivariate modelling method, the PLS-DA algorithm combines dimensionality reduction and discriminant analysis, using the group ID of samples. Hence, PLS-DA provides a robust predictive and descriptive regression model (Lee et al., 2018). The score scatter plot obtained from PLS-DA analysis revealed a significant shift in the metabolic profile of the three gonadal stages (Regressed, Mid and Late; **Figure 1**). Statistical significance of the identified shift was assessed by the R^2 and Q^2 parameters ($R^2 = 0.842$, $Q^2 = 0.658$) and by CV-ANOVA ($p = 2.75 \times 10^{-5}$) (**Figure 1**). To further investigate the observed metabolic shift, we performed pairwise analysis for each group and obtained significant differences for all PLS-DA models: Regressed/Mid: 0.0011; Mid/Late: 0.0009; Late/Regressed: 4.91×10^{-5} (**Figure 1**). In the present study, each season was compared with the other two. We identified the dominant metabolites in each PLS-DA model by selecting the metabolites with VIP score >1 to characterize the phenotypes at the three recrudescence stages investigated (**Figure 2**). Given the large number of variables provided by LC-MS analysis, data sets are often difficult to interpret and feature selection prior to pattern recognition becomes a critical step in the metabolomics studies (Lê Cao et al., 2011). Thus, metabolites with a VIP score >1 can be regarded as molecular markers that indicate the status of a given condition and differences among the treatment groups (Gorrochategui et al., 2016). The stacked bar graph shown in **Figure 2** compares the VIP score (>1) of the identified metabolites in each model as a contribution to the whole dataset (**Figure 2**). Furthermore, **Figure 2** shows similarities between models and highlights differences in the contribution of variables, suggesting that the hepatic metabolic profile of the three stages of reproduction is considerably different. **Figure 3** illustrates the relationship between the three built models by showing the number of overlapping variables. The Venn diagram can directly compare models, determine the number of identified VIP > 1 metabolites in each model, and highlight the number of unique and shared variables. In the Regressed/Mid models, we identified 30 VIP > 1 metabolites where 15 metabolites were similar to the Late/Regressed model and 11 with the Mid/Late model. We also identified 30 metabolites with VIP > 1 in the Late/Regressed model and 31 in the Mid/Late-model, with 14 common metabolites between these two. The three metabolites with a VIP score >1 common in all groups were Acetoacetic acid, Guanosine monophosphate (GMP) and Uric acid. We combined the metabolites with VIP > 1 of each model for heatmap generation among the 52 distinguishing metabolites. The clustered heatmap presented in **Figure 4** shows the group-average concentration of all VIP > 1 metabolites, providing insight into the relationship between metabolites in the three reproductive stages, facilitating the visualization of their relative abundance (**Figure 4**). Additionally, the hierarchical clustering analysis accompanying the heatmap revealed the presence of three primary metabolites clusters since three main branches occur at similar distances (**Figure 4**). The interpretation of the heatmap is further facilitated by one-way ANOVA results (**Table 2**) and multiple t-test comparisons (**Supplementary Table S5**). Finally, to fully characterize the changes in basal metabolism related to the three reproductive stages, we conducted a pairwise pathways analysis to investigate the differences. Metabolites with VIP > 1 obtained in the three built models were submitted to the Metaboanalyst 4.0

platform for the pathway analysis (Xia et al., 2010). The analysis of the biochemical processes data in this study was based on the zebrafish (Danio rerio) pathway library of the Kyoto Encyclopedia of Genes and Genomes (KEGG) (Kanehisa et al., 2019). Pathway analysis used in this study integrates quantitative pathway enrichment analysis (QEA) that measures differences in metabolites concentration between groups (*p*-value), and network topology analysis that estimates the relative importance of metabolites based on their relative position in a given pathway (pathway impact). The results of the pairwise pathway analysis shown in **Figure 5** describe differences in metabolic activities and patterns of energy allocation between the seasons. The detailed results of the pathways impacted in each comparison are presented in **Supplementary Tables S2–S4**. Our results demonstrate that purine and pyrimidine metabolism are among the main pathways contributing to the differences observed between the fish at regressed phase and mid recrudescence, and between mid and late recrudescence groups (**Figure 5**). Changes in the concentration of metabolites such as guanosine, inosine, adenine, and adenosine suggest increased activity of the purine salvage pathway during the regressed phase compared to mid recrudescence (**Figure 4**). On the other hand, the high levels of inosinic acid, AMP and GMP suggest an increased *de novo* purine synthesis during mid recrudescence, compared to regressed and late recrudescence (**Figure 4**). On the contrary, elevated concentration of allantoin, hypoxanthine and xanthine in late compared to mid recrudescence suggests an enhanced purine degradation in the late recrudescence stage (**Figure 4**). Pathway analysis comparing regressed and mid recrudescence and regressed and late recrudescence indicate changes in the metabolism of several amino acids, including taurine, arginine, tyrosine, lysine, methionine, valine, leucine, histidine, alanine, threonine and phenylalanine (**Figure 5**). The heatmap, supported by ANOVA and multiple t-test analysis (**Table 2**; **Supplementary Table S5**), indicates that these amino acids have significantly higher concentrations during the regressed phase than mid and late recrudescence. Thus, the results suggest higher levels of amino acid turnover to support protein synthesis during the stage of maximal growth (gonadal regressed phase; **Figure 4**). The glycogen concentration was significantly higher in the regressed than the mid and late recrudescence groups, as shown in the heatmap (**Figure 4**) and the ANOVA and t-test analysis (**Table 2**; **Supplementary Table S5**). In fish, the liver is the main site for glycogen buildup, and lower concentrations occur in the brain and the skeletal muscle (Soengas et al., 1993). Our results demonstrate an enhanced glycogen synthesis during the regressed phase, consistent with previous studies in brackish-water fish, common roach *R. rutilus* (Rinchard and Kestemont, 2003) and flounder (Petersen and Emmersen, 1977). Finally, taurine, hypotaurine and tyrosine metabolism are enhanced during the regressed phase, as shown in the heatmap and pathway analysis comparing regressed to mid and late recrudescence (**Figures 4**, **5**). The functional amino acid taurine and thyroid hormones (derived from tyrosine) are essential for normal growth (Power et al., 2001; Andersen et al., 2016). The results demonstrate enhanced anabolic pathways such as protein and glycogen synthesis during the regressed gonadal phase, corresponding to the stage of the maximal growth period. Pathway analysis comparing mid and late recrudescence metabolic profiles demonstrate significant differences in lipid metabolism (**Figure 5**). Based on the results of distinguishing VIP metabolites and enriched pathways, fatty acid biosynthesis, sphingolipid, and glycerophospholipid metabolism were more active in the liver of mid recrudescence fish than late (**Figure 4**). This is corroborated by the ANOVA results of *O*-Phosphoethanolamine (a metabolite of the phospholipid synthesis pathway; EAP in the heatmap) and malonate (first step product of fatty acids synthesis) that indicate a significant increase of these metabolites in mid compared to late recrudescence (**Table 2**). Consistent with previous studies, these results indicate an enhanced lipid production and mobilization in the liver supporting the vitellogenesis process during mid recrudescence (Rinchard and Kestemont, 2003). Validated by the ANOVA results, mid recrudescence is characterized by high levels of ornithine and citrulline, metabolites derived from arginine metabolism (**Table 2**). Results of pathway analysis confirm the different activity of the arginine biosynthesis pathway when comparing regressed and mid recrudescence fish (**Figure 5**). Arginine metabolism is associated with the reproductive system and can affect fecundity by regulating vitellogenesis and egg quality (Waters et al., 1992). Pathway analysis comparing Mid and late recrudescence highlights changes in the metabolism of several amino acids, including arginine, cysteine, methionine, taurine, hypotaurine, histidine, leucine, tyrosine, phenylalanine, and glutamine (**Figure 5**). The heatmap in **Figure 4** demonstrates lower concentrations of these and other amino acids during the late recrudescence than regressed and mid, suggesting a lower activity of amino acids and protein metabolism in the final stages of gonadal recrudescence. The late recrudescence is also characterized by significantly lower levels of the ketone bodies acetoacetic acid and hydroxybutyric acid compared to regressed and mid recrudescence as shown in the heatmap and ANOVA analysis (**Figure 4**; **Table 2**). In male fish, however, late recrudesce was characterized by significantly higher levels of ketone bodies than those at regressed and mid recrudescence (Ladisa et al., 2021). Furthermore, late recrudescence is characterized by significantly higher glutathione levels (**Figure 4**; **Table 2**), indicating an enhanced glutathione metabolism as demonstrated by the pathway analysis results comparing late to both regressed and mid recrudescence (**Figure 5**).

3.2 Effects of Acute Treatments With Gonadotropin-Releasing Hormone and Gonadotropin-Inhibitory Hormone on Metabolism

GnRH and GnIH can regulate both gonadotropic and somatotropic activities and are involved in the multifactorial regulation of growth and reproduction in goldfish. We injected GnRH and GnIH in adult female goldfish at three stages of the gonadal cycle to investigate their potential effects on liver

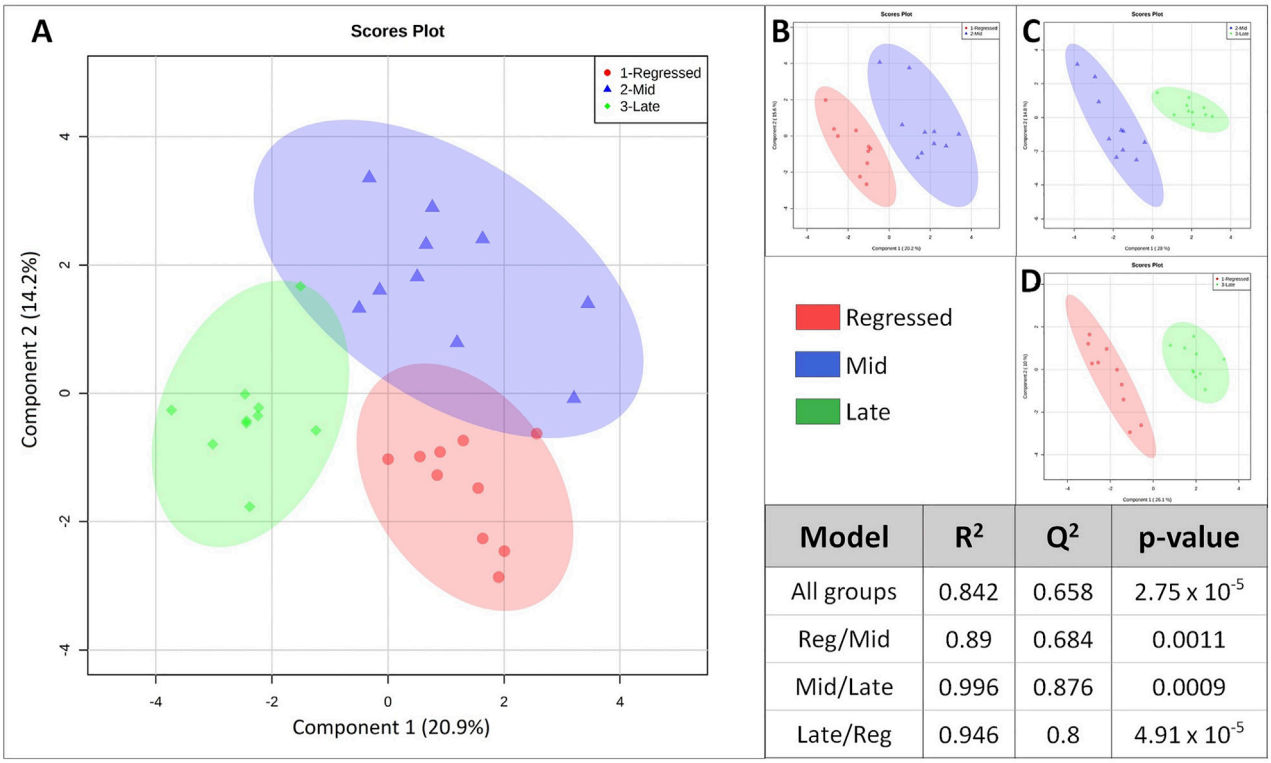

Model	R^2	Q^2	p-value
All groups	0.842	0.658	2.75×10^{-5}
Reg/Mid	0.89	0.684	0.0011
Mid/Late	0.996	0.876	0.0009
Late/Reg	0.946	0.8	4.91×10^{-5}

FIGURE 1 | Score scatter plot of the built Partial-Least Squares—Discriminant analysis (PLS-DA) models. The "All groups" model investigate the change in liver metabolism of the three groups corresponding to the three reproductive stages **(A)**. Groups were also analyzed in a pair-wise manner: Regressed/Mid **(B)**, Mid/Late **(C)** and Late/Regressed **(D)**. Each axis represents a component that is a source of variation between samples (shown as percentage in parenthesis). Each point represents normalized concentrations of the complete metabolite set of a liver sample. Regressed: regressed gonadal phase/somatotropic phase (n:10); Mid: mid gonadal recrudescence (n:10); Late: late gonadal recrudescence (n:10). The table shows results for statistical analysis obtained for the built models. R^2 assess the "goodness of fit" and Q^2 asses the "goodness of prediction". *p*-values were measured *via* CV-ANOVA based on a 7-fold cross validation permutation testing method. *p*-value <0.05 indicate significant difference.

metabolism. GnRH-III, one of the two native isoforms in goldfish (Yu et al., 1991), and goldfish GnIH (gGnIH) were used in the present study. Fish received a single or double injection of GnRH-III or GnIH at T0 and T12 h and sacrificed 24 h after the first injection, as shown in **Table 1**. Injections with PBS (PBS + PBS) served as the control (Ctrl) in the present study. The time-course of the treatments was based on previous studies with GnRH on goldfish in which the first injection served as a priming treatment. Multiple GnRH injections were shown to enhance subsequent LH production (Omeljaniuk et al., 1989; Moussavi et al., 2012, Moussavi et al., 2013, Moussavi et al., 2014). However, it is likely that the acute nature of GnRH and GnIH treatments used in the present study may not be sufficient to elicit changes seen in different seasons. The metabolomics data collected for GnRH (Ctrl, PBS + GnRH, GnRH + GnRH) and GnIH (Ctrl, PBS + GnIH, GnIH + GnIH) treatments were analyzed independently to reduce the impact of artifacts and maximize the predictive ability of multivariate analysis. A standard library of retention times and *m/z*, with Maven software, led to the identification of 64 metabolites in the GnRH treated and 59 metabolites in the GnIH treated groups. PLS-DA was performed on the three treatment groups (control, single and double hormone injection) for each reproductive phase to investigate differences in the metabolic profiles of the three groups tested (**Figure 6**). PLS-DA models built for GnRH treatments show a statistically significant difference in the metabolic profile of the three treatment groups in the regressed (*p*-value = 0.001) and mid recrudescence (*p*-value = 0.046; **Table 3**) stages. On the other hand, GnRH treatment in the late recrudesce and GnIH treatment in all reproductive stages did not result in a statistically significant PLS-DA model for various treatment groups (**Table 3**). Variable selection based on the VIP score >1 criterion identified 26 metabolites in the regressed stage, 25 in the mid and 24 in the late recrudescence for the GnRH treatment groups (**Figure 7A**). For the GnIH treated groups, variable selection based on the VIP score >1 criterion identified 23 metabolites in the regressed stage, and 16 and 18 for the mid and late recrudesce, respectively (**Figure 7B**). The stacked bar graphs presented in **Figure 7** show differences between models in terms of metabolite importance (VIP score >1), indicating different metabolic actions of hormones at different stages of gonadal recrudescence and providing a basis for comparing GnRH and GnIH effects. We employed multivariate and univariate statistical and visualization methods for each

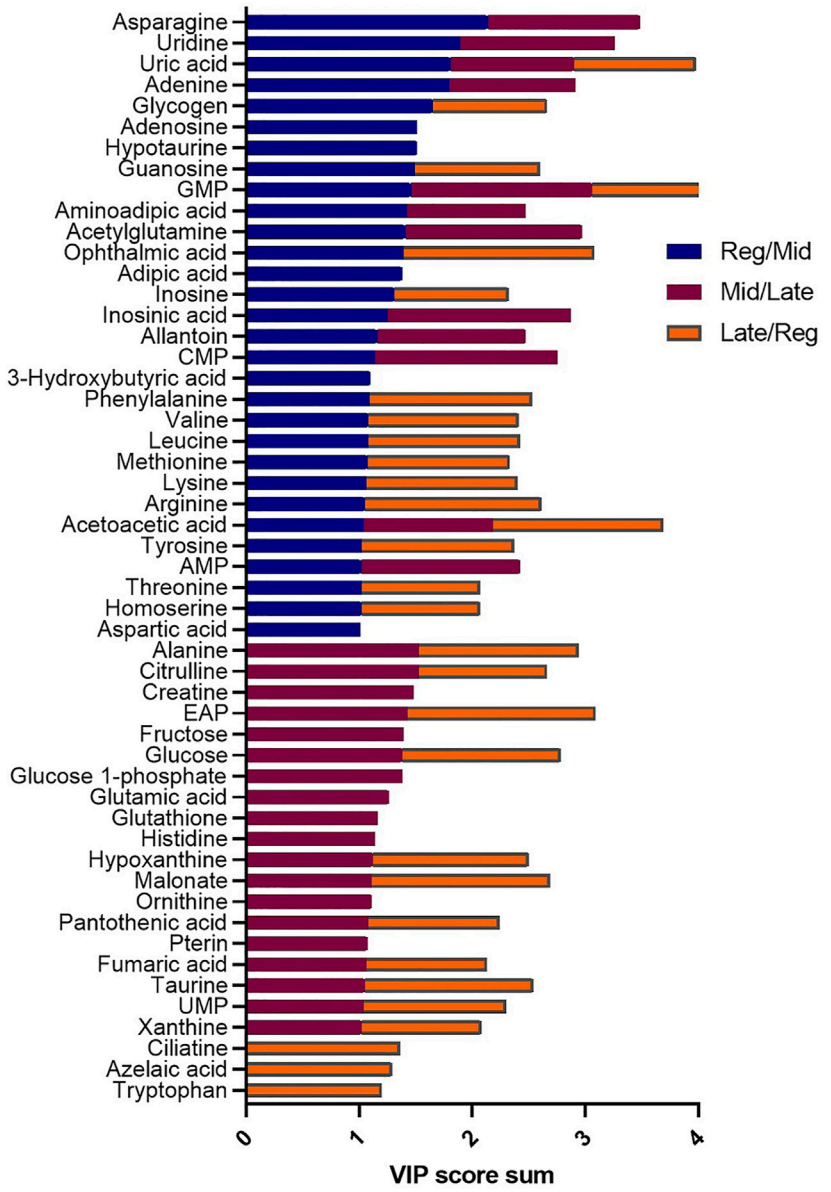

FIGURE 2 | Stacked bar graph comparing the VIP > 1 metabolites the three PLS-DA models: Reg/Mid (blue), Mid/Late (burgundy), Late/Reg (orange). Colored bars represent the VIP score (>1) in each model as contribution to the whole. The VIP score estimates the importance of each metabolite in the PLS-DA models providing useful insight on the differences between models.

model's VIP > 1 metabolites to investigate differences between treatment groups. To analyze the acute effect of GnRH and GnIH on seasonally-dependent basal metabolism, one clustered heatmap was built for each PLS-DA model highlighting the impact of single and double injection treatment (six in total, **Figure 8**). One-way ANOVA accompanied by multiple t-tests identified significant changes between experimental groups (**Supplementary Tables S6-S13**). Pathway analysis performed on the Metaboanalyst 4.0 platform identified metabolic pathways and physiological processes altered by treatments with GnRH and GnIH (**Table 4**). Within each reproductive phase, single and double hormone injected groups were compared independently to their respective control groups as the pathway analysis tool only allows the comparison between two groups at a time. The metabolic pathways impacted by single and double injection with GnRH or GnIH in the three stages of gonadal recrudescence are summarized in **Table 4**. **Supplementary Tables S14, S15** provides more details on pathways analysis results.

3.2.1 Regressed Gonadal Phase—Growth Phase

During the regressed phase corresponding to the period of maximal growth, a single injection with GnRH significantly impacted purine and pyrimidine metabolism (**Table 4**). As shown in the heatmap (**Figure 8**) and confirmed by ANOVA

FIGURE 3 | Venn diagram displaying the number of unique and common VIP > 1 metabolites between PLS-DA models. The Regressed/Mid PLS-DA model has 30 metabolites with VIP score >1 and share 15 metabolites with the Late/Regressed model and 11 with the Mid/Late model. The Late/Regressed and the Mid/Late model have 30 and 31 VIP > 1 metabolites, respectively and 14 are in common between the two models. Three metabolites are shared by the three models: Acetoacetic acid, Guanosine monophosphate (GMP) and Uric acid.

results (**Supplementary Table S6**), hypoxanthine, xanthine, and uric acid were significantly increased following a single GnRH injection, compared to the control, suggesting elevated purine degradation. Interestingly, in the regressed phase, purine metabolism was also significantly altered by double injection with GnIH (**Table 4**). Single GnRH injection and single and double injections with GnIH increased purine degradation by inducing higher hypoxanthine, xanthine, and uric acid levels than the control (**Figure 8**). It should be noted that basal hypoxanthine, xanthine and uric acid levels were also higher in the late recrudescence than regressed and mid recrudescence, indicating that GnRH and GnIH treatment in the regressed phase can alter the pathways to resemble that observed during late recrudescence. As shown in the heatmap, a single injection with GnRH decreased the concentration of several carbohydrates such as glycogen, raffinose, oligomaltose, sucrose, fructose, glucose and glucose 6-phosphate (**Figure 8**). However, based on ANOVA, only differences for sucrose, fructose and glucose were statistically significant (**Supplementary Table S6**), and starch, sucrose and galactose metabolism were not significantly impacted (**Table 4**). Furthermore, single injection with GnRH enhanced ketone bodies metabolism resulting in a higher concentration of 3-hydroxybutyric acid than the control, as highlighted by the heatmap (**Figure 8**). Unlike single injection, double injection with GnRH did not change the metabolic pathways (**Table 4**), and the level of metabolites shown in the heatmap are similar to the control (**Figure 8**). Single injection with GnIH during the regressed phase also altered the metabolism of several amino acids, including alanine, aspartate, glutamate, glycine, serine and threonine metabolism, while double injection with GnIH significantly impacted the metabolism of carbohydrates, including galactose (**Table 4**). Accordingly, sucrose concentration was decreased by both single and double injection with GnIH (**Figure 8**). Single and double GnIH injection increased creatine level (**Figure 8**), suggesting the involvement of GnIH in the energy homeostasis. Creatine and its phosphorylated form function as an energy buffer facilitating ATP recycling to support the cellular energy balance (Borchel et al., 2019).

3.2.2 Mid Recrudescence

Pathway analysis during mid recrudescence revealed different metabolic pathways affected following single and double injection with GnRH (**Table 4**). This is supported by the VIP > 1 metabolites' heatmap, also showing a significantly different profile between single and double GnRH-injected groups (**Figure 8**). Single GnRH injection significantly altered metabolic pathways connected to the lipid metabolism (glycerophospholipid and glycerolipid metabolism; **Table 4**), which correlated with significantly lower levels of *O*-phosphoethanolamine (EAP) compared to the control (**Figure 8**; **Supplementary Table S6**). Single injection with GnRH also altered the purine and pyrimidine metabolism (**Table 4**). In this context, changes in the concentration of relevant metabolites indicate decreased purine and pyrimidine synthesis and increased purine degradation (**Figure 8**). Double injection with GnRH altered pathways connected to the carbohydrate metabolism. We observed significant changes in starch, sucrose, galactose, ketone bodies metabolism as well as the metabolism of several amino acids, including taurine, valine, leucine, isoleucine and tyrosine (**Table 4**). As for GnIH, single injection during mid recrudescence did not significantly change metabolic pathways annotated in the KEGG Danio rerio database (**Table 4**). However, double injection with GnIH significantly altered the metabolism of purine and pyrimidine, pantothenate, and the metabolism of several amino acids (**Table 4**). As shown in the heatmap, double injection with GnIH also increased the glucose and glucose 6-phosphate and decreased glutamine levels, compared to control (**Figure 8**; **Supplementary Table S10**).

3.2.3 Late Recrudescence

Single injection with GnRH in late recrudescence altered pathways related to carbohydrate and energy metabolism such as fructose and mannose metabolism, glycolysis/gluconeogenesis and TCA cycle (**Table 4**). On the other hand, double injection with GnRH impacted the metabolism of amino acids such as alanine, aspartate, glutamate, and arginine (**Table 4**). Also shown in the heatmap of VIP > 1 metabolites, single and double injection with GnRH decreased the levels of carbohydrates such as glycogen, raffinose, oligomaltose and sucrose, while increasing the levels of glucose, fructose, dihydroxyacetone phosphate (DHAP) and succinic acid (**Figure 8**). These results suggest that GnRH promotes the degradation of carbohydrate storage

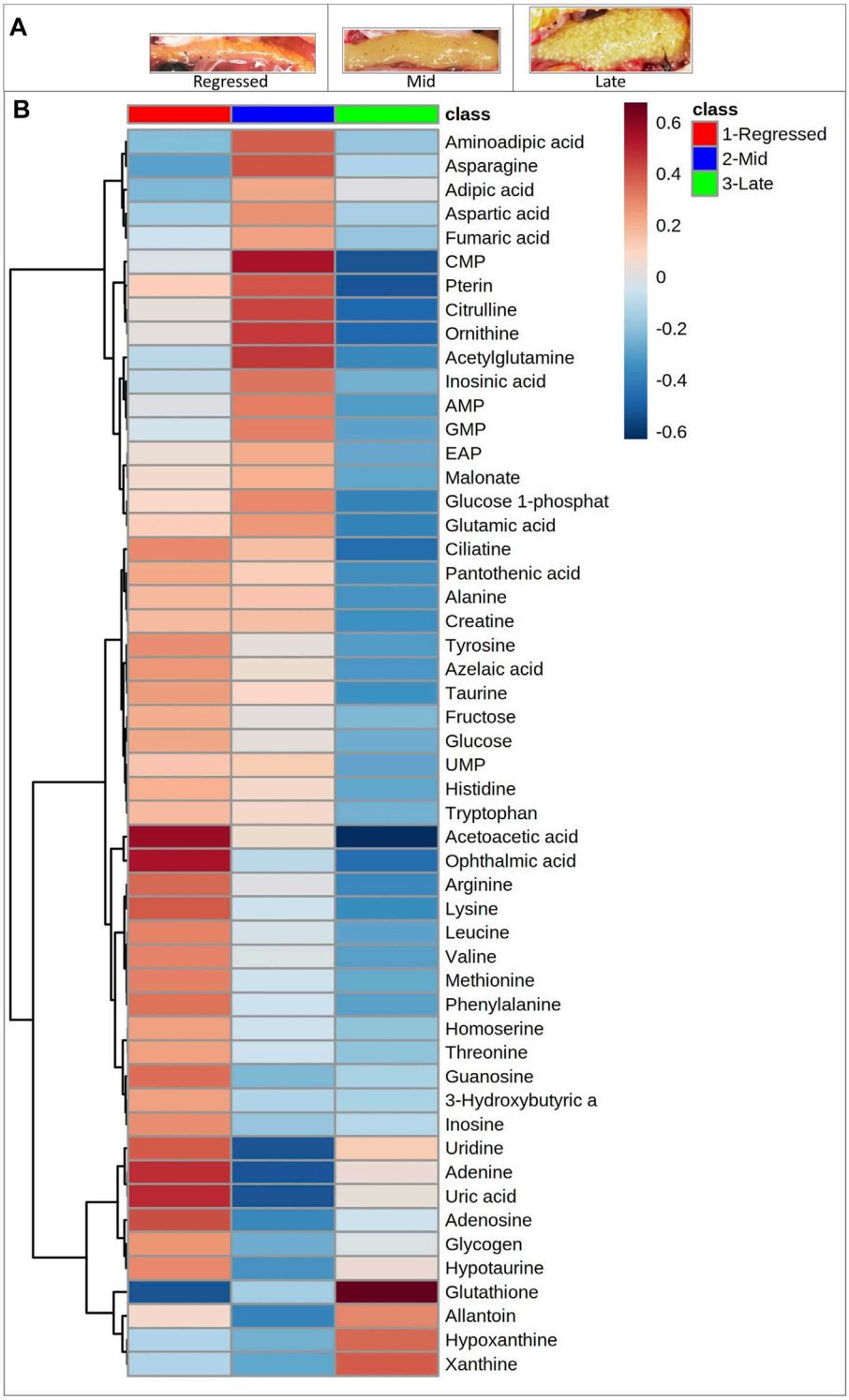

FIGURE 4 | Photographs of ovaries used at different gonadal stages **(A)**. Clustered heatmap of the VIP > 1 metabolites identified in the three models. Shades of blue and red indicate decreases and increases in the concentrations of metabolites in each reproductive phase, respectively **(B)**.

to be used as an energy source *via* glycolysis and the TCA cycle. In the case of GnIH, both single and double injections affected similar pathways, although double injection exerted greater effects than single injection (**Figure 8**). As shown in the heatmap of VIP > 1 metabolites, the concentrations of several metabolites, including raffinose, fumaric acid and succinic acid,

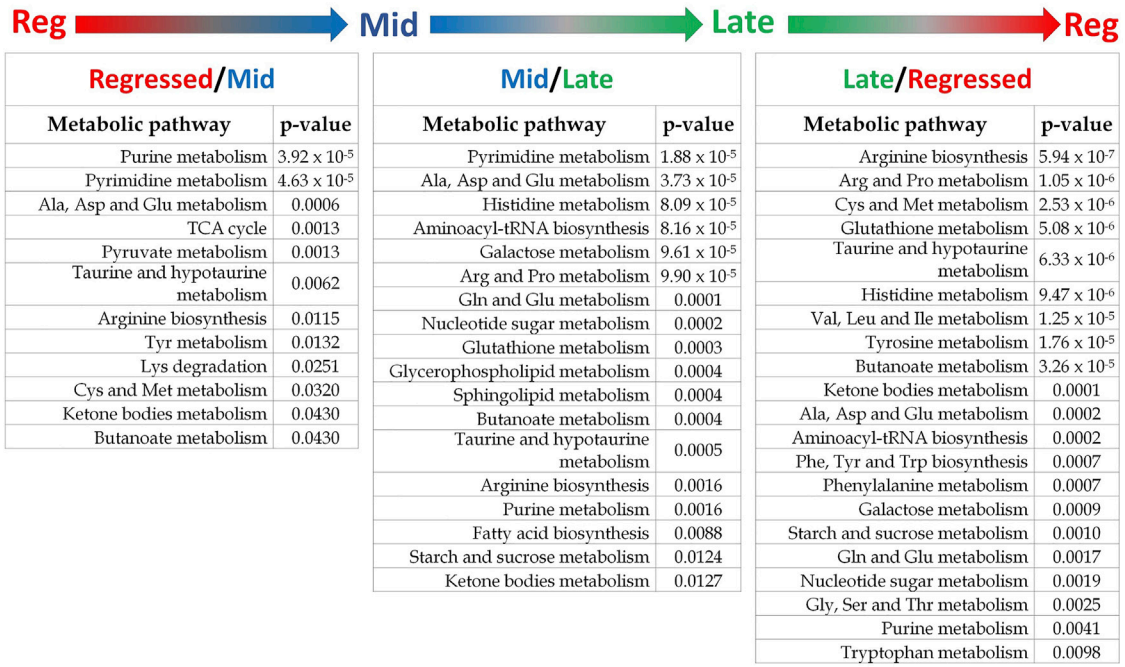

Regressed/Mid

Metabolic pathway	p-value
Purine metabolism	3.92×10^{-5}
Pyrimidine metabolism	4.63×10^{-5}
Ala, Asp and Glu metabolism	0.0006
TCA cycle	0.0013
Pyruvate metabolism	0.0013
Taurine and hypotaurine metabolism	0.0062
Arginine biosynthesis	0.0115
Tyr metabolism	0.0132
Lys degradation	0.0251
Cys and Met metabolism	0.0320
Ketone bodies metabolism	0.0430
Butanoate metabolism	0.0430

Mid/Late

Metabolic pathway	p-value
Pyrimidine metabolism	1.88×10^{-5}
Ala, Asp and Glu metabolism	3.73×10^{-5}
Histidine metabolism	8.09×10^{-5}
Aminoacyl-tRNA biosynthesis	8.16×10^{-5}
Galactose metabolism	9.61×10^{-5}
Arg and Pro metabolism	9.90×10^{-5}
Gln and Glu metabolism	0.0001
Nucleotide sugar metabolism	0.0002
Glutathione metabolism	0.0003
Glycerophospholipid metabolism	0.0004
Sphingolipid metabolism	0.0004
Butanoate metabolism	0.0004
Taurine and hypotaurine metabolism	0.0005
Arginine biosynthesis	0.0016
Purine metabolism	0.0016
Fatty acid biosynthesis	0.0088
Starch and sucrose metabolism	0.0124
Ketone bodies metabolism	0.0127

Late/Regressed

Metabolic pathway	p-value
Arginine biosynthesis	5.94×10^{-7}
Arg and Pro metabolism	1.05×10^{-6}
Cys and Met metabolism	2.53×10^{-6}
Glutathione metabolism	5.08×10^{-6}
Taurine and hypotaurine metabolism	6.33×10^{-6}
Histidine metabolism	9.47×10^{-6}
Val, Leu and Ile metabolism	1.25×10^{-5}
Tyrosine metabolism	1.76×10^{-5}
Butanoate metabolism	3.26×10^{-5}
Ketone bodies metabolism	0.0001
Ala, Asp and Glu metabolism	0.0002
Aminoacyl-tRNA biosynthesis	0.0002
Phe, Tyr and Trp biosynthesis	0.0007
Phenylalanine metabolism	0.0007
Galactose metabolism	0.0009
Starch and sucrose metabolism	0.0010
Gln and Glu metabolism	0.0017
Nucleotide sugar metabolism	0.0019
Gly, Ser and Thr metabolism	0.0025
Purine metabolism	0.0041
Tryptophan metabolism	0.0098

FIGURE 5 | Results summary of pathway analysis showing the main altered metabolic pathways in each comparison. Pathways with p-value < 0.05 are considered significantly altered between the investigated phases. The detailed results of pathway analysis for each comparison are shown in **Supplementary Tables S2–S4**.

were progressively reduced following single and double treatment with GnIH (**Figure 8**). In this context, pathways related to energy metabolism (propanoate and pyruvate metabolism, TCA cycle) were impacted to a greater extent by double injection than single injection with GnIH (**Table 4**). Double injection with GnIH significantly affected lipid metabolism by altering pathways such as biosynthesis of unsaturated fatty acids, glycerolipid and sphingolipid metabolism (**Table 4**). Changes in the concentration of relevant metabolites such as docosahexaenoic acid (DHA) and *O*-phosphoethanolamine (EAP) suggest a stimulatory action of GnIH on these metabolic pathways (**Figure 8**). Furthermore, double injection with GnIH significantly inhibited ketone bodies metabolism as the levels of 3-hydroxybutiric acid are decreased by single and double injections (**Figures 8**).

4 DISCUSSION

In the present study, we used an LC-MS-based targeted metabolomics approach to investigate the hepatic metabolic profile of sexually mature female goldfish in three stages of the reproductive cycle, including the regressed gonadal stage corresponding to the period of maximal growth as well as mid and late gonadal recrudescence. Moreover, we investigated the effects of acute injections with GnRH and GnIH on liver metabolism to explore the potential involvement of these hormones in the control of energy allocation during growth and reproduction in goldfish. The liver was chosen as a tissue of interest since it is the primary energy hub and is responsive to hormonal and metabolic signals, influencing the whole-body metabolism (Rui, 2014). Furthermore, the liver is the site of Vtg synthesis, which is a precursor molecule for yolk proteins (Reading and Sullivan, 2011).

4.1 Metabolic Changes During Growth and Reproductive Phase

The multivariate and univariate analysis allowed the identification of significant changes in the hepatic metabolic profile of female goldfish during different stages of the reproductive cycle. Based on the observed changes in the levels of metabolites and active metabolic pathways, we were able to identify changes in amino acid, carbohydrate, lipid, nucleotide, and energy metabolism during growth and reproductive cycles.

4.1.1 Regressed Gonadal Phase is Characterized by Growth-Promoting Processes

Maximal growth is observed during the regressed gonadal phase in fish, and our results demonstrate an enhanced nucleotide and protein metabolism during this period. Higher concentrations of amino acids including tyrosine, arginine, alanine, lysine, leucine, valine, methionine, histidine, tryptophan and phenylalanine indicate an increased amino acids metabolism and turnover possibly in support of enhanced protein synthesis (**Figure 4**; **Table 2**). The observed higher concentration of tyrosine in regressed, compared to mid and late recrudescence, is correlated with higher circulating thyroid hormones (T3 and T4) in the regressed goldfish (Sohn et al., 1999). Our results

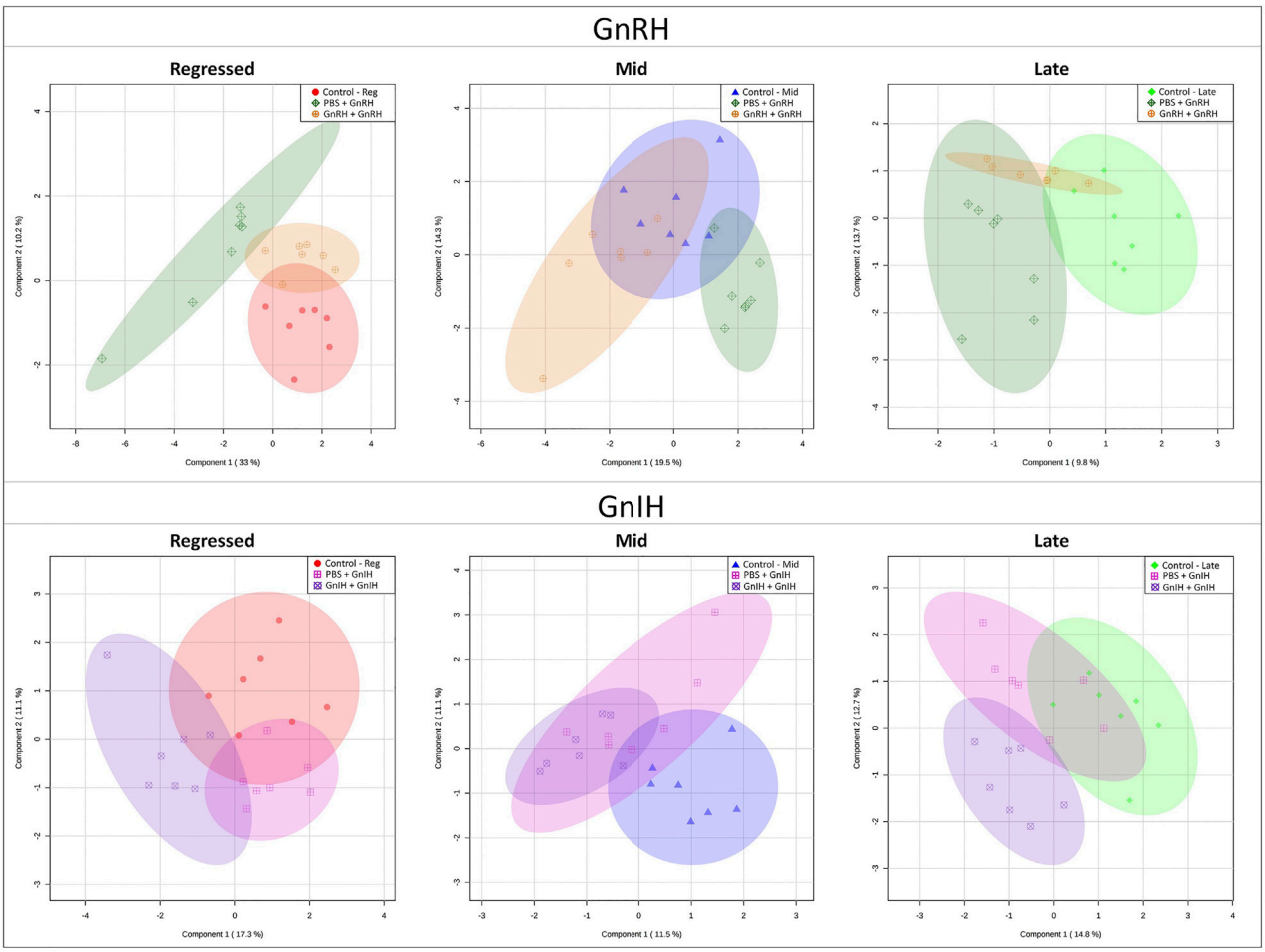

FIGURE 6 | PLS-DA score scatter plots of the models investigating the acute effect of GnRH and GnIH in the three investigated reproductive phases: regressed phase/growth phase, mid recrudescence and late recrudescence. Each graph shows the shift in liver metabolism between Control (PBS + PBS), single injection with GnRH or GnIH (PBS + GnRH/GnIH) and double injection with GnRH or GnIH (GnRH/GnIH + GnRH/GnIH). Each point represents concentrations of the complete metabolite set of a liver sample of the respective group. Axes represent the first and second component that is a source of variation between samples.

TABLE 3 | Statistical values for the Partial Least Squares—Discriminant Analysis (PLS-DA) models investigating the effect of GnRH and GnIH in the three investigated reproductive stages (Regressed, Mid and Late). Each model represents the comparison of three groups: control, single and double injection with **GnRH** or **GnIH**. R^2 and Q^2 parameters measure the "goodness of fit" and "goodness of prediction" respectively for each model. Statistical significance (p-value < 0.05) of models was assessed *via* Cross Validated—ANOVA (CV-ANOVA) based on a 7-fold cross validation permutation testing method.

GnRH			
Model	R^2	Q^2	p-value
Regressed	0.39	0.296	0.001
Mid	0.393	0.279	0.046
Late	0.395	0.117	0.097
GnIH			
Regressed	0.618	0.195	0.579
Mid	0.306	0	0.99
Late	0.626	0.282	0.99

combined with observed higher thyroid hormone receptor (TRβ) mRNA level in the regressed female goldfish liver (Ma et al., 2020b), provide further support for the hypothesis that thyroid hormones are essential components of growth response during the regressed gonadal phase in fish. It should be noted that the role of thyroid hormones in the control of growth is widely recognized (Cabello and Wrutniak, 1989; Nelson and Habibi, 2009). Thyroid hormones regulate GH and IGF-1 production as well as liver GH receptor synthesis in several vertebrates (Tsukada et al., 1998; Schmid et al., 2003). Besides interacting with the somatotropic axis, thyroid hormones can directly stimulate growth by enhancing protein synthesis and regulating glucose homeostasis. T3 was shown to increase protein synthesis at a pre-translational level through stimulation of ribosomal and nuclear RNA synthesis (Müller and Seitz, 1984). We hypothesize that the enhanced amino acid metabolism demonstrated during the regressed phase results from increased protein synthesis

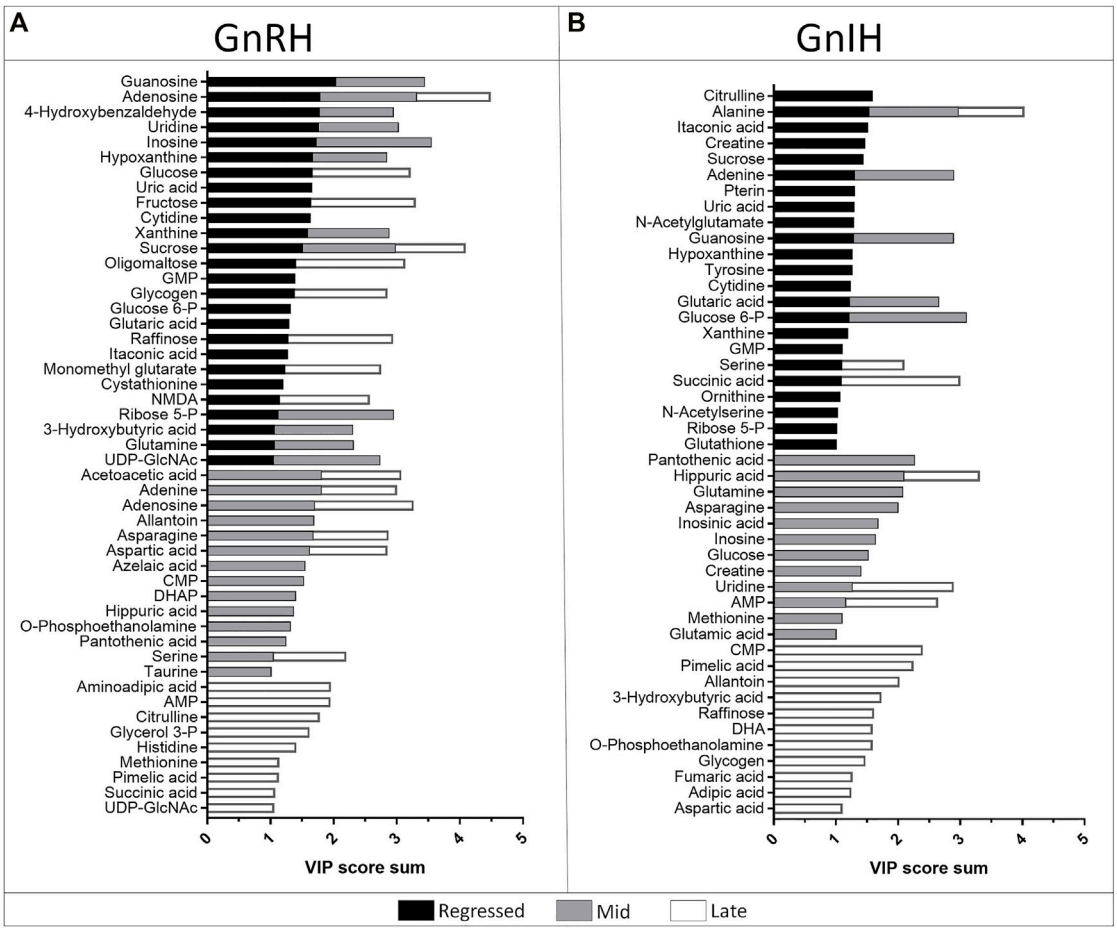

FIGURE 7 | Stacked bar graph showing the metabolites with VIP score >1 identified in the PLS-DA models of GnRH **(A)** and GnIH **(B)** treatments in the three investigated reproductive phases: regressed phase/growth phase (black), mid recrudescence (grey) and late recrudescence (white). Colored bars represent the VIP score of the metabolite as contribution to the whole. For each reproductive phase, the model represents the comparison between three groups: control, single and double injection with GnRH or GnIH.

stimulated by thyroid hormones and GH. These hormones are present at higher levels during the regressed phase (Marchant and Peter, 1986; Sohn et al., 1999). Thyroid hormones stimulate enzymes of the gluconeogenic pathway, resulting in increased plasma glucose levels in several fish species (Deal and Volkoff, 2020). The hyperglycemic effect of thyroid hormones may be a contributing reason for higher concentrations of glucose and fructose observed in the present study during the regressed phase, compared to late recrudescence (**Figure 4**; **Table 2**). Increased glucose utilization would support protein synthesis by enhancing energy metabolism and synthesis of amino acids from intermediates of the TCA cycle. This is validated by the pathway analysis results comparing regressed and mid-recrudescent fish that show a significant impact on pathways related to energy metabolism, such as pyruvate metabolism and the TCA cycle (**Figure 5**). We hypothesize that the observed increases in taurine and hypotaurine metabolism in the growth stage result from increased anabolic pathways activity (**Figure 5**). The sulphur-containing amino acid taurine plays a crucial role in supporting growth-related processes by modulating metabolism and nutrient utilization (Salze and Davis, 2015; de Moura et al., 2018). Taurine effects on growth and reproductive performances have been widely explored in fish nutrition. In several teleost species, dietary taurine supplementation improved glucose metabolism by increasing gene expressions and activity of enzymes involved in glycogen synthesis and anabolic pathways (Sampath et al., 2020). Thus, taurine may contribute to the enhanced glycogen synthesis observed during the regressed phase (**Figure 4**; **Table 2**).

4.1.2 Metabolic Profile During Mid and Late Recrudescence

The investigation of the metabolic profile of mid and late recrudescence highlighted differences concerning amino acid, nucleotide, lipid and carbohydrate metabolism. In accordance with previous studies conducted on goldfish (Delahunty et al., 1978), common roach, white bream (Rinchard and Kestemont, 2003), singi fish (Dasmahapatra and Medda, 1982) and flounder (Petersen and Emmersen, 1977), our results demonstrate a significantly lower concentration of glycogen in mid recrudescence compared to

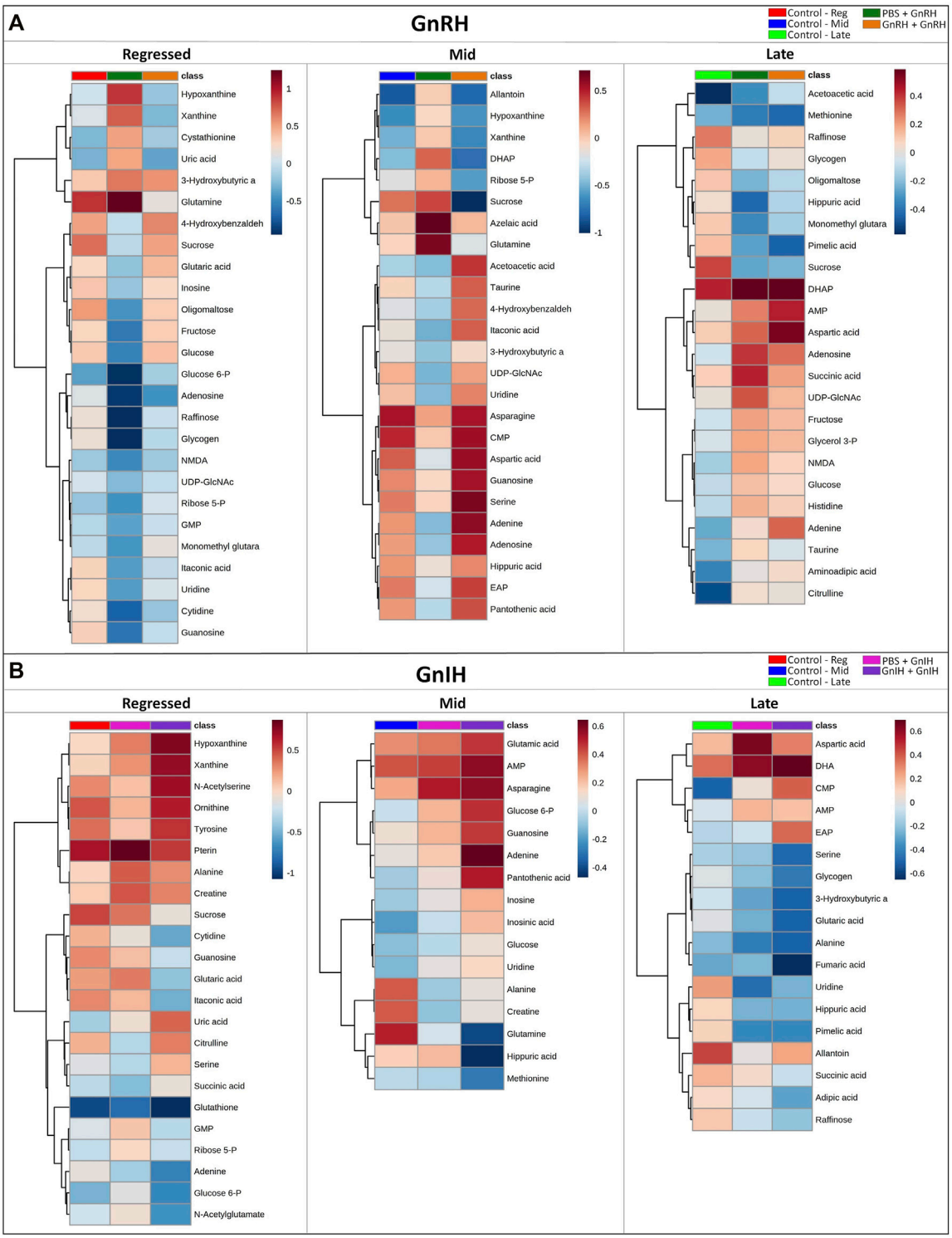

FIGURE 8 | Clustered heatmap showing the metabolites with VIP score >1 of the PLS-DA models for GnRH **(A)** and GnIH **(B)** treatments in the three investigated reproductive phases (Regressed, Mid and Late). For each reproductive phase, the effect of hormones on metabolites was investigated comparing the corresponding control group, single and double injection with GnRH or GnIH groups. Each column represents the group-average concentration of all VIP > 1 metabolites. Decrease or increase of metabolites concentration is indicated by shades of blue and red, respectively. The heatmap was constructed using Ward's algorithm and the accompanying clustering analysis measures Euclidean distance.

TABLE 4 | Summary of the main altered metabolic pathways resulted from pathway analysis investigating the effect of single and double injection with GnRH (above) and GnIH (below) during the three investigated reproductive stages (Regressed, Mid and Late).

GnRH

Regressed			Mid			Late		
Metabolic pathway	**PBS + GnRH**	**GnRH + GnRH**	**Metabolic pathway**	**PBS + GnRH**	**GnRH + GnRH**	**Metabolic pathway**	**PBS + GnRH**	**GnRH + GnRH**
Purine metabolism	2.71×10^{-7}	0.1783	Glycerophospholipid metabolism	0.0005	0.4777	Citrate cycle (TCA cycle)	0.0006	0.3684
Ketone bodies metabolism	0.0175	0.1322	Glycerolipid metabolism	0.0011	0.4256	Nucleotide sugar metabolism	0.0258	0.2765
Butanoate metabolism	0.0175	0.1322	Histidine metabolism	0.0038	0.3139	Fructose and mannose metabolism	0.0274	0.1099
Pyrimidine metabolism	0.0257	0.1479	beta-Alanine metabolism	0.0038	0.3139	Glycolysis/Gluconeogenesis	0.0274	0.1099
Nucleotide sugar metabolism	0.0347	0.8826	Nucleotide sugar metabolism	0.0100	0.7549	Ala, Asp and Glu metabolism	0.0332	0.0354
Starch and sucrose metabolism	0.0548	0.3393	Aminoacyl-tRNA biosynthesis	0.0247	0.5035	Arginine biosynthesis	0.0699	0.0461
Cys and Met metabolism	0.0591	0.7977	Ala, Asp and Glu metabolism	0.0269	0.7510	Ketone bodies metabolism	0.3557	0.0519
Gly, Ser and Thr metabolism	0.0591	0.7977	Pyrimidine metabolism	0.0282	0.8588	Val, Leu and Ile degradation	0.3557	0.0519
Galactose metabolism	0.0653	0.3897	Arginine biosynthesis	0.0382	0.7014	Tyrosine metabolism	0.3557	0.0519
Ala, Asp and Glu metabolism	0.2830	0.1446	Purine metabolism	0.0422	0.3811	Butanoate metabolism	0.1174	0.0520
Arginine biosynthesis	0.2830	0.1446	Pentose phosphate pathway	0.1051	0.0397	Purine metabolism	0.0785	0.0639
Gln and Glu metabolism	0.2830	0.1446	Tau and hypotaurine metabolism	0.1557	0.0297	Starch and sucrose metabolism	0.1230	0.1476
Pentose phosphate pathway	0.2939	0.1893	Ketone bodies metabolism	0.3316	0.0166	Galactose metabolism	0.1179	0.1502
			Butanoate metabolism	0.3316	0.0166	Glycerophospholipid metabolism	0.0682	0.2940
			Starch and sucrose metabolism	0.5779	0.0405	Glycerolipid metabolism	0.0682	0.2940
			Galactose metabolism	0.5779	0.0405	Tau and hypotaurine metabolism	0.1665	0.3996
			Val, Leu and Ile degradation	0.6408	0.0142			
			Tyrosine metabolism	0.6408	0.0142			

GnIH

Regressed			Mid			Late		
Metabolic pathway	**PBS + GnIH**	**GnIH + GnIH**	**Metabolic pathway**	**PBS + GnIH**	**GnIH + GnRH**	**Metabolic pathway**	**PBS + GnIH**	**GnIH + GnIH**
Aminoacyl-tRNA biosynthesis	0.0306	0.2793	Ala, Asp and Glu metabolism	0.1954	0.0124	Histidine metabolism	0.0287	0.4272
Ala, Asp and Glu metabolism	0.0310	0.1733	Aminoacyl-tRNA biosynthesis	0.2608	0.0121	beta-Alanine metabolism	0.1954	0.4272
Gly, Ser and Thr metabolism	0.0358	0.2188	Pyrimidine metabolism	0.3752	0.0230	Purine metabolism	0.0307	0.2047
Galactose metabolism	0.4527	0.0286	Gln and Glu metabolism	0.3617	0.0216	Pyrimidine metabolism	0.0046	0.0061
Purine metabolism	0.5252	0.0009	Arginine biosynthesis	0.3617	0.0216	Arginine biosynthesis	0.461	0.0356
Arg and Pro metabolism	0.0628	0.3981	Nitrogen metabolism	0.3617	0.0216	Propanoate metabolism	0.1462	0.0277
Phe, Tyr and Trp biosynthesis	0.0944	0.4458	Pantothenate and CoA biosynthesis	0.5322	0.0084	Synthesis of unsaturated fatty acids	0.1842	0.0186
Tyrosine metabolism	0.0944	0.4458	Purine metabolism	0.6246	0.0133	Butanoate metabolism	0.2504	0.0108
Arginine biosynthesis	0.1445	0.2148	Gly, Ser and Thr metabolism	0.0502	0.1918	Ketone bodies metabolism	0.2841	0.0279
Starch and sucrose metabolism	0.2016	0.0522	Arginine and proline metabolism	0.0695	0.2354	Citrate cycle (TCA cycle)	0.5722	0.0083
Pentose phosphate pathway	0.2138	0.9407	Starch and sucrose metabolism	0.5782	0.0852	Glycerophospholipid metabolism	0.7752	0.0101
Glutathione metabolism	0.2604	0.5881				Tyrosine metabolism	0.7836	0.0166
Citrate cycle (TCA cycle)	0.3507	0.2370				Pyruvate metabolism	0.7836	0.0166
						Gly, Ser and Thr metabolism	0.8491	0.0496
						Cys and Met metabolism	0.8491	0.0496
						Sphingolipid metabolism	0.9411	0.0078

Values indicate the p*-value obtained from the independent comparison between control and single injection groups (PBS + GnRH or PBS + GnIH) and control and double injection groups (GnRH + GnRH or GnIH + GnIH).* p*-values in red indicate significantly altered metabolic pathways (*p*-value < 0.05). The detailed results of pathway analysis for each comparison are shown in* ***Supplementary Tables S14, S15****.*

regressed phase. This result suggests an elevated breakdown of glycogen as an energy source to support the vitellogenic process. This is consistent with the observed higher glucose 1-phosphate in mid compared to late recrudescence (**Figure 4**; **Table 2**). Furthermore, the elevated degradation of glycogen can be correlated to the higher circulating estrogen and liver estrogen receptor levels measured in mid recrudescence compared to other reproductive stages (Nelson and Habibi, 2013; Ma et al., 2020b). Accordingly, injections of estrogen in singi fish reduced glycogen and increased liver lipid content of vitellogenic female fish (Dasmahapatra and Medda, 1982). Our results also demonstrate enhanced lipid metabolism, particularly glycerophospholipid and sphingolipid

metabolism and fatty acids biosynthesis, in mid compared to late recrudescence (**Figure 5**). This is consistent with elevated levels of *O*-phosphoethanolamine and malonate in mid compared to late recrudescence (**Table 2**). Lipovitellin, a major product of Vtg degradation, is the main component in fish egg yolk and has a lipid content of about 20% by mass, primarily consisting of phospholipids and triglycerides (Hara et al., 2016). The lipid content of ovaries from wild Tilapia nilotica ranged from 12.2% to 25.5% of the wet weight (James Henderson and Tocher, 1987). We hypothesize that the enhanced lipid metabolism in the liver of mid-recrudescent fish characterizes the peak vitellogenic period, during which the mobilization of lipid from the liver is essential to support gonadal maturation. Accordingly, transcript levels of vitellogenin in goldfish liver in significantly higher in mid compared to regressed fish (Ma et al., 2020b). Furthermore, the serum levels of total lipids and phospholipids were elevated during flounder vitellogenesis (Petersen and Emmersen, 1977). Significantly higher ornithine and citrulline levels were also observed in mid compared to late recrudescence (**Figure 4**; **Table 2**). These metabolites derive from arginine and proline catabolism and are precursors in the synthesis of polyamines such as spermidine and spermine, known to be essential for the success of several reproductive functions in mammals (Lefèvre et al., 2011). Polyamine synthesis seems necessary for the function and differentiation of the somatic cell component of the ovary (Lefèvre et al., 2011). Furthermore, studies on *Xenopus* oocytes indicate that polyamines are essential for cytoplasmic maturation and protect the oocyte in the metaphase II stage from ROS-induced apoptosis (Bassez et al., 1990). In line with this, our results demonstrate enhanced polyamine synthesis during mid recrudescence, indicating the importance of these molecules in the reproductive cycle of female goldfish. The heatmap and multiple t-test results indicate significantly lower concentrations of several essential amino acids, including histidine, tryptophan, arginine, lysine, leucine, valine, methionine, phenylalanine and threonine in late recrudescence compared to the regressed phase (**Figure 4**; **Table 2**). Studies investigating the composition of marine pelagic fish eggs showed an abrupt increase in free amino acids content shortly before ovulation, reaching a total amino acid content of 40–60% of dry mass in newly spawned eggs (Rønnestad et al., 1999). In another study by Qari et al. (2013) higher concentrations of essential amino acids were observed in the ovaries of ripe goldlined seabream compared to nearly ripe fish. The lower liver content of amino acids in late compared to the regressed phase described in this study suggests protein mobilization from the liver to the ovaries as the fish reaches maturation and highlights the importance of essential amino acids in the reproductive phase of the annual cycle. Pathway analysis results indicate that late recrudescence is also characterized by significantly altered purine metabolism compared to mid recrudescence (**Figure 5**). Accordingly, the heatmap shows higher levels of hypoxanthine, xanthine, uric acid and allantoin (**Figures 4**, **5**) that are metabolites of the degradation pathway of purine metabolism. In fish, purine degradation ends with the oxidation of uric acid to allantoin by the enzyme urate oxidase (Kinsella et al., 1985). Uric acid is an important antioxidant in humans, and several studies have demonstrated its potent ability as a scavenger of oxygen singlet and hydroxyl radicals (Kand'ár et al., 2006). In the liver of mildly diabetic rats, uric acid and xanthine concentration were threefold and sixfold higher than control, respectively, revealing the role of these molecules in the homeostatic response to the oxidative stress (Kristal et al., 1999). Studies on the inclusion of nucleotides in fish diet have demonstrated they may increase oxidative stress tolerance in part by offsetting the inhibitory effect of cortisol on the fish immune system (Li and Gatlin, 2006). Furthermore, red sea bream fed diets with different content of guanosine monophosphate (GMP) resulted in a lower intensity of oxidative stress and higher antioxidant capacity against the oxidative stress (Hossain et al., 2016). Glutathione was also shown to have significantly higher concentration levels in late than regressed and mid recrudescence (**Figure 4**; **Table 2**). Accordingly, glutathione metabolism was found to be significantly different in mid/late and late/regressed pathway analysis results (**Figure 5**). Glutathione is the most abundant and important intracellular antioxidant, produced mainly in the liver from glutamate, glycine and cysteine (Wu, 2009). Reproduction is an energy-demanding process resulting in changes in the balance between pro-oxidant and antioxidant molecules due to increased metabolic rates (Alonso-Alvarez et al., 2004). Gonadotropins, testosterone and estrogen directly interact with energy metabolism and influence oxidative balance and glutathione metabolism (Lamartiniere, 1981; Norris and Hobbs, 2011). Indeed, total antioxidant capacity and antioxidant enzymes activity in the liver of sea trout were higher in the adult and spawner stages than post-spawning fish (Kurhaluk, 2019). Although elevated oxidative stress can impair reproduction, reactive oxygen species (ROS) are important signalling molecules in oocyte maturation. *In vivo* and *ex vivo* studies on mice ovaries show that ROS present in the preovulatory ovarian follicles are essential for ovulation and are most likely caused by the preovulatory LH surge induced inflammatory response (Shkolnik et al., 2011). Similarly, follicular ROS generated by NADPH oxidase is essential for ovulation in *Drosophila* and suggests a conserved role in regulating ovulation in other species (Li et al., 2018). Based on our results, we hypothesize that elevated liver content of antioxidant molecules such as uric acid and glutathione in late recrudescence compared to mid and regressed female fish is necessary to protect the liver from the potential oxidative damage induced by the preovulatory surge of LH. In contrast to what was measured in the liver of male goldfish (Ladisa et al., 2021), the concentration of acetoacetic acid is significantly lower in late compared to regressed and mid recrudescence (**Table 2**). This is accompanied by lower levels of 3-hydroxybutyrate in mid and late recrudescence, compared to regressed (**Figure 4**). Accordingly, ketone bodies metabolism and butanoate metabolism were found to be different in our pathway analysis comparisons (**Figure 5**). Our results indicate that the synthesis of ketone bodies is downregulated in mid and late recrudescence compared to the regressed stage. Little information is available regarding the involvement of ketone bodies metabolism in fish growth and reproduction. In mammals, high ketone bodies are typical during starvation since they function as energy sources derived from accelerated fatty acid degradation (Fukao et al., 2004). Previous studies on mammals have demonstrated the role of ketone bodies in regulating food intake and energy homeostasis by showing that central infusion of β-hydroxybutyrate increased food intake in rats (Iwata et al., 2011b) and mice (Carneiro et al., 2016). However, starvation of carp (Segner et al., 1997) bass (Zammit and Newsholme, 1979), and rainbow trout (Jonas and Bilinski, 1965) did

not affect food intake or ketogenesis. Together these results suggest that in fish ketone bodies metabolism might be less important in the regulation of food intake when compared to mammals and might have a significant role in other physiological processes. Injection of β-hydroxybutyrate in the brain of female rats suppressed the pulsatile secretion of LH (Iwata et al., 2011a). Finally, higher than normal serum and milk levels of β-hydroxybutyrate during lactation in dairy cows results in a delayed start of the postpartum ovarian cycle (Koller et al., 2003). Based on our results, we hypothesize that low levels of ketone bodies as a consequence of reduced liver ketogenesis in late recrudesce compared to the regressed phase is a permissive/stimulating mechanism for the pre-spawning surge of LH. This hypothesis can be linked to the significantly higher levels of circulating LH recorded in female goldfish during late recrudescence than regressed and mid recrudescence (Ma et al., 2020b).

4.2 Acute Effect of Gonadotropin-Inhibitory Hormone and Gonadotropin-Releasing Hormone on Liver Metabolism of Regressed, Mid and Late Recrudescence Fish

Metabolomics results presented in this study indicate that treatments with GnRH induced significant changes during regressed and mid recrudescence but not during late recrudescence, as measured by the PLS-DA regression models (**Table 3**). On the other hand, PLS-DA models for GnIH treatments did not indicate significant changes between groups in any investigated reproductive stages (**Table 3**). In this study, we did not investigate the time-related effects of GnRH and GnIH on metabolism, and the acute nature of the treatments may have affected metabolic pathways to a lesser extent than that observed at different periods of the reproductive cycle. It is possible that the PLS-DA models constructed on control, single and double injected groups may not have identified all the changes that would be induced by more prolonged exposure to GnRH and GnIH treatments. However, variable selection based on the criteria of VIP score >1 is still a robust method for identifying variables that influence the separation between groups and characterize changes in the metabolic profile (Gromski et al., 2014).

4.2.1 Regressed Gonadal Phase Corresponding to Maximal Growth Phase

During the regressed gonadal stage, single and double injections with GnRH had different effects on liver metabolism. Pathway analysis identified significant changes in metabolic pathways after a single injection with GnRH (**Table 4**). However, double injection with GnRH did not affect pathways noted in the zebrafish KEGG database (**Table 4**). Accordingly, the metabolic profile following double injection in the heatmap is similar to the control (**Figure 8**). A similar study in goldfish demonstrated that single but not double injection with GnRH significantly increased circulating GH levels and decreased Erα, ERβ1 TRα and TRβ mRNA liver transcript levels in the regressed female goldfish (Ma et al., 2020b). In the present study, single injection with GnRH significantly altered purine and pyrimidine metabolism due to decreased levels of guanosine, adenosine, uridine, cytidine and inosine and increased levels of hypoxanthine, xanthine and uric acids (**Figure 8**; **Table 4**). Moreover, the clustered heatmap shows lower levels of several carbohydrates such as glycogen, raffinose, sucrose, oligomaltose, fructose, glucose and glucose 6-phosphate in the single GnRH injected group, compared to the control (**Figure 8**). Similar changes in purine and carbohydrates metabolism were observed in fish at late recrudesce, compared to regressed and mid recrudescence (**Figure 4**). Single and double GnIH injection treatments affected different pathways than the control (**Table 4**). According to the heatmap results, single and double injection with GnIH progressively increased the concentrations of several metabolites, including hypoxanthine, xanthine, uric acid and sucrose (**Figure 8**). This is consistent with a previous study that demonstrated that single and double GnIH injection significantly altered the liver ERα, ERβ1, TRβ and IGF-I transcript levels (Ma et al., 2020b). Double injection with GnIH at the regressed phase significantly inhibited purine and carbohydrate metabolism (**Table 4**), resulting in increased hypoxanthine and xanthine levels and decreased concentration of sucrose and glucose 6-phosphate (**Figure 8**). Together, our results indicate that GnIH affects reproduction, in part, by influencing metabolic pathways related to the late recrudescence stage.

4.2.2 Mid Recrudescence

Pathway analysis revealed significant differences between single and double injection effects with GnRH. Single injection with GnRH inhibited amino acid and lipid metabolism pathways and enhanced purine degradation and ketone bodies metabolism (**Figure 8**; **Table 4**). However, double injection with GnRH stimulated ketone bodies synthesis and increased the concentrations of several amino acids, including asparagine, aspartic acid and serine, and inhibited carbohydrates metabolism (**Figure 8**; **Table 4**). In general, single GnRH injection inhibited metabolic pathways related to reproductive processes, whereas double injection enhanced the pathways related to reproduction at mid recrudescence (**Table 4**). This is consistent with the observation that single GnRH injection decreased Vtg and IGF-I mRNA levels, which was increased following double injection with GnRH in goldfish at mid recrudescence (Ma et al., 2020b). In the present study, double injection with GnRH also enhanced taurine and hypotaurine metabolism (**Figure 8**; **Table 4**). Previous studies identified taurine as an essential component of broodstock diets for Japanese yellowtail (Matsunari et al., 2006) and greater amberjack (Sarih et al., 2019), necessary to improve fecundity, egg viability and fertilization rates. Thus, our results demonstrate a potential role of GnRH in stimulating metabolic pathways favouring reproductive processes. Furthermore, double injection with GnIH also altered metabolic pathways related to amino acid, pyrimidine and purine metabolism (**Table 4**). The clustered heatmap suggests that the effect of GnIH is dose-dependent and double injection with GnIH potentiates the effect induced by single injection treatment (**Figure 8**). Similar results were obtained after treatments with GnIH during the regressed phase (**Figure 8**). The metabolic changes induced by GnIH treatments characterize the basal metabolic profile of regressed fish, compared to mid and late recrudescence

(**Figures 4**, **8**). The results suggest that treatments with GnIH in mid recrudescence inhibit reproductive processes and stimulate metabolic pathways related to the growth phase.

4.2.3 Late Recrudescence

The pathway analysis demonstrates that GnRH injections alter carbohydrate and energy metabolism in late recrudescence (**Table 4**). Single and double injection with GnRH resulted in lower levels of carbohydrates such as glycogen, raffinose, oligomaltose and sucrose and higher levels of glucose, fructose, dihydroxyacetone phosphate (DHAP) and succinic acid. Injection with GnRH stimulated carbohydrate mobilization and energy production during late recrudescence (**Figure 8**). Observed changes in late recrudescence indicate that GnRH stimulates metabolic processes related to vitellogenesis and gonadal maturation. Our results are consistent with reported stimulation of circulating LH concentration and increased expression of ERα and ERβ1 mRNA following injection with GnRH in female goldfish at late recrudescence (Ma et al., 2020b). Similarly, GnIH stimulated metabolic pathways related to the mid recrudescence stage. The clustered heatmap demonstrates a progressive decrease in glycogen, raffinose, fumaric acid, succinic acid, and 3-hydroxybutyrate stimulated following GnIH treatments. Single and double injection with GnIH also reduced the levels of *O*-phosphoethanolamine (EAP) and docosahexaenoic acid (DHA; **Figure 8**; **Supplementary Table S10**).

5 CONCLUSION

Results from this study characterize the liver metabolic profile of female goldfish at three stages of the reproductive cycle. In the regressed gonadal phase, carbohydrate and amino acid metabolism were enhanced, possibly supporting anabolic processes related to growth. On the other hand, the liver metabolism of mid-recrudescent fish is characterized by elevated lipid synthesis during the peak of vitellogenesis and lipid mobilization from the liver to support maximal gonadal maturation. The metabolic profile of goldfish during late recrudescence revealed a high concentration of antioxidant molecules such as uric acid and glutathione and reduced ketone bodies. These molecules may play a vital role in the final stages of the gonadal cycle. In the present study, we also demonstrated that GnRH and GnIH are involved in the multifactorial regulation of metabolism in supporting growth and reproduction in female goldfish. Results indicate that acute treatment with GnRH and GnIH induce metabolic changes depending on the season and mode of administration. GnRH treatments had similar effects during the regressed phase and mid recrudescence. Double injection with GnRH enhanced pathways related to growth and reproduction in regressed and mid recrudescence, respectively. On the other hand, GnRH treatments during late recrudescence stimulated pathways supporting vitellogenesis and gonadal maturation. GnIH showed an additive effect of single and double injections and changed the metabolic profile resembling the previous reproductive stage. During the regressed phase, GnIH treatments stimulated metabolic pathways related to the final stages of reproduction. In contrast, GnIH promoted a shift toward growth processes during mid recrudescence. Finally, during late recrudescence, GnIH stimulated metabolic pathways characteristic of the mid recrudescence metabolic profile. Overall, our results provide new information on the metabolic changes that accompany the growth and reproductive processes during the annual reproductive cycle of female goldfish and provide an insight into the role of GnRH and GnIH in the multifactorial control of growth and reproduction in goldfish and other oviparous species.

DATA AVAILABILITY STATEMENT

The original contributions presented in the study are included in the article/**Supplementary Material**, further inquiries can be directed to the corresponding author.

ETHICS STATEMENT

The animal study was reviewed and approved by the University of Calgary animal care committee (protocol #AC19-0161) under the guidelines of the Canadian Council of Animal Care.

AUTHOR CONTRIBUTIONS

CL, YM, and HH designed the research; CL, YM, and HH performed the research; CL analyzed the data; CL and HH wrote the paper. HH provided funding and intellectual input on the whole study.

FUNDING

This work was supported by the funding from Natural Sciences and Engineering Research Council of Canada to HH (NSERC Discovery Grant; project no. 1254045). CL and YM were supported by NSERC grants to HH. CL was also supported by the Alberta Graduate Excellence Scholarship (AGES).

ACKNOWLEDGMENTS

Metabolomics data were acquired at the Calgary Metabolomics Research Facility (CMRF), which is supported by grants to Dr. Ian A. Lewis including International Microbiome Centre, Canada Foundation for Innovation (CFI-JELF534986), Alberta Innovates Translational Health Chair, and NSERC-DG 5 04547. The authors thank Dr. Ian Lewis for his expertise in metabolomics and the members of the University of Calgary's Metabolomics Research Facility for the technical support.

SUPPLEMENTARY MATERIAL

The Supplementary Material for this article can be found online at: https://www.frontiersin.org/articles/10.3389/fcell.2022.834688/full#supplementary-material

REFERENCES

Alonso-Alvarez, C., Bertrand, S., Devevey, G., Prost, J., Faivre, B., and Sorci, G. (2004). Increased Susceptibility to Oxidative Stress as a Proximate Cost of Reproduction. *Ecol. Lett.* 7, 363–368. doi:10.1111/j.1461-0248.2004.00594.x

Amano, M., Moriyama, S., Iigo, M., Kitamura, S., Amiya, N., Yamamori, K., et al. (2006). Novel Fish Hypothalamic Neuropeptides Stimulate the Release of Gonadotrophins and Growth Hormone from the Pituitary of Sockeye salmon. *J. Endocrinol.* 188, 417–423. doi:10.1677/joe.1.06494

A. Qari, S., Moharram, G. S., and Alowaidi, A. S. (2014). Fatty Acids Compositions in Male's Gonads of the Red Sea Fish *Rhabdosargus sarba* during the Spawning Season. *Ajls* 2, 103. doi:10.11648/j.ajls.20140202.21

Bassez, T., Paris, J., Omilli, F., Dorel, C., and Osborne, H. B. (1990). Post-transcriptional Regulation of Ornithine Decarboxylase in *Xenopus laevis* Oocytes. *Development* 110, 955–962. doi:10.1242/dev.110.3.955

Borchel, A., Verleih, M., Kühn, C., Rebl, A., and Goldammer, T. (2019). Evolutionary Expression Differences of Creatine Synthesis-Related Genes: Implications for Skeletal Muscle Metabolism in Fish. *Sci. Rep.* 9, 5429. doi:10.1038/s41598-019-41907-6

Cabello, G., and Wrutniak, C. (1989). Thyroid Hormone and Growth : Relationships with Growth Hormone Effects and Regulation. *Reprod. Nutr. Dévelop.* 29, 387–402. doi:10.1051/rnd:19890401

Canosa, L. F., Chang, J. P., and Peter, R. E. (2007). Neuroendocrine Control of Growth Hormone in Fish. *Gen. Comp. Endocrinol.* 151, 1–26. doi:10.1016/j.ygcen.2006.12.010

Carneiro, L., Geller, S., Fioramonti, X., Hébert, A., Repond, C., Leloup, C., et al. (2016). Evidence for Hypothalamic Ketone Body Sensing: Impact on Food Intake and Peripheral Metabolic Responses in Mice. *Am. J. Physiology-Endocrinology Metab.* 310, E103–E115. doi:10.1152/ajpendo.00282.2015

Chang, J. P., Johnson, J. D., Goor, F. V., Wong, C. J., Yunker, W. K., Uretsky, A. D., et al. (2000). Signal Transduction Mechanisms Mediating Secretion in Goldfish Gonadotropes and Somatotropes. *Biochem. Cel Biol.* 78, 139–153. doi:10.1139/o00-011

Chang, J. P., and Pemberton, J. G. (2018). Comparative Aspects of GnRH-Stimulated Signal Transduction in the Vertebrate Pituitary - Contributions from Teleost Model Systems. *Mol. Cell Endocrinol.* 463, 142–167. doi:10.1016/j.mce.2017.06.002

Chang, J. P., and Wong, A. O. L. (2009). "Growth Hormone Regulation in Fish: A Multifactorial Model with Hypothalamic, Peripheral and Local Autocrine/Paracrine Signals." In *Fish Physiology*, Bernier, N., Van Der Kraak, G., Ferrell, A., Brauner, C. (Eds.), vol. 28, New York, NY: Academic Press, 151–195.

Chong, J., Wishart, D. S., and Xia, J. (2019). Using MetaboAnalyst 4.0 for Comprehensive and Integrative Metabolomics Data Analysis. *Curr. Protoc. Bioinformatics* 68, e86. doi:10.1002/cpbi.86

Clarke, I. J. (2014). Interface between Metabolic Balance and Reproduction in Ruminants: Focus on the Hypothalamus and Pituitary. *Horm. Behav.* 66, 15–40. doi:10.1016/j.yhbeh.2014.02.005

Clasquin, M. F., Melamud, E., and Rabinowitz, J. D. (2012). LC-MS Data Processing with MAVEN: A Metabolomic Analysis and Visualization Engine. *Curr. Protoc. Bioinforma.* Chapter 14, Unit14.11. doi:10.1002/0471250953.bi1411s37

Dasmahapatra, A. K., and Medda, A. K. (1982). Effect of Estradiol Dipropionate and Testosterone Propionate on the Glycogen, Lipid, and Water Contents of Liver, Muscle, and Gonad of Male and Female (Vitellogenic and Nonvitellogenic) Singi Fish (Heteropneustes Fossilis Bloch). *Gen. Comp. Endocrinol.* 48, 476–484. doi:10.1016/0016-6480(82)90183-6

De Leeuw, R., Habibi, H. R., Nahorniak, C. S., and Peter, R. E. (1989). Dopaminergic Regulation of Pituitary Gonadotrophin-Releasing Hormone Receptor Activity in the Goldfish (*Carassius auratus*). *J. Endocrinol.* 121, 239–247. doi:10.1677/joe.0.1210239

de Moura, L. B., Diógenes, A. F., Campelo, D. A. V., Almeida, F. L. A. d., Pousão-Ferreira, P. M., Furuya, W. M., et al. (2018). Taurine and Methionine Supplementation as a Nutritional Strategy for Growth Promotion of Meagre (Argyrosomus Regius) Fed High Plant Protein Diets. *Aquaculture* 497, 389–395. doi:10.1016/j.aquaculture.2018.07.038

Deal, C. K., and Volkoff, H. (2020). The Role of the Thyroid Axis in Fish. *Front. Endocrinol.* 11. doi:10.3389/fendo.2020.596585

Delahunty, G., Olcese, J., Prack, M., Jo Vodicnik, M., Schreck, C. B., and de Vlaming, V. (1978). Diurnal Variations in the Physiology of the Goldfish,*Carassius auratus*. *J. Interdisiplinary Cycle Res.* 9, 73–88. doi:10.1080/09291017809359626

Espe, M., Waagbø, R., and Espe, M. (2016). Functional Amino Acids in Fish Nutrition Health and Welfare. *Front. Biosci.* 8, 143–169. doi:10.2741/757

Fernandez-Fernandez, R., Martini, A. C., Navarro, V. M., Castellano, J. M., Dieguez, C., Aguilar, E., et al. (2006). Novel Signals for the Integration of Energy Balance and Reproduction. *Mol. Cell Endocrinol.* 254-255, 127–132. doi:10.1016/j.mce.2006.04.026

Fukao, T., Lopaschuk, G. D., and Mitchell, G. A. (2004). Pathways and Control of Ketone Body Metabolism: On the Fringe of Lipid Biochemistry. *Prostaglandins, Leukot. Essent. Fatty Acids* 70, 243–251. doi:10.1016/j.plefa.2003.11.001

Gamba, M., and Pralong, F. P. (2006). Control of GnRH Neuronal Activity by Metabolic Factors: The Role of Leptin and Insulin. *Mol. Cell Endocrinol.* 254-255, 133–139. doi:10.1016/j.mce.2006.04.023

Gorrochategui, E., Jaumot, J., Lacorte, S., and Tauler, R. (2016). Data Analysis Strategies for Targeted and Untargeted LC-MS Metabolomic Studies: Overview and Workflow. *Trac Trends Anal. Chem.* 82, 425–442. doi:10.1016/j.trac.2016.07.004

Gromski, P. S., Xu, Y., Correa, E., Ellis, D. I., Turner, M. L., and Goodacre, R. (2014). A Comparative Investigation of Modern Feature Selection and Classification Approaches for the Analysis of Mass Spectrometry Data. *Analytica Chim. Acta* 829, 1–8. doi:10.1016/j.aca.2014.03.039

Habibi, H. R., De Leeuw, R., Nahorniak, C. S., Goos, H. J. T., and Peter, R. E. (1989). Pituitary Gonadotropin-Releasing Hormone (GnRH) Receptor Activity in Goldfish and Catfish: Seasonal and Gonadal Effects. *Fish. Physiol. Biochem.* 7, 109–118. doi:10.1007/BF00004696

Habibi, H. R., Nelson, E. R., and Allan, E. R. O. (2012). New Insights into Thyroid Hormone Function and Modulation of Reproduction in Goldfish. *Gen. Comp. Endocrinol.* 175, 19–26. doi:10.1016/j.ygcen.2011.11.003

Hara, A., Hiramatsu, N., and Fujita, T. (2016). Vitellogenesis and Choriogenesis in Fishes. *Fish. Sci.* 82, 187–202. doi:10.1007/s12562-015-0957-5

Hossain, M. S., Koshio, S., Ishikawa, M., Yokoyama, S., and Sony, N. M. (2016). Effects of Dietary Administration of Guanosine Monophosphate on the Growth, Digestibility, Innate Immune Responses and Stress Resistance of Juvenile Red Sea Bream, *Pagrus major*. *Fish Shellfish Immunol.* 57, 96–106. doi:10.1016/j.fsi.2016.08.026

Iwata, K., Kinoshita, M., Susaki, N., Uenoyama, Y., Tsukamura, H., and Maeda, K.-i. (2011a). Central Injection of Ketone Body Suppresses Luteinizing Hormone Release via the Catecholaminergic Pathway in Female Rats. *J. Reprod. Develop.* 57, 379–384. doi:10.1262/jrd.11-001S

Iwata, K., Kinoshita, M., Yamada, S., Imamura, T., Uenoyama, Y., Tsukamura, H., et al. (2011b). Involvement of Brain Ketone Bodies and the Noradrenergic Pathway in Diabetic Hyperphagia in Rats. *J. Physiol. Sci.* 61, 103–113. doi:10.1007/s12576-010-0127-6

Jalabert, B. (2005). Particularities of Reproduction and Oogenesis in Teleost Fish Compared to Mammals. *Reprod. Nutr. Dev.* 45, 261–279. doi:10.1051/rnd:2005019

James Henderson, R., and Tocher, D. R. (1987). The Lipid Composition and Biochemistry of Freshwater Fish. *Prog. Lipid Res.* 26, 281–347. doi:10.1016/0163-7827(87)90002-6

Johnson, M. A., Tsutsui, K., and Fraley, G. S. (2007). Rat RFamide-Related Peptide-3 Stimulates GH Secretion, Inhibits LH Secretion, and Has Variable Effects on Sex Behavior in the Adult Male Rat. *Horm. Behav.* 51, 171–180. doi:10.1016/j.yhbeh.2006.09.009

Jonas, R. E. E., and Bilinski, E. (1965). Ketone Bodies in the Blood of Salmonoid Fishes. *J. Fish. Res. Bd. Can.* 22, 891–898. doi:10.1139/f65-084

Kand'ár, R., Žáková, P., and Mužáková, V. (2006). Monitoring of Antioxidant Properties of Uric Acid in Humans for a Consideration Measuring of Levels of Allantoin in Plasma by Liquid Chromatography. *Clinica Chim. Acta* 365, 249–256. doi:10.1016/j.cca.2005.09.002

Kanehisa, M., Sato, Y., Furumichi, M., Morishima, K., and Tanabe, M. (2019). New Approach for Understanding Genome Variations in KEGG. *Nucleic Acids Res.* 47, D590–D595. doi:10.1093/nar/gky962

Katajamaa, M., and Orešič, M. (2007). Data Processing for Mass Spectrometry-Based Metabolomics. *J. Chromatogr. A* 1158, 318–328. doi:10.1016/j.chroma.2007.04.021

Kim, M.-H., Oka, Y., Amano, M., Kobayashi, M., Okuzawa, K., Hasegawa, Y., et al. (1995). Immunocytochemical Localization of sGnRH and cGnRH-II in the Brain of Goldfish,*Carassius auratus*. *J. Comp. Neurol.* 356, 72–82. doi:10.1002/cne.903560105

Kinsella, J. E., German, B., and Shetty, J. (1985). Uricase from Fish Liver: Isolation and Some Properties. *Comp. Biochem. Physiol. B: Comp. Biochem.* 82, 621–624. doi:10.1016/0305-0491(85)90498-5

Klausen, C., Chang, J. P., and Habibi, H. R. (2001). The Effect of Gonadotropin-Releasing Hormone on Growth Hormone and Gonadotropin Subunit Gene Expression in the Pituitary of Goldfish, *Carassius auratus*. *Comp. Biochem. Physiol. B: Biochem. Mol. Biol.* 129, 511–516. doi:10.1016/S1096-4959(01)00351-7

Klausen, C., Chang, J. P., and Habibi, H. R. (2002). Time- and Dose-Related Effects of Gonadotropin-Releasing Hormone on Growth Hormone and Gonadotropin Subunit Gene Expression in the Goldfish Pituitary. *Can. J. Physiol. Pharmacol.* 80, 915–924. doi:10.1139/y02-118

Koda, A., Ukena, K., Teranishi, H., Ohta, S., Yamamoto, K., Kikuyama, S., et al. (2002). A Novel Amphibian Hypothalamic Neuropeptide: Isolation, Localization, and Biological Activity. *Endocrinology* 143, 411–419. Available at: https://oup.silverchair-cdn.com/oup/backfile/Content_public/Journal/endo/143/2/10.1210_endo.143.2.8630/1/endo0411.pdf?Expires=1500501870&Signature=McRAHxGrrmUwg130-er181pAGVq32z46GhdVYxqfmc5ksHTsltiMqC76MWfTEA8A2TOoisWOWYTNr3L-qx9Qwve6rumHzROqsYUjxTGdtaC1 (Accessed July 18, 2017). doi:10.1210/endo.143.2.8630

Koller, A., Reist, M., Blum, J., and Küpfer, U. (2003). Time Empty and Ketone Body Status in the Early Postpartum Period of Dairy Cows. *Reprod. Domest. Anim.* 38, 41–49. doi:10.1046/j.1439-0531.2003.00393.x

Kriegsfeld, L. J., Gibson, E. M., Williams, W. P., Zhao, S., Mason, A. O., Bentley, G. E., et al. (2010). The Roles of RFamide-Related Peptide-3 in Mammalian Reproductive Function and Behaviour. *J. Neuroendocrinol.* 22, 692–700. doi:10.1111/j.1365-2826.2010.02031.x

Kristal, B. S., Vigneau-Callahan, K. E., Moskowitz, A. J., and Matson, W. R. (1999). Purine Catabolism: Links to Mitochondrial Respiration and Antioxidant Defenses. *Arch. Biochem. Biophys.* 370, 22–33. doi:10.1006/abbi.1999.1387

Kumar Bhandari, R., Taniyama, S., Kitahashi, T., Ando, H., Yamauchi, K., Zohar, Y., et al. (2003). Seasonal Changes of Responses to Gonadotropin-Releasing Hormone Analog in Expression of Growth Hormone/prolactin/somatolactin Genes in the Pituitary of Masu salmon. *Gen. Comp. Endocrinol.* 130, 55–63. Available at: www.elsevier.com/locate/ygcen. doi:10.1016/s0016-6480(02)00536-1

Kurhaluk, N. (2019). Formation of an Antioxidant Profile in the Sea trout (*Salmo trutta* M. Trutta L.) from the Slupia River. *Zoology* 133, 54–65. doi:10.1016/j.zool.2019.02.002

Ladisa, C., Ma, Y., and Habibi, H. R. (2021). Seasonally Related Metabolic Changes and Energy Allocation Associated with Growth and Reproductive Phases in the Liver of Male Goldfish (*Carassius auratus*). *J. Proteomics* 241, 104237. doi:10.1016/j.jprot.2021.104237

Lamartiniere, C. A. (1981). The Hypothalamic-Hypophyseal-Gonadal Regulation of Hepatic Glutathione S-Transferases in the Rat. *Biochem. J.* 198, 211–217. doi:10.1042/bj1980211

Lê Cao, K.-A., Boitard, S., and Besse, P. (2011). Sparse PLS Discriminant Analysis: Biologically Relevant Feature Selection and Graphical Displays for Multiclass Problems. *BMC Bioinformatics* 12, 253. doi:10.1186/1471-2105-12-253

Lee, L. C., Liong, C.-Y., and Jemain, A. A. (2018). Partial Least Squares-Discriminant Analysis (PLS-DA) for Classification of High-Dimensional (HD) Data: A Review of Contemporary Practice Strategies and Knowledge Gaps. *Analyst* 143, 3526–3539. doi:10.1039/c8an00599k

Lefèvre, P. L. C., Palin, M.-F., and Murphy, B. D. (2011). Polyamines on the Reproductive Landscape. *Endocr. Rev.* 32, 694–712. doi:10.1210/er.2011-0012

Lethimonier, C., Madigou, T., Muñoz-Cueto, J.-A., Lareyre, J.-J., and Kah, O. (2004). Evolutionary Aspects of GnRHs, GnRH Neuronal Systems and GnRH Receptors in Teleost Fish. *Gen. Comp. Endocrinol.* 135, 1–16. doi:10.1016/j.ygcen.2003.10.007

Li, P., and Bartlett, M. G. (2014). A Review of Sample Preparation Methods for Quantitation of Small-Molecule Analytes in Brain Tissue by Liquid Chromatography Tandem Mass Spectrometry (LC-MS/MS). *Anal. Methods* 6, 6183–6207. doi:10.1039/c4ay00915k

Li, P., and Gatlin, D. M. (2006). Nucleotide Nutrition in Fish: Current Knowledge and Future Applications. *Aquaculture* 251, 141–152. doi:10.1016/j.aquaculture.2005.01.009

Li, W., Young, J. F., and Sun, J. (2018). NADPH Oxidase-Generated Reactive Oxygen Species in Mature Follicles Are Essential for Drosophila Ovulation. *Proc. Natl. Acad. Sci. USA* 115, 7765–7770. doi:10.1073/pnas.1800115115

Lin, C. Y., Viant, M. R., and Tjeerdema, R. S. (2006). Metabolomics: Methodologies and Applications in the Environmental Sciences. *J. Pestic. Sci.* 31, 245–251. doi:10.1584/jpestics.31.245

Ma, Y., Ladisa, C., Chang, J. P., and Habibi, H. R. (2020a). Multifactorial Control of Reproductive and Growth axis in Male Goldfish: Influences of GnRH, GnIH and Thyroid Hormone. *Mol. Cell Endocrinol.* 500, 110629. doi:10.1016/j.mce.2019.110629

Ma, Y., Ladisa, C., Chang, J. P., and Habibi, H. R. (2020b). Seasonal Related Multifactorial Control of Pituitary Gonadotropin and Growth Hormone in Female Goldfish: Influences of Neuropeptides and Thyroid Hormone. *Front. Endocrinol.* 11, 175. doi:10.3389/fendo.2020.00175

Marchant, T. A., and Peter, R. E. (1986). Seasonal Variations in Body Growth Rates and Circulating Levels of Growth Hormone in the Goldfish,*Carassius auratus*. *J. Exp. Zool.* 237, 231–239. doi:10.1002/jez.1402370209

Matsunari, H., Hamada, K., Mushiake, K., and Takeuchi, T. (2006). Effects of Taurine Levels in Broodstock Diet on Reproductive Performance of Yellowtail *Seriola quinqueradiata*. *Fish. Sci.* 72, 955–960. doi:10.1111/j.1444-2906.2006.01243.x

Mcbride, R. S., Somarakis, S., Fitzhugh, G. R., Albert, A., Yaragina, N. A., Wuenschel, M. J., et al. (2015). Energy Acquisition and Allocation to Egg Production in Relation to Fish Reproductive Strategies. *Fish Fish* 16, 23–57. doi:10.1111/faf.12043

Melamed, P., Eliahu, N., Levavi-Sivan, B., Ofir, M., Farchi-Pisanty, O., Rentier-Delrue, F., et al. (1995). Hypothalamic and Thyroidal Regulation of Growth Hormone in Tilapia. *Gen. Comp. Endocrinol.* 97, 13–30. doi:10.1006/gcen.1995.1002

Melamud, E., Vastag, L., and Rabinowitz, J. D. (2010). Metabolomic Analysis and Visualization Engine for LC−MS Data. *Anal. Chem.* 82, 9818–9826. doi:10.1021/ac1021166

Moussavi, M., Wlasichuk, M., Chang, J. P., and Habibi, H. R. (2012). Seasonal Effect of GnIH on Gonadotrope Functions in the Pituitary of Goldfish. *Mol. Cell Endocrinol.* 350, 53–60. doi:10.1016/j.mce.2011.11.020

Moussavi, M., Wlasichuk, M., Chang, J. P., and Habibi, H. R. (2013). Seasonal Effect of Gonadotrophin Inhibitory Hormone on Gonadotrophin-Releasing Hormone-Induced Gonadotroph Functions in the Goldfish Pituitary. *J. Neuroendocrinol.* 25, 506–516. doi:10.1111/jne.12024

Moussavi, M., Wlasichuk, M., Chang, J. P., and Habibi, H. R. (2014). Seasonal Effects of GnIH on Basal and GnRH-Induced Goldfish Somatotrope Functions. *J. Endocrinol.* 223, 191–202. doi:10.1530/JOE-14-0441

Müller, M. J., and Seitz, H. J. (1984). Thyroid Hormone Action on Intermediary Metabolism. *Klin. Wochenschr.* 62, 97–102. doi:10.1007/BF01738699

Nelson, E. R., and Habibi, H. R. (2013). Estrogen Receptor Function and Regulation in Fish and Other Vertebrates. *Gen. Comp. Endocrinol.* 192, 15–24. doi:10.1016/j.ygcen.2013.03.032

Nelson, E. R., and Habibi, H. R. (2009). Thyroid Receptor Subtypes: Structure and Function in Fish. *Gen. Comp. Endocrinol.* 161, 90–96. doi:10.1016/j.ygcen.2008.09.006

Norris, D. O., and Hobbs, S. L. (2020). "The HPA Axis and Functions of Corticosteroids in Fishes," in *Fish Endocrinology*, 722–766. Enfield, New Hampshire: Science Publishers. doi:10.1201/b10745-29

Okubo, K., and Nagahama, Y. (2008). Structural and Functional Evolution of Gonadotropin-Releasing Hormone in Vertebrates. *Acta Physiol.* 193, 3–15. doi:10.1111/j.1748-1716.2008.01832.x

Omeljaniuk, R. J., Habibi, H. R., and Peter, R. E. (1989). Alterations in Pituitary GnRH and Dopamine Receptors Associated with the Seasonal Variation and Regulation of Gonadotropin Release in the Goldfish (*Carassius auratus*). *Gen. Comp. Endocrinol.* 74, 392–399. doi:10.1016/S0016-6480(89)80036-X

Peter, R. E., Nahorniak, C. S., Sokolowska, M., Chang, J. P., Rivier, J. E., Vale, W. W., et al. (1985). Structure-activity Relationships of Mammalian, Chicken, and salmon Gonadotropin Releasing Hormones *In Vivo* in Goldfish. *Gen. Comp. Endocrinol.* 58, 231–242. doi:10.1016/0016-6480(85)90339-9

Petersen, I. M., and Emmersen, B. K. (1977). Changes in Serum Glucose and Lipids, and Liver Glycogen and Phosphorylase during Vitellogenesis in Nature in the Flounder (Platichtys Flesus, L.). *Comp. Biochem. Physiol. Part B: Comp. Biochem.* 58, 167–171. doi:10.1016/0305-0491(77)90104-3

Pineda, R., Garcia-Galiano, D., Sanchez-Garrido, M. A., Romero, M., Ruiz-Pino, F., Aguilar, E., et al. (2010). Characterization of the Inhibitory Roles of RFRP3, the Mammalian Ortholog of GnIH, in the Control of Gonadotropin Secretion in the Rat: *In Vivo* and *In Vitro* Studies. *Am. J. Physiology-Endocrinology Metab.* 299, E39–E46. doi:10.1152/ajpendo.00108.2010

Plant, T. M. (2015). 60 Years of Neuroendocrinology: The Hypothalamo-Pituitary-Gonadal axis. *J. Endocrinol.* 226, T41–T54. doi:10.1530/JOE-15-0113

Power, D. M., Llewellyn, L., Faustino, M., Nowell, M. A., Björnsson, B. T., Einarsdottir, I. E., et al. (2001). Thyroid Hormones in Growth and Development of Fish. *Comp. Biochem. Physiol. C: Toxicol. Pharmacol.* 130, 447–459. Available at: http://ac.els-cdn.com/S153204560100271X/1-s2.0-S153204560100271X-main.pdf?_tid=eae952f8-672b-11e7-9e4f-00000aacb35e&acdnat=1499882579_ca2d581d6df3eb1c5b2f10aa6f0e685a (Accessed February 27, 2017). doi:10.1016/s1532-0456(01)00271-x

Rajeswari, J. J., Hatef, A., and Unniappan, S. (2020). Nesfatin-1-like Peptide Suppresses Hypothalamo-Pituitary-Gonadal mRNAs, Gonadal Steroidogenesis, and Oocyte Maturation in Fish†. *Biol. Reprod.* 103, 802–816. doi:10.1093/biolre/ioaa106

Reading, B. J., and Sullivan, C. V. (2011). *The Reproductive Organs and Processes: Vitellogenesis in Fishes*. Maryland Heights, MO: Elsevier, 635–646. doi:10.1016/B978-0-12-374553-8.00257-4

Rinchard, J., and Kestemont, P. (2003). Liver Changes Related to Oocyte Growth in Roach, a Single Spawner Fish, and in Bleak and White Bream, Two Multiple Spawner Fish. *Internat. Rev. Hydrobiol.* 88, 68–76. doi:10.1002/iroh.200390006

Rønnestad, I., Thorsen, A., and Finn, R. N. (1999). Fish Larval Nutrition: A Review of Recent Advances in the Roles of Amino Acids. *Aquaculture* 177, 201–216. doi:10.1016/S0044-8486(99)00082-4

Rui, L. (2014). Energy Metabolism in the Liver. *Compr. Physiol.* 4, 177–197. doi:10.1002/cphy.c130024

Salze, G. P., and Davis, D. A. (2015). Taurine: A Critical Nutrient for Future Fish Feeds. *Aquaculture* 437, 215–229. doi:10.1016/j.aquaculture.2014.12.006

Sampath, W. W. H. A., Rathnayake, R. M. D. S., Yang, M., Zhang, W., and Mai, K. (2020). Roles of Dietary Taurine in Fish Nutrition. *Mar. Life Sci. Technol.* 2, 360–375. doi:10.1007/s42995-020-00051-1

Sangster, T., Major, H., Plumb, R., Wilson, A. J., and Wilson, I. D. (2006). A Pragmatic and Readily Implemented Quality Control Strategy for HPLC-MS and GC-MS-based Metabonomic Analysis. *Analyst* 131, 1075–1078. doi:10.1039/b604498k

Sarih, S., Djellata, A., Roo, J., Hernández-Cruz, C. M., Fontanillas, R., Rosenlund, G., et al. (2019). Effects of Increased Protein, Histidine and Taurine Dietary Levels on Egg Quality of Greater Amberjack (*Seriola dumerili*, Risso, 1810). *Aquaculture* 499, 72–79. doi:10.1016/j.aquaculture.2018.09.011

Sawada, K., Ukena, K., Satake, H., Iwakoshi, E., Minakata, H., and Tsutsui, K. (2002). Novel Fish Hypothalamic Neuropeptide. *Eur. J. Biochem.* 269, 6000–6008. doi:10.1046/j.1432-1033.2002.03351.x

Schmid, A. C., Lutz, I., Kloas, W., and Reinecke, M. (2003). Thyroid Hormone Stimulates Hepatic IGF-I mRNA Expression in a Bony Fish, the tilapia *Oreochromis mossambicus*, *In Vitro* and *In Vivo*. *Gen. Comp. Endocrinol.* 130, 129–134. doi:10.1016/S0016-6480(02)00577-4

Schneider, J. E. (2004). Energy Balance and Reproduction. *Physiol. Behav.* 81, 289–317. doi:10.1016/j.physbeh.2004.02.007

Segner, H., Dölle, A., and Böhm, R. (1997). Ketone Body Metabolism in the Carp *Cyprinus carpio*: Biochemical and 1H NMR Spectroscopical Analysis. *Comp. Biochem. Physiol. Part B: Biochem. Mol. Biol.* 116, 257–262. doi:10.1016/S0305-0491(96)00213-1

Shahjahan, M., Kitahashi, T., and Parhar, I. S. (2014). Central Pathways Integrating Metabolism and Reproduction in Teleosts. *Front. Endocrinol.* 5, 1–17. doi:10.3389/fendo.2014.00036

Shkolnik, K., Tadmor, A., Ben-Dor, S., Nevo, N., Galiani, D., and Dekel, N. (2011). Reactive Oxygen Species Are Indispensable in Ovulation. *Proc. Natl. Acad. Sci.* 108, 1462–1467. doi:10.1073/pnas.1017213108

Soengas, J. L., Sanmartín, B., Barciela, P., Aldegunde, M., and Rozas, G. (1993). Changes in Carbohydrate Metabolism in Domesticated Rainbow trout (*Oncorhynchus mykiss*) Related to Spermatogenesis. *Comp. Biochem. Physiol. Part B: Comp. Biochem.* 105, 665–671. doi:10.1016/0305-0491(93)90103-C

Sohn, Y. C., Yoshiura, Y., Kobayashi, M., and Aida, K. (1999). Seasonal Changes in mRNA Levels of Gonadotropin and Thyrotropin Subunits in the Goldfish,*Carassius auratus*. *Gen. Comp. Endocrinol.* 113, 436–444. doi:10.1006/gcen.1998.7224

Somoza, G. M., Mechaly, A. S., and Trudeau, V. L. (2020). Kisspeptin and GnRH Interactions in the Reproductive Brain of Teleosts. *Gen. Comp. Endocrinol.* 298, 113568. doi:10.1016/j.ygcen.2020.113568

Triba, M. N., Le Moyec, L., Amathieu, R., Goossens, C., Bouchemal, N., Nahon, P., et al. (2015). PLS/OPLS Models in Metabolomics: The Impact of Permutation of Dataset Rows on the K-fold Cross-Validation Quality Parameters. *Mol. Biosyst.* 11, 13–19. doi:10.1039/c4mb00414k

Trudeau, V. L., and Somoza, G. M. (2020). Multimodal Hypothalamo-Hypophysial Communication in the Vertebrates. *Gen. Comp. Endocrinol.* 293, 113475. doi:10.1016/j.ygcen.2020.113475

Tsukada, A., Ohkubo, T., Sakaguchi, K., Tanaka, M., Nakashima, K., Hayashida, Y., et al. (1998). Thyroid Hormones Are Involved in Insulin-like Growth Factor-I (IGF-I) Production by Stimulating Hepatic Growth Hormone Receptor (GHR) Gene Expression in the Chicken. *Growth Horm. IGF Res.* 8, 235–242. doi:10.1016/S1096-6374(98)80116-0

Tsutsui, K., Saigoh, E., Ukena, K., Teranishi, H., Fujisawa, Y., Kikuchi, M., et al. (2000). A Novel Avian Hypothalamic Peptide Inhibiting Gonadotropin Release. *Biochem. Biophysical Res. Commun.* 275, 661–667. doi:10.1006/bbrc.2000.3350

Tsutsui, K., Ubuka, T., Bentley, G. E., and Kriegsfeld, L. J. (2013). Review: Regulatory Mechanisms of Gonadotropin-Inhibitory Hormone (GnIH) Synthesis and Release in Photoperiodic Animals. *Front. Neurosci.* 7. doi:10.3389/fnins.2013.00060

Tyler, C. R., Sumpter, J. P., and Witthames, P. R. (1990). The Dynamics of Oocyte Growth during Vitellogenesis in the Rainbow Trout (Oncorhynchus Mykiss). *Biol. Reprod.* 43, 202–209. doi:10.1095/biolreprod43.2.202

Ubuka, T., Ukena, K., Sharp, P. J., Bentley, G. E., and Tsutsui, K. (2006). Gonadotropin-inhibitory Hormone Inhibits Gonadal Development and Maintenance by Decreasing Gonadotropin Synthesis and Release in Male Quail. *Endocrinology* 147, 1187–1194. doi:10.1210/en.2005-1178

Ukena, K., Koda, A., Yamamoto, K., Kobayashi, T., Iwakoshi-Ukena, E., Minakata, H., et al. (2003). Novel Neuropeptides Related to Frog Growth Hormone-Releasing Peptide: Isolation, Sequence, and Functional Analysis. *Endocrinology* 144, 3879–3884. doi:10.1210/en.2003-0359

Vuckovic, D. (2012). Current Trends and Challenges in Sample Preparation for Global Metabolomics Using Liquid Chromatography-Mass Spectrometry. *Anal. Bioanal. Chem.* 403, 1523–1548. doi:10.1007/s00216-012-6039-y

Waters, S., Khamis, M., and von der Decken, A. (1992). Polyamines in Liver and Their Influence on Chromatin Condensation after 17-β Estradiol Treatment of Atlantic salmon. *Mol. Cel. Biochem.* 109, 17–24. doi:10.1007/BF00230869

Wu, G. (2009). Amino Acids: Metabolism, Functions, and Nutrition. *Amino Acids* 37, 1–17. doi:10.1007/s00726-009-0269-0

Wu, H., Southam, A. D., Hines, A., and Viant, M. R. (2008). High-throughput Tissue Extraction Protocol for NMR- and MS-based Metabolomics. *Anal. Biochem.* 372, 204–212. doi:10.1016/j.ab.2007.10.002

Xia, J., Wishart, D. S., and Valencia, A. (2010). MetPA: A Web-Based Metabolomics Tool for Pathway Analysis and Visualization. *Bioinformatics* 26, 2342–2344. doi:10.1093/bioinformatics/btq418

Yaron, Z. (2011). *Endocrine Regulation of Fish Reproduction*. San Diego, CA: Elsevier. doi:10.1016/B978-0-1237-4553-8.00058-7

Yu, K. L., Rosenblum, P. M., and Peter, R. E. (1991). *In Vitro* release of Gonadotropin-Releasing Hormone from the Brain Preoptic-Anterior Hypothalamic Region and Pituitary of Female Goldfish. *Gen. Comp. Endocrinol.* 81, 256–267. doi:10.1016/0016-6480(91)90010-4

Yu, K. L., Sherwood, N. M., and Peter, R. E. (1988). Differential Distribution of Two Molecular Forms of Gonadotropin-Releasing Hormone in Discrete Brain Areas of Goldfish (*Carassius auratus*). *Peptides* 9, 625–630. doi:10.1016/0196-9781(88)90174-X

Zammit, V. A., and Newsholme, E. A. (1979). Activities of Enzymes of Fat and Ketone-Body Metabolism and Effects of Starvation on Blood Concentrations of Glucose and Fat Fuels in Teleost and Elasmobranch Fish. *Biochem. J.* 184, 313–322. doi:10.1042/bj1840313

Zohar, Y., Muñoz-Cueto, J. A., Elizur, A., and Kah, O. (2010). Neuroendocrinology of Reproduction in Teleost Fish. *Gen. Comp. Endocrinol.* 165, 438–455. doi:10.1016/j.ygcen.2009.04.017

Conflict of Interest: The authors declare that the research was conducted in the absence of any commercial or financial relationships that could be construed as a potential conflict of interest.

frontiers in Cell and Developmental Biology

PERSPECTIVE
published: 14 March 2022
doi: 10.3389/fcell.2022.778901

Simvastatin and Muscle: Zebrafish and Chicken Show that the Benefits are not Worth the Damage

Laise M. Campos[1], Livia Guapyassu[2], Cyro Gomes[2], Victor Midlej[3], Marlene Benchimol[4,5], Claudia Mermelstein[2] and Manoel Luis Costa[2]*

[1]Instituto de Ciências da Saúde, Universidade Federal da Bahia, Salvador, Brazil, [2]Instituto de Ciências Biomédicas, Universidade Federal do Rio de Janeiro, Rio de Janeiro, Brazil, [3]Laboratório de Ultraestrutura Celular, Instituto Oswaldo Cruz, Fundação Oswaldo Cruz, Rio de Janeiro, Brazil, [4]Centro Nacional de Biologia Estrutural e Bioimagem, Universidade Federal do Rio de Janeiro, Rio de Janeiro, Brazil, [5]Universidade do Grande Rio (UNIGRANRIO), Duque de Caxias, Rio de Janeiro, Brazil

Simvastatin is one of the most common medicines prescribed to treat human hypercholesterolemia. Simvastatin acts through the inhibition of cholesterol synthesis. Unfortunately, simvastatin causes unwanted side effects on muscles, such as soreness, tiredness, or weakness. Therefore, to understand the mechanism of action of simvastatin, it is important to study its physiological and structural impacts on muscle in varied animal models. Here we report on the effects of simvastatin on two biological models: zebrafish embryos and chicken muscle culture. In the last years, our group and others showed that simvastatin treatment in zebrafish embryos reduces fish movements and induces major structural alterations in skeletal muscles. We also showed that simvastatin and membrane cholesterol depletion induce major changes in proliferation and differentiation of muscle cells in chick muscle cultures. Here, we review and discuss these observations considering reported data on the use of simvastatin as a potential therapy for Duchenne muscular dystrophy.

Keywords: simvastatin, muscle, cholesterol, embryo, zebrafish

OPEN ACCESS

Edited by:
Natalia Martins Feitosa, Federal University of Rio de Janeiro, Brazil

Reviewed by:
Gillian Sandra Butler-Browne, Centre of Research in Myology, France
Ingo Riederer, Oswaldo Cruz Foundation (Fiocruz), Brazil

****Correspondence:***
Claudia Mermelstein
mermelstein@ufrj.br

Specialty section:
This article was submitted to Molecular and Cellular Pathology, a section of the journal Frontiers in Cell and Developmental Biology

Received: *17 September 2021*
Accepted: *17 February 2022*
Published: *14 March 2022*

Citation:
Campos LM, Guapyassu L, Gomes C, Midlej V, Benchimol M, Mermelstein C and Costa ML (2022) Simvastatin and Muscle: Zebrafish and Chicken Show that the Benefits are not Worth the Damage. Front. Cell Dev. Biol. 10:778901. doi: 10.3389/fcell.2022.778901

INTRODUCTION

High cholesterol levels in the blood are associated with an increased risk of cardiovascular disease in humans. Therefore, statins have been the number one choice of physicians to control blood cholesterol levels since these drugs inhibit 3-hydroxy-3-methylglutaryl coenzyme A reductase (HMG-CoA), a key enzyme of the cholesterol biosynthetic pathway. Simvastatin effectively decreases blood cholesterol levels and the risk of heart problems in those at high risk. Unfortunately, simvastatin can induce myalgia, myopathy, and rhabdomyolysis (Nikolic et al., 2020; Turner and Pirmohamed, 2019). To further analyze the effects of statins in muscle at the cellular level, our group has been studying the effects of simvastatin treatment in zebrafish (*Danio rerio*) embryos. Zebrafish is a vertebrate biological model with several advantages, such as a well-characterized genome, easy of maintenance in laboratory conditions, and fast growth (Horzmann and Freeman, 2018).

MATERIALS AND METHODS

Zebrafish Husbandry and Simvastatin Treatment

Adult, wild-type zebrafish (*Danio rerio*) were maintained in aquaria with recirculating water system at 28 ± 1°C on a 14:10 light/dark cycle in a vivarium localized at the Institute of Biomedical Sciences,

Federal University of Rio de Janeiro (Rio de Janeiro, Brazil). Embryos were collected after breeding. Animals were handled and experimented according to Institutional Animal Care and Use Committee protocols under the number 039/20.

Simvastatin Treatment

Embryos were dechorionated at 6 hpf and 11 hpf (hours post-fertilization) and placed in 100-mm Petri dishes filled with 50 ml of egg water (60 mg/L sea salts and 0.15% methylene blue). Embryos were treated with simvastatin (University Pharmacy, UFRJ) at low concentrations (from 3 to 6 nM) or higher concentrations (from 0.375 to 1 mM). Embryos were treated with simvastatin for 18 hs at 28°C until they completed 24 hpf and then were processed as necessary. Simvastatin was dissolved in ethanol (final concentration of 0.02%).

Antibodies and Probes

Rabbit polyclonal antibody against desmin (code # D-8281) was from Sigma-Aldrich (United States). DNA-binding probe 4,6-Diamino-2-phenylindole dihydrochloride (DAPI) and Alexa Fluor 546-goat anti-rabbit IgG antibody was from Molecular Probes (United States).

Immunofluorescence

Dechorionated zebrafish embryos were fixed in 4% paraformaldehyde in phosphate buffered saline (PBS) for 1 h at room temperature. Embryos were then permeabilized with 0.5% Triton-X 100 in PBS (PBS/T) three times for 30 min and incubated overnight at 4°C with primary antibodies (diluted 1:100 in PBS/T). Then, embryos were washed for 30 min with PBS/T and incubated for 1 h at 37°C with Alexa Fluor-conjugated secondary antibodies (diluted 1:200 in PBS/T). Nuclei were labeled with 0.1 μg/ml of DAPI in 0.9% NaCl. Embryos were mounted on #1.5 24 × 60-mm glass coverslips (with spacers) using Prolong Gold (Molecular Probes). Experiments were repeated four times.

Image Acquisition and Processing

Zebrafish embryos were examined with brightfield microscopy in an Axiovert 100 microscope (Carl Zeiss, Germany) coupled to an Olympus DP71 high-resolution camera and with fluorescence microscopy in a DSU Spinning Disk confocal scanner mounted on an inverted fluorescent microscope (Olympus, Japan). Control experiments with only secondary antibodies showed only a faint background staining (data not shown). Image processing (brightness and contrast adjustments) was performed using Fiji software (Schindelin et al., 2012) and figure panels were produced with Adobe Photoshop software (Adobe Systems Inc., San Jose, CA, United States).

Transmission Electron Microscopy

Dechorionated embryos were washed gently in warm PBS, pH 7.2, and fixed overnight in 2.5% glutaraldehyde, 4% formaldehyde and 5 mM $CaCl_2$ in 0.1 M cacodylate buffer (pH 7.2), and were then post-fixed for 90 min in 1% OsO_4 in 0.1 M cacodylate buffer containing 5 mM $CaCl_2$ and 0.8% potassium ferricyanide. Embryos were then dehydrated in acetone and embedded in Epon. Ultra-thin sections were cut and stained with uranyl acetate and lead citrate, and analyzed using a JEOL 1210 transmission electron microscope (Jeol, Japan). Experiments were repeated four times.

RESULTS

Zebrafish Embryo as a Robust Model to Study Structural Muscle Alterations After Simvastatin Treatment

Zebrafish is an ideal system to analyze somite development. It allows the study and comparison of different stages of muscle/somite development (anterior-posterior axis) within the same embryo (Stickney et al., 2000); while the anterior somites are older, the posterior somites are younger. Our lab has been exploring the optical transparency of the zebrafish embryo by using high-resolution fluorescence microscopy, which enables us to do a thorough structural analysis of the distribution of key muscle proteins during somite formation (Costa et al., 2002, 2008). After this characterization of normal myogenesis, we showed that simvastatin causes several alterations in zebrafish embryos, such as body shortening and bending, depending on the dose (Campos et al., 2015, 2016). In these papers, we reported that low concentrations (from 3 to 6 nM) had mild structural and important physiological changes, including decrease in intermediate filaments, myofibrils and adhesion structures, and reduction in heart beat and body movement. We also observed that higher concentrations (from 0.375 to 1 mM) caused extensive structural and physiological alterations, including almost complete absence of intermediate filaments, myofibrils, adhesion structures, heart beat and body movement (Campos et al., 2015, 2016). The dose range and accompanying alterations was about the same for embryos treated at 6 and 11 h post-fertilization (hpf) (Campos et al., 2015, 2016).

In our earlier work we analyzed several aspects of the distribution of actin, desmin, vinculin, and laminin in simvastatin-treated embryos (Campos et al., 2015). To evaluate the specificity of simvastatin-induced alterations to cholesterol withdrawal, we treated embryos with simvastatin together with cholesterol, obtained from human blood in the form of low-density lipoprotein-LDL (Campos et al., 2015, 2016). Here we further explored the effects of simvastatin in zebrafish embryos. Using confocal microscopy analysis of the distribution of the muscle-specific protein desmin, it is possible to observe mild alterations in embryos treated with lower doses (3 nM) of simvastatin (**Figure 1**). While in control embryos desmin is concentrated in the septa (arrow in **Figure 1A**) and distributed in sarcomeres (arrow in **Figure 1B**), the protein is restricted to aggregates in simvastatin treated embryos (arrows in **Figure 1G**). The concomitant treatment of simvastatin and cholesterol preserved the concentration of desmin in the septa adhesion region (arrow in **Figure 1J**). We also observed structural alterations (extreme body shortening) in zebrafish embryos treated with high concentrations of simvastatin (**Figures 1M,N**), which could again be reverted to a certain degree by

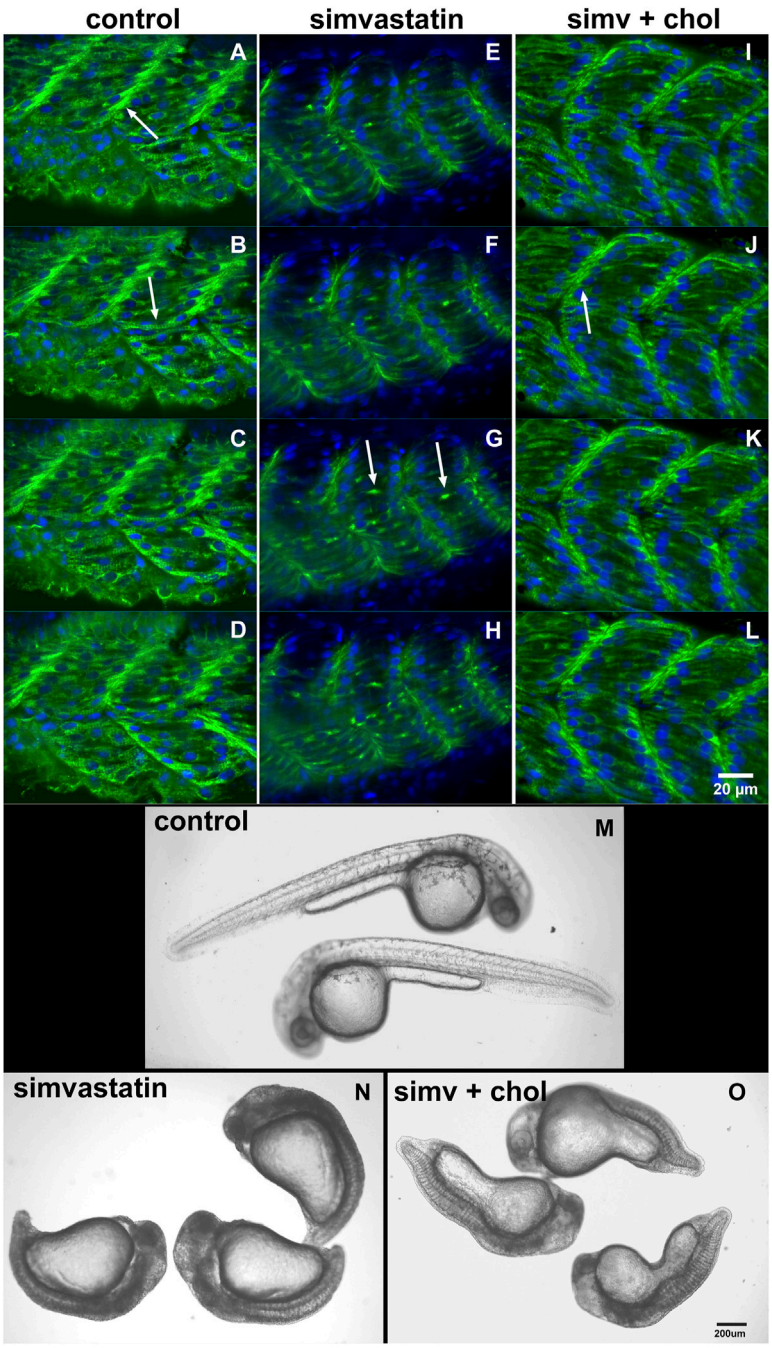

FIGURE 1 | Cholesterol rescues the simvastatin-affected phenotype. The distribution of desmin (green) and nuclei (blue) in four consecutive focal planes of control **(A–D)**, 0.3 nM (low-dose) simvastatin-treated 48 hpf embryos **(E–H)**, and simvastatin combined with cholesterol **(I–L)** show that simvastatin causes important alterations that are rescued with cholesterol. Note that in control [non treated embryos, **(A–D)**] and in embryos treated with simvastatin together with cholesterol **(I–L)**, desmin concentrates in the septa between adjacent somites [arrows in **(A)** and **(J)**] and in sarcomeres along the somites [arrow in **(B)**]. Conversely, desmin accumulates in aggregates in somites [arrows in **(G)**] in simvastatin treated embryos **(E–H)**. In embryos treated with 0.75 µM simvastatin (high-dose), an important body compression is observed **(N)**, while 24 hpf control embryos have a long straight body **(M)**. Note that the addition of exogenous cholesterol can partially rescue the effects of simvastatin on body compression **(O)**. Scale bars: **(A–L)** = 20 µm, **(M–O)** = 200 µm.

cholesterol (**Figure 1O**). While the whole-body development is affected with simvastatin treatment, we show using transmission electron microscopy that, compared to control (**Figures 2A–C**), there is extensive muscle-specific damage, particularly in the organization of sarcomeres and in mitochondria, both with low simvastatin doses (**Figures 2D–F**) and with high simvastatin doses (**Figures 2G–I**). Simvastatin induces alterations in myofibril alignment, vacuoles formation, and

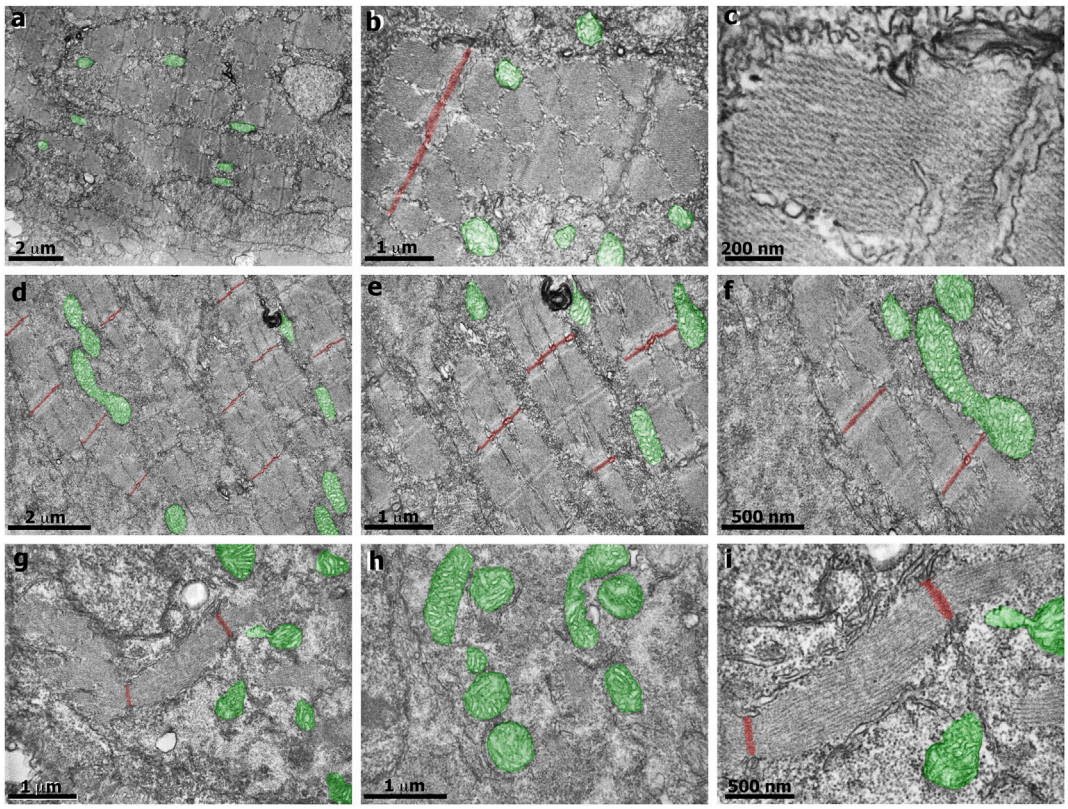

FIGURE 2 | Transmission electron microscopy of zebrafish embryos treated with simvastatin. Control untreated zebrafish embryos **(A–C)** present organized bundles of myofibrils and exhibit well-preserved mitochondria (green). Note that the Z lines (red) are aligned and periodically spaced. The sarcomeric organization is better visualized in figure **(C)**. In the mild phenotype of simvastatin-treated embryos **(D–F)**, myofibrils are well-organized, and the alignment of Z lines is preserved. In the severe phenotype of simvastatin-treated embryos **(G–I)**, myofibrils are not aligned, vacuoles are observed **(G)**, as well as a higher number of mitochondria (green). Scale **(A,D)** 2 µm; **(B,E,G,H)** 1 µm; **(C)**, 200 nm; **(F,I)**, 500 nm.

increased number of mitochondria. The effects of different doses of simvastatin treatment and/or treatment with simvastatin and exogenous cholesterol have not been previously described in the conditions we are showing here, and are in agreement with previous results of our group (Campos et al., 2015, 2016).

Interfering With Cholesterol Availability in Chicken Muscle Cell Cultures

To address the mechanism of action and compare the impact of simvastatin in a different model, we also analyzed 24 h-chick primary myogenic cells treated with simvastatin (0.5 mM for 30 min). Our previous results showed a 20% decrease in cell number after simvastatin treatment (Portilho et al., 2012), in accordance with other studies in cultured human myoblasts (Van Vliet et al., 1996). It is interesting to point out that simvastatin, as we have shown before, reduces the number of cells compared to control zebrafish embryos (Campos et al., 2016). One possible mechanism of action of simvastatin is its effect on cell membrane stability. Cholesterol is a sterol lipid involved in the maintenance of plasma membrane fluidity and the formation and maintenance of lipid rafts. Lipid rafts are specialized membrane microdomains that contain high concentrations of cholesterol and glycosphingolipids and are involved in different cellular processes, such as signal transduction, endocytosis, and cell fusion and adhesion (Sezgin et al., 2017). Our lab has studied the consequences of membrane cholesterol depletion during chick myogenesis using primary cultures of embryonic chick muscle cells (Mermelstein et al., 2005; Mermelstein et al., 2007; Portilho et al., 2007; Costa et al., 2021). We showed that cholesterol depletion by MbCD (methyl-beta-cyclodextrin) induces an increase in the proliferation of myoblasts and the formation of myotubes (Portilho et al., 2012). These processes involve the release of Wnt3a molecules from chick muscle cells. The Wnt/beta-catenin pathway is involved in the proliferation of myoblasts, and we showed that cholesterol depletion by MbCD leads to an increase in the expression of cell cycle regulators and the master switch gene MyoD1 in chick myoblast cells (Portilho et al., 2012). The collection of these results supports the view that alterations in the amount of membrane cholesterol can lead to profound changes in muscle proliferation and differentiation (Possidonio et al., 2014). Curiously, the above-described data shows that MbCD and simvastatin have opposite effects in muscle cells: while cholesterol depletion (by MbCD) induces increased muscle cell proliferation, inhibition of cholesterol synthesis resulted in a reduction of muscle cell proliferation.

These results point to a complex intracellular network of events associated with cholesterol in muscle cells and the importance of further investigations on the role of this lipid in muscle.

DISCUSSION

Simvastatin is used in treatment of human adult cholesteremia, and it is not recommend during pregnancy. Here we presented studies on the effects of simvastatin during myogenesis in zebrafish embryos and chick embryonic cultured cells. Therefore, a valid criticism of these models is that they are not equivalent to simvastatin effects in adult human muscle, and that adult tissues would be a better model. The advanges of using zebrafish embryos and cultured cells is that they are more susceptible to treatments and they allow a better visualization of muscle response at the molecular and cellular levels, which contribute to the understanding of mechanisms of action of drugs. Some of these processes, such as muscle proliferation and differentiation, also happen in adult muscle, during regeneration or in response to exercise. However, to correlate our current data with adult muscle, we are planning future experiments on the effects of simvastatin in adult zebrafish.

Our results show that simvastatin, depending on the dose, can induce major muscle alterations according to the work from several other groups using different statins and different animal or cell models. Hanai et al. (2007) reported that lovastatin promotes muscle fiber damage in zebrafish embryos and that atrogin-1 knockdown prevented these effects. These results suggest that atrogin-1 may be a critical mediator of the muscle damage induced by statins. Yu et al. (2009) showed that treatment of mouse C2C12 myotubes with simvastatin resulted in significant changes in gene expression, suggesting that alterations in the expression of some statin-regulated genes could be causative factors for statin toxicity in muscle. Wagner et al. (2011) used a small-molecule screening strategy to identify statin myopathy suppressors. They found one compound that attenuated the muscle side effects of statin toxicity, likely by influencing Rab prenylation. Huang et al. (2011) showed that the effects of statins on muscle were dependent on both the dosage and the duration of treatment. Piette et al. (2016) reported that a short-term statin treatment induced significant changes in the contractile profile of mice fast-twitch muscle EDL. In contrast, no effects were observed in the slow-twitch muscle Soleus. Furthermore, Pasha and Moon (2017) showed that statin-induced reduction in zebrafish larval response to tactile stimuli was reversed with coenzyme Q10, contributing to the understanding of the mechanisms of action of statin-induced myopathies.

The collection of our results shows that in zebrafish embryos, simvastatin treatment induces 1) a significant cholesterol reduction, 2) several dose-dependent alterations, 3) extensive changes in the distribution of microfilaments (actin), intermediate filaments (desmin), adhesion structures (vinculin) and extracellular matrix (laminin), 4) a reduction in cell number, and that 5) exogenous cholesterol is capable of recovering, at least in part, embryos treated with both low and high simvastatin doses. Furthermore, in chick muscle cultures, simvastatin induces a decrease in the number of cells while MbCD induces an increase in cell proliferation and muscle differentiation. These results provide a detailed characterization of the simvastatin-induced effects in muscles of zebrafish embryos and chicken muscle in culture. Since simvastatin reduces cell proliferation this may inhibit muscle regeneration. Future experiments are needed to study the possible consequences of simvastatin-induced reduction in cell proliferation during muscle regeneration. Also, it will be important in the future to analyse if these same effects occur when human muscle cells cultures are treated with simvastatin.

We suggest that these results should be considered in the discussion of the medical use of simvastatin, particularly in muscle degenerative diseases. Several studies were conducted in the last years aiming to understand the impact of simvastatin in the treatment of Duchenne muscular dystrophy (DMD), since statins have been shown to improve skeletal muscle health in ischemic limb diseases (Cowled et al., 2007; Köksoy et al., 2007; El-Azab et al., 2012). Whitehead and colleagues (2015) reported that simvastatin reduced plasma creatine kinase (CK) activity, muscle inflammation, and muscle damage while enhancing physiological function of skeletal muscle in dystrophic mdx mice. In contrast with these results, Mucha et al. (2021) and Verhaart et al. (2021) have recently shown that simvastatin does not alleviate muscle pathology in DMD mdx mice. Mucha et al. (2021) suggested that these conflicting results might be related to several divergences in methodology, including age and genetic background of the mdx mice, type and dose of the statin, route of administration, and length of time the drug was given to the animals. Whitehead and coworkers published a rebuttal letter (Whitehead et al., 2021) arguing that the conflicting results could be explained by the fact that neither Mucha et al. (2021) nor Verhaart et al. (2021) were able to achieve in their studies the therapeutic levels of plasma simvastatin, that Whitehead et al. (2015) attained. According to Whitehead and colleagues, low plasma levels of simvastatin are not sufficient to improve mdx muscle health and function. Aartsma-Rus et al. (2021) published another rebuttal corroborating that the differences in the result of the studies could be related to plasma levels of simvastatin. More studies are necessary to unravel the molecular and cellular mechanisms involved in statin-induced effects in different experimental models (animals and 3D muscle cell cultures) of degenerative muscle diseases, and zebrafish is among the most promising vertebrate models for these studies.

DATA AVAILABILITY STATEMENT

The raw data supporting the conclusion of this article will be made available by the authors, without undue reservation.

ETHICS STATEMENT

The use of zebrafish embryos was approved by the Ethics Committee for Animal Care and Use in Scientific Research

from the Federal University of Rio de Janeiro and received the approval number 039/20. The use of chick embryos was approved by the Ethics Committee for Animal Care and Use in Scientific Research from the Federal University of Rio de Janeiro and received the approval number: 069/19.

AUTHOR CONTRIBUTIONS

CM and MLC wrote the draft and revised it. CG, CM, LG, LMC, MB, MLC and VM collected the data. CM, MB, MLC and VM prepared the figures. All authors approved the submitted version.

REFERENCES

Aartsma-Rus, A., Verhaart, I., and Wells, D. (2021). Author's Response to: Rebuttal to: Simvastatin treatment does not ameliorate muscle pathophysiology in a mouse model for Duchenne muscular dystrophy. *J Neuromuscul. Dis.* 8, 867–868. doi:10.3233/JND-219004

Campos, L. M., Rios, E. A., Guapyassu, L., Midlej, V., Atella, G. C., Herculano-Houzel, S., et al. (2016). Alterations in Zebrafish Development Induced by Simvastatin: Comprehensive Morphological and Physiological Study, Focusing on Muscle. *Exp. Biol. Med. (Maywood)* 241, 1950–1960. doi:10.1177/1535370216659944

Campos, L. M., Rios, E. A., Midlej, V., Atella, G. C., Herculano-Houzel, S., Benchimol, M., et al. (2015). Structural Analysis of Alterations in Zebrafish Muscle Differentiation Induced by Simvastatin and Their Recovery with Cholesterol. *J. Histochem. Cytochem.* 63, 427–437. doi:10.1369/0022155415580396

Costa, M. L., Escaleira, R. C., Jazenko, F., and Mermelstein, C. S. (2008). Cell Adhesion in Zebrafish Myogenesis: Distribution of Intermediate Filaments, Microfilaments, Intracellular Adhesion Structures and Extracellular Matrix. *Cell Motil. Cytoskeleton* 65, 801–815. doi:10.1002/cm.20301

Costa, M. L., Escaleira, R. C., Rodrigues, V. B., Manasfi, M., and Mermelstein, C. S. (2002). Some Distinctive Features of Zebrafish Myogenesis Based on Unexpected Distributions of the Muscle Cytoskeletal Proteins Actin, Myosin, Desmin, α-actinin, Troponin and Titin. *Mech. Dev.* 116, 95–104. doi:10.1016/s0925-4773(02)00149-1

Costa, M. L., Jurberg, A. D., and Mermelstein, C. (2021). The Role of Embryonic Chick Muscle Cell Culture in the Study of Skeletal Myogenesis. *Front. Physiol.* 12, 668600. doi:10.3389/fphys.2021.668600

Cowled, P. A., Khanna, A., Laws, P. E., Field, J. B. F., Varelias, A., and Fitridge, R. A. (2007). Statins Inhibit Neutrophil Infiltration in Skeletal Muscle Reperfusion Injury. *J. Surg. Res.* 141, 267–276. doi:10.1016/j.jss.2006.11.021

El-Azab, M. F., Hazem, R. M., and Moustafa, Y. M. (2012). Role of Simvastatin And/or Antioxidant Vitamins in Therapeutic Angiogenesis in Experimental Diabetic Hindlimb Ischemia: Effects on Capillary Density, Angiogenesis Markers, and Oxidative Stress. *Eur. J. Pharmacol.* 690, 31–41. doi:10.1016/j.ejphar.2012.06.002

Hanai, J., Cao, P., Tanksale, P., Imamura, S., Koshimizu, E., Zhao, J., et al. (2007). The Muscle-specific Ubiquitin Ligase atrogin-1/MAFbx Mediates Statin-Induced Muscle Toxicity. *J. Clin. Invest.* 117, 3940–3951. doi:10.1172/JCI32741

Horzmann, K. A., and Freeman, J. L. (2018). Making Waves: New Developments in Toxicology with the Zebrafish. *Toxicol. Sci.* 163, 5–12. doi:10.1093/toxsci/kfy044

Huang, S.-H., Hsiao, C.-D., Lin, D.-S., Chow, C.-Y., Chang, C.-J., and Liau, I. (2011). Imaging of Zebrafish *In Vivo* with Second-Harmonic Generation Reveals Shortened Sarcomeres Associated with Myopathy Induced by Statin. *PLoS One* 6, e24764. doi:10.1371/journal.pone.0024764

Köksoy, C., Oziş, E., Çakmak, A., Yazgan, U., Okcu-Heper, A., Köksoy, A., et al. (2007). Simvastatin pretreatment reduces the severity of limb ischemia in an experimental diabetes model. *J. Vasc. Surg.* 45, 590–596. doi:10.1016/j.jvs.2006.10.048

Mermelstein, C. S., Portilho, D. M., Mendes, F. A., Costa, M. L., and Abreu, J. G. (2007). Wnt/β-catenin Pathway Activation and Myogenic Differentiation Are Induced by Cholesterol Depletion. *Differentiation* 75, 184–192. doi:10.1111/j.1432-0436.2006.00129.x

Mermelstein, C. u. S., Portilho, D. b. M., Medeiros, R. B., Matos, A. R., Einicker-Lamas, M., Tortelote, G. G., et al. (2005). Cholesterol Depletion by Methyl-β-Cyclodextrin Enhances Myoblast Fusion and Induces the Formation of Myotubes with Disorganized Nuclei. *Cell Tissue Res.* 319, 289–297. doi:10.1007/s00441-004-1004-5

Mucha, O., Podkalicka, P., Kaziród, K., Samborowska, E., Dulak, J., and Łoboda, A. (2021). Simvastatin Does Not Alleviate Muscle Pathology in a Mouse Model of Duchenne Muscular Dystrophy. *Skeletal Muscle* 11, 21. doi:10.1186/s13395-021-00276-3

Nikolic, D., Banach, M., Chianetta, R., Luzzu, L. M., Citarrella, R., Montalto, G., et al. (2020). An Overview of Statin-Induced Myopathy and Perspectives for the Future. *Expert Opin. Drug Saf.* 19, 601–615. doi:10.1080/14740338.2020.1747431

Pasha, R., and Moon, T. W. (2017). Coenzyme Q10 Protects against Statin-Induced Myotoxicity in Zebrafish Larvae (*Danio rerio*). *Environ. Toxicol. Pharmacol.* 52, 150–160. doi:10.1016/j.etap.2017.03.021

Piette, A. B., Dufresne, S. S., and Frenette, J. (2016). A Short-Term Statin Treatment Changes the Contractile Properties of Fast-Twitch Skeletal Muscles. *BMC Musculoskelet. Disord.* 17, 449. doi:10.1186/s12891-016-1306-2

Portilho, D. M., Martins, E. R., Costa, M. L., and Mermelstein, C. S. (2007). A Soluble and Active Form of Wnt-3a Protein Is Involved in Myogenic Differentiation after Cholesterol Depletion. *FEBS Lett.* 581, 5787–5795. doi:10.1016/j.febslet.2007.11.047

Portilho, D. M., Soares, C. P., Morrot, A., Thiago, L. S., Butler-Browne, G., Savino, W., et al. (2012). Cholesterol Depletion by Methyl-β-Cyclodextrin Enhances Cell Proliferation and Increases the Number of Desmin-Positive Cells in Myoblast Cultures. *Eur. J. Pharmacol.* 694, 1–12. doi:10.1016/j.ejphar.2012.07.035

Possidonio, A. C., Miranda, M., Gregoracci, G. B., Thompson, F. L., Costa, M. L., and Mermelstein, C. (2014). Cholesterol Depletion Induces Transcriptional Changes during Skeletal Muscle Differentiation. *BMC Genomics* 15, 544. doi:10.1186/1471-2164-15-544

Schindelin, J., Arganda-Carreras, I., Frise, E., et al. (2012). Fiji: an Open-Source Platform for Biological-Image Analysis. *Nat. Methods* 9, 676–682. doi:10.1038/nmeth.2019

Sezgin, E., Levental, I., Mayor, S., and Eggeling, C. (2017). The Mystery of Membrane Organization: Composition, Regulation and Roles of Lipid Rafts. *Nat. Rev. Mol. Cel Biol.* 18, 361–374. doi:10.1038/nrm.2017.16

Stickney, H. L., Barresi, M. J. F., and Devoto, S. H. (2000). Somite Development in Zebrafish. *Dev. Dyn.* 219, 287–303. doi:10.1002/1097-0177(2000)9999

Turner, R. M., and Pirmohamed, M. (2019). Statin-related Myotoxicity: A Comprehensive Review of Pharmacokinetic, Pharmacogenomic and Muscle Components. *Jcm* 9, 22. doi:10.3390/jcm9010022

Van Vliet, A. K., Negre-Aminou, P., Van Thiel, G. C., Bolhuis, P. A., and Cohen, L. H. (1996). Action of Lovastatin, Simvastatin, and Pravastatin on Sterol Synthesis and Their Antiproliferative Effect in Cultured Myoblasts From Human Striated Muscle. *Biochem. Pharmacol.* 52, 1387–1392.

Verhaart, I. E. C., Cappellari, O., Tanganyika-de Winter, C. L., Plomp, J. J., Nnorom, S., Wells, K. E., et al. (2021). Simvastatin Treatment Does Not Ameliorate Muscle Pathophysiology in a Mouse Model for Duchenne Muscular Dystrophy. *Jnd* 8, 845–863. doi:10.3233/JND-200524

Wagner, B. K., Gilbert, T. J., Hanai, J.-i., Imamura, S., Bodycombe, N. E., Bon, R. S., et al. (2011). A Small-Molecule Screening Strategy to Identify Suppressors of Statin Myopathy. *ACS Chem. Biol.* 6, 900–904. doi:10.1021/cb200206w

Whitehead, N. P., Kim, M. J., Bible, K. L., Adams, M. E., and Froehner, S. C. (2015). A New Therapeutic Effect of Simvastatin Revealed by Functional Improvement in Muscular Dystrophy. *Proc. Natl. Acad. Sci. USA* 112, 12864–12869. doi:10.1073/pnas.1509536112

Whitehead, N. P., Kim, M. J., Bible, K. L., Adams, M. E., and Froehner, S. C. (2021). Rebuttal to: Simvastatin Treatment Does Not Ameliorate Muscle Pathophysiology in a Mouse Model for Duchenne Muscular Dystrophy. *Jnd* 8, 865–866. doi:10.3233/JND-219005

Yu, J.-G., Sewright, K., Hubal, M. J., Liu, J.-X., Schwartz, L. M., Hoffman, E. P., et al. (2009). Investigation of Gene Expression in C2C12 Myotubes Following Simvastatin Application and Mechanical Strain. *Jat* 16, 21–29. doi:10.5551/jat.e551

Conflict of Interest: The authors declare that the research was conducted in the absence of any commercial or financial relationships that could be construed as a potential conflict of interest.

Publisher's Note: All claims expressed in this article are solely those of the authors and do not necessarily represent those of their affiliated organizations, or those of the publisher, the editors and the reviewers. Any product that may be evaluated in this article, or claim that may be made by its manufacturer, is not guaranteed or endorsed by the publisher.

frontiers in Cell and Developmental Biology

ORIGINAL RESEARCH
published: 24 March 2022
doi: 10.3389/fcell.2022.798551

Integrative Analysis of RNA Expression and Regulatory Networks in Mice Liver Infected by *Echinococcus multilocularis*

Tingli Liu[1], Hong Li[1], Yanping Li[1], Liqun Wang[1], Guoliang Chen[1], Guiting Pu[1], Xiaola Guo[1], William C. Cho[2], Majid Fasihi Harandi[3], Yadong Zheng[4] and Xuenong Luo[1]**

[1]State Key Laboratory of Veterinary Etiological Biology, Key Laboratory of Veterinary Parasitology of Gansu Province, Lanzhou Veterinary Research Institute, CAAS, Lanzhou, China, [2]Department of Clinical Oncology, Queen Elizabeth Hospital, Hong Kong SAR, China, [3]Research Center for Hydatid Disease in Iran, Kerman University of Medical Sciences, Kerman, Iran, [4]Key Laboratory of Applied Technology on Green-Eco-Healthy Animal Husbandry of Zhejiang Province, Zhejiang International Science and Technology Cooperation Base for Veterinary Medicine and Health Management, Zhejiang Provincial Engineering Laboratory for Animal Health Inspection and Internet Technology, Zhejiang International Science and Technology Cooperation Base for Veterinary Medicine and Health Management, China-Australia Joint Laboratory for Animal Health Big Data Analytics, College of Animal Science and Technology and College of Veterinary Medicine of Zhejiang A&F University, Hangzhou, China

OPEN ACCESS

Edited by:
Natalia Martins Feitosa, Federal University of Rio de Janeiro, Brazil

Reviewed by:
Deborah Stroka, University of Bern, Switzerland
Maude Giroud, Ludwig Maximilian University of Munich, Germany

***Correspondence:**
Xuenong Luo
luoxuenong@caas.cn
Yadong Zheng
zhengyadong@zafu.edu.cn

Specialty section:
This article was submitted to Molecular and Cellular Pathology, a section of the journal Frontiers in Cell and Developmental Biology

Received: *20 October 2021*
Accepted: *17 February 2022*
Published: *24 March 2022*

Citation:
Liu T, Li H, Li Y, Wang L, Chen G, Pu G, Guo X, Cho WC, Fasihi Harandi M, Zheng Y and Luo X (2022) Integrative Analysis of RNA Expression and Regulatory Networks in Mice Liver Infected by Echinococcus multilocularis. Front. Cell Dev. Biol. 10:798551. doi: 10.3389/fcell.2022.798551

The larvae of *Echinococcus multilocularis* causes alveolar echinococcosis, which poses a great threat to the public health. However, the molecular mechanisms underlying the host and parasite interactions are still unclear. Exploring the transcriptomic maps of mRNA, miRNA and lncRNA expressed in the liver in response to *E. multilocularis* infection will help us to understand its pathogenesis. Using liver perfusion, different cell populations including the hepatic cells, hepatic stellate cells and Kupffer cells were isolated from mice interperitoneally inoculated with protoscoleces. Their transcriptional profiles including lncRNAs, miRNAs and mRNAs were done by RNA-seq. Among these cell populations, the most differentially-expressed (DE) mRNA, lncRNAs and miRNAs were annotated and may involve in the pathological processes, mainly including metabolic disorders, immune responses and liver fibrosis. Following the integrative analysis of 38 differentially-expressed DEmiRNAs and 8 DElncRNAs, the lncRNA-mRNA-miRNA networks were constructed, including F63-miR-223-3p-Fbxw7/ZFP36/map1b, F63-miR-27-5p-Tdrd6/Dip2c/Wdfy4 and IFNgAS1-IFN-γ. These results unveil the presence of several potential lncRNA-mRNA-miRNA axes during *E. multilocularis* infection, and further exploring of these axes may contribute to better understanding of the pathogenic mechanisms.

Keywords: *Echinococcus multilocularis*, hepatic cells, hepatic stellate cells, kupffer cells, regulatory network

INTRODUCTION

Alveolar echinococcosis (AE), a zoonosis with an increasing concern, is caused by a canine parasite *Echinococcus multilocularis* (Eckert and Deplazes, 2004). At which human beings are infected by intake of food or water contaminated with the eggs shed by definitive hosts, such as dogs and foxes (Conraths et al., 2017; Liu et al., 2018; Wang et al., 2018; Kotwa et al., 2019). Once infected, the eggs penetrate the small intestine wall, finally reach the liver and lung and then grow in an infiltrative pattern (Czermak et al., 2008; Mueller et al., 2020). The clinical manifestations of human AE are

diverse, including jaundice, weight loss, fever, anaemia, and abdominal pain (Kolářová et al., 2015; Massolo et al., 2019).

The main treatment strategies for AE are surgery and anti-echinococcal drugs, such as albendazole (ABZ) and mebendazole (MBZ) (Craig et al., 2007; Gottstein et al., 2015; Wang S. et al., 2021; Huang et al., 2021). However, both strategies have limitations. For surgical treatment, it is prone to recurrent due to diffuse and undetected parasite infiltration into host tissues (Huang et al., 2021). In terms of drug treatment, the poor intestinal absorption and some side effects are concerned (Gottstein et al., 2015; Craig et al., 2017). Some other treatment strategies such as traditional Chinese medicines and new formulation drug have limited treatment efficacy (Maggiore et al., 2015; Almalki et al., 2017; Pensel et al., 2017; Torabi et al., 2018). Therefore, it is urgent to study the genome-scale transcriptional background of the liver in response to the infection for discovering the potential molecular target for the effective therapeutics.

lncRNAs, with the length of more than 200 bp, have been confirmed as a momentous regulatory factor in many cellular processes, such as genomic imprinting, post transcriptional regulation, and cell differentiation (Kallen et al., 2013; Myant et al., 2013; Yang Q. et al., 2018). lncRNAs show a competing endogenous effect by acting as miRNA sponges, which is helpful to decipher the miRNA-lncRNA regulatory networks (Li et al., 2020; Zheng et al., 2020). Another non-coding RNAs, miRNAs, are members of endogenous small RNA with the length of about 18–24 nucleotides, involved in the regulation of mRNA expression. By binding to the 3′-untranslated region, miRNAs block the translation or induce the degradation of the target mRNA, thus modulating cell differentiation, growth, proliferation and apoptosis (Li et al., 2021; Mohammadi et al., 2021; Xiang et al., 2021). miRNAs have been reported as diagnostic markers and therapeutic targets for the control of diseases (Broermann et al., 2020; Tombolan et al., 2020). For instance, miR-155 was exploited as the potential target for treatment of the disease by *Toxoplasma gondii* (Xu et al., 2021). Another study found that the novel-miR-1 derived from *Cysticercus pisiformis* was released into host serum, which could be exploited for diagnosis of *C. pisiformis* infection (Chen et al., 2021).

Clinically, the intrahepatic lesions are the most common clinical trait of AE (Woolsey and Miller, 2021). The liver is comprised of a number of specialized cells, e,g, hepatocytes (HCs) as the hepatic parenchyma are the most abundant cell population, performing the fundamental functions in endocrine homeostasis and metabolism (Wang et al., 2015). Besides, there is a small proportion of nonparenchymal cells (NPCs), including hepatic stellate cells (HSCs), Kupffer cells (KCs), and hepatic sinusoidal endothelial cells (LSECs). Among these cells, HSCs reside in the perisinusoidal space (space of Disse) filled with thin permeable connective tissues, which have been recognized as the major source of type I and III collagens and fibronectin. Under normal condition, quiescent HSCs (qHSCs) are characterized by enrichment of vitamin A in cytoplasm, responsible for tissue homeostasis by involving in proliferation and differentiation signaling (Balmer and Blomhoff. 2002). Upon stimuli, they transfer into activated HSCs (aHSCs) that secret a-SMA and extracellular matrix (ECM) components (type I and III collagens and fibronectin). As a result, the persisting increase of ECM components will trigger liver fibrosis, possibly leading to liver cancer. However, once the stimuli disappear, the aHSCs gradually return back to the quiescent ones and the degree of fibrosis decreases (Kisseleva et al., 2012; Khomich et al., 2019). Another important component of NPCs, KCs, is the major immune cells that reside in the liver, responsible for clearing foreign materials under the normal conditions. Moreover, KCs protect liver from injury by releasing cytokines, reactive oxygen and others, playing a key role in the acute and chronic responses in the liver injury (Roberts et al., 2007).

Various liver cell populations perform distinct biological functions, and thus it is important to elucidate their role during *E. multilocularis* infection. In this study, we defined the transcriptomes of HCs, HSCs and KCs at two time points (2 and 3 months) post infection (p.i.) of *E. multilocularis*. Besides, the potential interaction networks among differentially expressed mRNAs, miRNAs and lncRNAs were identified. The current results provide the transcriptional expression of three liver cell populations in response to *E. multilocularis* infection and a clue for further investigation of a role of the networks in the pathogenesis.

MATERIALS AND METHODS

Parasites

The protoscolices used in this study were obtained from *Mongolian gerbil* infected with *E. multilocularis* as previously described (Spiliotis and Brehm, 2009). In brief, cysts were dissected from infected *Mongolian gerbil* under sterile conditions. After cutting the cysts into pieces, the protoscolices were collected by gravity and washed several times in cold PBS. The purity and activity of protoscolices were checked using optical microscopy and trypan blue exclusion, respectively.

Animal Infection

100 six-week old BALB/c mice were purchased from Laboratory Animal Center of Lanzhou Veterinary Research Institute and were randomly divided two groups: experimental (E) group (60 mice) and control (C) group (40 mice). In E group, 600 protoscolices were injected into the abdominal cavity. In C group, the same volume of phosphate buffer saline (PBS) was injected. In E group, whose cysts in the liver were considered as infected, otherwise not. In order to obtain enough cells at two timepoints 2 m p.i. and 3 m p.i., by the cause of a few HSCs and KCs in the liver, we mixed cells from six mice for RNA-seq and qRT-PCR, and three batches of samples were concluded in two groups. All mice were reared under standard feeding conditions, free access to food and water.

Isolation of HCs, HSCs and KCs

We collected the HCs, HSCs and KCs samples from mice 2 m p.i. and 3 m p.i. in E and C groups, accordingly named as HC-2M-E, HC-2M-C, HC-3M-E, HC-3M-C, HSC-2M-E, HSC-2M-C, HSC-

3M-E, HSC-3M-C, KC-2M-E, KC-2M-C, KC-3M-E and KC-3M-C. In each group, the cells of six mice were mixed together to obtain enough HSCs and KCs. The perfusion procedure for mouse liver was strictly followed as previously reported (Mederacke et al., 2015). In detail, 10 ml of 0.019% EGTA and 30 ml of 0.04% collagenase Ⅳ solution were sequentially perfused into every liver, followed by further liver digestion using 80 ml of 0.08% collagenase Ⅳ solution with 1% DNase. The digested liver tissues were filtered into a 50 ml tube through a 70 μm cell strainer. The mixture was centrifuged at 50 ×*g* for 4 min at 4°C, and the cell pellet was washed three times in the DMEM with 5% FBS to obtain HCs. The supernatant was sequentially centrifuged at 600 ×*g* and 500 ×*g* for 10 min at 4°C to obtain NPCs. The NPC-containing solution was mixed with 5 ml Gey's Balanced Salt Solution (GBSS), then the mixture was gently overlaid onto the Optiprep solutions at different concentrations, which contained 8 ml of 11.5% Optiprep in the upper layer and 4 ml of 20% Optiprep in the bottom, followed by centrifugation at 1,400 ×*g* for 17 min at 4°C without break. The cells in the upper layer (HSCs) and the lower layer (KCs and ECs) were transferred into two centrifuge tubes, respectively, and washed three times in GBSS. Then, KCs and ECs were cultured in RPMI 1640 medium with 10% fetal bovine serum (FBS). After 4 h, KCs were adhered completely and collected after 0.25% trypsin digestion, while ECs were not adhered and abandoned after PBS washed (Zheng et al., 2008). The HCs, HSCs and KCs were immediately stored at −80°C for later use.

RNA-Seq

Following the manufacturer's instructions, total RNA was extracted using TRIzol reagent. After evaluation of RNA concentration and integrity, these samples were used to construct the libraries for sequencing (BGI, Wuhan, China). For construction of the lncRNA + mRNA library, rRNA-depleted RNA was fragmented by adding first strand master mix (Invitrogen, United States), and the first-strand and second-strand cDNA was generated separately by using random primers reverse transcription. Then, the cDNA was subjected to end-repair and was 3′ adenylated, the adapters were ligated to the end of 3′ adenylated cDNA. After PCR amplification, the cDNA fragments (lncRNA + mRNA library) were enriched and purified with Ampure XP beads.

For small RNA library, the 18–30 nt bands were excised and recovered from total RNA by using 15% urea denaturing polyacrylamide gel electrophoresis (PAGE) gel. Subsequently, the 18–30 nt small RNAs were ligated to adenylated 3′ and 5′ adapters separately and transcripted into cDNA by SuperScript Reverse Transcriptase (Invitrogen, United States). After PCR amplification, the cDNA fragments was enriched and 110–130 nt fragments (small RNA library) were selected by agarose gel electrophoresis. Last, the BGISEQ-500 platform (BGI, Wuhan, China) was used to sequence. In order to get clean reads, the reads with low quality and adaptor contaminants were removed from the raw data using SOAPnuke software (v1.5.2; -l 15 -q 0.2 -n 0.05) and the Q20, Q30 and GC content were calculated to assess the quality of the clean reads.

Data Analysis

Using HISAT2 software (v2.0.4; http://www.ccb,jhu.edu/software/hisat/index.shtml), the clean reads were aligned against the *Mus musculus* genome (GCF_000001635.26_GRCm38.p6). Bowtie2 (v2.2.5; http://bowtiebio.sourceforge.net/%20Bowtie2%20/index.shtml) was used to align the clean reads to known and novel, coding and noncoding transcripts. Subsequently, the expression levels of mRNA and lncRNAs were calculated by using RESM (v1.2.12; http://github.com/deweylab/RSEM) with the FPKM standardized method. After analyzing the results of the relative expression of genes in this study, we found the genes was mainly enriched near 2 in fold change. Besides, we used multiple hypothesis test correction for the *p*-value of the difference test, and False Discover Rate (FDR) ≤ 0.001 was considered as statistically different. Based on these, the differentially expressed lncRNAs (DElncRNAs) and differentially expressed mRNA (DEmRNAs) with a fold change ≥2 and FDR ≤0.001 were screened out.

Functional Enrichment Analysis

We predicted the potential targets of DElncRNAs by analyzing the position between genes in the genome as previously reported (Ren et al., 2018). If the relative position between genes was less than 10 kb, we defined it as cis-regulation. Otherwise, we defined it as trans-regulation. Besides, for constructing the lncRNA-mRNA-miRNA networks, target prediction of miRNAs to the DEmRNAs and DElncRNAs was performed using RNAhybrid, miRanda and TargetScan databases.

Gene Ontology (GO) was used to describe the genetic attributes with terms under the biological process, cellular component, and molecular function categories. By comparing the DElncRNAs, DEmRNAs and the targets of DEmiRNAs with the genes of mouse, the significantly enriched GO terms were determined. Similarly, the significantly enriched pathway terms were obtained using the KEGG pathway database. The GO and pathway terms with Q value ≤0.05 was defined as a term which was significantly enriched.

qRT-PCR Assay

For evaluation of the purity of liver cell populations and the expression of DEmRNAs, DElncRNAs and DEmiRNAs, qRT-PCR was performed. The genes for the cell markers (Alb, F4/80, α-SMA, Col1α1, Col3α1 and GFAP), DElncRNAs and their nearby genes located within the 10 kb upstream and downstream in the genome, and the metabolism- and inflammation-related DEmRNAs were selected for validation. 1 μg of total RNA was reversely transcribed to cDNA using HiScript Ⅲ First-strand cDNA Synthesis Kit (Vazyme, Munich, Germany) as recommended by the manufacturer. qRT-PCR was performed using All-in-One^{TM} qPCR Mix (GeneCopoeia) with an ABI 7500 Thermal Cycler (ThermoFisher Scientific, United States) according to the standard method. Specific primers for the selected DElncRNAs and DEmRNAs were obtained from TSINGKE (Xi'an, China) (**Supplementary Table S1**), and specific primers for miRNAs were purchased from GeneCopoeia (United States). The relative expression level was normalized to GAPDH for DEmRNAs and DElncRNAs or to U6 for DEmiRNAs. The $2^{-\Delta\Delta Ct}$ algorithm was used to calculate the relative expression levels represented as relative fold-change (FC). All experiments were performed in triplicate.

TABLE 1 | The statistics of sequencing data.

Cell	Genes	Group	2 m p.i.						3 m p.i.					
			mRNA + lncRNA			miRNA			mRNA + lncRNA			miRNA		
			Total reads (M)	Clean reads (M)	Mapped percent (%)	Total reads (M)	Clean reads (M)	Mapped percent (%)	Total reads (M)	Clean reads (M)	Mapped percent (%)	Total reads (M)	Clean reads (M)	Mapped percent (%)
HC	33,065	Control	112.4	111.2	96.2	25.2	23.6	91.6	111.9	113.9	96.3	23.7	22.1	89.9
		Infected	112.4	111.7	95.9	25.2	24.1	93.4	111.9	113.9	96.3	25.2	23.6	88.2
HSC	37,637	Control	114.9	113.7	96.3	25.2	24.5	94.8	114.9	113.8	95.6	25.2	24.6	92.1
		Infected	112.4	111.8	96.0	25.2	24.5	92.6	114.9	113.8	96.0	25.2	24.6	94.4
KC	39,174	Control	112.4	111.7	94.9	25.2	24.6	95.7	114.9	113.8	95.0	25.2	24.6	94.5
		Infected	112.4	111.8	95.0	25.2	24.6	95.9	112.4	111.4	95.3	25.2	24.5	94.4

Statistical Analysis

The statistical analysis was conducted using Prism 6 (GraphPad) software. The comparison between E and C groups was analyzed using Student's *t*-test. The results were presented as mean ± standard deviation (SD). Significant differences were indicated as $^{*}p < 0.05$, $^{**}p < 0.01$ and $^{***}p < 0.001$.

RESULTS

Primary HC, HSC and KC Isolation and Characterization

The primary HCs, HSCs and KCs were isolated from liver of anesthetized mice by using 0.04% collagenase Ⅳ solution, with the largest number of HCs, followed by KCs and then HSCs. By comparing the relative expression levels of cell markers (HCs: Alb, HSCs: α-SMA, GFAP, Col1α1 and Col1α3; KCs: F4/80), the results showed that Alb was predominantly expressed in HCs, with the percentage of 69.44, F4/80 predominantly expressed in KC with 73.19, and α-SMA, GFAP, Col1α1 and Col1α3 predominantly expressed in HSC (**Supplementary Figure S1**) with 83.09, 87.70, 93.36 and 89.55, respectively, suggesting each type of cell was enrichment.

Sequencing Data

As shown in **Table 1**, after removal of the low quality reads, 112M–115M total reads were produced in mRNA + lncRNA libraries and 24–25M in miRNA libraries. In mRNA + lncRNA libraries, the mapped percent was ranged from 95 to 96 with the average mapped rate of 96% and a total of 43,183 genes were identified. In miRNA libraries, 88–96% clean reads were mapped with the average mapped rate of 93% and a total of 1,201 small RNAs were predicted. Additionally, a total of 33,065 genes were detected in HCs, 37,637 in HSCs and 39,174 in KCs.

LncRNA, mRNA and miRNA Profiles in HCs, HSCs and KCs

As shown in **Figure 1**, in 2 m p.i. HC samples, 274 upregulated and 219 downregulated mRNA were identified. Simultaneously, 1,111 upregulated and 119 downregulated mRNA were identified in 3 m p.i. samples. Additionally, 65 upregulated and 97 downregulated lncRNAs, and 12 upregulated and 23 downregulated miRNAs were found in 2 m p.i. samples, while 136 upregulated and 82 downregulated lncRNAs, and 93 upregulated and 6 downregulated miRNAs in 3 m p.i. samples (**Figure 1A**, **Supplementary Table S2**). Furthermore, DEmRNAs, DElncRNAs and DEmiRNAs of two time point were identified, with the commonly shared 151 DEmRNAs (9.6%), 28 DElncRNAs (8%) and 14 DEmiRNAs (11.7%) (**Figure 1B**).

In 2 m p.i. HSC samples, total 293 upregulated and 335 downregulated mRNAs, 98 upregulated and 127 downregulated lncRNAs, and 11 upregulated and 20 downregulated miRNAs were found, while total 241 upregulated and 142 downregulated mRNAs, 66 upregulated and 63 downregulated lncRNAs, and 56 upregulated and 21 downregulated miRNAs were found in 3 m p.i. HSC samples (**Supplementary Figure S2A**, **Supplementary Table S2**). The 80 (8.6%), 22 (6.6%) and 18 (20%) common differentially-expressed genes (DEGs) were identified as DEmRNAs, DElncRNAs and DEmiRNAs, respectively (**Supplementary Figure S2B**).

In 2 m p.i. KC samples, total 102 upregulated and 1,291 downregulated mRNAs, 85 upregulated and 177 downregulated lncRNAs, and 5 upregulated and 38 downregulated miRNAs were found, while total 79 upregulated and 205 downregulated mRNAs, 69 upregulated and 32 downregulated lncRNAs, and 9 upregulated and 12 downregulated miRNAs were found in 3 m p.i. KC samples (**Supplementary Figure S3A**, **Supplementary Table S2**). The 111 (7.1%), 18 (5.2%) and 3 (4.9%) common DEGs were identified as DEmRNAs, DElncRNAs and DEmiRNAs, respectively (**Supplementary Figure S3B**).

GO and KEGG Analyses of DElncRNAs and DEmiRNAs

Of the 195 DEmiRNAs identified, the most was functionally annotated, such as miR-7a-5p, miR-223-3p, miR-22-3p, miR-146a-5p, miR-378a-3p, miR-467a-5p, miR-532-5p, miR-652-3p, miR-871-3p and miR-96-5p (Coffey et al., 2019; Ota et al., 2019; Chu et al., 2020; Du et al., 2020; Liang et al., 2020; Yan et al., 2020; Wang X. et al., 2021; Gajeton et al., 2021; Han et al., 2021; Kinoshita et al., 2021). Unlike the DEmiRNAs, most of the

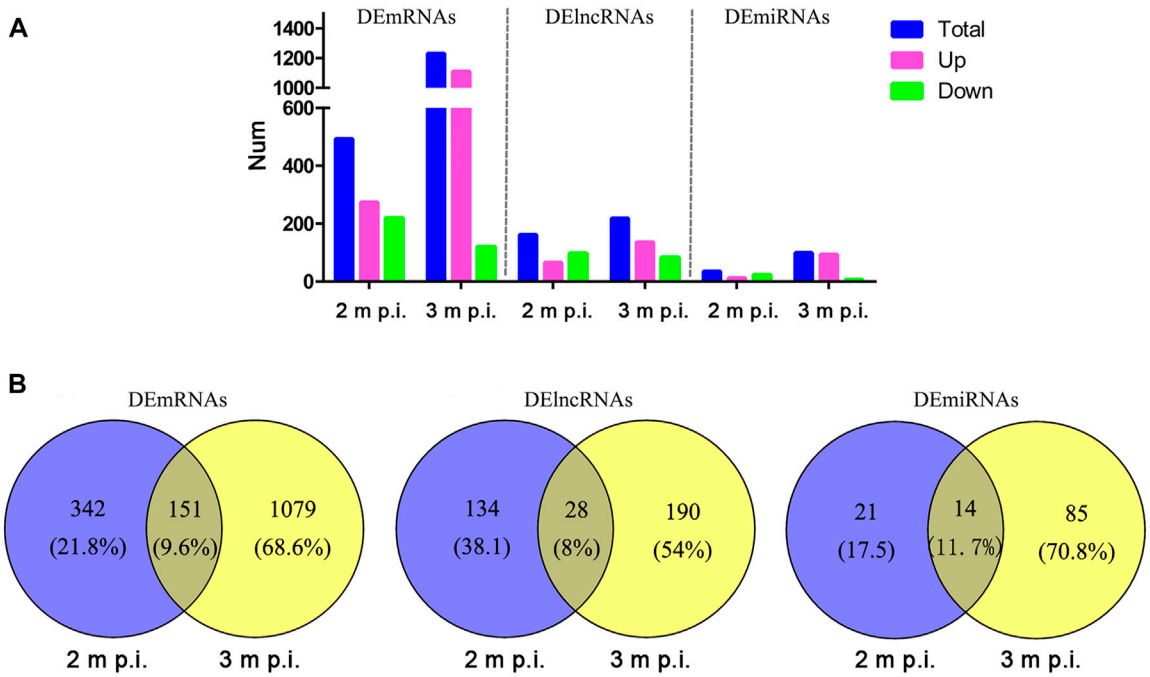

FIGURE 1 | Comparisons of DElncRNAs, DEmRNAs and DEmiRNAs differentially expressed in HCs at 2 m p.i. and 3 m p.i **(A)** The number of DElncRNAs, DEmRNAs and DEmiRNAs at two infection stages. Sky blue represents the total number of DEgemes, red and violet represents upregulated and downregulated genes, respectively. **(B)** Veen diagrams showing the common and unique DElncRNAs, DEmRNAs and DEmiRNAs at two infection stages.

DElncRNAs were not annotated with unknown functions. Based on this, this study focused on the biological function of DElncRNAs, with the most enriched biological processes of DEmRNAs and DElncRNAs in HCs were immune system process, innate immune response, inflammatory response and cell adhesion (**Figures 2A,B**, **Supplementary Table S4**), and the enriched pathways included pancreatic secretion, protein digestion and absorption, fatty acid biosynthesis, ECM-receptor interaction and PI3K-Akt signaling pathway (**Figures 2C, D**, **Supplementary Table S3**).

In HSCs, the enriched biological processes included immune system process, adaptive immune response, negative regulation of lipid biosynthetic and receptor-mediated endocytosis (**Supplementary Figures S4A, B**, **Supplementary Table S5**), and the enriched pathways included T cell receptor signaling pathway, Th1 and Th2 cell differentiation, IL-17 signaling pathway, Toll-like receptor signaling pathway and NF-κB signaling pathway (**Supplementary Figures S4C, D**, **Supplementary Table S4**), indicating that HSCs may play an immune regulatory role after *E. multilocularis* infection.

While in KCs, the enriched biological processes included immune system process, acute-phase response, cellular response to IFN-β and exogenous drug catabolic process (**Supplementary Figures S5 A, B**, **Supplementary Table S6**), and the enriched pathways included complement and coagulation cascades, TNF signaling pathway, cytokine-cytokine receptor interaction, IL-17 signaling pathway and PPAR signaling pathway (**Supplementary Figures S5C,D**, **Supplementary Table S5**).

LncRNA-mRNA-miRNA Networks

It has been demonstrated that lncRNAs function as miRNA "sponges", which competitively suppress the activity of miRNAs (Alkan and Akgül, 2022). Since lncRNAs interact with miRNAs through miRNA Response Elements (MREs), combined using the free energy and score of RNAhybrid, miRanda and TargetScan databases, the potential MREs were predicted and 38 DEmiRNAs that putatively targeted 8 DElncRNAs were then identified (**Supplementary Table S6**). Based on these, partial lncRNA-mRNA-miRNA networks were obtained (**Figure 3**). In this network, some DElncRNAs were predicted to bind multiple DEmiRNAs, and DEmiRNAs were predicted to bind multiple DEmRNAs, such as F630028O10Rik (abbreviated as F63)-miR-223-3p-Fbxw7/ZFP36/map1b and F63-miR-27-5p-Tdrd6/Dip2c/Wdfy4. Considering these RNAs are differentially expressed in various cells, some important roles may play by these lncRNAs and miRNAs through these regulatory pathways, which provide some clues for further studies of DElncRNAs and DEmiRNAs.

qRT-PCR Validation

To verify the lncRNA-mRNA-miRNA networks and the data of RNA-seq, qRT-PCR was used to examine the expression of 9 DElncRNAs (IFNgAS1, GM39584, F63, GM32721, GM11747, GM41107, BGIG10090-47695, BGIG10090-39612 and BGIG10090-34058) (**Figure 4**), 12 DEmRNAs (IFN-γ, IL-4, IL-12, IL-10, a-SMA, COL1a1, TGF-β1, ZFP36, VDR, EGFR, Fbxw7 and map1b) (**Figure 5**) and 5 DEmiRNAs (miR-143-3p,

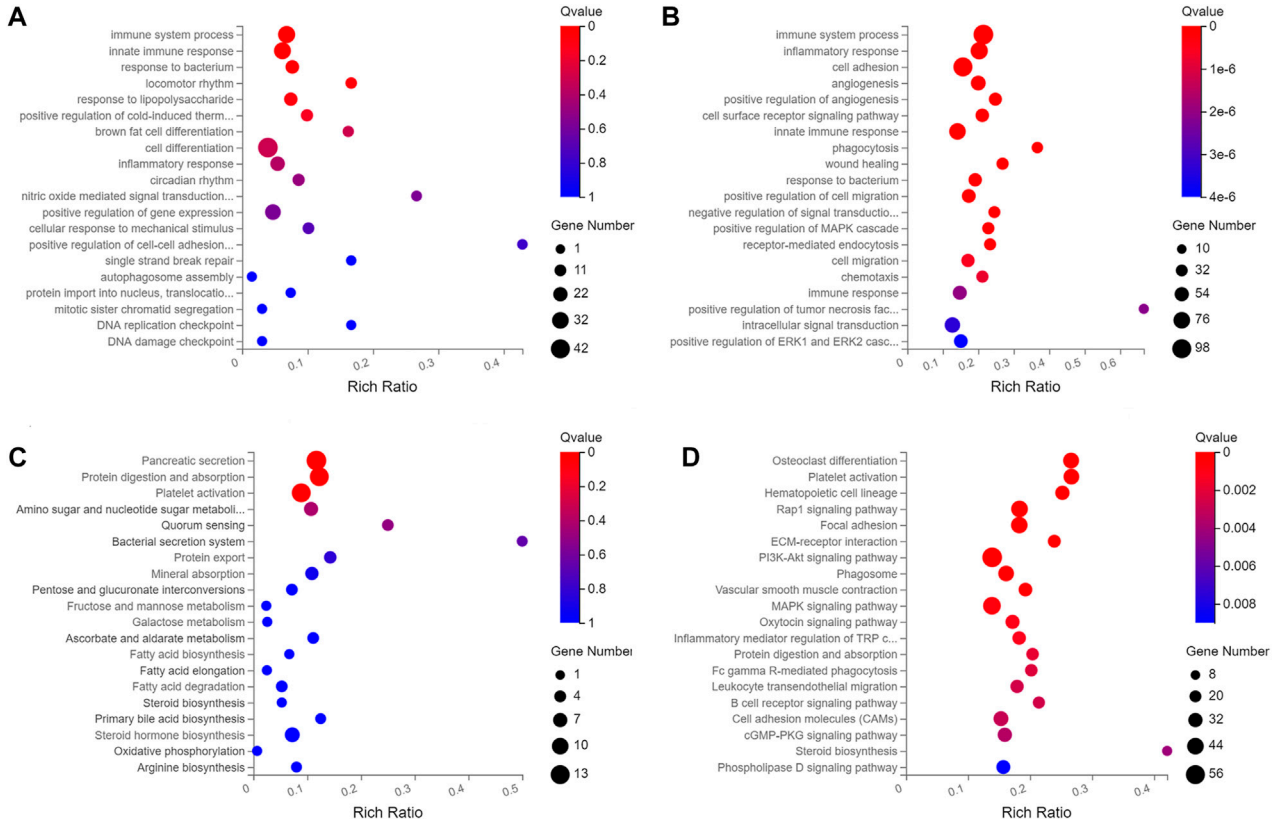

FIGURE 2 | The top twenty enriched biological process and pathways of DElncRNAs and DEmRNAs in HCs at 2 m p.i. and 3 m p.i.. **(A)** Predicted biological process terms of DElncRNAs and DEmRNAs in HCs at 2 m p.i.. **(B)** Predicted biological process terms of DElncRNAs and DEmRNAs in HCs at 3 m p.i.. **(C)** Predicted pathways of DElncRNAs and DEmRNAs in HCs at 2 m p.i.. **(D)** Predicted pathways of DElncRNAs and DEmRNAs in HCs at 3 m p.i..

miR-451a, miR-146b-5p, miR-222-3p and miR-342-3p) (**Figure 6**). The overall expression patterns of these DElncRNAs, DEmRNAs and DEmiRNAs between qRT-PCR and RNA-seq was consistent, suggesting the reliability of RNA-seq. It was worth mentioning that the expression of inflammation related genes (IFN-γ and IL-4) were remarkably upregulated in HSCs at 2 m p.i. and 3 m p.i. However, in KCs, the IFN-γ was remarkably downregulated and IL-4 still upregulated at 2 m p.i. and 3 m p.i. Additionally, the fibrosis related factors including α-SMA and Col1α1 showed a sharp increase in 3 m p.i., suggesting the persistence of inflammatory responses in the infection and the occurrence of fibrosis. Additionally, some lncRNA-mRNA pairs in the network were identified with a similar expression trend, such as GM39584-Egfr, F63-Fbxw7/map1b and IFNgAS1-IFN-γ, suggesting the potential regulatory role of these DElncRNAs.

In addition, we identified some potential markers for HCs, HSCs and KCs (**Figure 7**). For instance, the expression of BGIG10090-47695, miR-146b-5p, miR-222-3p and EGFR was remarkably abundant in HCs comparing HSCs and KCs, while F63, GM41107 and GM32721 were remarkably abundant in HSCs, and BGIG10090-39612, map1b and VDR in KCs.

DISCUSSION

E. multilocularis is one of zoonotic tapeworms with public health concern. Elucidating the pathogenic mechanisms of the parasite in the liver will help us to take better prevention and treatment measures. It is known that HCs, HSCs, KCs together with others constitute the liver and play divergent roles. Exploring the specific biological processes of these cells after *E. multilocularis* infection will systematically clarify the pathogenic mechanisms. Therefore, the current study focuses on the transcriptomic maps of mRNA, miRNAs and lncRNAs expressed in HCs, HSCs and KCs in the liver after infection, which aims to provide clues for further investigation of the pathogenic mechanisms to better control AE.

The current results showed that, after the infection, the expression of a number of mRNAs, lncRNAs and miRNAs in HCs, HSCs and KCs was changed. One of our interests is the genes related to metabolism in HCs. For example, the F-box family member F-box- and WD repeat domain-containing 7 (Fbxw7) was up- and downregulated in 2 m p.i. and 3 m p.i., respectively. A previous study showed massive lipid deposition and increasing proliferation of hepatocytes in Fbxw7-deficient mice (Onoyama et al., 2011). Therefore, the changes in the

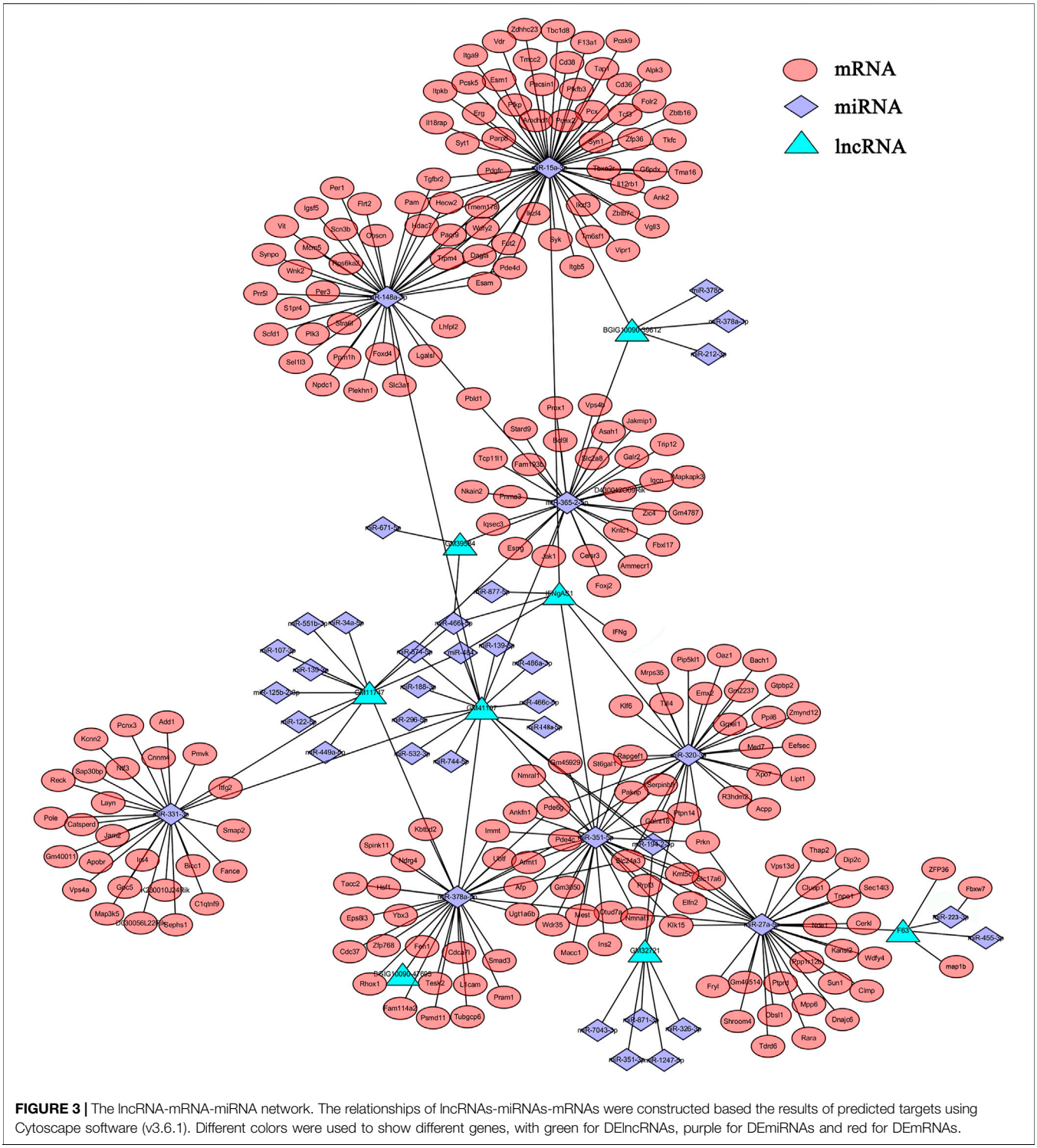

FIGURE 3 | The lncRNA-mRNA-miRNA network. The relationships of lncRNAs-miRNAs-mRNAs were constructed based the results of predicted targets using Cytoscape software (v3.6.1). Different colors were used to show different genes, with green for DElncRNAs, purple for DEmiRNAs and red for DEmRNAs.

expression of Fbxw7 may reflect the host's response to eliminate the parasite in 2 m p.i. and the parasite's strategy for persistent infection in 3 m p.i. Consistent with the lncRNA-mRNA-miRNA networks constructed, the qRT-PCR results suggested that Fbxw7 might be the potential target gene of miR-223-3p, which was regulated by F63 (lncRNA). It was reported that in *Cryptosporidium parvum* infection, cirs-7 was upregulated and promoted *C. parvum* propagation by

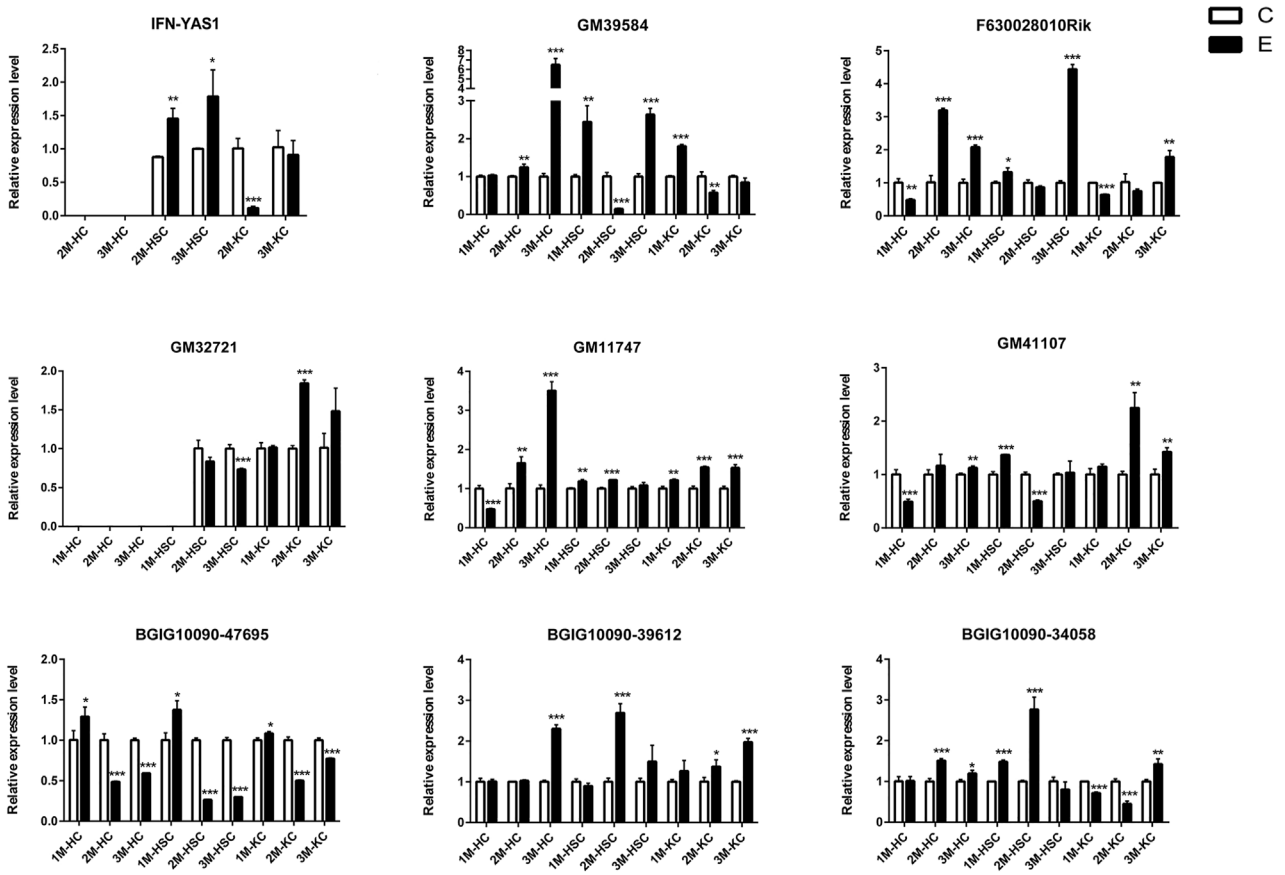

FIGURE 4 | The relative expression levels of 9 lncRNAs in 2M-HC, 3M-HC, 2M-HSC, 3M-HSC, 2M-KC and 3M-KC were determined by qRT-PCR. The number of biological replicates for each experiment was 3 and the relative expression levels were normalized to the expression levels of GAPDH. Data are presented as means with SD. *p*-values were analyzed by Student's *t*-test. ***$p < 0.001$, **$p < 0.01$ and *$p < 0.05$.

regulating the miR-1270-RelA axis, which provided a control strategy against *C. parvum* infection (Yin et al., 2021). Therefore, elucidating the regulatory mechanism of F63-miR-223-3p-Fbxw7 may provide a potential target for the development of anti-*E. multilocularis* drugs. Another gene enriched in HCs, epidermal growth factor receptor (EGFR), was found to be highly expressed and was predicted to participate in the PI3K/AKT signaling pathway in 3 m p.i., suggesting an essential role in host defense against the infection. It is worth mentioning that EGFR was located upstream within 10 kb of GM39584 (lncRNA). Interestingly, their expression trend was consistent, suggesting that GM39584 play a *cis*-regulation role. It is worth exploring whether and how the EGFR-GM39584 axis plays a role during *E. multilocularis* infection.

For HSCs, we focused on the expression patterns of fibrosis-related genes, such as α-SMA, Col1α1 and Col1α3. As expected, *E. multilocularis* infection induced these genes to be upregulated, suggesting the tendency of liver fibrosis. Besides, Col1α1, one of the target genes of F63, was most enriched in HSCs. F63 acts as a competing endogenous RNA (ceRNA) for the miR-1231-5p/Col1α1 axis, involved in regulating post-spinal cord injury pyroptosis by activating the PI3K/AKT pathway (Xu et al., 2020). It is therefore hypothesized that F63 regulate the expression of Col1α1 indirectly and be involved in the apoptosis of hepatocytes. By analyzing the DEgenes of HSCs at 2 m p.i. and 3 m p.i., we found the inflammation-related pathways were enriched significantly, including cytokine-cytokine receptor interaction, chemokine signaling pathway, IL-17 signaling pathway, NF-kappa B signaling pathway, T cell receptor signaling pathway and Th1, Th2 and Th17 cell differentiation. Consistently, IFN-γ, IL-4 and IL-12 were remarkable upregulated in HSCs at 1 m p.i., 2 m p.i. and 3m p.i, suggesting that HSCs may be involved in immune regulation together with KCs. However, the level of IFN-γ in HSCs was higher than that of KCs and its expression trend in both cells was just opposite during the course of infection. Previous studies identified IFNgAS1 involved in IFN-γ-mediated host defense as an important regulator of IFN-γ expression and AW112010 promoted pro-inflammatory pathways by suppressing IL10 expression, which reduced

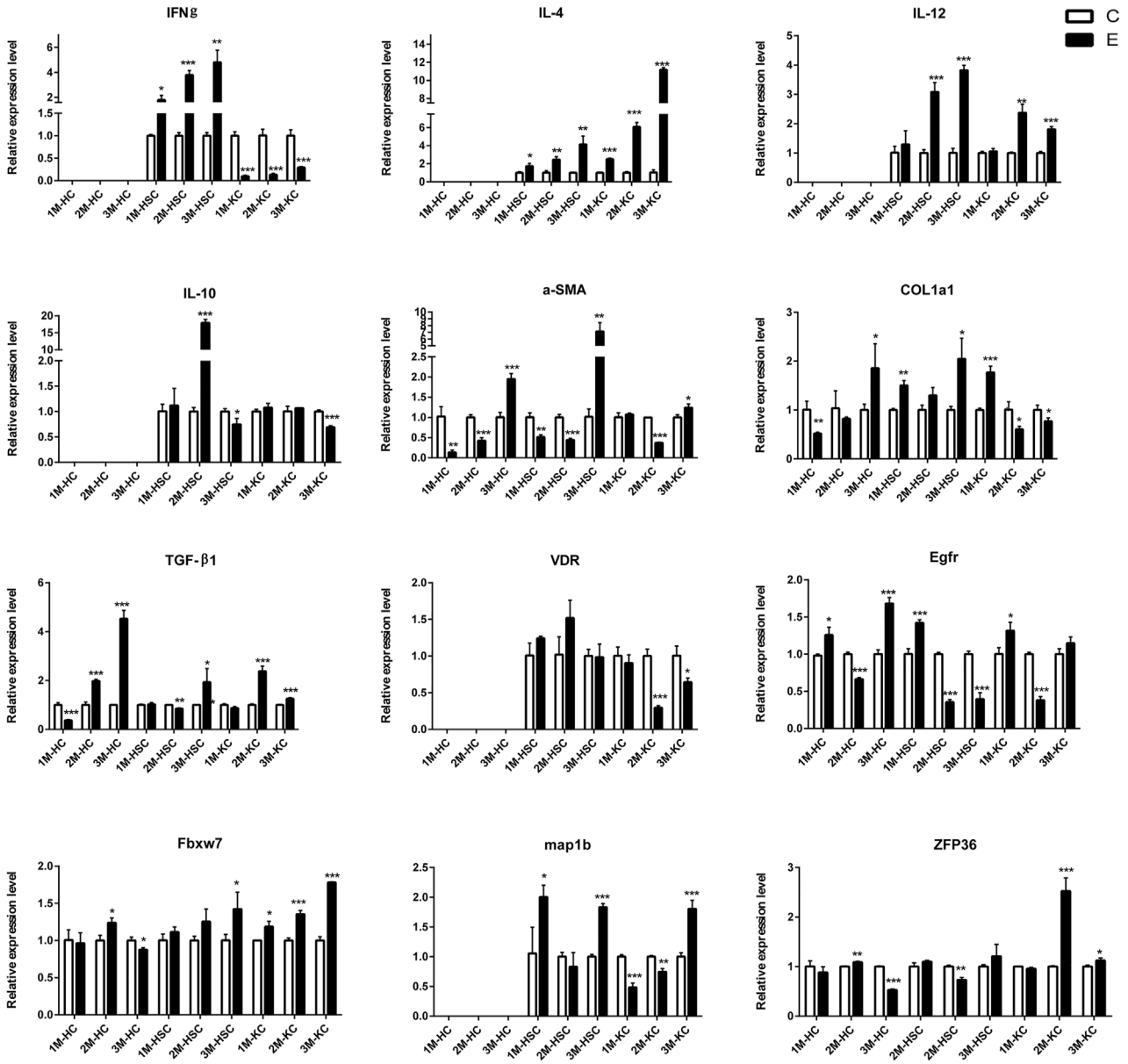

FIGURE 5 | The relative expression levels of 12 mRNAs in 2M-HC, 3M-HC, 2M-HSC, 3M-HSC, 2M-KC and 3M-KC were determined by qRT-PCR. The number of biological replicates for each experiment was 3 and the relative expression levels were normalized to the expression levels of GAPDH. Data are presented as means with SD. *p*-values were analyzed by Student's *t*-test. ***$p < 0.001$, **$p < 0.01$ and *$p < 0.05$.

the number of IFN-γ expression after knocked the expression of AW112010 (Petermann et al., 2019; Peng et al., 2020; Yang et al., 2020). In this work, the expression of IFN-γ in HSCs and KCs was positively correlated with AW112010 and IFNgAS1. Considering the similar expression pattern between IFNgAS1, AW112010 and IFN-γ, we guess that the similar role be played in HSCs after *E. multilocularis* infection. Therefore, whether the expression of IFN-γ is regulated by both AW112010 and IFNgAS1 is worthy of further exploration. Besides, it was reported that miR-155 positively regulates IFN-γ expression via the Tim-3 pathway in NK cells, and miR-29b/142-5p also induces IFN-γ upregulation by targeting DNMTs (Cheng et al., 2015; Yang Y. et al., 2018). In our work, we found that both miR-155 and miR-29b were downregulated expressed in HSCs at 3 m p.i., which provides a clue for investigation of the mechanism of IFN-γ regulation.

It is known that the liver resident macrophages, KCs, are the first line of defense against inflammation/infections in the liver. It has been shown that the activation of vitamin D receptor (VDR), expressed on KCs, decreases hepatic

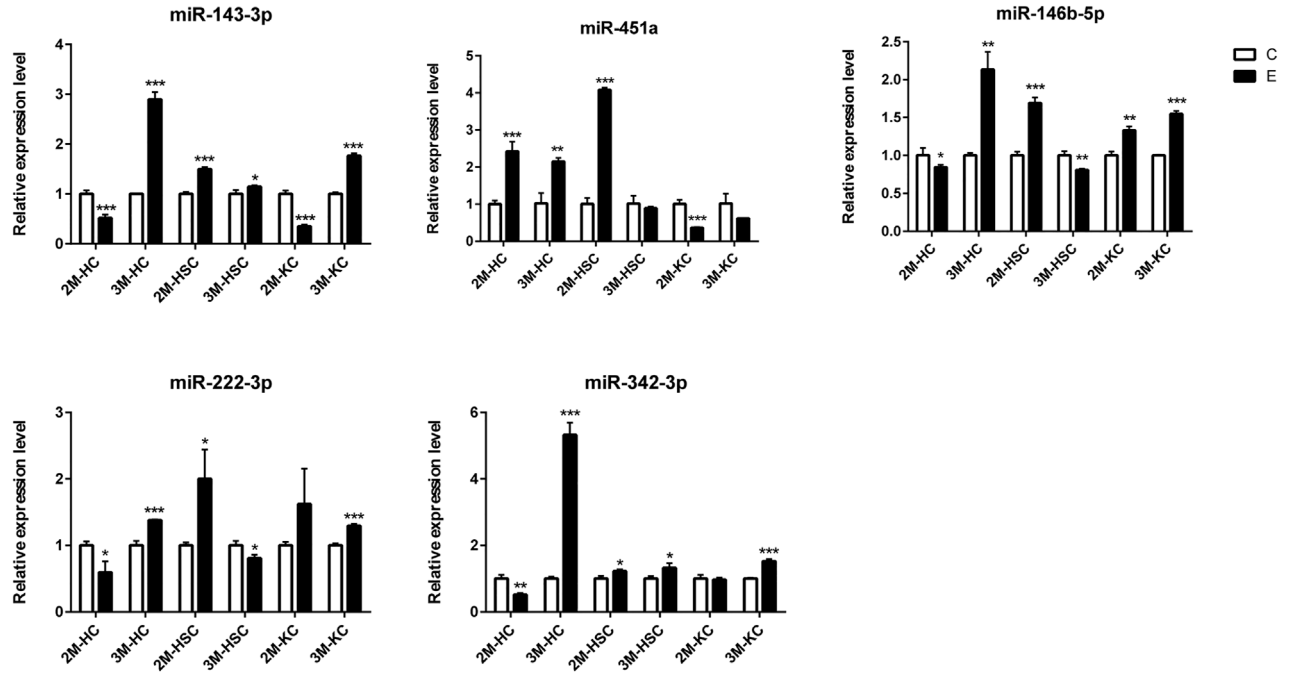

FIGURE 6 | The relative expression levels of 5 miRNAs in 2M-HC, 3M-HC, 2M-HSC, 3M-HSC, 2M-KC and 3M-KC were determined by qRT-PCR. The number of biological replicates for each experiment was 3 and the relative expression levels were normalized to the expression levels of U6. Data are presented as means with SD. *p*-values were analyzed by Student's *t*-test. ***$p < 0.001$, **$p < 0.01$ and *$p < 0.05$.

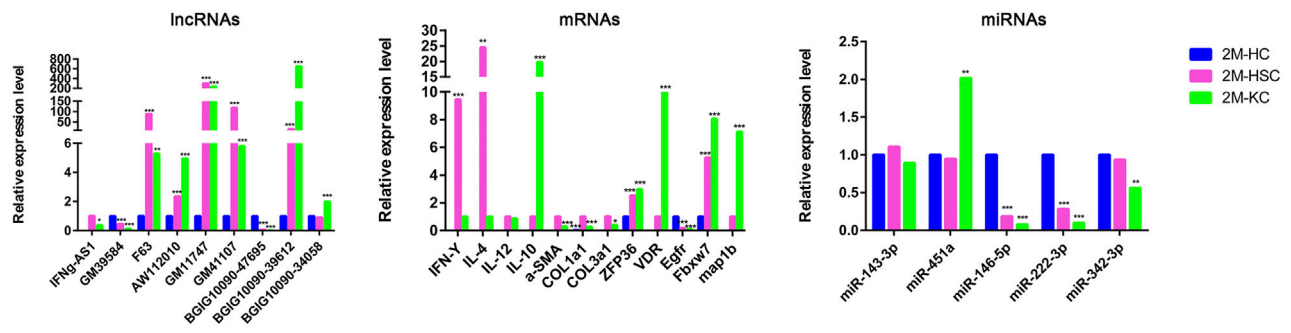

FIGURE 7 | The relative expression level of DElncRNAs, DEmRNAs, and DEmiRNAs in different cells at 2 m p.i.. Sky blue represents the expression of genes in HCs, red and purple represents HSCs and KCs, respectively.

inflammation in diet-induced model of NASH (Dong et al., 2020). In this study, the expression of VDR was downregulated continuously, suggesting that KCs may be active against *E. multilocularis* infection. Previous studies identified that miR-125b and miR-351-5p involved in the pathological process by targeting VDR (Mohri et al., 2009; He et al., 2018). It is possible that miR-125b and miR-351-5p may play a similar regulatory role in KCs. Moreover, the expression of IFN-γ was decreased, while IL-4 and IL-10 were increased in KCs, implying that *E. multilocularis* infection cause a Th2 immune response rather than Th1 immune response. Additionally, the KEGG pathway analysis revealed that the DEgenes were significantly enriched in the IL-17 signaling pathway, TNF signaling pathway and cytokine-cytokine receptor interaction. We found some metabolism-related pathways were also enriched, such as ascorbate and aldarate metabolism, steroid hormone biosynthesis, glycine, serine and threonine metabolism, tryptophan metabolism, biosynthesis of secondary metabolites, arginine biosynthesis and fatty acid biosynthesis, indicating that KCs also play a role in metabolism regulation during *E. multilocularis* infection.

In summary, the present study revealed the transcriptomic maps of mRNA, miRNAs and lncRNAs expressed in HCs,

HSCs and KCs during *E. multilocularis* infection. Additionally, by integrate analyzing the RNA-seq data, we found some potential regulatory axis, such as F63-miR-223-3p-Fbxw7, GM39584-EGFR, F63-miR-1231-5p-Col1α1, IFNgAS1/AW112010-IFN-γ, and miR-125b/miR-351-5p-VDR. The future studies need to insight into clarify these regulatory axis and provide potential treatment targets for AEs.

DATA AVAILABILITY STATEMENT

The original contributions presented in the study are publicly available. This data can be found here: PRJNA732233 and PRJNA770143.

ETHICS STATEMENT

The animal study was reviewed and approved by Animal Ethics Committee of Lanzhou Veterinary Research Institute, Chinese Academy of Agricultural Sciences.

AUTHOR CONTRIBUTIONS

TL performed the animal experiments and analyzed the data. TL and YZ performed RNA-seq analysis and analyzed the data. TL wrote portions of the manuscript draft. HL, YL, LW, GC, GP, and XG participated in some experiments and data analysis. TL, YZ, and XL designed the experiments, analyzed the data, and revised the manuscript. WC, MH, YZ, and XL oversaw the overall execution of the project and gave final approval of the version. All authors contributed to the article and approved the submitted version.

FUNDING

This research was funded by the National Natural Science Foundation of China (No. 32072889).

SUPPLEMENTARY MATERIAL

The Supplementary Material for this article can be found online at: https://www.frontiersin.org/articles/10.3389/fcell.2022.798551/full#supplementary-material

Supplementary Figure 1 | The expression of cell markers in HCs, HSCs and KCs.

Supplementary Figure 2 | Comparisons of DElncRNAs, DEmRNAs and DEmiRNAs differentially expressed in HSCs at 2 m p.i. and 3 m p.i.. **(A)** The number of DElncRNAs, DEmRNAs and DEmiRNAs at two infection stages. Sky blue represents the total number of DEgemes, red and violet represents upregulated and downregulated genes, respectively. **(B)** Veen diagrams showing the common and unique DElncRNAs, DEmRNAs and DEmiRNAs at two infection stages.

Supplementary Figure 3 | Comparisons of DElncRNAs, DEmRNAs and DEmiRNAs differentially expressed in KCs at 2 m p.i. and 3 m p.i.. **(A)** The number of DElncRNAs, DEmRNAs and DEmiRNAs at two infection stages. Sky blue represents the total number of DEgemes, red and purple represents upregulated and downregulated genes, respectively. **(B)** Veen diagrams showing the common and unique DElncRNAs, DEmRNAs and DEmiRNAs at two infection stages.

Supplementary Figure 4 | The top twenty enriched biological process and pathways of DElncRNAs and DEmRNAs in HSCs at 2 m p.i. and 3 m p.i.. **(A)** Predicted biological process terms of DElncRNAs and DEmRNAs in HSCs at 2 m p.i.. **(B)** Predicted biological process terms of DElncRNAs and DEmRNAs in HSCs at 3 m p.i.. **(C)** Predicted pathways of DElncRNAs and DEmRNAs in HSCs at 2 m p.i.. **(D)** Predicted pathways of DElncRNAs and DEmRNAs in HSCs at 3 m p.i..

Supplementary Figure 5 | The top twenty enriched biological process and pathways of DElncRNAs and DEmRNAs in KCs at 2 m p.i. and 3 m p.i.. **(A)** Predicted biological process terms of DElncRNAs and DEmRNAs in KCs at 2 m p.i.. **(B)** Predicted biological process terms of DElncRNAs and DEmRNAs in KCs at 3 m p.i.. **(C)** Predicted pathways of DElncRNAs and DEmRNAs in KCs at 2 m p.i.. **(D)** Predicted pathways of DElncRNAs and DEmRNAs in KCs at 3 m p.i..

REFERENCES

Alkan, A. H., and Akgül, B. (2022). Endogenous miRNA Sponges. *Methods Mol. Biol.* 2257, 91–104. doi:10.1007/978-1-0716-1170-8_5

Almalki, E., Al-Shaebi, E. M., Al-Quarishy, S., El-Matbouli, M., and Abdel-Baki, A.-A. S. (2017). *In Vitro* effectiveness of Curcuma Longa and Zingiber Officinale Extracts on Echinococcus Protoscoleces. *Saudi J. Biol. Sci.* 24, 90–94. doi:10.1016/j.sjbs.2016.05.007

Balmer, J. E., and Blomhoff, R. (2002). Gene Expression Regulation by Retinoic Acid. *J. Lipid Res.* 43, 1773–1808. doi:10.1194/jlr.r100015-jlr200

Broermann, A., Schmid, R., Gabrielyan, O., Sakowski, M., Eisele, C., Keller, S., et al. (2020). Exosomal miRNAs as Potential Biomarkers to Monitor Phosphodiesterase 5 Inhibitor Induced Anti-fibrotic Effects on CCl4 Treated Rats. *Ijms* 22, 382. doi:10.3390/ijms22010382

Chen, G., Wang, L., Liu, T., Li, Y., Zhang, S., Li, H., et al. (2021). Identification and Expression Profiling of Circulating MicroRNAs in Serum of *Cysticercus Pisiformis*-Infected Rabbits. *Genes* 12, 1591. doi:10.3390/genes12101591

Cheng, Y. Q., Ren, J. P., Zhao, J., Wang, J. M., Zhou, Y., Li, G. Y., et al. (2015). MicroRNA-155 Regulates Interferon-Γproduction in Natural Killer Cells via Tim-3 Signalling in Chronic Hepatitis C Virus Infection. *Immunology* 145, 485–497. doi:10.1111/imm.12463

Chu, X., Zheng, W., Wang, J., Zhang, J., Pan, Y., and Shao, C. (2020). CDK6 Inhibition Targeted by miR-378a-3p Protects against Intestinal Injury Induced by Ionizing Radiation. *Biochem. Biophysical Res. Commun.* 531, 328–334. doi:10.1016/j.bbrc.2020.07.093

Coffey, A. R., Kanke, M., Smallwood, T. L., Albright, J., Pitman, W., Gharaibeh, R. Z., et al. (2019). microRNA-146a-5p Association with the Cardiometabolic Disease Risk Factor TMAO. *Physiol. Genomics* 51, 59–71. doi:10.1152/physiolgenomics.00079.2018

Conraths, F. J., Probst, C., Possenti, A., Boufana, B., Saulle, R., LaTorre, G., et al. (2017). Potential Risk Factors Associated with Human Alveolar Echinococcosis: Systematic Review and Meta-Analysis. *Plos Negl. Trop. Dis.* 11, e0005801. doi:10.1371/journal.pntd.0005801

Craig, P. S., Hegglin, D., Lightowlers, M. W., Torgerson, P. R., and Wang, Q. (2017). Echinococcosis. *Adv. Parasitol.* 96, 55–158. doi:10.1016/bs.apar.2016.09.002

Craig, P. S., McManus, D. P., Lightowlers, M. W., Chabalgoity, J. A., Garcia, H. H., Gavidia, C. M., et al. (2007). Prevention and Control of Cystic Echinococcosis. *Lancet Infect. Dis.* 7, 385–394. doi:10.1016/S1473-3099(07)70134-2

Czermak, B. V., Akhan, O., Hiemetzberger, R., Zelger, B., Vogel, W., Jaschke, W., et al. (2008). Echinococcosis of the Liver. *Abdom. Imaging* 33, 133–143. doi:10.1007/s00261-007-9331-0

Dong, B., Zhou, Y., Wang, W., Scott, J., Kim, K., Sun, Z., et al. (2020). Vitamin D Receptor Activation in Liver Macrophages Ameliorates Hepatic Inflammation, Steatosis, and Insulin Resistance in Mice. *Hepatology* 71, 1559–1574. doi:10.1002/hep.30937

Du, Y., Yang, Y. T., Tang, G., Jia, J. S., Zhu, N., and Yuan, W. J. (2020). Butyrate Alleviates Diabetic Kidney Disease by Mediating the miR-7a-5p/P311/TGF-β1 Pathway. *FASEB j.* 34, 10462–10475. doi:10.1096/fj.202000431R

Eckert, J., and Deplazes, P. (2004). Biological, Epidemiological, and Clinical Aspects of Echinococcosis, a Zoonosis of Increasing Concern. *Clin. Microbiol. Rev.* 17, 107–135. doi:10.1128/CMR.17.1.107-135.2004

Gajeton, J., Krukovets, I., Yendamuri, R., Verbovetskiy, D., Vasanj,i, A., Sul, L., et al. (2021). miR-467 Regulates Inflammation and Blood Insulin and Glucose. *J. Cell. Mol. Medi* 25, 2549–2562. doi:10.1111/jcmm.16224

Gottstein, B., Stojkovic, M., Vuitton, D. A., Millon, L., Marcinkute, A., and Deplazes, P. (2015). Threat of Alveolar Echinococcosis to Public Health - a challenge for Europe. *Trends Parasitol.* 31, 407–412. doi:10.1016/j.pt.2015.06.001

Han, Y., Zhang, J., Huang, S., Cheng, N., Zhang, C., Li, Y., et al. (2021). MicroRNA-223-3p Inhibits Vascular Calcification and the Osteogenic Switch of Vascular Smooth Muscle Cells. *J. Biol. Chem.* 296, 100483. doi:10.1016/j.jbc.2021.100483

He, X., Sun, Y., Lei, N., Fan, X., Zhang, C., Wang, Y., et al. (2018). MicroRNA-351 Promotes Schistosomiasis-Induced Hepatic Fibrosis by Targeting the Vitamin D Receptor. *Proc. Natl. Acad. Sci. USA* 115, 180–185. doi:10.1073/pnas.1715965115

Huang, G. Q., Yexie, Z. H., Guo, Y. M., and Zhao, S. Y. (2021). Treatment of End-Stage Hepatic Alveolar Echinococcosis in Qinghai: Current Status and Future Perspectives. *Chin. J. Clinicians (Electronic Edition)* 15, 209–212.

Kallen, A. N., Zhou, X.-B., Xu, J., Qiao, C., Ma, J., Yan, L., et al. (2013). The Imprinted H19 lncRNA Antagonizes Let-7 microRNAs. *Mol. Cell* 52, 101–112. doi:10.1016/j.molcel.2013.08.027

Khomich, O., Ivanov, A. V., and Bartosch, B. (2019). Metabolic Hallmarks of Hepatic Stellate Cells in Liver Fibrosis. *Cells* 9, 24. doi:10.3390/cells9010024

Kinoshita, C., Kikuchi-Utsumi, K., Aoyama, K., Suzuki, R., Okamoto, Y., Matsumura, N., et al. (2021). Inhibition of miR-96-5p in the Mouse Brain Increases Glutathione Levels by Altering NOVA1 Expression. *Commun. Biol.* 4, 182. doi:10.1038/s42003-021-01706-0

Kisseleva, T., Cong, M., Paik, Y., Scholten, D., Jiang, C., Benner, C., et al. (2012). Myofibroblasts Revert to an Inactive Phenotype during Regression of Liver Fibrosis. *Proc. Natl. Acad. Sci.* 109, 9448–9453. doi:10.1073/pnas.1201840109

Kolářová, L., Matějů, J., Hrdý, J., Kolářová, H., Hozáková, L., Žampachová, V., et al. (2015). Human Alveolar Echinococcosis, Czech Republic, 2007-2014. *Emerg. Infect. Dis.* 21, 2263–2265. doi:10.3201/eid2112.150743

Kotwa, J. D., Isaksson, M., Jardine, C. M., Campbell, G. D., Berke, O., Pearl, D. L., et al. (2019). *Echinococcus Multilocularis* Infection, Southern Ontario, Canada. *Emerg. Infect. Dis.* 25, 265–272. doi:10.3201/eid2502.180299

Li, Q., Li, H., Liang, J., Mei, J., Cao, Z., Zhang, L., et al. (2021). Sertoli Cell-derived Exosomal MicroRNA-486-5p Regulates Differentiation of Spermatogonial Stem Cell through PTEN in Mice. *J. Cell Mol Med* 25, 3950–3962. doi:10.1111/jcmm.16347

Li, X., Rui, B., Cao, Y., Gong, X., and Li, H. (2020). Long Non-coding RNA LINC00152 Acts as a Sponge of miRNA-193b-3p to Promote Tongue Squamous Cell Carcinoma Progression. *Oncol. Lett.* 19, 2035–2042. doi:10.3892/ol.2020.11293

Liang, L., Su, W., Zhou, L., Cao, Y., Zhou, X., Liu, S., et al. (2020). Statin Downregulation of miR-652-3p Protects Endothelium from Dyslipidemia by Promoting ISL1 Expression. *Metabolism* 107, 154226. doi:10.1016/j.metabol.2020.154226

Liu, C.-N., Xu, Y.-Y., Cadavid-Restrepo, A. M., Lou, Z.-Z., Yan, H.-B., Li, L., et al. (2018). Estimating the Prevalence of *Echinococcus* in Domestic Dogs in Highly Endemic for Echinococcosis. *Infect. Dis. Poverty* 7, 77. doi:10.1186/s40249-018-0458-8

Maggiore, M., Pensel, P. E., Denegri, G., and Elissondo, M. C. (2015). Chemoprophylactic and Therapeutic Efficacy of Thymol in Murine Cystic Echinococcosis. *Parasitol. Int.* 64, 435–440. doi:10.1016/j.parint.2015.06.005

Massolo, A., Klein, C., Kowalewska-Grochowska, K., Belga, S., MacDonald, C., Vaughan, S., et al. (2019). European *Echinococcus Multilocularis* Identified in Patients in Canada. *N. Engl. J. Med.* 381, 384–385. doi:10.1056/NEJMc1814975

Mederacke, I., Dapito, D. H., Affò, S., Uchinami, H., and Schwabe, R. F. (2015). High-yield and High-Purity Isolation of Hepatic Stellate Cells from normal and Fibrotic Mouse Livers. *Nat. Protoc.* 10, 305–315. doi:10.1038/nprot.2015.017

Mohammadi, M., Spotin, A., Mahami-Oskouei, M., Shanehbandi, D., Ahmadpour, E., Casulli, A., et al. (2021). MicroRNA-365 Promotes Apoptosis in Human Melanoma Cell A375 Treated with Hydatid Cyst Fluid of *Echinococcus Granulosus* Sensu Stricto. *Microb. Pathogenesis* 153, 104804. doi:10.1016/j.micpath.2021.104804

Mohri, T., Nakajima, M., Takagi, S., Komagata, S., and Yokoi, T. (2009). MicroRNA Regulates Human Vitamin D Receptor. *Int. J. Cancer* 125, 1328–1333. doi:10.1002/ijc.24459

Mueller, M. C., Marx, M., Peyerl-Hoffmann, G., and Kern, W. V. (2020). Spatial Distribution and Incidence Trend of Human Alveolar Echinococcosis in Southwest Germany: Increased Incidence and Urbanization of the Disease? *Infection* 48, 923–927. doi:10.1007/s15010-020-01479-4

Myant, K. B., Cammareri, P., McGhee, E. J., Ridgway, R. A., Huels, D. J., Cordero, J. B., et al. (2013). ROS Production and NF-Kb Activation Triggered by RAC1 Facilitate WNT-Driven Intestinal Stem Cell Proliferation and Colorectal Cancer Initiation. *Cell Stem Cell.* 12, 761–773. doi:10.1016/j.stem.2013.04.006

Onoyama, I., Suzuki, A., Matsumoto, A., Tomita, K., Katagiri, H., Oike, Y., et al. (2011). Fbxw7 Regulates Lipid Metabolism and Cell Fate Decisions in the Mouse Liver. *J. Clin. Invest.* 121, 342–354. doi:10.1172/JCI40725

Ota, H., Ito-Matsuoka, Y., and Matsui, Y. (2019). Identification of the X-Linked Germ Cell Specific miRNAs (XmiRs) and Their Functions. *PLoS One* 14, e0211739. doi:10.1371/journal.pone.0211739

Peng, H., Ren, S., Liu, Y., Zhou, H., Tang, X., Yang, J., et al. (2020). Elevated Expression of the Long Noncoding RNA IFNG-AS1 in the Peripheral Blood from Patients with Rheumatoid Arthritis. *J. Immunol. Res.* 2020, 6401978. doi:10.1155/2020/6401978

Pensel, P. E., Elissondo, N., Gambino, G., Gamboa, G. U., Benoit, J. P., and Elissondo, M. C. (2017). Experimental Cystic Echinococcosis Therapy: *In Vitro* and *In Vivo* Combined 5-fluorouracil/albendazole Treatment. *Vet. Parasitol.* 245, 62–70. doi:10.1016/j.vetpar.2017.08.011

Petermann, F., Pękowska, A., Johnson, C. A., Jankovic, D., Shih, H.-Y., Jiang, K., et al. (2019). The Magnitude of IFN-γ Responses Is Fine-Tuned by DNA Architecture and the Non-coding Transcript of Ifng-As1. *Mol. Cell* 75, 1229–1242. doi:10.1016/j.molcel.2019.06.025

Peters, L., Burkert, S., and Grüner, B. (2021). Parasites of the Liver - Epidemiology, Diagnosis and Clinical Management in the European Context. *J. Hepatol.* 75, 202–218. doi:10.1016/j.jhep.2021.02.015

Ren, G.-J., Fan, X.-C., Liu, T.-L., Wang, S.-S., and Zhao, G.-H. (2018). Genome-wide Analysis of Differentially Expressed Profiles of mRNAs, lncRNAs and circRNAs during *Cryptosporidium Baileyi* Infection. *BMC Genomics* 19, 356. doi:10.1186/s12864-018-4754-2

Roberts, R. A., Ganey, P. E., Ju, C., Kamendulis, L. M., Rusyn, I., and Klaunig, J. E. (2007). Role of the Kupffer Cell in Mediating Hepatic Toxicity and Carcinogenesis. *Toxicol. Sci.* 96, 2–15. doi:10.1093/toxsci/kfl173

Spiliotis, M., and Brehm, K. (2009). Axenic *In Vitro* Cultivation of Echinococcus Multilocularis Metacestode Vesicles and the Generationof Primary Cell Cultures. *Methods Mol. Biol.* 470, 245–262. doi:10.1007/978-1-59745-204-5_17

Tombolan, L., Millino, C., Pacchioni, B., Cattelan, M., Zin, A., Bonvini, P., et al. (2020). Circulating miR-26a as Potential Prognostic Biomarkers in Pediatric Rhabdomyosarcoma. *Front. Genet.* 11, 606274. doi:10.3389/fgene.2020.606274

Torabi, N., Dobakhti, F., Faghihzadeh, S., and Haniloo, A. (2018). *In Vitro* and *In Vivo* Effects of Chitosan-Praziquantel and Chitosan-Albendazole Nanoparticles on *Echinococcus Granulosus* Metacestodes. *Parasitol. Res.* 117, 2015–2023. doi:10.1007/s00436-018-5849-z

Wang, H., Thorling, C. A., Liang, X., Bridle, K. R., Grice, J. E., Zhu, Y., et al. (2015). Diagnostic Imaging and Therapeutic Application of Nanoparticles Targeting the Liver. *J. Mater. Chem. B* 3, 939–958. doi:10.1039/c4tb01611d

Wang, S., Ma, Y., Wang, W., Dai, Y., Sun, H., Li, J., et al. (2021a). Status and prospect of Novel Treatment Options toward Alveolar and Cystic Echinococcosis. *Acta Trop.* 226, 106252. doi:10.1016/j.actatropica.2021.106252

Wang, X., Chi, J., Dong, B., Xu, L., Zhou, Y., Huang, Y., et al. (2021b). MiR-223-3p and miR-22-3p Inhibit Monosodium Urate-induced Gouty Inflammation by Targeting NLRP3. *Int. J. Rheum. Dis.* 24, 599–607. doi:10.1111/1756-185X.14089

Wang, X., Liu, J., Zuo, Q., Mu, Z., Weng, X., Sun, X., et al. (2018). *Echinococcus Multilocularis* and *Echinococcus Shiquicus* in a Small Mammal Community on the Eastern Tibetan Plateau: Host Species Composition, Molecular Prevalence,

and Epidemiological Implications. *Parasites Vectors* 11, 302. doi:10.1186/s13071-018-2873-x

Woolsey, I. D., and Miller, A. L. (2021). *Echinococcus Granulosus* Sensu Lato and *Echinococcus Multilocularis*: A Review. *Res. Vet. Sci.* 135, 517–522. doi:10.1016/j.rvsc.2020.11.010

Xiang, P., Yeung, Y. T., Wang, J., Wu, Q., Du, R., Huang, C., et al. (2021). miR -17-3p Promotes the Proliferation of Multiple Myeloma Cells by Downregulating P21 Expression through LMLN Inhibition. *Int. J. Cancer* 148, 3071–3085. doi:10.1002/ijc.33528

Xu, S., Wang, J., Jiang, J., Song, J., Zhu, W., Zhang, F., et al. (2020). TLR4 Promotes Microglial Pyroptosis via lncRNA-F630028O10Rik by Activating PI3K/AKT Pathway after Spinal Cord Injury. *Cell Death Dis* 11, 693. doi:10.1038/s41419-020-02824-z

Xu, Y., Wu, J., Yuan, X., Liu, W., Pan, J., and Xu, B. (2021). MicroRNA-155 Contributes to Host Immunity against Toxoplasma Gondii. *Parasite* 28, 83. doi:10.1051/parasite/2021082

Yan, X., Zeng, D., Zhu, H., Zhang, Y., Shi, Y., Wu, Y., et al. (2020). MiRNA-532-5p Regulates CUMS-Induced Depression-like Behaviors and Modulates LPS-Induced Proinflammatory Cytokine Signaling by Targeting STAT3. *Ndt* Vol. 16, 2753–2764. doi:10.2147/NDT.S251152

Yang, Q., Wan, Q., Zhang, L., Li, Y., Zhang, P., Li, D., et al. (2018a). Analysis of LncRNA Expression in Cell Differentiation. *RNA Biol.* 15, 413–422. doi:10.1080/15476286.2018.1441665

Yang, X., Bam, M., Becker, W., Nagarkatti, P. S., and Nagarkatti, M. (2020). Long Noncoding RNA AW112010 Promotes the Differentiation of Inflammatory T Cells by Suppressing IL-10 Expression through Histone Demethylation. *J.I.* 205, 987–993. doi:10.4049/jimmunol.2000330

Yang, Y., Jin, Z., Dong, R., Zheng, C., Huang, Y., Zheng, Y., et al. (2018b). MicroRNA-29b/142-5p Contribute to the Pathogenesis of Biliary Atresia by Regulating the IFN-γ Gene. *Cell Death Dis* 9, 545. doi:10.1038/s41419-018-0605-y

Yin, Y.-L., Liu, T.-L., Yao, Q., Wang, Y.-X., Wu, X.-M., Wang, X.-T., et al. (2021). Circular RNA ciRS-7 Affects the Propagation of Cryptosporidium Parvum in HCT-8 Cells by Sponging miR-1270 to Activate the NF-Kb Signaling Pathway. *Parasites Vectors* 14, 238. doi:10.1186/s13071-021-04739-w

Zheng, B., Wang, H., Cui, G., Guo, Q., Si, L., Yan, H., et al. (2020). ERG-associated lncRNA (ERGAL) Promotes the Stability and Integrity of Vascular Endothelial Barrier during Dengue Viral Infection via Interaction with miR-183-5p. *Front. Cel. Infect. Microbiol.* 10, 477. doi:10.3389/fcimb.2020.00477

Zheng, X. L., Yan, M. L., Liao, D. Q., Zhou, Z. G., and Chen, K. L. (2008). Mixed Enzyme Applied to Develop the Method on BAlb/c Mouse Kupffer Cell Isolated and Cultured *In Vitro*. *Sichuan Da Xue Xue Bao Yi Xue Ban* 39, 298–301.

Conflict of Interest: The authors declare that the research was conducted in the absence of any commercial or financial relationships that could be construed as a potential conflict of interest.

Publisher's Note: All claims expressed in this article are solely those of the authors and do not necessarily represent those of their affiliated organizations, or those of the publisher, the editors and the reviewers. Any product that may be evaluated in this article, or claim that may be made by its manufacturer, is not guaranteed or endorsed by the publisher.

frontiers | Frontiers in Cell and Developmental Biology

ORIGINAL RESEARCH
published: 28 April 2022
doi: 10.3389/fcell.2022.861327

Gender Differential Expression of AR/miR-21 Signaling Axis and Its Protective Effect on Renal Ischemia-Reperfusion Injury

*Gaomin Huang, Qiu Yao, Zhenfeng Ye, Yawei Huang, Chiyu Zhang, Yi Jiang and Xiaoqing Xi**

Department of Urology, Second Affiliated Hospital of Nanchang University, Nanchang, China

Objective: The aim of this study was to investigate gender differences after renal ischemia-reperfusion injury in mice and the effects of androgen receptor (AR) and microRNA-21 (miR-21) on apoptosis in renal ischemia-reperfusion injury.

Methods: Renal ischemia-reperfusion injury model was induced by 45 min of bilateral renal artery ischemia and reperfusion. BALB/c mice were randomly divided into groups according to different experimental protocols. The levels of renal function were evaluated by serum creatinine and blood urea nitrogen. TUNEL staining was used to analyze the pathological changes and apoptosis levels of renal tissue, and western blotting and qPCR were used to detect the expressions of miR-21, AR, PDCD4 and caspase3.

Results: After renal ischemia-reperfusion injury in mice with different genders, the levels of plasma urea nitrogen and creatinine in female and male mice increased, the histopathological score increased, and TUNEL staining in renal tissue indicated increased apoptosis. The expressions of miR-21, PDCD4, and active caspase-3 protein were up-regulated. The above trend was more pronounced in male mice, and a significant decrease in AR mRNA expression was detected. Silencing the expression of AR aggravated the decline of renal function and renal tubular injury after renal ischemia in mice. The expression of PDCD4 and active caspase-3 increased, while the level of miR-21 was correspondingly decreased. Up-regulation of miR-21 expression by pre-miR-21 could negatively regulate PDCD4, reduce the expression level of active caspase3, and yet induce AR expression accordingly. MiR-21 alleviated renal ischemia-reperfusion injury by inhibiting renal tubular epithelial cell apoptosis. The effect of antagomiR-21 was the opposite, which aggravated renal ischemia-reperfusion injury.

Conclusion: There are gender differences in renal ischemia-reperfusion injury. Male mice are more susceptible to renal ischemia-reperfusion injury than female. Silencing AR expression or down-regulating the level of miR-21 can promote the expression of PDCD4 and apoptosis protein caspase3, thereby aggravating ischemia-reperfusion injury in mice. The protective effect of AR and miR-21 in renal ischemia-reperfusion injury has a certain synergy.

Keywords: gender difference, androgen receptor, miR-21, renal ischemia-reperfusion, PDCD4

OPEN ACCESS

Edited by:
Natalia Martins Feitosa, Federal University of Rio de Janeiro, Brazil

Reviewed by:
Anindita Das, Virginia Commonwealth University, United States
Danshen Zhang, Hebei University of Science and Technology, China

****Correspondence:***
Xiaoqing Xi
xxiaoqing112@126.com

Specialty section:
This article was submitted to Molecular and Cellular Pathology, a section of the journal Frontiers in Cell and Developmental Biology

Received: *24 January 2022*
Accepted: *05 April 2022*
Published: *28 April 2022*

Citation:
Huang G, Yao Q, Ye Z, Huang Y, Zhang C, Jiang Y and Xi X (2022) Gender Differential Expression of AR/miR-21 Signaling Axis and Its Protective Effect on Renal Ischemia-Reperfusion Injury. Front. Cell Dev. Biol. 10:861327. doi: 10.3389/fcell.2022.861327

INTRODUCTION

Renal ischemia-reperfusion (renal IR) injury is a common pathophysiological process in clinical practice and the main cause of acute renal failure (Murugan and Kellum, 2011). At present, the mechanism of renal IR is not fully recognized. It usually involves a variety of pathophysiological processes such as oxidative stress, inflammatory response, and apoptosis of renal tubular epithelial cells (Lee et al., 2019). In the early stage of renal ischemia, the interaction between damaged renal tubular epithelial cells, activated endothelial cells and macrophages induces oxidative stress and complement activation, aggravating the process of cell damage. Acute inflammation occurs after blood flow reperfusion, including the production of many pro-inflammatory factors, such as tumor necrosis factor-alpha (TNF-α), interleukin-1beta (IL-1β), and induces a large amount of apoptosis of renal tubular epithelial cells (Mulay et al., 2016). The pathophysiological mechanism of renal IR is definite complicated, and the molecular mechanism of IR-induced renal tubular cell death has not yet been fully elucidated. Therefore, the research on the protection strategy and pathogenesis of renal IR is of great significance.

In recent years, studies have found that in acute ischemic injury, there are gender differences between male and female individuals. According to reports, androgens protect male mice from ischemia-induced castration-related damage by regulating angiogenesis in cardiovascular diseases, and rely on the transcriptional activation of androgen receptors (Lam et al., 2016). Some scholars have found through animal experiments and clinical cases that there are obvious gender differences in the sensitivity and tolerance of the kidney to ischemia-reperfusion injury. The animals show that female rats are more resistant to ischemic kidney injury than male rats (Mehta et al., 2002; Kim et al., 2006; Kang et al., 2014), we also observed this phenomenon in the experiment of sex difference in mice. According to reports, acute ischemic diseases may reduce androgen levels (Wagner et al., 2011). Further studies by researchers have shown that renal ischemia-reperfusion injury leads to a decrease in androgen levels, and androgen supplementation can protect renal ischemic injury, and castration can promote renal injury and renal failure (Robert et al., 2011; Soljancic et al., 2013). The effects of androgens on target organs are mainly mediated by nuclear androgen receptor (AR) transcriptional control of target genes. Androgens also interact with a variety of signaling pathways independent of transcriptional control through AR in the cytoplasm, thereby inducing rapid activation of the kinase signaling cascade (Baron et al., 2004). In order to clarify the role of AR in the gender difference of renal IR, we detected the AR transcription level of the mouse kidney 24 h after IR in the mouse ischemia-reperfusion injury model, and found that the AR level in the kidney tissue of male mice decreased significantly. However, it is not clear whether AR plays a unique pathophysiological role in renal ischemia.

MicroRNAs (miRNAs) are a type of endogenous non-coding RNA found in eukaryotes, with a size of about 20 nucleotides in length. miRNAs inhibit gene expression after transcription by targeting the 3′UTR of mRNA, and participate in a variety of regulatory pathways, including immune response, metabolic processes, tumorigenesis and development, organ formation, cell proliferation, and apoptosis (Hwang and Mendell, 2006; Tavazoie et al., 2008; Lu et al., 2011; Rottiers and Näär, 2012; Lu and Rothenberg, 2018). More and more studies have found that microRNA can regulate IR-induced kidney damage by regulating the expression of target genes (Hao et al., 2017; Jia et al., 2020). Studies have shown that miR-21 participates in ischemia-reperfusion injury of a variety of tissues and organs, including the heart, kidney, intestine, and brain through the regulation of apoptosis, inflammation, and oxidative stress (He et al., 2016; Yang et al., 2016; Jia et al., 2017). We have previously reported that miR-21 can reduce renal ischemia-reperfusion injury by reducing the expression of its target gene PDCD4 and inhibiting apoptosis (Hu et al., 2014). Here, we found that the expression of miR-21 in kidney tissues of mice of different genders has obvious gender differences after renal IR. The mechanism of miR-21 involved in renal ischemia-reperfusion is still worth studying. In addition, some researchers recently found that AR can positively regulate the expression of miR-21 in prostate cancer, and there is a positive feedback loop between the regulation of AR and miR-21 (Mishra et al., 2014). However, whether miR-21 could interact with AR to participate in gender differences in renal IR injury remains unknown. In order to clarify this question, this study used a mouse ischemia-reperfusion injury model to explore the role of AR and miR-21 in renal ischemia-reperfusion injury.

MATERIALS AND METHODS

Experiment Animals

A total of 90 male and female BALB/c mice (6–8 weeks old, weighing about 20–25 g) were purchased from the Animal Experimental Center of Nanchang University. Animals are kept in a 12/12 h light/dark cycle environment, where food and water are freely available. The experimental protocol in this study was approved by the Animal Care and Use Committee of Nanchang University.

Renal Ischemia-Reperfusion Injury Model

Based on our previous work, mouse renal ischemia-reperfusion model was established. The mice were fasted for 8 h before the operation, injected with sodium pentobarbital (50–60 mg/kg, ip) into the abdominal cavity to induce anesthesia, fixed the limbs and disinfected with iodophor before the operation. The renal pedicles were exposed through an abdominal incision, and the bilateral renal arteries were clamped for 45 min. During reperfusion, loosen the hemostatic clip, observe the color change of the kidney, confirm that the blood flow is normal, and suture the incision. The sham operation group performed the same operation without clamping the renal artery. We used a heating pad to maintain the mouse's body temperature at 35–37°C to ensure that the operation was performed at a constant temperature and promote the recovery of the mouse after surgery. The kidney was obtained 24 h after the operation and the serum was collected. Two weeks before surgery, the

kidney was exposed through an incision in the subcostal renal region. Then 50 ul lentivirus constructs containing AR-shRNA (3*10E7 TU/ml, Genechem, Shanghai, China) was injected into the upper and lower poles of the renal, while equal concentration lentivirus of scrambled shRNA was used as negative control. Pre-miR-21 (RiboBio, Guangzhou, China) was used as an activator of miR-21 overexpression at a concentration of 5 mg/kg, and AntagomiR-21 (RiboBio, Guangzhou, China) was used as an inhibitor of miR-21 at 10 mg/kg. Activators and inhibitors were injected intraperitoneally 24 and 1 h before renal IR surgery.

Grouping

According to the experimental protocol, the mice were divided into several groups, $n \geq 5$ in each group. We tested the effects of IR on AR and miR-21 in renal tissues of different genders, and divided them into four groups: 1) male renal IR, 2) female renal IR, 3) male sham operation, and 4) female sham operation. We studied the effect of interfering with AR expression on IR injury and divided male mice into six groups: 1) AR-shRNA + IR, 2) AR-NC + IR, 3) Control + IR, 4) AR-shRNA + sham operation, 5) AR-NC + sham operation, and 6) Control + sham operation. We explored the role of miRNA in protecting renal IR injury. Male mice were randomized into six groups: 1) pre-miR-21 + IR, 2) AntagomiR-21 + IR, 3) Control + IR, 4) pre-miR-21 + sham operation, 5) AntagomiR-21 + sham operation, and 6) Control + sham operation.

Serum Creatinine and Blood Urea Nitrogen Determination

Serum creatinine (Cr) and blood urea nitrogen (BUN) were measured using Cr determination kit and BUN determination kit (Rayto, Shenzhen, China). Collect blood samples from the animal's tail or at the time of execution. After standing at room temperature for 2 h, the serum was collected by centrifugation. The samples were analyzed on a fully automatic biochemical analyzer (Rayto, Chemray 240, Shenzhen, China), and the corresponding parameters followed the manufacturer's instructions.

Histopathological Analysis

Kidney tissues were separated from mice and fixed with 4% paraformaldehyde, embedded in paraffin, and sliced at 4 um. Tissue sections were stained with hematoxylin and eosin (HE) using standard procedures. Observe the tissue sections under an optical microscope (Olympus, Tokyo, Japan), and score the pathology according to the percentage of necrosis or necrotic fragments in the proximal tubules of the cortex and outer medulla: 0, normal kidney; 1, <10%; 2, 10–25%; 3, 26–75%; 4, >75%.

TUNEL Staining

TUNEL method was used to detect renal tissue apoptosis. According to the manufacturer's instructions, use TUNEL detection kit (Servicebio, Wuhan, China) to detect 4 um tissue sections. First, the paraffin-embedded tissue sections were deparaffinized and transparent, and then the sections were repaired with proteinase K working solution for 30 min, and 0.1% triton was added dropwise to the sections and incubated at room temperature for 20 min. Then, the sections were incubated in a mixed buffer containing TDT enzyme-dUTP at 37°C for 2 h. DAPI staining solution was added dropwise and incubated at room temperature in the dark for 10 min. The sections were washed with PBS, and finally mounted with anti-fluorescence quenching mounting tablets, and the sections were observed through a fluorescence microscope to estimate the number of TUNEL-positive staining cells.

Quantitative PCR

Total RNA was extracted from the tissues using TransZol Up kit (Transgen, Beijing, China). Use Easyscript kit with gDNA Remover (Transgen, Beijing, China) to reverse transcribe the extracted RNA into cDNA, and then use Green qPCR Supermix kit (Transgen) to perform qPCR in real-time fluorescence quantitative PCR Detection System (Applied Biosystems, 7900, United States). PCR primers are synthesized by Sangon (Shanghai, China), using to obtain the expression level of mRNA. The primers (5′-3′) used were listed as follows: AR (mice) forward primer: TCCAAGACCTATCGA GGAGCG, reverse primer: GTGGGCTTGAGGAGAACCAT; PDCD4 (mice) forward primer: AAAGACGACTGCGGAAAA ATTCA, reverse primer: CTTCTAACCGCTTCACTTCCATT; GAPDH (mice) forward primer: AGGTCGGTGTGAACGGAT TTG, reverse primer: TGTAGACCATGTAGTTGAGGTCA; U6 (mice) forward primer: CTCGCTTCGGCAGCACA, reverse primer: AACGCTTCACGAATTTGCGT. For the detection of miR-21 expression, use the mmu-miR-21a-5p bulge-loop RT primer designed by RiboBio (Guangzhou, China) for reverse transcription, and then use the mmu-miR-21a-5p specific primer pair for qPCR. MiRNA uses U6 as an internal reference, and mRNA uses GADPH as an internal reference. Use the 2-ΔΔCt value to quantify the fold change and determine relative gene expression.

Western Blot

The western blot analysis was performed according to the standard protocol. The tissue was lysed with RIPA buffer (Solarbio, Beijing, China) containing 1 mM PMSF. After high-speed centrifugation, use the loading buffer to collect the tissue lysate. An equal amount of protein samples is separated on a 10% SDS-PAGE gel and then transferred to a PVDF membrane. And sealed in 5% skimmed milk for 1 h. PDCD4 antibody, cleaved caspase-3 antibody, Caspase-3 antibody, and GAPDH antibody were diluted by 1:500, 1:1000, 1:1000, and 1:5000, respectively. The membrane was incubated with the primary antibody overnight at 4°C, and then incubated with the horseradish peroxidase (HRP) secondary antibody (1:10,000) for 1 h at room temperature, and finally the detection strip was incubated with ECL working solution (Us Everbright, Suzhou, China). Antibodies were purchased from the following sources: anti-PDCD4 (catalogue number: ab80590) from Abcam, anti-cleaved-caspase-3 (catalogue number: 9661) from Cell Signaling Technology, anti-caspase-3 (catalogue number: 66470-2-Ig) and anti-GAPDH (catalogue number: 60004-1-Ig) from Proteintech.

Statistical Analysis

The data are expressed as mean ± standard deviation (SD) ($n > 5$), and the difference between the two groups was tested by t test. A two-way ANOVA multiple-comparisons test is used to estimate

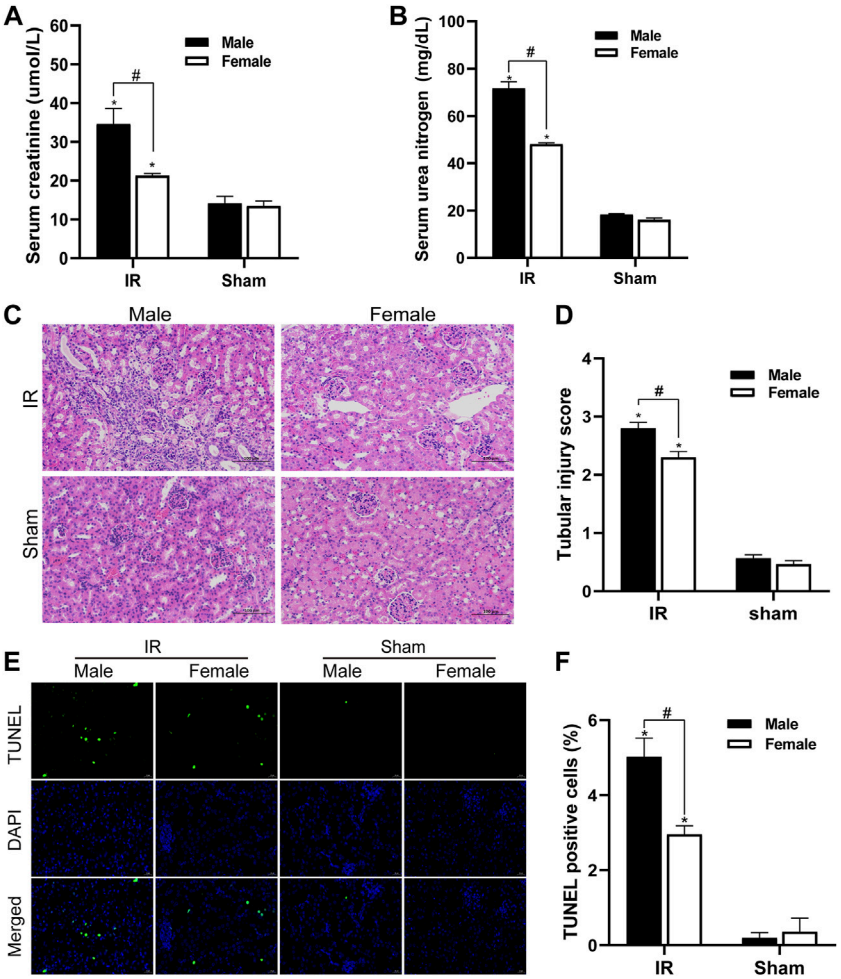

FIGURE 1 | Gender differences in renal ischemia-reperfusion injury. **(A,B)** Serum creatinine levels **(A)** and serum urea nitrogen levels **(B)** of male and female mice in renal ischemia for 45 min and 24 h after reperfusion. **(C)** HE staining of renal tissue (original magnification ×200). Renal tubule injury is characterized by renal tubular atrophy and dilation, accompanied by tubular type. **(D)** Corresponding renal tissue pathological damage score. **(E)** Representative photograph for TUNEL staining section of renal tubular epithelial cells (green) in each group. Original magnification: ×400. Scale bar: 20 μm. **(F)** Quantitative evaluation of TUNEL-positive cells in renal tissue. The data displayed are mean ± SEM ($n > 5$). Compared with sham operation group, $^*p < 0.05$. Compared with female renal IR group, $\#p < 0.05$.

how two factors affect a response variable. $p < 0.05$ is considered to reflect a significant difference between the two sets of data.

RESULTS

Effect of Sex Difference on Renal Function and Histological Changes After Renal Ischemia-Reperfusion Injury

We detected the changes in serum creatinine and serum urea nitrogen levels in female and male mice after renal ischemia for 45 min and reperfusion for 24 h. The serum creatinine level of the control group animals was 12–16 umol/l, and the BUN value was about 17 mg/dl. There was no significant difference between male and female individuals. Compared with the control group, serum creatinine and serum urea nitrogen levels increased significantly after IR injury. However, compared with female mice, male mice had a more significant decline in renal function caused by IR injury (**Figures 1A,B**). The HE staining of kidney tissue is as shown in **Figure 1C**. There was no significant change in the kidney histology of mice in the control group. After ischemia-reperfusion, both male and female mice showed renal tubular injury, and many renal tubular atrophy and dilation were seen in the renal tissue, but the degree of injury in male animals was significantly higher. In order to quantify the kidney tissue damage in mice, the renal tissue pathological damage score was used to determine the percentage of renal tubular necrosis and dissolution. The results showed that the pathological score of the renal tissue of male mice was close to three and that of female mice was approximately 2. The pathological score increased after IR injury, but the increase in male mice was more obvious (**Figure 1D**). Tubular damage and necrosis under ischemic conditions are closely related to cell apoptosis. In order to study the effect of gender on renal tubular cell apoptosis after IR injury, the TUNEL method was

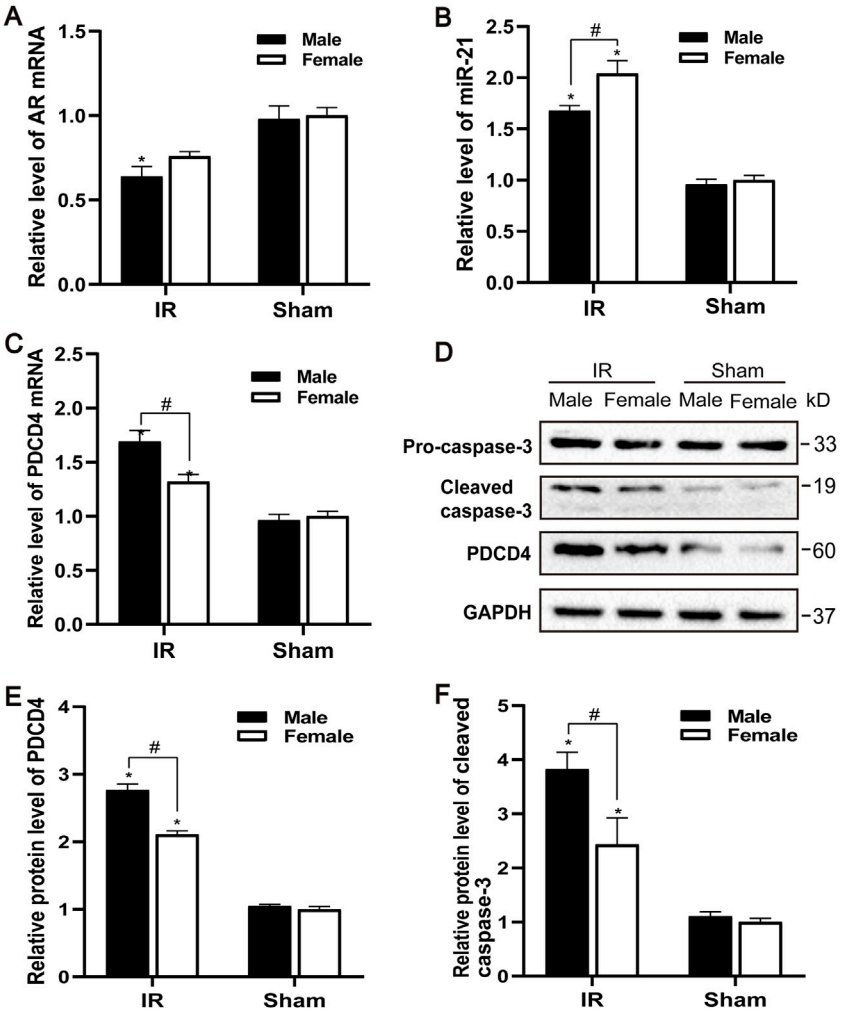

FIGURE 2 | Gender difference expression of AR and miR-21 after renal IR injury. **(A–C)** qPCR showing AR **(A)**, miR-21**(B)**, and PDCD4 **(C)** mRNA levels of male and female mice in renal ischemia for 45 min and 24 h after reperfusion. **(D)** The expression of cleaved caspase-3 and PDCD4 protein in renal tissue after renal ischemia-reperfusion was detected by Western blot. **(E)** Quantitative evaluation of PDCD4 protein levels in renal tissue. **(F)** Quantitative evaluation of cleaved caspase-3 protein levels in renal tissue. Data presented are mean ± SEM ($n > 5$). Compared with sham operation group, $^*p < 0.05$. Compared with female renal IR group, $\#p < 0.05$.

used to detect renal tissue in our experiment. After ischemia-reperfusion, a large number of TUNEL-positive cells appeared in the kidney tissue of male mice, while TUNEL-stained cells were relatively few in female mice. TUNEL-positive cells were not found in the control group. TUNEL staining of renal tissues indicated that the renal cell apoptosis in the IR group was significantly increased, and the male renal cell apoptosis in the IR group was more severe than that of the female (**Figures 1E,F**).

The Influence of Gender Differences on the Expression Levels of Androgen Receptor and miR-21 After Ischemia-Reperfusion injury

The AR expression of male and female mice after IR injury was evaluated. Compared with the control group, the levels of AR mRNA in male mice decreased to varying degrees, and the decrease of AR in female mice was not significant (**Figure 2A**). Male mice may be more sensitive to AR decline than female mice, causing renal ischemia-reperfusion injury more severe than female mice. Compared with the sham group, the expression of PDCD4 mRNA and protein in the IR group was significantly increased, and male mice were more significant than female mice (**Figures 2C–E**). Compared with the control group, the expression of miR-21 was significantly increased after IR injury, while the expression of miR-21 between male and female mice was also significantly different. Compared with male mice, the expression of miR-21 in female mice risen more significantly (**Figure 2B**). Caspase-3 is an important part of the caspase-dependent apoptosis pathway. In the experiment, we used western blotting to detect the expression of caspase-3 protein in kidney tissue. Compared with the sham group, the expression of apoptotic factor caspase-3 was increased after IR injury, while the expression of caspase-3 in the renal tissue of male mice was

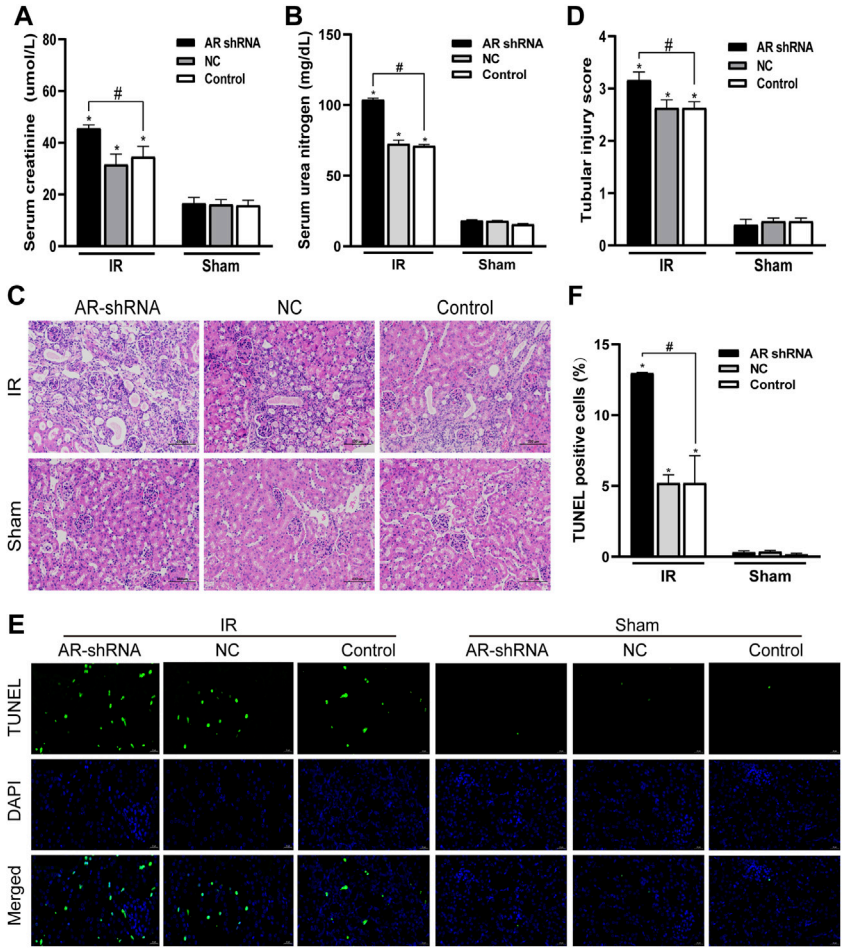

FIGURE 3 | Silencing AR expression aggravates renal ischemia-reperfusion injury in male mice. **(A,B)** Effects of AR-shRNA silencing AR expression on the level of serum creatinine **(A)** and serum urea nitrogen **(B)** in male mice. **(C)** HE staining of renal tissue in each group (original magnification ×200). **(D)** Corresponding renal tissue pathological damage score. **(E)** Representative photograph for TUNEL staining section of renal tubular epithelial cells (green) in each group. Original magnification: ×400. Scale bar: 20 μm. **(F)** Quantitative evaluation of TUNEL-positive cells in renal tissue. Data displayed are mean ± SEM ($n > 5$). Compared with sham operation group, $^{*}p < 0.05$. Compared with Control + IR group, $\#p < 0.05$.

significantly higher than that of female mice, which is consistent with the TUNEL results (**Figures 2D,F**).

Silencing Androgen Receptor Expression Aggravates Renal Ischemia-Reperfusion Injury

In order to study the role of AR in ischemia-reperfusion injury, AR was used to interfere with the lentiviral vector to silence the expression of AR in male mice, to observe the changes in renal function and histology after renal ischemia-reperfusion injury, and to detect changes in renal tissue. The effect of apoptosis. Compared with the sham group, the serum creatinine and serum urea nitrogen levels of the IR groups were significantly increased; In the IR group, compared with the Control + IR, the serum creatinine and serum urea nitrogen levels of the AR-shRNA + IR group were significantly increased, while there was no significant difference between the AR-NC group and the Control group (**Figures 3A,B**). Kidney HE staining showed that many renal tubules were atrophied and dilated in the renal tissues of the IR group, accompanied by vacuoles and edema of epithelial cells, but there were no obvious changes in the renal tissues of the sham groups. In the IR group, the renal tissue damage in the AR-shRNA + IR group was more severe than that of the other two groups (**Figure 3C**). The renal tissue pathological damage score showed that compared with the Control + sham operation group, the degree of renal tissue damage in each IR group was aggravated. Compared with Control + IR, the degree of renal tissue damage in the AR-shRNA + IR group was aggravated, but there was no significant difference in the degree of renal tissue damage in the NC + IR group (**Figure 3D**). As can be seen in TUNEL staining, compared with Control + Sham operation group, renal cell apoptosis in each IR group increased; compared with Control + IR, renal cell apoptosis increased in AR + IR group, but no significant difference in NC + IR group (**Figures 3E,F**). After

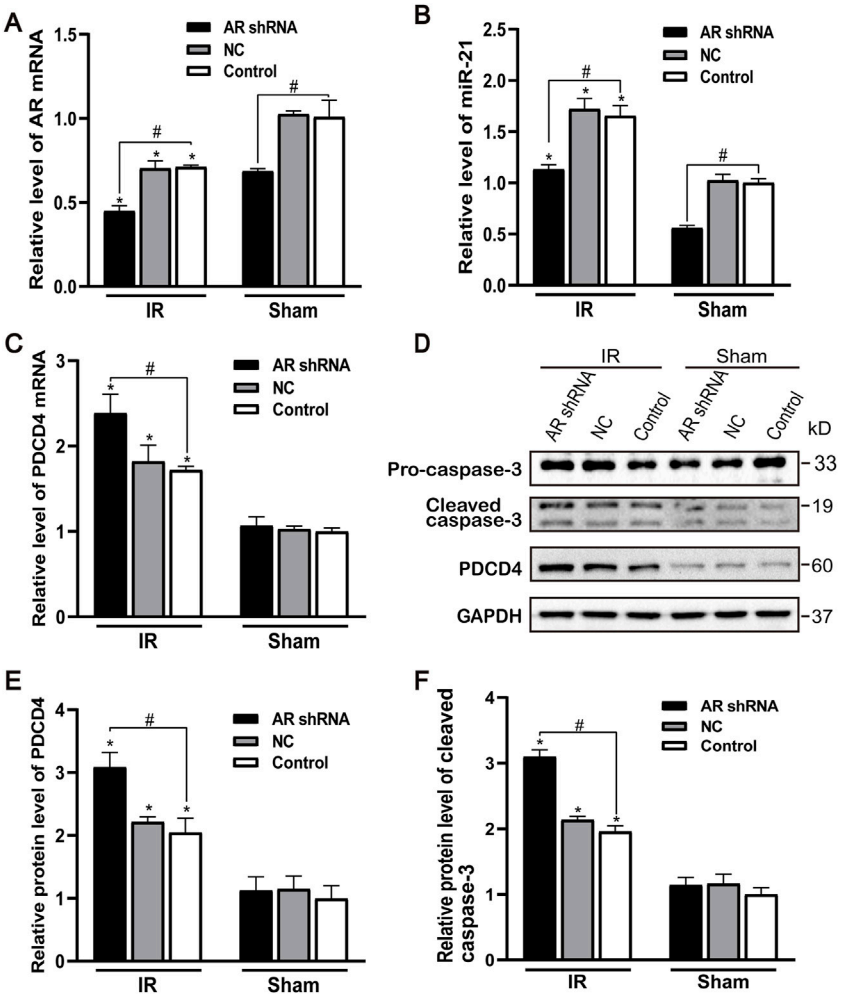

FIGURE 4 | Effect of silencing AR expression on miR-21 level and renal tubular cell apoptosis. **(A)** qPCR showing knocking down AR decreased AR mRNA level after renal ischemia-reperfusion injury in male mice. **(B)** Silencing AR decreased miR-21 level after renal ischemia-reperfusion injury. **(C)** Silencing AR increased PDCD4 mRNA level renal after ischemia-reperfusion injury. **(D)** Western blot showing knocking down AR increased cleaved caspase-3 and PDCD4 protein levels in renal tissue after renal ischemia-reperfusion. **(E)** Quantitative evaluation of PDCD4 protein levels in renal tissue. **(F)** Quantitative evaluation of cleaved caspase-3 protein levels in renal tissue. Data presented are mean ± SEM ($n > 5$). Compared with sham operation group, $^{*}p < 0.05$. Compared with Control + IR group, $\#p < 0.05$.

down-regulating the expression of AR, renal cell apoptosis significantly increased.

The Effect of Silencing Androgen Receptor Expression on Renal Tubular Cell Apoptosis and miR-21 Expression Level

After silencing the expression of AR in male mice, compared with the control group and the NC group, the AR expression of the AR interference group decreased, and there was no difference between the control group and the NC group. Compared with the sham group, AR expression in each IR group showed different degrees of decline (**Figure 4A**). After AR interference, the expression of miR-21 in the AR interference group also decreased compared with the control group (**Figure 4B**). Compared with the sham group, the mRNA level of PDCD4 in each IR group was significantly increased (**Figure 4C**). We detected and quantified the expression of PDCD4 and caspase-3 protein in kidney tissue and found that the expression of PDCD4 protein was consistent with mRNA. Compared with the Control + sham operation group, the expression of caspase-3 in each IR group increased; compared with the Control + IR group, the expression of caspase-3 protein increased in the AR-shRNA + IR group (**Figures 4D–F**). These results suggest that apoptosis is more serious after renal ischemia-reperfusion injury, and the down-regulation of AR increases the degree of apoptosis, thereby aggravating renal ischemia-reperfusion injury.

Effects of AntagomiR-21 and Pre-MicroRNA-21 on the Renal Function and Histological Changes in Mice

In each IR group, compared with the control group, pre-miR-21 significantly inhibited the increase in serum BUN and

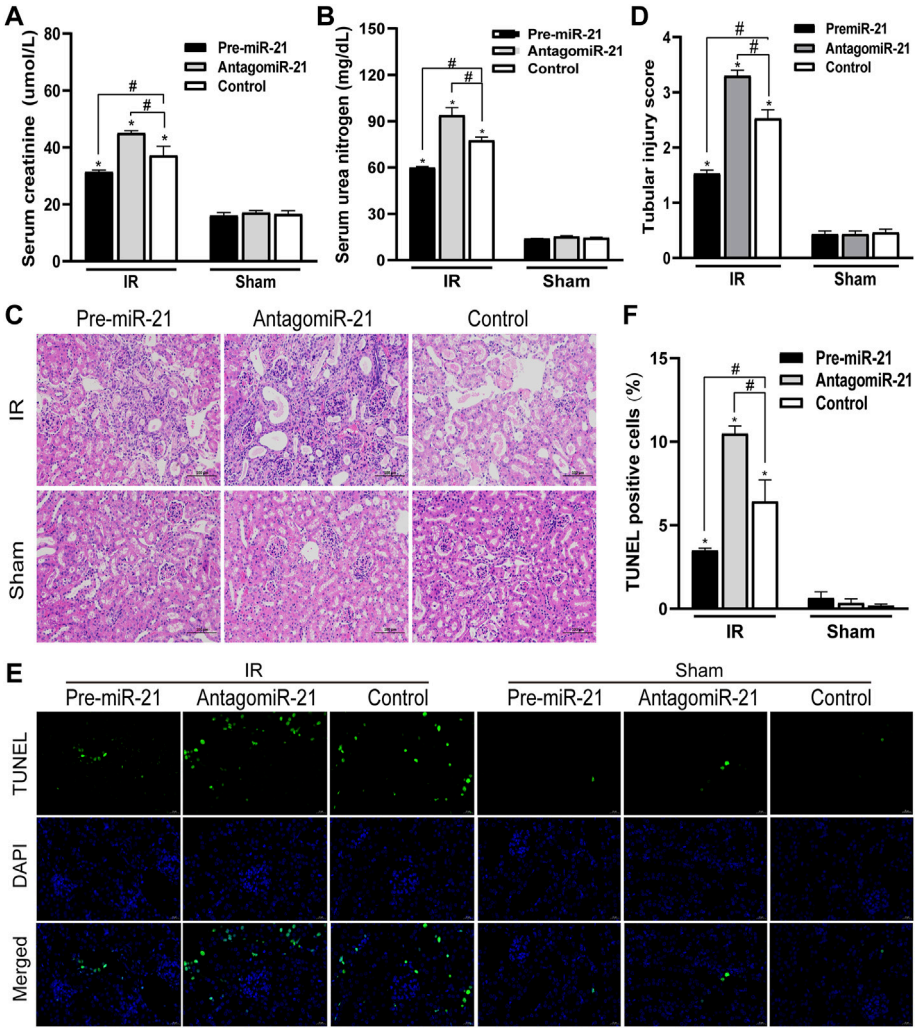

FIGURE 5 | MiR-21 ameliorated the decline of renal function and tubular damage in mice. **(A,B)** pre-miR-21 reduces serum creatinine **(A)** and serum urea nitrogen **(A)** levels after renal ischemia-perfusion, while antagomiR-21 intervention aggravated the decline of renal function. **(C)** HE staining of renal tissue in each group (original magnification ×200). **(D)** Corresponding renal tissue pathological damage score. **(E)** Representative photograph for TUNEL staining section of renal tubular epithelial cells (green) in each group. Original magnification: ×400. Scale bar: 20 μm. **(F)** Quantitative evaluation of TUNEL-positive cells in renal tissue. Data displayed are mean ± SEM ($n > 5$). Compared with sham operation group, $^{*}p < 0.05$. Compared with Control + IR group, $\#p < 0.05$.

creatinine levels after IR, while the increase in serum BUN and creatinine levels in the antagomiR-21 + IR group was more significant (**Figures 5A,B**). Histopathology of the kidney showed that there was no obvious damage and necrosis in the renal tissue of the sham-operated mice. Compared with the Control + IR group, pre-miR-21 treatment can reduce renal tubular atrophy, dilation and swelling, accompanied by a significant reduction in tubular necrosis (**Figure 5C**). Renal tissue pathological damage score confirms the protective effect of pre-miR-21 on the kidney, while renal tubular injury was not significantly improved in the antagomiR-21 + IR group (**Figure 5D**). TUNEL staining was used to evaluate the degree of apoptosis of kidney tissue. The results showed that pre-miR-21 pre-treatment can significantly reduce the number of positive cells stained by TUNEL, while the effect of antagomiR-21 is opposite (**Figures 5E,F**). After ischemia-reperfusion 24 h, cell apoptosis in each IR group was obvious. The supplementation of exogenous miR-21 can effectively reduce renal tubular injury and renal tissue cell apoptosis.

MicroRNA-21 Reduces Renal Tubular Cell Apoptosis After IR by Targeting PDCD4

The expression of endogenous miR-21 was increased in male mice 24 h after ischemia-reperfusion. Pre-miR-21 treatment up-regulated the level of miR-21, while antagomiR-21 treatment down-regulated the expression of miR-21. However, the

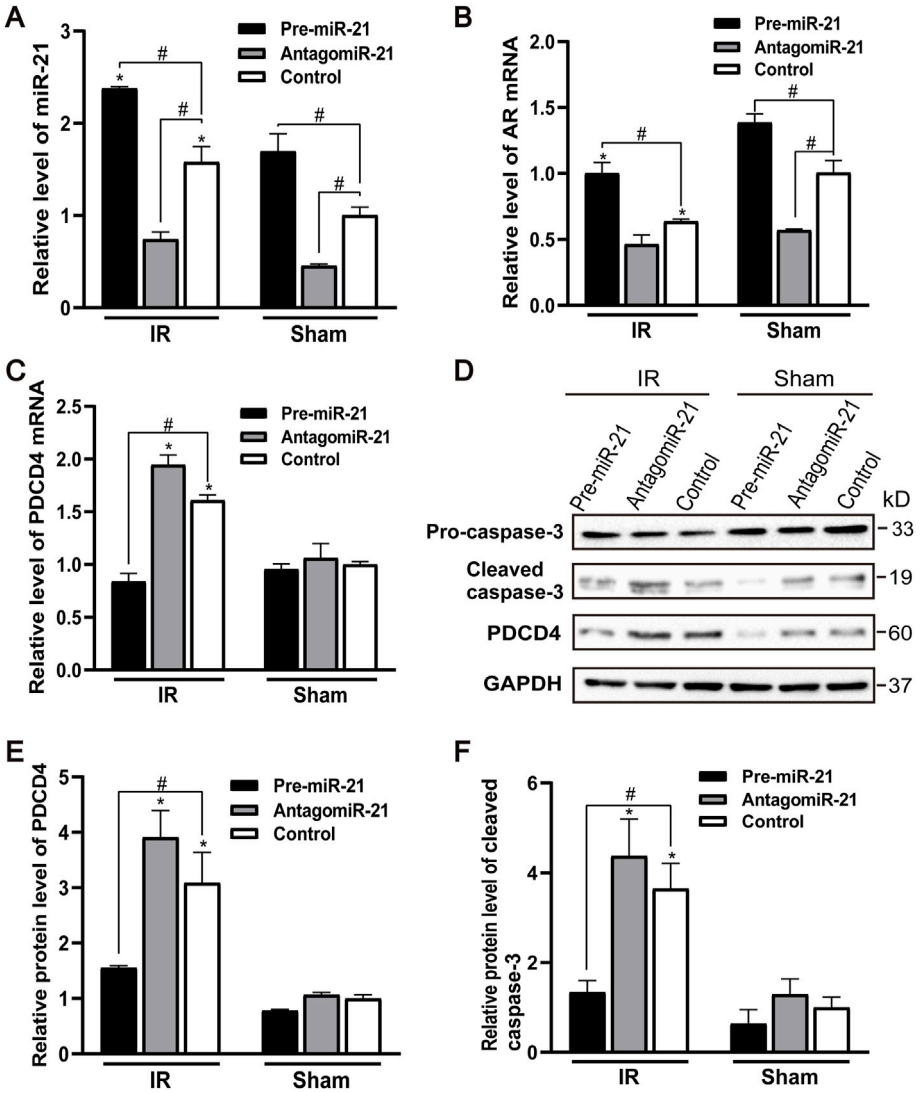

FIGURE 6 | MiR-21 reduces renal tubular cell apoptosis by targeting PDCD4 after ischemia-reperfusion injury. **(A)** qPCR showing pre-miR-21 treatment up-regulated miR-21 level, whereas antagomiR-21 down-regulated the expression of miR-21. **(B)** The expression of AR mRNA in the renal tissue by qPCR. **(C)** PDCD4 mRNA level was negatively correlated with the expression of miR-21 in mice with ischemia-reperfusion injury. **(D)** pre-miR-21 induced the expression of cleaved caspase-3 and PDCD4 protein after renal ischemia-reperfusion, yet antagomiR-21 reduced. **(E)** Quantitative evaluation of PDCD4 protein levels in renal tissue. **(F)** Quantitative evaluation of cleaved caspase-3 protein levels in renal tissue. Data displayed are mean ± SEM ($n > 5$). Compared with sham operation group, $^*p < 0.05$. Compared with Control + IR group, $\#p < 0.05$.

expression level of miR-21 did not change significantly after renal IR injury in the antagomiR-21 group (**Figure 6A**). Pre-miR-21 can increase the expression of AR mRNA, and antagomiR-21 can decrease the expression of AR mRNA (**Figure 6B**). The expression level of AR in mouse kidney tissue shows the same trend as the expression of miR-21. Compared with the IR group, the PDCD4 mRNA and protein expression levels in the kidney tissue of the pre-miR-21 + IR group mice were reduced, while the PDCD4 mRNA and protein expression levels in the antagomiR-21 + IR mice were increased. The expression level of PDCD4 was negatively correlated with the change of miR-21 expression (**Figures 6C–E**), which had also been confirmed in other studies (Pan et al., 2019). The expression of pro-apoptotic protein caspase-3 was significantly increased in mice with renal ischemia reperfusion for 24 h. Compared with the control + IR group, pre-miR-21 reduced the expression level of caspase-3, and the up-regulation of miR-21 could alleviate cell apoptosis under the condition of renal ischemia-reperfusion in mice. While the antagomiR-21 + IR group was the opposite, indicating that miR-21 has a protective effect on renal ischemia-reperfusion injury (**Figures 6D,F**).

DISCUSSION

Our research results show that there are obvious gender differences in renal ischemia-reperfusion injury in animals. Male mice are more sensitive to IR than female mice and are more susceptible to renal ischemia-reperfusion injury. What mechanism causes gender differences in renal IR? We found that the expression of androgen receptor in the kidney tissues of female and male mice was similar before renal ischemia-reperfusion in the female and male mice with renal ischemia for 45 min and reperfusion for 24 h, but the expression of AR in male mice was obvious after ischemia-reperfusion injury. Decrease, which indicates that the higher expression of AR helps to improve the renal function of female mice after renal ischemia-reperfusion. Our further experiments showed that silencing the expression of AR would aggravate the decline of renal function and renal tubular damage after renal ischemia in mice, and activation of caspase3, a key factor for apoptosis in the Caspase family, was also significantly increased. These results suggest that the down-regulation of AR in animals will increase the degree of apoptosis, thereby aggravating renal ischemia-reperfusion injury. This may be explained by the decline of androgen receptors in the body that makes male mice more sensitive to renal ischemia-reperfusion injury.

A large amount of evidence indicates that hypoandrogenemia is associated with an increased risk of ischemic disease (Yeap, 2018), and androgen is mediated through the transcriptional control of target genes by androgen receptor (AR). Sumiko et al. found in the skeletal muscle ischemia model that the blood flow recovery of male and female AR knockout mice was impaired, apoptosis increased, and the incidence of autologous amputation after ischemia was higher. In *in vitro* studies, AR was silent of vascular endothelial cells showed reduced angiogenesis (Yoshida et al., 2013). Another study showed that the loss of AR in vascular smooth muscle, rather than the loss of AR in endothelial cells, led to ischemia-reperfusion injury in the hind limbs of androgen receptor knockout mice (Wu et al., 2016). After transient middle cerebral artery occlusion in male and female adult rats, a decrease in androgen receptor expression can be detected in the ischemic ipsilateral cerebral hemisphere of male rats (Acaz-Fonseca et al., 2020). These findings suggest the role of androgen receptors in the development of acute ischemic diseases.

MiR-21 is generally up-regulated in several different animal models of kidney disease, as well as human acute kidney injury and chronic kidney disease (Lorenzen, 2015; Loboda et al., 2016; Kölling et al., 2017). From the perspective of miRNA, we analyzed the levels of miR-21 in the kidney tissues of mice of different genders under renal ischemia-reperfusion injury, and found that the expression of miR-21 in the kidney tissues has obvious gender differences. Compared with male mice, the level of miR-21 in female mice increased more significantly after IR injury. The expression of miR-21 in kidney tissue increases after IR, which is considered to be a self-protection mechanism against ischemic injury in animals (Li et al., 2013).

We further analyzed the effect of miR-21 on renal ischemia-reperfusion injury. Up-regulating the expression of miR-21 in male mice by pre-miR-21 treatment can reduce renal IR, while the effect of antagomiR-21 is the opposite. The results of qPCR and Western Blot suggest that miR-21 mainly negatively regulates PDCD4 and reduces the expression level of caspase3, thereby inhibiting renal tubular epithelial cell apoptosis. Programmed cell death 4 (PDCD4) was first thought to be a tumor suppressor gene, which played an anti-tumor effect by promoting apoptosis and inhibiting tumor cell proliferation, invasion, and metastasis (Matsuhashi et al., 2019). As an important downstream target of miR-21, PDCD4 is a pro-apoptotic protein that plays an important role in cell apoptosis. miR-21 directly targets the 3′-UTR region of PDCD4 and down-regulates the expression of PDCD4 to inhibit cell apoptosis (Asangani et al., 2008; Pan et al., 2019).

It has been reported that AR can positively regulate the expression of miR-21 in prostate cancer. On the contrary, AR mRNA level is significantly up-regulated after overexpression of miR-21 using miR-21 mimic, and there is a positive feedback loop between the regulation and expression (Mishra et al., 2014). Similarly, in a study of clear cell renal cell carcinoma, AR enhanced miR-185-5p expression by binding to an androgen response element located on the miR-185-5p promoter, thereby affecting the metastatic pathway, which is dependent on Molecular regulation of AR signaling is also accompanied by sex differences (Huang et al., 2017). Our study preliminarily explored the interaction between AR and miR-21 *in vivo*, the expression level of miR-21 is up-regulated in renal ischemia-reperfusion injury, and silencing AR can reduce the expression of miR-21 and aggravate renal tubular epithelial cell apoptosis. When miR-21 was overexpressed or inhibited, AR mRNA expression showed the same trend of change. These results indicated that AR and miR-21 had a certain synergy in the protection of renal ischemia-reperfusion injury.

CONCLUSION

In our experiments, we found that there are obvious gender differences in the sensitivity and tolerance of the kidney to ischemia-reperfusion injury, showing that male mice are more susceptible to renal ischemia-reperfusion injury than female mice. Male mice after ischemia-reperfusion injury can detect a significant decrease in AR expression and an increase in miR-21 level. Silencing the expression of AR can aggravate renal ischemia-reperfusion injury in mice and promote the expression of apoptotic protein caspase3. After *in vivo* application of pre-miR-21 up-regulates endogenous miR-21, it can inhibit the expression of PDCD4 gene and the expression level of apoptotic protein caspase three to play an anti-apoptotic effect, while the effect of antagomiR-21 is opposite. These results prove that protective effect of miR-

21 for renal IR is mediated by inhibiting the apoptosis of renal tubular epithelial cells. In the renal ischemia-reperfusion injury model, interference with AR expression will reduce the expression level of miR-21, and up-regulation of miR-21 can promote AR expression. The protective effects of AR and miR-21 on renal ischemia-reperfusion injury have a certain degree of synergy, and there is a feedback loop. Inhibiting this feedback loop will aggravate IR-induced apoptosis of renal tubular epithelial cells. Therefore, AR and miR-21 are expected to become the crucial "keys" for studying the pathogenesis of IR, so as to discover new therapeutic targets for renal IR in the clinic.

DATA AVAILABILITY STATEMENT

The raw data supporting the conclusions of this article will be made available by the authors, without undue reservation.

ETHICS STATEMENT

The animal study was reviewed and approved by the Animal Care and Use Committee of Nanchang University.

AUTHOR CONTRIBUTIONS

XX designed and supervised the project. GH, QY, and CZ performed all experiments. ZY, YH, and YJ analyzed the data. GH and QY wrote the manuscript. All authors read and approved the final manuscript.

FUNDING STATEMENT

This work was supported by the grants from National Nature Science Foundation of China (No.81660119).

REFERENCES

Acaz-Fonseca, E., Castelló-Ruiz, M., Burguete, M. C., Aliena-Valero, A., Salom, J. B., Torregrosa, G., et al. (2020). Insight into the Molecular Sex Dimorphism of Ischaemic Stroke in Rat Cerebral Cortex: Focus on Neuroglobin, Sex Steroids and Autophagy. *Eur. J. Neurosci.* 52 (1), 2756–2770. doi:10.1111/ejn.14731

Asangani, I. A., Rasheed, S. A. K., Nikolova, D. A., Leupold, J. H., Colburn, N. H., Post, S., et al. (2008). MicroRNA-21 (miR-21) post-transcriptionally Downregulates Tumor Suppressor Pdcd4 and Stimulates Invasion, Intravasation and Metastasis in Colorectal Cancer. *Oncogene* 27 (15), 2128–2136. doi:10.1038/sj.onc.1210856

Baron, S., Manin, M., Beaudoin, C., Leotoing, L., Communal, Y., Veyssiere, G., et al. (2004). Androgen Receptor Mediates Non-genomic Activation of Phosphatidylinositol 3-OH Kinase in Androgen-Sensitive Epithelial Cells. *J. Biol. Chem.* 279 (15), 14579–14586. doi:10.1074/jbc.M306143200

Hao, J., Wei, Q., Mei, S., Li, L., Su, Y., Mei, C., et al. (2017). Induction of microRNA-17-5p by P53 Protects against Renal Ischemia-Reperfusion Injury by Targeting Death Receptor 6. *Kidney Int.* 91 (1), 106–118. doi:10.1016/j.kint.2016.07.017

He, F., Ren, Y., Shi, E., Liu, K., Yan, L., and Jiang, X. (2016). Overexpression of microRNA-21 Protects Spinal Cords against Transient Ischemia. *J. Thorac. Cardiovasc. Surg.* 152 (6), 1602–1608. doi:10.1016/j.jtcvs.2016.07.065

Hu, H., Jiang, W., Xi, X., Zou, C., and Ye, Z. (2014). MicroRNA-21 Attenuates Renal Ischemia Reperfusion Injury via Targeting Caspase Signaling in Mice. *Am. J. Nephrol.* 40 (3), 215–223. doi:10.1159/000368202

Huang, Q., Sun, Y., Ma, X., Gao, Y., Li, X., Niu, Y., et al. (2017). Androgen Receptor Increases Hematogenous Metastasis yet Decreases Lymphatic Metastasis of Renal Cell Carcinoma. *Nat. Commun.* 8 (1), 918. doi:10.1038/s41467-017-00701-6

Hwang, H.-W., and Mendell, J. T. (2006). MicroRNAs in Cell Proliferation, Cell Death, and Tumorigenesis. *Br. J. Cancer* 94 (6), 776–780. doi:10.1038/sj.bjc.6603023

Jia, P., Pan, T., Xu, S., Fang, Y., Song, N., Guo, M., et al. (2020). Depletion of miR-21 in Dendritic Cells Aggravates Renal Ischemia-reperfusion Injury. *FASEB j.* 34 (9), 11729–11740. doi:10.1096/fj.201903222RR

Jia, Z., Lian, W., Shi, H., Cao, C., Han, S., Wang, K., et al. (2017). Ischemic Postconditioning Protects against Intestinal Ischemia/Reperfusion Injury via the HIF-1α/miR-21 Axis. *Sci. Rep.* 7 (1), 16190. doi:10.1038/s41598-017-16366-6

Kang, K. P., Lee, J. E., Lee, A. S., Jung, Y. J., Kim, D., Lee, S., et al. (2014). Effect of Gender Differences on the Regulation of Renal Ischemia-Reperfusion-Induced Inflammation in Mice. *Mol. Med. Rep.* 9 (6), 2061–2068. doi:10.3892/mmr.2014.2089

Kim, J., Kil, I. S., Seok, Y. M., Yang, E. S., Kim, D. K., Lim, D. G., et al. (2006). Orchiectomy Attenuates Post-ischemic Oxidative Stress and Ischemia/Reperfusion Injury in Mice. *J. Biol. Chem.* 281 (29), 20349–20356. doi:10.1074/jbc.M512740200

Kölling, M., Kaucsar, T., Schauerte, C., Hübner, A., Dettling, A., Park, J.-K., et al. (2017). Therapeutic miR-21 Silencing Ameliorates Diabetic Kidney Disease in Mice. *Mol. Ther.* 25 (1), 165–180. doi:10.1016/j.ymthe.2016.08.001

Lam, Y. T., Lecce, L., Tan, J. T. M., Bursill, C. A., Handelsman, D. J., and Ng, M. K. C. (2016). Androgen Receptor-Mediated Genomic Androgen Action Augments Ischemia-Induced Neovascularization. *Endocrinology* 157 (12), 4853–4864. doi:10.1210/en.2016-1301

Lee, K.-H., Tseng, W.-C., Yang, C.-Y., and Tarng, D.-C. (2019). The Anti-inflammatory, Anti-oxidative, and Anti-apoptotic Benefits of Stem Cells in Acute Ischemic Kidney Injury. *Ijms* 20 (14), 3529. doi:10.3390/ijms20143529

Li, Y.-F., Jing, Y., Hao, J., Frankfort, N. C., Zhou, X., Shen, B., et al. (2013). MicroRNA-21 in the Pathogenesis of Acute Kidney Injury. *Protein Cell* 4 (11), 813–819. doi:10.1007/s13238-013-3085-y

Loboda, A., Sobczak, M., Jozkowicz, A., and Dulak, J. (2016). TGF-β1/Smads and miR-21 in Renal Fibrosis and Inflammation. *Mediators Inflamm.* 2016, 1–12. doi:10.1155/2016/8319283

Lorenzen, J. M. (2015). Vascular and Circulating microRNAs in Renal Ischaemia-Reperfusion Injury. *J. Physiol.* 593 (8), 1777–1784. doi:10.1113/jp270318

Lu, T. X., Hartner, J., Lim, E.-J., Fabry, V., Mingler, M. K., Cole, E. T., et al. (2011). MicroRNA-21 Limits *In Vivo* Immune Response-Mediated Activation of the IL-12/IFN-γ Pathway, Th1 Polarization, and the Severity of Delayed-type Hypersensitivity. *J.I.* 187 (6), 3362–3373. doi:10.4049/jimmunol.1101235

Lu, T. X., and Rothenberg, M. E. (2018). MicroRNA. *J. Allergy Clin. Immunol.* 141 (4), 1202–1207. doi:10.1016/j.jaci.2017.08.034

Matsuhashi, S., Manirujjaman, M., Hamajima, H., and Ozaki, I. (2019). Control Mechanisms of the Tumor Suppressor PDCD4: Expression and Functions. *Ijms* 20 (9), 2304. doi:10.3390/ijms20092304

Mehta, R. L., Pascual, M. T., Gruta, C. G., Zhuang, S., and Chertow, G. M. (2002). Refining Predictive Models in Critically Ill Patients with Acute Renal Failure. *Jasn* 13 (5), 1350–1357. doi:10.1097/01.asn.0000014692.19351.52

Mishra, S., Deng, J. J., Gowda, P. S., Rao, M. K., Lin, C.-L., Chen, C. L., et al. (2014). Androgen Receptor and microRNA-21 axis Downregulates Transforming Growth Factor Beta Receptor II (TGFBR2) Expression in Prostate Cancer. *Oncogene* 33 (31), 4097–4106. doi:10.1038/onc.2013.374

Mulay, S. R., Holderied, A., Kumar, S. V., and Anders, H.-J. (2016). Targeting Inflammation in So-Called Acute Kidney Injury. *Semin. Nephrol.* 36 (1), 17–30. doi:10.1016/j.semnephrol.2016.01.006

Murugan, R., and Kellum, J. A. (2011). Acute Kidney Injury: What's the Prognosis? *Nat. Rev. Nephrol.* 7 (4), 209–217. doi:10.1038/nrneph.2011.13

Pan, T., Jia, P., Chen, N., Fang, Y., Liang, Y., Guo, M., et al. (2019). Delayed Remote Ischemic Preconditioning ConfersRenoprotection against Septic Acute Kidney Injury via Exosomal miR-21. *Theranostics* 9 (2), 405–423. doi:10.7150/thno.29832

Robert, R., Ghazali, D., Favreau, F., Mauco, G., Hauet, T., and Goujon, J.-M. (2011). Gender Difference and Sex Hormone Production in Rodent Renal Ischemia Reperfusion Injury and Repair. *J. Inflamm.* 8, 14. doi:10.1186/1476-9255-8-14

Rottiers, V., and Näär, A. M. (2012). MicroRNAs in Metabolism and Metabolic Disorders. *Nat. Rev. Mol. Cel Biol* 13 (4), 239–250. doi:10.1038/nrm3313

Soljancic, A., Ruiz, A. L., Chandrashekar, K., Maranon, R., Liu, R., Reckelhoff, J. F., et al. (2013). Protective Role of Testosterone in Ischemia-Reperfusion-Induced Acute Kidney Injury. *Am. J. Physiology-Regulatory, Integr. Comp. Physiol.* 304 (11), R951–R958. doi:10.1152/ajpregu.00360.2012

Tavazoie, S. F., Alarcón, C., Oskarsson, T., Padua, D., Wang, Q., Bos, P. D., et al. (2008). Endogenous Human microRNAs that Suppress Breast Cancer Metastasis. *Nature* 451 (7175), 147–152. doi:10.1038/nature06487

Wagner, A. K., McCullough, E. H., Niyonkuru, C., Ozawa, H., Loucks, T. L., Dobos, J. A., et al. (2011). Acute Serum Hormone Levels: Characterization and Prognosis after Severe Traumatic Brain Injury. *J. Neurotrauma* 28 (6), 871–888. doi:10.1089/neu.2010.1586

Wu, J., Hadoke, P. W. F., Takov, K., Korczak, A., Denvir, M. A., and Smith, L. B. (2016). Influence of Androgen Receptor in Vascular Cells on Reperfusion Following Hindlimb Ischaemia. *PLoS One* 11 (5), e0154987. doi:10.1371/journal.pone.0154987

Yang, L., Ren, Y., Pan, W., Yu, Z., Tong, L., Li, N., et al. (2016). Fluorescent Nanocomposite for Visualizing Cross-Talk between MicroRNA-21 and Hydrogen Peroxide in Ischemia-Reperfusion Injury in Live Cells and *In Vivo*. *Anal. Chem.* 88 (23), 11886–11891. doi:10.1021/acs.analchem.6b03701

Yeap, B. (2018). Testosterone and its Metabolites: Differential Associations with Cardiovascular and Cerebrovascular Events in Men. *Asian J. Androl.* 20 (2), 109–114. doi:10.4103/aja.aja_50_17

Yoshida, S., Aihara, K.-i., Ikeda, Y., Sumitomo-Ueda, Y., Uemoto, R., Ishikawa, K., et al. (2013). Androgen Receptor Promotes Sex-independent Angiogenesis in Response to Ischemia and Is Required for Activation of Vascular Endothelial Growth Factor Receptor Signaling. *Circulation* 128 (1), 60–71. doi:10.1161/circulationaha.113.001533

Conflict of Interest: The authors declare that the research was conducted in the absence of any commercial or financial relationships that could be construed as a potential conflict of interest.

Publisher's Note: All claims expressed in this article are solely those of the authors and do not necessarily represent those of their affiliated organizations, or those of the publisher, the editors and the reviewers. Any product that may be evaluated in this article, or claim that may be made by its manufacturer, is not guaranteed or endorsed by the publisher.

frontiers | Frontiers in Cell and Developmental Biology

ORIGINAL RESEARCH
published: 12 May 2022
doi: 10.3389/fcell.2022.865948

Thyroid Hormones Deficiency Impairs Male Germ Cell Development: A Cross Talk Between Hypothalamic-Pituitary-Thyroid, and—Gonadal Axes in Zebra fish

Maira S. Rodrigues[1,2†], *Aldo Tovo-Neto*[1,2†], *Ivana F. Rosa*[2], *Lucas B. Doretto*[2], *Hamideh P. Fallah*[3], *Hamid R. Habibi*[3] *and Rafael H. Nóbrega*[2*]

[1]*Aquaculture Program (CAUNESP), São Paulo State University (UNESP), São Paulo, Brazil,* [2]*Reproductive and Molecular Biology Group, Department of Structural and Functional Biology, Institute of Biosciences, São Paulo State University (UNESP), Botucatu, Brazil,* [3]*Department of Biological Sciences, University of Calgary, Calgary, AB, Canada*

OPEN ACCESS

Edited by:
Roland Wohlgemuth, Lodz University of Technology, Poland

Reviewed by:
Taisen Iguchi, Graduate University for Advanced Studies (Sokendai), Japan
Li Shuisheng, Sun Yat-sen University, China

***Correspondence:**
Rafael H. Nóbrega
rafael.nobrega@unesp.br

[†]*These authors contributed equally to this work*

Specialty section:
This article was submitted to Molecular and Cellular Pathology, a section of the journal Frontiers in Cell and Developmental Biology

Received: *30 January 2022*
Accepted: *21 April 2022*
Published: *12 May 2022*

Citation:
Rodrigues MS, Tovo-Neto A, Rosa IF, Doretto LB, Fallah HP, Habibi HR and Nóbrega RH (2022) Thyroid Hormones Deficiency Impairs Male Germ Cell Development: A Cross Talk Between Hypothalamic-Pituitary-Thyroid, and—Gonadal Axes in Zebrafish. Front. Cell Dev. Biol. 10:865948. doi: 10.3389/fcell.2022.865948

In vertebrates, thyroid hormones are critical players in controlling different physiological processes such as development, growth, metabolism among others. There is evidence in mammals that thyroid hormones are also an important component of the hormonal system that controls reproduction, although studies in fish remain poorly investigated. Here, we tested this hypothesis by investigating the effects of methimazole-induced hypothyroidism on the testicular function in adult zebrafish. Treatment of fish with methimazole, *in vivo*, significantly altered zebrafish spermatogenesis by inhibiting cell differentiation and meiosis, as well as decreasing the relative number of spermatozoa. The observed impairment of spermatogenesis by methimazole was correlated with significant changes in transcript levels for several genes implicated in the control of reproduction. Using an *in vitro* approach, we also demonstrated that in addition to affecting the components of the brain-pituitary-peripheral axis, T3 (triiodothyronine) also exerts direct action on the testis. These results reinforce the hypothesis that thyroid hormones are an essential element of multifactorial control of reproduction and testicular function in zebrafish and possibly other vertebrate species.

Keywords: hypothyroidism, methimazole, thyroid hormones, spermatogenesis, zebrafish, germ cell

1 INTRODUCTION

The production of thyroid hormones in fish and other vertebrates is under the control of the hypothalamic-pituitary–thyroid (HPT) axis (Cooke et al., 1994; Tousson et al., 2011; Duarte-Guterman et al., 2014; Kang et al., 2020). The thyrotropin-releasing factor [thyrotropin-releasing hormone (TRH)/corticotropin-releasing hormone (CRH)] stimulates the pituitary to release the thyrotropic hormone (TSH), which in turn, promotes the synthesis and release of thyroid hormones, thyroxine (T4) and triiodothyronine (T3), by thyroid follicles (Larsen et al., 1998). Of the two, T3 is the more biologically active thyroid hormone owing to its affinity for the nuclear thyroid hormone receptor (Carr and Patiño, 2011). The HPT axis acts parallel to the hypothalamic-pituitary–gonadal (HPG) axis, which involves a large number of hormones, including the gonadotropin-releasing hormone (GnRH) that promotes the secretion of gonadotropin hormones, follicle-stimulating

hormone (FSH) and luteinizing hormone (LH) (Schulz et al., 2010; Pankhurst, 2016) which are crucial for testis development and spermatogenesis in fish (Schulz et al., 2010; for a review see Xie et al., 2020). There is evidence for interaction between HPT and HPG axes in vertebrates (Teerds et al., 1998; Ariyaratne et al., 2000; Matta et al., 2002; Wagner et al., 2009; Morais et al., 2013; Kang et al., 2020), although this subject remains poorly investigated in fish, particularly, in the male reproductive system (Habibi et al., 2012; Castañeda-Cortés et al., 2014; Tovo-Neto et al., 2018; Ma et al., 2020a; Ma et al., 2020b). In mammals, it has been shown that T3 regulates the growth and maturation of testis by inhibiting immature Sertoli cell proliferation and stimulating their terminal differentiation (Cooke and Meisami, 1991; Hess et al., 1993; Cooke et al., 1994). Furthermore, in postnatal rat testis, an important action of thyroid hormones is to initiate the onset of Leydig cell differentiation and stimulation of steroidogenesis (Ariyaratne et al., 2000), in part, by stimulating the expression of steroidogenic acute regulatory protein (StAR) (Mendis-Handagama and Ariyaratne, 2005). The presence of thyroid hormone receptors in the mammalian testis, particularly in Leydig cells, suggests both direct and indirect actions of thyroid hormones on testicular function (Hernandez, 2018). The regulatory role of thyroid hormones is complex, species specific, and dependent on developmental stages. Neonatal hypothyroidism was shown to impair testicular growth and sperm production in rats (França et al., 1995), hamsters (*Mesocricetus auratus*) (Jansen et al., 2007), and juvenile teleost fish (*Oreochromis niloticus*) (Matta et al., 2002).

A number of researchers have investigated the role of thyroid hormones in fish embryogenesis, larval development, and growth (Blanton and Specker, 2007; Mukhi et al., 2007; Orozco et al., 2012). With regards to fish male reproduction, there are some evidence that thyroid hormones can affect spermatogenesis (Cyr and Eales, 1996; Wagner et al., 2009; Nelson et al., 2010; Habibi et al., 2012; Morais et al., 2013; Safian et al., 2016; Tovo-Neto et al., 2018). In adult catfish, *Clarias gariepinus*, treatment with thiourea (a thyroid disruptor) decreased 11-ketostestosterone (11-KT) and testosterone (T) production (Swapna et al., 2006), leading to male reproductive system disruption. Morais and collaborators (2013) demonstrated the influence of thyroid hormones on zebrafish spermatogenesis using an *ex vivo* approach. In the same study, the authors revealed that T3 stimulated the increase in mitotic index of type A undifferentiated spermatogonia (A_{und}) and Sertoli cells through Igf3 (Insulin-like growth factor like 3), a Sertoli cell stimulatory growth factor (Morais et al., 2013). Moreover, the same authors showed that T3 potentiated FSH actions on steroid release and enhanced Fsh-stimulated *cyp17a1* (17α-hydroxylase/17, 20 lyase) and *ar* mRNA levels in adult zebrafish testis (Morais et al., 2013). There is also evidence that thyroid hormones interact with other reproductive peptides such as GnRH and gonadotropin-inhibitory hormones (GnIH) *in vivo* (Ma et al., 2020a, Ma et al., 2020b) and *in vitro* in the zebrafish testis (Rodrigues et al., 2021). Other studies have demonstrated that GnRH stimulates thyroid activity in a freshwater murrel, *Channa gachua*, and two carp species, *Catla* and *Cirrhinus mrigala* (Roy et al., 2000). GnRH injection increases plasma T4 levels in different species (Jacobs et al., 1988; Roy et al., 2000; Chiba et al., 2004), suggesting an effect of endogenous pituitary gonadotropin release due to the heterothyrotropic activities of GnRH on the thyroid (Mackenzie, 1982, Mackenzie et al.,1987). In general, these findings support the hypothesis that normal thyroid hormone action is critical for HPG axis function and normal gonadal function. However, significant gaps remain regarding exact physiological significance of thyroid hormones on male fish reproductive function.

The aim of this research was to further explore the influence of thyroid hormones on male zebrafish reproduction adopting *in vivo* and *ex vivo* approaches. We first evaluated the effect of hypothyroidism induced by methimazole and co-treatment with T4 on zebrafish spermatogenesis by histomorphometrical measurement and measured testicular transcript levels for genes related to reproduction, as well as 11-KT plasma levels and basal and FSH-induced 11-KT release *in vitro*. Subsequently, we investigated the hypothyroidism induced by methimazole treatment and T3 injection on zebrafish brain and pituitary by transcript measurement. Finally, we investigated long-term effects of T3 on zebrafish spermatogenesis by histomorphometrical analysis, and transcript levels of a selected genes. The results provide a framework for understanding of the influence of thyroid hormone in the control of male reproduction in adult zebrafish.

2 MATERIALS AND METHODS

2.1 Animals

Sexually mature male zebrafish (outbred) (4–5 months-old) were maintained in the aquarium facility of the Department of Structural and Functional Biology, Institute of Biosciences, Botucatu, São Paulo State University (UNESP) in 6-L tanks in the recirculating system under constant temperature conditions (28°C), and proper photothermal conditions (14-h light/10-h dark). The following water parameters were monitored in all tanks every other day: pH, salinity, dissolved oxygen, and ammonia concentration. The animals were fed twice a day with commercial food (Sera Vipan Flakes®). Handling and experimentation were performed according to the Brazilian legislation regulated by National Council for the Control of Animal Experimental (CONCEA) and Ethical Principles in Animal Research (Protocol n. 1031-CEUA) and University of Calgary animal care committee and in agreement with the procedures of the Canadian Council of Animal Care (Protocol #AC19-0161).

2.2 Treatment Solutions: Methimazole-Induced Hypothyroidism and Reversal Treatment With T4

In this study, we used methimazole (1-methyl-3H-imidazole-2-thione) (CAS 60-56-0; MW, 114.17 g/mol; purity, ≥99%; Sigma-Aldrich, St. Louis, MO, United States) to chemically generate

hypothyroidism in adult zebrafish males. Exposure concentration of 1 mM was prepared following the methodology described in Rodrigues et al. (2021). The working concentration of 1 mM methimazole and 100 µg/L T4 (L-Thyroxine) (CAS 51-48-9; MW, 776.87 g/mol; purity ≥98%; Sigma-Aldrich, St. Louis, MO, United States) were chosen based on previous studies (Sharma and Patiño, 2013; Sharma et al., 2016; Rodrigues et al., 2021). In this study, adult male zebrafish (n = 144) were divided into four replicate tanks per experimental group: control [only filtered water (n = 36)]; group I [filtered water with T4 (100 µg/L) (n = 36)]; group II [filtered water with methimazole (1 mM) (n = 36)]; group III [1 mM of methimazole followed by addition of T4 (100 µg/L) (n = 36) as reversal treatment group (methimazole + T4)]. In the T4 group, males were exposed to T4 (100 µg/L) from the second week until the end of treatment. In the methimazole group, males were exposed to 1 mM methimazole for 21 days. In addition, zebrafish males were exposed to 1 mM methimazole for 21 days, and T4 (100 µg/L) was added in the water from the second week until the end of treatment. The reversal treatment was performed to assess whether the apparent effects were due to lowering thyroid hormone levels. After euthanasia, plasma T3 levels were measured on the treatments and the heads were sampled for histology (control, methimazole and methimazole + T4), while the testes were dissected and immediately used for *in vivo* experiments (histomorphometric analysis and gene expression); androgen plasma levels and *ex vivo* organ culture experiment [short-term (18 h) incubation for androgen release by zebrafish testicular explants] were available on the treatments (control, T4, methimazole and methimazole + T4 groups). The brain and pituitary from the control and methimazole groups were sampled for gene expression.

2.3 Thyroid Hormone Extraction and Measurement

Blood from adult male zebrafish were collected in different conditions (control, methimazole and methimazole + T4) (n = 5 per condition) to confirm the hypothyroidism status. Animals were euthanized, and the caudal peduncle was cut for blood sampling using heparinized syringes and tubes. Plasma fractions were isolated after blood centrifugation at 4°C for 10 min at 800 × g (Eppendorf Centrifuge 5424 R) for thyroid hormone analysis. Plasma Triiodothyronine (T3) levels were measured by Enzyme-Linked Immunosorbent Assay (Competitive ELISA kit) (Invitrogen, TX061-1 EA, Carlsbad, CA, United States). This assay is designed to detect and quantify the levels of T3 in different sample types such as serum, urine, and plasma. Here, we prepare plasma sample according to the manufacturer's procedure. Briefly, high binding 96-well strip-well plate was coated with donkey anti-sheep IgG. Plasma samples were extracted with ethyl acetate (5:1) (v/v) solvent: sample ratio. Samples were frozen and solvent solution was collected (this step was repeated for maximum extraction); and dry pooled solvent extracts down in a speedvac for 2–3 h. Then, samples were reconstituted at room temperature in the 1X Assay Buffer, and 100 µl of either standards or samples were added to the wells in duplicate. 25 µl of T3 conjugated and T3 antibody were added to each well. Plate was incubated for 2 h, shaking, at room temperature. The plate was washed with 1X Wash Buffer, followed by the addition of the detection reagent (TMB substrate solution). After, 30 min, the reaction was stopped with 1 M HCL, CAUSTIC and read at 450 nm using a microplate reader (Epoch, Agilent, Santa Clara, CA, United States). Data were evaluated as nanograms of Triiodothyronine (T3) per milliliter of plasma.

2.4 Thyroid Follicles Histology

Thyroid follicles from the different experimental groups were analyzed histologically. As thyroid follicles in fish appear distributed among the afferent branchial arterioles (Patinõ et a., 2003; Van der Ven et al., 2006), head was separated from the trunk and fixed in 2% glutaraldehyde and 4% paraformaldehyde in Sorensen buffer [0.1 M, pH 7.2] for at least 24 h at room temperature. The material was dehydrated, embedded in glycol methacrylate (GMA) resin (Technovit 7100 - Heraeus Kulzer, Wehrheim, Germany), and serial sections (3 µm thickness) were stained with 0.1% toluidine blue in 1% sodium borate and examined and documented using a Leica DMI6000 microscope (Leica, Heidelberg, Germany).

2.5 Histomorphometrical Evaluation of Zebrafish Spermatogenesis

After exposure to methimazole or methimazole + T4, zebrafish testes (n = 8 per treatment) were dissected and immediately fixed in 2% glutaraldehyde and 4% paraformaldehyde in Sorensen buffer [0.1 M, pH 7.2] at 4°C overnight. Subsequently, testes were dehydrated, embedded in GMA resin (Technovit 7100—Heraeus Kulzer, Wehrheim, Germany), sectioned at 3 µm thickness, and stained with 0.1% toluidine blue. The slides were evaluated, and the proportion of section surface area of spermatogenic cysts containing different germ cell types were determined: type A undifferentiated spermatogonia (A_{und*} and A_{und}), type A differentiated spermatogonia (A_{diff}), type B spermatogonia (SpgB), spermatocytes (Spc), and spermatids (Spt). Intersection points were counted on the histologic fields, for which five fields per slide (n = 8 slides per treatment) were quantified using a grid of 540 (54 × 10) intersections under 100x objective lens. The proportion of section area occupied by spermatogenic cysts containing different germ cell types were represented as fold-change of control value.

For the quantification of the relative number of spermatozoa, twenty different histological fields were captured at 100x objective lens and analyzed by IMAGEJ Software (available at http://imagej.nih.gov/ij/index.html) according to Fallah and collaborators (2019, 2020), Tovo-Neto and collaborators (2020) and Rodrigues and collaborators (2021).

2.6 Transcript Analysis by Quantitative Real-Time PCR (qPCR)

Total RNA from testes (control, methimazole, and methimazole + T4 groups) was extracted using TRIzol™ (Invitrogen, Carlsbad, CA,

United States), according to the manufacturer's instructions, and quantity and purity were checked with a NanoDrop™ One Spectrophotometer (Thermo Scientific, Madison, WI, United States). cDNA synthesis was performed as described previously (Nóbrega et al., 2010). qPCR reactions were conducted using 5 µL of 2x SYBR-Green Universal Master Mix, 1 µL of forward primer (9 mM), 1 µL of reverse primer (9 mM), 0.5 µL of DEPC water, and 2.5 µL of cDNA. The relative mRNA levels of *thrα* and *thrβ* (thyroid hormone receptors), *fshr* (follicle-stimulating hormone receptor), *cyp17a1* (17α-hydroxylase/17,20 lyase/17,20 desmolase), *insl3* (insulin-like peptide 3), *cx43* (testicular connexin), *igf3* (insulin-like growth factor 3), *amh* (anti-Müllerian hormone), *gsdf* (gonadal somatic cell derived factor), *nanos2* (marker of undifferentiated spermatogonia), *dazl* (deleted in azoospermia-like), *sycp3l* (synaptonemal complex protein 3) and *odf3a* (outer dense fiber protein 3) were measured in the different treatments.

Brain ($n = 8$) and pituitary ($n = 4$ pools of 4 pituitaries for each pool) were collected from control and methimazole groups. Brain of each fish was kept separate. Total RNA was extracted from the brain using TRIzol™ (Invitrogen, Carlsbad, CA, United States) method. At least four pituitary glands were pooled per group ($n = 4$ pools per treatment), and total RNA was extracted using a commercial kit (PureLink™ RNA Mini Kit, Ambion, Life Technologies, Carlsbad, CA, United States). After RNA extraction, the usual downstream methods were followed according to procedures described above. The relative mRNA levels of *gnrh2* and *gnrh3* (gonadotropin-releasing hormones), *gnih* (gonadotropin-inhibitory hormone), and *crf* (corticotropin-releasing hormone) were analyzed in the brain, and the *lhb* (luteinizing hormone), *fshb* (follicle-stimulating hormone), and *tsh* (thyroid-stimulating hormone) mRNA levels were determined in the pituitary gland. mRNA levels of the targets (Cts) were normalized by the transcript levels of *β-actin* and expressed as relative values of the control group. Primers were designed according to zebrafish sequences (**Supplementary Table S1**).

2.7 11-KT Plasma Levels

Blood from adult male zebrafish in different conditions (control, T4, methimazole, and methimazole + T4 groups) were collected ($n = 8$ per condition). Fish were euthanized, and the caudal peduncle was cut for blood sampling using heparinized syringes and tubes. Subsequently, blood was centrifuged at 4°C for 10 min at 800 ×*g* (Eppendorf Centrifuge 5424 R), and 11-Ketotestosterone (11-KT) plasma levels were quantified by ELISA (582751, Cayman Chemical, Ann Arbor, MI, United States), following the manufacturer's instructions. The results were evaluated as nanograms of 11-KT per milliliter of plasma.

2.8 Testis Tissue Culture

An *ex vivo* testis culture system described previously (Leal et al., 2009) was used to culture zebrafish testes. For short-term incubations (18 h for 11-KT release analysis), testes were submerged in a culture medium, whereas for long-term exposure (7 days for histomorphometrical analysis and gene expression), testes were placed on a nitrocellulose membrane on top of a cylinder of agarose (1.5% w/v, Ringer's solution, pH 7.4) and exposed to 1 ml of medium culture in 24-well flat-bottom plates, as described by Leal and collaborators (2009).

2.9 Short-Term (18 h) Incubation

Zebrafish testes were collected from eight animals per condition (control, T4, methimazole, methimazole + T4) post-dissection. One testis was cultivated in the Lebovitz medium (L-15), whereas its contra-lateral one in L-15 containing recombinant zebrafish Fsh (rzfFsh; 100 ng/ml). The rzfFsh protein was obtained from ImmunoPrecise Antibodies (Europe) B.V. Science Park Utrecht, Netherlands. Following incubation, testes were individually weighed, and the medium was collected and stored at −20°C for androgen release (11-KT) assay (see **Sub-Section 2.9**).

2.10 *In Vitro* 11-KT Release by Zebrafish Testicular Explants in Short-Term Incubation

This technique was used to examine whether treatment conditions (T4, methimazole, methimazole + T4) modulated rzfFsh (100 ng/ml)-induced androgen release by zebrafish testis. The androgen (11-KT) release capacity of zebrafish testes into culture medium was measured after 18 h incubation as described previously (García-López et al., 2010). The levels of 11-KT released by zebrafish were quantified by ELISA using a commercial kit (Cayman Chemical) following manufacturer's instructions.

2.11 Long-Term (7 days) Incubation

To examine the effects of 100 nM T3 (3,3',5- Triiodo-L-Thyronine) (CAS 6893-02-3; MW, 650.97 g/mol; purity ≥95%; Sigma-Aldrich, St. Louis, MO, United States) ($n = 8$) on zebrafish spermatogenesis, long-term incubations were performed according to Leal and collaborators (2009). For that, one testis was incubated in the presence of T3 alone and its contralateral one in a basal culture medium. The proportion of section area occupied by different germ cell types were represented as fold-change of basal value. The relative number of spermatozoa per area was quantified as described above (see **Sub-Section 2.4**). Also, this technique was used to analyze if different concentrations of T3 and T4 (10, 100 and 1,000 nM) modulate expression of selected genes in zebrafish testis. For that, total RNA from testis explants ($n = 8$) was extracted and the relative mRNA levels of *nanos2*, *sycp3l*, *3β-HSD* (3-beta (β)-hydroxysteroid dehydrogenase), and *cyp17a1* were evaluated as described above (see **Sub-Section 2.5**) (**Supplementary Table S1**).

2.12 T3 Injections

In this study, we used T4 for the long-term experiments as the hormone is converted into T3 over time (see above), while to assess the rapid effects of thyroid hormones (short-term experiments), we used the active hormone (T3). Therefore, adult zebrafish were intracelomically injected with 0 and 250 ng of T3 per fish ($n = 16$). The dose was selected according to its ability to stimulate deiodinase type 3 mRNA levels as described previously (Nelson and Habibi, 2008; Nelson et al., 2010). A stock solution of T3 was dissolved in sodium hydroxide (0.02 M) and further diluted in physiologic saline. The control group was injected only with the physiologic saline solution. After 12 h, the animals were euthanized,

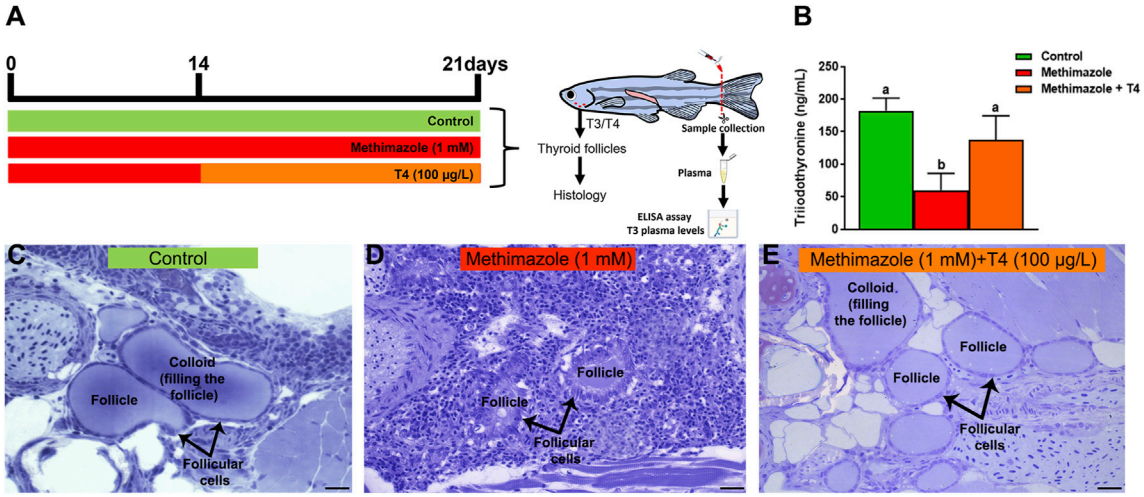

FIGURE 1 | (A) Experimental design representation of treatments: control (non-treated fish), methimazole (1 mM) and methimazole (1 mM) co-treated with T4 (100 µg/L**)** groups. Zebrafish adult males were exposed to reconstituted water containing 1 mM methimazole (goitrogen) for 21 days or 1 mM methimazole following T4 (100 µg/L) added in the water from the second week until the end of exposure. The control group received the same volume of vehicle solution. T3 levels (ng/mL plasma) and thyroid follicles were evaluated after treatments. **(B)** Levels of Triiodothyronine (T3) in the plasma of adult male zebrafish following methimazole induced-hypothyroidism and methimazole co-treated with T4. Bars represent the mean ± SEM (n = 5 per condition). ANOVA followed by Dunnett's multiple comparison tests. Distinct letters denote significant differences ($p < 0.05$) between different treatment conditions with the control group. After 3 weeks heads were dissected for histological analysis of thyroid follicles **(C–E)**. Control group **(C)** have thyroid follicles typical of euthyroid animals. These thyroid follicles display squamous or cuboidal epithelial cells and are totally filled with colloid. However, animals treated with methimazole **(D)** revealed disturbed thyroid follicles with columnar epithelium, follicle cell hypertrophy and colloid depletion, while fish co-treated with T4 **(E)** showed follicles similar to the control animals. Staining: Toluidine blue with sodium borate. Scale bar = 20 µm.

and brain and pituitary glands were sampled. Brain of each fish (n = 8) was kept separate. The pituitaries were pooled (n = 4 pools of 4 pituitaries per condition) for RNA extraction. mRNA levels of *gnrh2* and *gnrh3*, *gnih*, and *crf* were quantified in the brain, and *lhb*, *fshb*, and *tsh* were quantified from pituitary glands (**Supplementary Table S1**). RNA extraction and downstream procedures were followed as described in **Sub-Section 2.5** (see the Figure below).

2.13 Statistical Analysis

All data were subjected to normality Shapiro-Wilk test followed by the Bartlett homogeneity variance test. Significant differences between two groups were identified using unpaired or paired t-tests, while for three or more groups, one-way ANOVA followed by the Student–Newman–Keuls or Dunnett's tests was used. Significance level (p) was considered ≤0.05 in both cases. Data are represented as mean ± SEM (Standard Error of Mean). All statistical analysis was performed using Graph Pad Prism software 7.04 (*Graph Pad Software*, Inc., San Diego, CA, United States, http://www.graphpad.com).

3 RESULTS

3.1 Plasma Thyroid Hormone (T3) Levels

To confirm that basal thyroid hormone levels were affected after methimazole or methimazole + T4 treatment, plasma samples were collected and T3 levels were measured in the different experimental groups (**Figure 1**). The analysis showed that plasma T3 levels were significantly decreased following methimazole treatment (approximately 59 ng/ml) when compared to control group (approximately 182 ng/ml) (**Figure 1B**). In contrast, the observed effect on T3 levels after methimazole treatment was recovered by co-treatment with T4, and plasma T3 levels (approximately 137 ng/ml) were significantly similar to the levels found in control animals (**Figure 1B**).

3.2 Thyroid Follicles Analysis

Thyroid gland follicles were examined histologically in the control group and following treatments with methimazole and methimazole + T4 (**Figures 1A,C,D,E**). The control group thyroid follicles consisted of squamous or cuboidal epithelial cells filled with colloid (**Figure 1C**). The results demonstrate a significant modification in the histological condition of thyroid follicles in fish treated with methimazole. Three-week exposure to 1 mM methimazole resulted in thyroid gland follicles with colloid depletion, columnar epithelium and follicle cell hypertrophy (**Figure 1D**). These morphological changes were consistent with previous studies in which adult male zebrafish were exposed to methimazole (Rodrigues et al., 2021), and other goitrogens, such as perchlorate (Patiño et al., 2003) and 6-n-propyl-2-thiouracil (PTU) (Van der Ven et al., 2006). The observed effect of methimazole was reversed by co-treatment with T4, in which the thyroid follicles were found to be morphologically similar to the control group (**Figure 1E**). The results demonstrate that methimazole-induced hypothyroidism in zebrafish had altered thyroid function following treatment with the goitrogen. Also, the results demonstrate that co-treatment with T4 restored the zebrafish thyroid follicular structure.

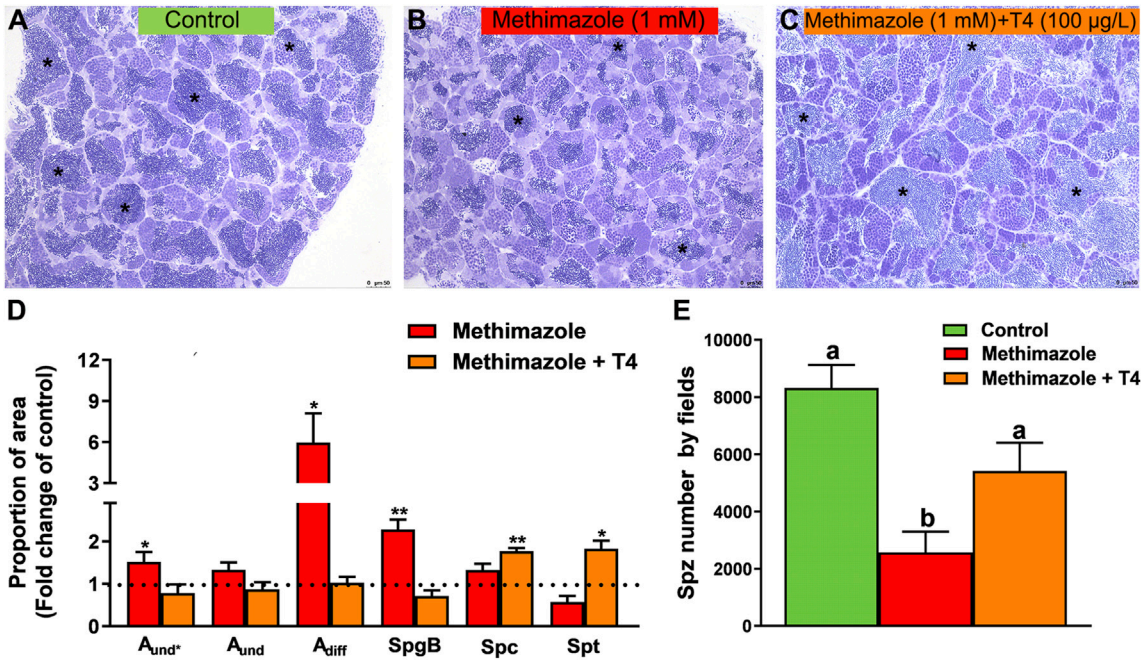

FIGURE 2 | Histomorphometrical evaluation of zebrafish testes after *in vivo* exposure to methimazole and co-treatment with T4 for 3 weeks. Control group (non-treated fish) **(A)**. Methimazole-treated group **(B)**. Methimazole co-treated with T4 **(C)**. Asterisks in **(A)**, **(B)** and **(C)** indicate the testicular lumen with spermatozoa that appeared reduced in the methimazole group. **(D)** Proportion of section area occupied by different spermatogenic cysts: type A undifferentiated spermatogonia (A_{und*}, A_{und}), type A differentiated spermatogonia (A_{diff}), type B spermatogonia (SpgB), spermatocytes (Spc), and spermatids (Spt). Bars (mean ± SEM; $n = 8$) are expressed as fold-change relative to the no-treated fish (control group) (dotted black line set at 1). **(E)** Spermatozoa number per field generated by using IMAGEJ Software from control and treatments. ANOVA followed by Dunnett's multiple comparison tests. Distinct letters denote significant differences ($p < 0.05$) between different treatment conditions with the untreated group. Asterisks denote statistical significance differences between control, methimazole and methimazole + T4 groups; $^{*}p < 0.05$; $^{**}p < 0.01$ (Student unpaired *t*-test; $n = 8$). Staining: Toluidine blue. Scale bar = 50 µm.

3.3 Methimazole-Induced Hypothyroidism and Reversal Treatment With T4: Histomorphometrical Analysis of the Zebrafish Testis

Methimazole-induced hypothyroidism promoted histomorphometrical alterations in the proportion of germ cell cysts compared to the control (**Figures 2A–D**). There was a significant increase in the proportion of the area occupied by type A undifferentiated spermatogonia (A_{und*}), type A differentiated (A_{diff}) and spermatogenic cysts containing type B spermatogonia (SpgB) in the methimazole group as compared to control (**Figure 2D**). The number of meiotic cells (Spc) and post-meiotic haploid cell population (Spt) did not change between control and methimazole-induced hypothyroidism group (**Figure 2D**). However, the relative number of spermatozoa reduced drastically when compared to control as clearly evidenced in the photomicrographs and analysis of spermatozoa number by field (**Figures 2A,B,E**). Co-treatment with T4 rescued the proportion of A_{und*}, A_{diff} and SpgB types returned to its basal values, while the proportion area occupied by Spc and Spt significantly increased (**Figure 2D**). Remarkably, the production of spermatozoa was recovered in the co-treatment with T4 (as viewed in the fields of **Figures 2A,C,E**).

3.4 Methimazole and Co-Treatment With T4: Testicular Transcript Levels

Transcript levels of selected genes involved in reproduction were measured by qPCR in the testis from methimazole-induced hypothyroidism and rescued groups (methimazole + T4) (**Figure 3**). In this study, we measured transcript levels of two thyroid hormone receptor subtypes (*thrα, thrβ*). The *thrα* transcript level was higher in the methimazole-treated group than control, but the difference was not statistically significant (**Figure 3A**). The *thrα* transcript level was further increased significantly in the methimazole + T4 treated group (**Figure 3A**). Similarly, the *thrβ* was increased in the methimazole and methimazole + T4 treated groups, compared to the control (**Figure 3B**).

We also measured mRNA levels of *fshr* which was not altered in the methimazole treated group, but considerably increased in the methimazole + T4 treated fish, compared to the control (**Figure 3C**).

In the present research, we quantified transcript levels for *cyp17a1* and insulin-like peptide 3 (*insl3*) genes. Treatment with methimazole significantly reduced the *cyp17a1* and *insl3* transcript levels compared to control (**Figure 3D,E**). Co-treatment with T4 did not influence the methimazole induced response on the expression of these transcripts (**Figure 3D,E**). We also observed significant reduction in the testicular connexin

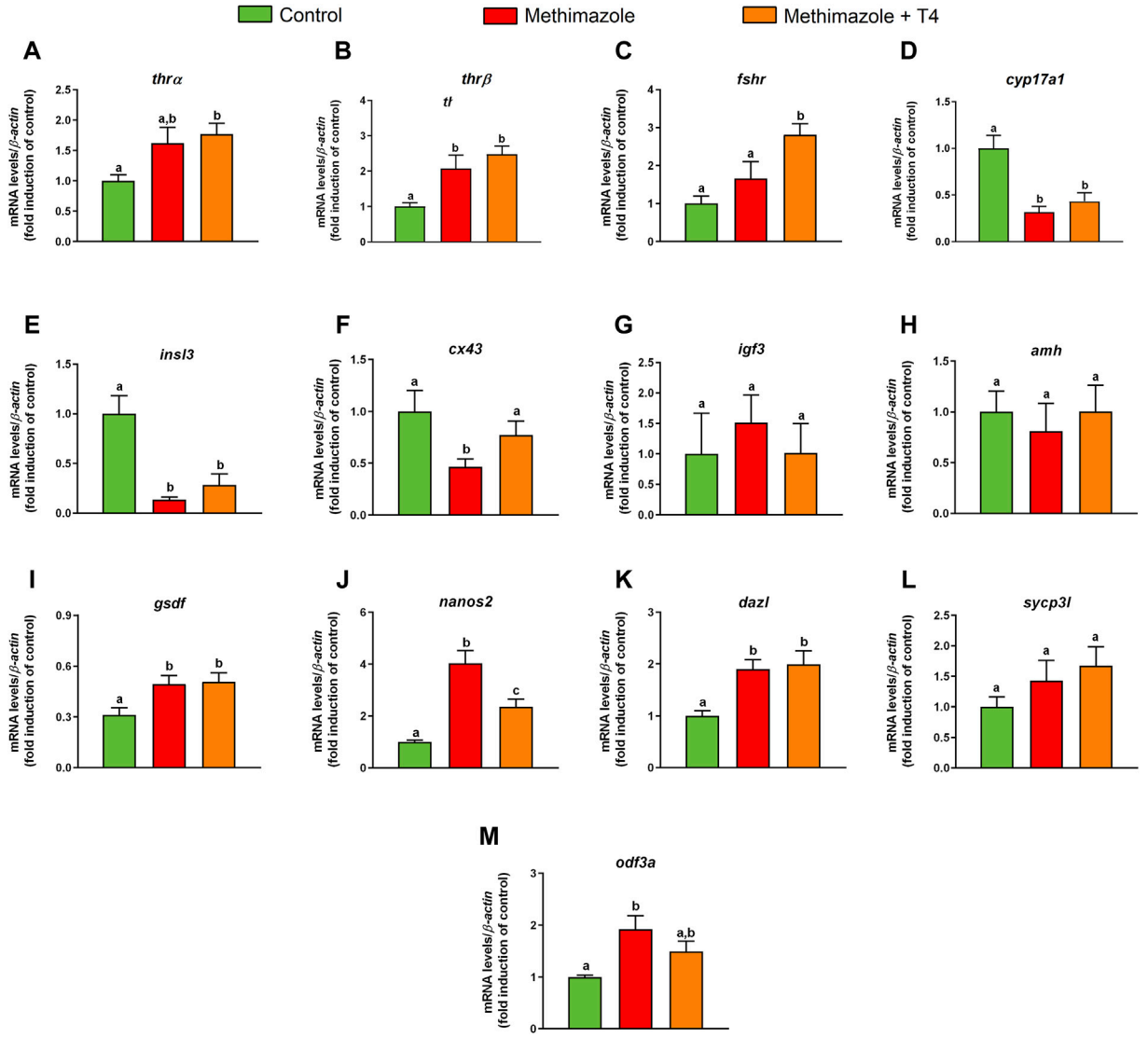

FIGURE 3 | Relative mRNA levels of selected genes expressed in zebrafish testis after *in vivo* exposure to methimazole and methimazole co-treated with T4 for 3 weeks. The selected genes *thrα* and *thrβ* (thyroid hormones receptor) **(A,B)**; *fshr* (follicle-stimulating hormone receptor) **(C)**; genes expressed by somatic cells (Leydig and Sertoli cells) **(D–I)**; *cyp17a1* (17α-hydroxylase/17,20 lyase) **(D)**; *insl3* (insulin-like peptide 3) **(E)**; *cx43* (testicular connexin) **(F)**; *igf3* (insulin-like growth factor 3) **(G)**; *amh* (anti-Müllerian hormone) **(H)**; *gsdf* (gonadal somatic cell derived factor) **(I)**; and germ cell markers **(J–M)**; *nanos2* **(J)**; *dazl* (deleted-in azoospermia-like) **(K)**; *sycp3l* (synaptonemal complex protein 3) **(L)**; *odf3a* (outer dense fiber of sperm tails 3B) **(M)** were evaluated. Ct values were normalized with *β-actin* and expressed as relative values of control levels of expression. Bars represent the mean ± SEM fold change ($n = 8$) relative to the control, which is set at 1. Student unpaired *t*-test. Different letters denote significant differences ($p < 0.05$) between different treatment conditions with the control.

(*cx43*) mRNA levels in the methimazole treated group, compared to control (**Figure 3F**). Co-treatment with T4 in this case increased the *cx43* mRNA to a level not significantly different from the control (**Figure 3F**).

Among others, *igf3*, *amh*, and *gsdf* genes are known to be expressed in the Sertoli cells. Treatment with methimazole or methimazole + T4 were without significant effects on *igf3* and *amh* transcript levels (**Figure 3G,H**). The *gsdf* mRNA level, however, was higher in the methimazole and methimazole + T4 treated groups (**Figure 3I**).

With regard to germ cell marker genes, such as marker for type A undifferentiated spermatogonia, *nanos2* mRNA level was considerably higher in the methimazole-treated group compared to control (**Figure 3J**). Co-treatment with T4, significantly reduced the methimazole-induced response to a level higher than the basal control (**Figure 3J**). The *dazl* (deleted-in azoospermia-like) transcript level expressed by A_{diff} and SpgB, increased in the methimazole treated group compared to the control (**Figure 3K**). Co-treatment with T4 did not influence the methimazole-induced response (**Figure 3K**). In

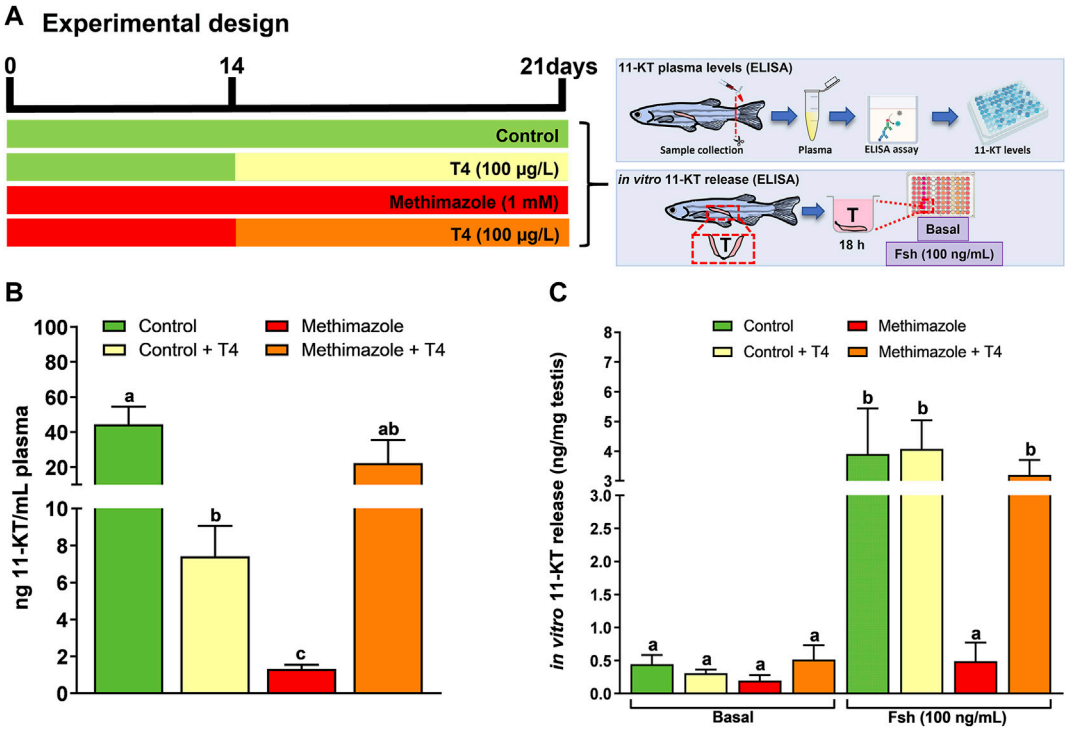

FIGURE 4 | (A) Experimental design. 11-Ketotestosterone (11-KT) plasma levels (ng/mL plasma) was evaluated in zebrafish males exposed to different treatments: Control (non-treated fish), T4 (100 µg/L), methimazole (1 mM) and methimazole (1 mM) + T4 (100 µg/L). Amounts of 11-KT (ng/mg of testis weight) released by zebrafish testes were measured in the incubation media after 18 h (short-term exposure) in the presence or absence of Fsh (100 ng/ml) from control, T4, methimazole and methimazole + T4 groups. **(B)** Effect of T4, methimazole and combination of methimazole and T4 on 11-KT plasma levels. **(C)** Androgen (11-KT) release from zebrafish testicular explants previously treated with T4, methimazole or methimazole co-treated with T4. Bars represent the mean ± SEM (n = 8). ANOVA followed by Tukey's test. Different letters denote significant difference ($p < 0.05$) between different treatments compared to the respective control group.

our study, synaptonemal complex protein 3 (*sycp3l*) which is a marker for spermatocytes was not significantly affected by methimazole or methimazole + T4 treatments (**Figure 3L**). However, the transcript level of the outer dense fiber protein 3 (*odf3a*) which is a marker for spermatids was increased following treatment with methimazole (**Figure 3M**). Co-treatment with T4 reduced the methimazole-induced response to a level not significantly different from the basal control (**Figure 3M**).

3.5 Measurement of 11-KT Levels

In the present research, we measured the 11-KT concentration to partially assess the effect of methimazole-induced hypothyroidism on steroidogenesis, *in vivo* and *in vitro* (**Figure 4A**). Four treatment groups were studied in this experiment, including control, control + T4, methimazole and co-treatment (methimazole + T4) groups (**Figure 4A**). Animal exposure with T4 (control + T4) significantly reduced the plasma 11-KT level as compared to control levels (**Figure 4B**). Also, treatment with methimazole significantly reduced the plasma 11-KT concentration to almost undetectable level compared to the control level of over 40 ng/ml (**Figure 4B**). However, co-treatment with T4 significantly increased and nullified the methimazole-induced response to a level not significantly different from the control (**Figure 4B**).

We also measured the androgen (11-KT) release capacity of zebrafish testicular tissue using the *ex vivo* culture system (**Figure 4A**). In this experiment, we compared testis taken from control and those exposed to T4 (100 µg/L), methimazole (1 mM) and methimazole co-treated with T4. We tested the 11-KT release response into culture media following *in vitro* treatment for 18 h to recombinant zebrafish Fsh (100 ng/ml) (**Figure 4A**). In the basal medium condition, the treatments (T4, methimazole and methimazole + T4) did not change the basal androgen (11-KT) release capacity of zebrafish testicular tissue (**Figure 4C**). However, as expected, treatment with Fsh significantly increased the 11-KT level in the control group (**Figure 4C**). Also, treatment with T4 was responsive to Fsh but to a level not significantly different from the control (**Figure 4C**). In comparison, the isolated testis from methimazole-treated zebrafish was completely unresponsive to Fsh (**Figure 4C**). However, co-treatment with T4 restored the Fsh-induced response by increasing the 11-KT concentration to the level observed following treatment of the control group with Fsh alone (**Figure 4C**).

3.6 Transcript Levels of Selected Genes in the Brain and Pituitary

In this experiment, we measured brain transcript levels of a number of neurohypothalamic peptides, including *gnrh2* and *gnrh3*, *gnih*, and *crf*, as well as pituitary gonadotropin hormone subunits, *fshb*, *lhb*, and *tshb* in the methimazole-

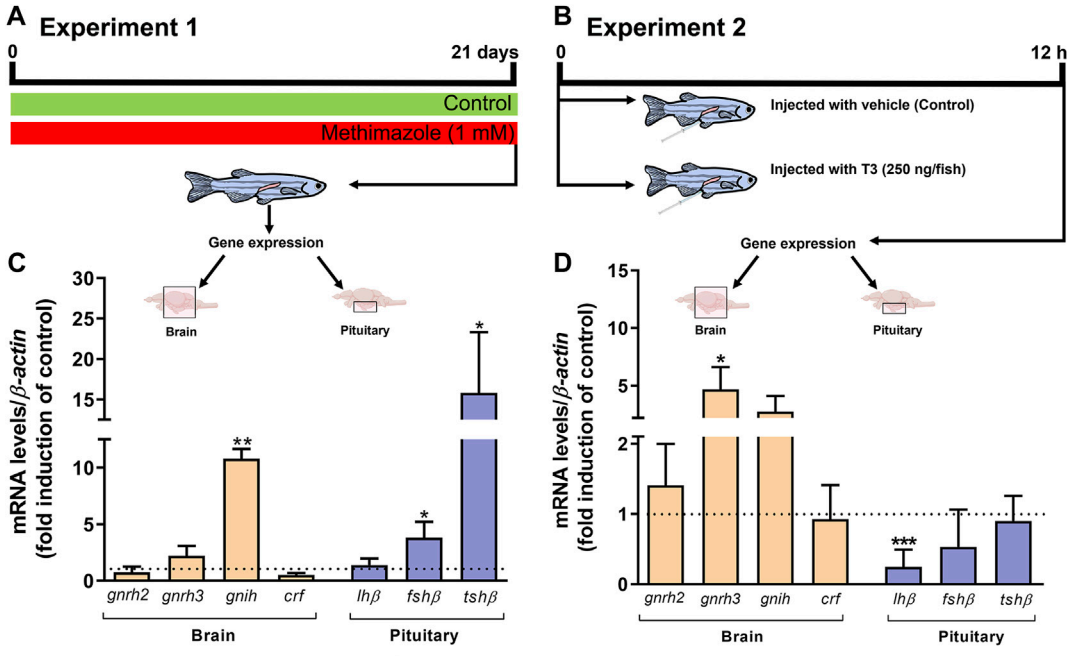

FIGURE 5 | (A) Experiment 1: zebrafish adult males were exposed to methimazole-induced hypothyroidism for 3 weeks. **(B)** Experiment 2: zebrafish adult males were injected with 0 or 250 ng of T3/fish and tissue were collected 12 h post-injection. Relative mRNA levels of selected genes, including *gnrh2* and *gnrh3* (gonadotropin-releasing hormones), *gnih* (gonadotropin-inhibitory hormone), and *crf* (corticotropin-releasing hormone), expressed in the brain ($n = 8$), and *lhβ* (luteinizing hormone), *fshβ* (follicle-stimulating hormone), and *tshβ* (thyroid-stimulating hormone) expressed in the pituitary ($n = 4$ pools of 4 pituitaries for each pool) from the methimazole group **(C)** and 12 h post-injection with 0 and 250 ng of T3/fish **(D)**. Ct values were normalized with *β-actin* and expressed as relative values of control (no-treated fish) levels of expression. Bars represent mean ± SEM fold-change relative to the control, which is set at 1. Student unpaired *t*-test, $^{*}p < 0.05$, $^{**}p < 0.01$ and $^{***}p < 0.001$.

induced hypothyroidism in fish (**Figure 5A,C**). As shown in **Figure 5C**, we observed a significant increase in the *gnih* transcript level compared to the control shown as the dotted line. Transcript levels of the other neuropeptides measured including *gnrh2*, *gnrh3* and *crf* remained unchanged. In the same group of methimazole-treated fish, the results the pituitary glycoprotein hormone subunits, demonstrate significant increase in *fshb* mRNA and a massive increase in *tshb* transcript levels in the methimazole-induced hypothyroid fish (**Figure 5C**). No change was observed in the *lhb* transcript level (**Figure 5C**).

We also measured the same transcript levels following 12 h acute treatment with 250 ng of T3/fish *in vivo* (**Figures 5B,D**). In this experiment T3 injection did not significantly alter *gnih, gnrh2* and *crf,* but significantly increased the *gnrh3* transcript level (**Figure 5D**). In the same group of fish, acute treatment with 250 ng of T3/fish significantly reduced the pituitary *lhb* but was without effect on the *fshb* and *tshb* transcript levels (**Figure 5D**).

3.7 *In Vitro*: Effects of T3 on Zebrafish Spermatogenesis

In this research, we also examined the direct action of T3 at 100 nM on *ex vivo* culture of zebrafish testis for 7 days (**Figure 6A**) and results provide information on the proportion of germ cells in the cultured testis. Histomorphometrical evaluation of zebrafish testis revealed that treatment with T3 significantly stimulated the type A undifferentiated spermatogonia (A_{und}) abundance with no effect on type A differentiated spermatogonia cells as compared to basal medium incubation (**Figure 6B**). In the same tissue, we observed a reduction in type B spermatogonia (SpgB) abundance (**Figure 6B**). As for meiotic and post-meiotic cells, treatment with T3 reduced the proportion of area occupied by Spc and Spt when compared to basal condition (**Figure 6B**). Interestingly, the number of spermatozoa was stimulated in zebrafish testis treated with T3 as clearly shown by the analysis of spermatozoa number by field (**Figure 6C**). In addition to these results, the effect of thyroid hormones on testicular gene expression was analyzed (**Figures 6D–G**) (**Supplementary Figure S1**). Several concentrations of T3 and T4 (10, 100 and 1,000 nM) were tested in zebrafish testis. T4 did not change the expression of any transcript (*nanos2*, *sycp3l*, *3β-HSD* and *cyp17a1*) (**Supplementary Figure S1**). On the other hand, expression analysis revealed that T3 (100 and 1,000 nM) increased *nanos2* (**Figure 6D**), and up-regulated *sycp3l* transcript levels at 100 nM (**Figure 6E**). Levels of *3β-HSD* and *cyp17a1* were also quantified and did not change within any levels of T3 (**Figures 6F,G**).

4 DISCUSSION

This study demonstrated the importance of thyroid hormones as a factor controlling zebrafish spermatogenesis, using

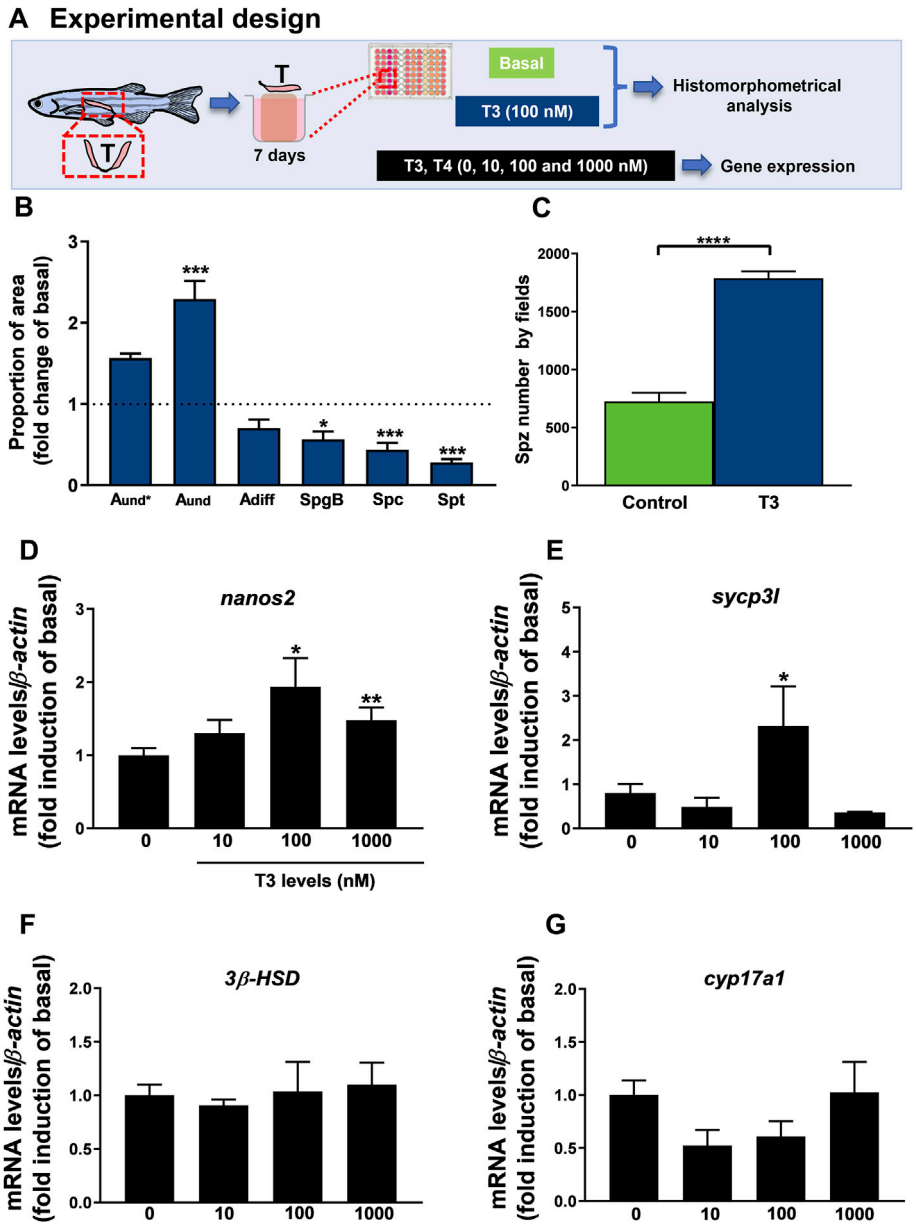

FIGURE 6 | (A) Experimental design of histomorphometrical analysis of zebrafish testicular explants incubated for 7 days (long-term exposure) with T3 (100 nM) compared to the control (basal) and gene expression of relative mRNA levels of several selected genes in zebrafish testis incubated to different concentrations of T3 (0, 10, 100 e 1,000 nM) for 7 days. **(B)** Histomorphometrical analysis of testicular explants containing types A undifferentiated spermatogonia (A_{und*}, A_{und}), type A differentiated spermatogonia (A_{diff}), type B spermatogonia (SpgB), spermatocytes (Spc), and spermatids (Spt). Bars (mean ± SEM; $n = 8$) are expressed as fold-change relative to the untreated group (control) (dotted black line set at 1). **(C)** Spermatozoa number per field generated by using IMAGEJ Software from zebrafish explants incubated for 7 days with basal (L-15) and T3 (100 nM). Bars (mean ± SEM; $n = 8$). Student paired *t*-test, $^{*}p < 0.05$ and $^{***}p < 0.001$ denote significant differences between control and treated fish. The selected genes *nanos2* **(D)**, *sycp3l* (synaptonemal complex protein 3) **(E)**, *3β-HSD* (3-beta (β)-hydroxysteroid dehydrogenase) **(F)**, and *cyp17a1* (17α-hydroxylase/17,20 lyase/17,20 desmolase) **(G)** were evaluated. Ct values were normalized with *β-actin* and expressed as relative values of basal levels of expression. Bars represent the mean ± SEM fold change ($n = 8$), relative to the control (basal), which is set at 1. Paired *t -test*, $^{*}p < 0.05$, $^{**}p < 0.01$.

methimazole-induced hypothyroidism in fish as a model organism. Methimazole is a thionamide antithyroid drug, and it is known to block thyroid hormone synthesis by affecting the iodination process of tyrosine residues in the thyroglobulin (Abraham and Acharya, 2010; Carvalho and Dupuy, 2017). Methimazole acts through suppressing the thyroid peroxidase (TPO) activity which is responsible to catalyze the conversion of iodide to iodine for the production of T4 and T3. In addition to this effect, methimazole is rapidly metabolized by the liver and may cause hepatotoxicity and other potent side effects (Heidari et al., 2015). In this study, we could not rule out or monitor the side effects caused by methimazole treatment. However, the

effects observed in zebrafish spermatogenesis are caused by thyroid hormone deficiency, and not due to methimazole side effect. We demonstrated that the defects observed in zebrafish spermatogenesis after methimazole treatment were completely recovered by adding T4 in the last week of methimazole treatment (see below). In addition, we confirmed that plasma T3 levels were significantly decreased following methimazole treatment when compared to control, and restored in the methimazole + T4 co-treatment. This data was also supported by histological analysis of thyroid follicles which displayed disturbed structure and less colloid production following methimazole exposure, while normal thyroid follicle histology and colloid production were found after co-treatment with T4. Another evidence is the testicular connexin (*cx43*), as it is the potential target for thyroid hormones (Poguet et al., 2003; Gilleron et al., 2006). Gilleron and collaborators (2006) demonstrated that propylthiouracil (PTU; another thyroid disruptor) decreases *cx43* mRNA levels in rat testes. In our study, the lower expression of *cx43* in the methimazole group indicates that methimazole treatment led to hypothyroidism in the male zebrafish. Altogether, this evidence confirmed that zebrafish testicular function and spermatogenesis are affected when lowering thyroid hormone levels, and the observed defects were nullified when plasma thyroid hormone levels were recovered to their basal levels.

Histomorphometric evaluation of zebrafish spermatogenesis demonstrated that methimazole-induced hypothyroidism remarkably increased the proportion area occupied by type A_{und*} (the most undifferentiated spermatogonia), type A_{diff} and type B spermatogonia, while the number of spermatozoa was decreased. Furthermore, our results demonstrate that the proportion of Spc and Spt were not affected in hypothyroid testis compared with the control animals. It has been well-established that spermatogenesis development is supported and regulated by gonadotropic hormones, FSH and LH which mainly target actions on somatic testicular cells such as Sertoli and Leydig cells (Planas et al., 1993; Campbell et al., 2003; Huhtaniemi and Themmen, 2005; García-López et al., 2010; Schulz et al., 2010; Flood et al., 2013). Likewise, thyroid hormones have also been shown to play an essential role in testicular physiology (Chiao et al., 2002; Cooke et al., 2004; Holsberger and Cooke, 2005; Wagner et al., 2008, 2009; Morais et al., 2013; Tovo-Neto et al., 2018). In rats, previous studies have reported that hypothyroidism decreases plasma levels of gonadotropins and reduces the number and size of gonadotrophs (Bruni et al., 1975; Ruiz et al., 1988), suggesting that the absence of thyroid hormones is associated with gonadal dysfunctions (Amin and El-Sheikh, 1977; Hernandez, 2018). Further, the level of relevant androgen (11-KT) that stimulates spermatogenesis decreased significantly in the plasma of zebrafish following treatment with methimazole. These results, in part, could explain the observed increase in different populations of spermatogonia (A_{und*}, A_{diff} and B) and decrease in spermatozoa number, demonstrating the impact of thyroid hormone depletion on germ cell development and testicular function. Similar findings have been reported for male Japanese quail, wherein treatment with methimazole decreased body and testes weight as well as plasma levels of LH and testosterone (Weng et al., 2007). In this same study, the data showed decreased spermatogenesis in seminiferous tubules of the treatment group (Weng et al., 2007). Altogether, these results demonstrate that gonadal function is associated with normal thyroid action. Fluctuations in thyroid hormone levels can directly modulate gonadotropin actions and affect Sertoli and Leydig cell proliferation (Castañeda-Cortés et al., 2014), resulting in the impairment of spermatogenesis, which may be caused by low FSH level and delay of Sertoli cell maturation (Hernandez, 2018).

We also examined the effects of methimazole co-treated with T4. Our results demonstrate that co-treatment with T4 partially restored zebrafish spermatogenesis and spermatozoa production in the methimazole-induced hypothyroid fish. Interestingly, the administration of T4 to the hypothyroid group increased the proportion of meiotic (Spc) and post-meiotic (Spt) cells compared with the control and methimazole groups. These results support the hypothesis that thyroid hormones are involved, directly or indirectly, with meiosis entry in the zebrafish testis.

The observed transcript analysis in zebrafish testis is to some extent in agreement with histomorphometric results. With respect to the germ cell markers genes of zebrafish spermatogenesis, the results indicated that mRNA levels of *nanos2* (marker of type A undifferentiated spermatogonia) (Aoki et al., 2009) and *dazl* (marker of differentiation) (Chen et al., 2013) were greater in the methimazole-treated group, in agreement with the histomorphometry showing an accumulation of pre-meiotic cells (A_{und*}, A_{diff} and B). The observed upregulation of these transcripts in the methimazole treated group suggest that euthyroid condition may be important for normal spermatogonial cell development in zebrafish. However, the level of *odf3a* (marker of spermatids) (Yano et al., 2008) was upregulated in the methimazole group, although the proportion of spermatids was not affected in the present study. The affected testicular functions did not always recover following co-treatment with T4 to counter hypothyroidism.

Other essential components of the thyroid hormones axis are the thyroid receptors (TRs), which are crucial for testis development and function (Valadares et al., 2008; Lema et al., 2009; Wajner et al., 2009; Dittrich et al., 2011). According to Habibi and collaborators (2012), TRs are expressed by some different cell types, and thyroid hormones have pleiotropic effects, including effects on the gonads. In the latter study in goldfish, *in vivo* and *in vitro*, thyroid hormones were shown to exert both direct and indirect actions on gonadal steroid synthesis, and steroid receptor expression in a seasonally dependent manner (Allan and Habibi, 2012; Habibi et al., 2012). In zebrafish testis, *thrα* was shown to be expressed in the Sertoli and Leydig cells, whereas *thrβ* expression was only observed in the Leydig cell (Morais et al., 2013). In the present study, methimazole-induced hypothyroidism stimulated *thrβ* transcript level, but increase in *thrα* was only significant in presence of T4 compared to control. Other investigators also reported that T3 treatment only elevated *thrβ* in the ovary and testis of *Pimephales promelas* (Lema et al., 2009). Similarly, *fshr* mRNA levels were also upregulated in hypothyroid co-treated with T4. These results suggest that chronic hyperthyroidism may alter thyroid hormone sensitivity and possibly alter other parameters not clear at the present time. Similarly, in rats, higher FSH-R mRNA levels were detected in hypothyroidism. It was suggested that the upregulated FSH-R mRNA level may have resulted from the elevated proportion of Sertoli cells in rats (Rao et al., 2003). Likewise, in zebrafish, the

increase of *fshr* transcripts following co-treatment with T4 could be due to Sertoli cell proliferation. Morais and collaborators (2013) revealed that T3 stimulates *in vitro* Sertoli cell proliferation in zebrafish testes. Moreover, the same study showed that Sertoli cells express both *thrα* and *fshr*, and treatment with T3 potentiates Fsh *in vitro* actions in the zebrafish testis (Morais et al., 2013). This is also consistent with the observation that *fshr* transcript levels was stimulated by methimazole-induced hypothyroid fish co-treated with T4. These results support the view that thyroid hormones and gonadotropins stimulate spermatogenesis by stimulating gonadal androgen production, which in turn mediate the start of spermatogenesis.

Interestingly, mRNA expression of other key gonadal growth factors as *igf3* (Wang et al., 2008) and *amh* (Miura et al., 2002) did not change in the methimazole or methimazole co-treated with T4 groups. However, *gsdf* (Gautier et al., 2011) was upregulated in both groups. *gsdf* is expressed by Sertoli cells and exerts an essential role in the control of spermatogenesis, including germ cell proliferation and differentiation (Gautier et al., 2011; Yan et al., 2017).

Decreased thyroid hormones levels by methimazole in male zebrafish are associated with decreased 11-KT plasma levels. Previous reports have demonstrated that PTU treatment also decreases serum testosterone concentrations in other vertebrate species, such as rats (Chiao et al., 2000). In another study, exposure of *Clarias gariepinus* to thiourea, reduced androgen levels leading to testicular regression (Swapna et al., 2006; Swapna and Senthikumaran, 2007). This is consistent with the present study demonstrating lower 11-KT plasma levels in the methimazole group, in addition to lower levels of steroidogenic enzyme (*cyp17a1*) and androgen-sensitive gene (*insl3*) mRNA levels. These transcript levels remained the same even after co-treatment with T4. However, treatment of methimazole-induced hypothyroid fish effectively rescued 11-KT levels in the plasma which was correlated with the revival of spermatozoa number in zebrafish testis. Thus, impairing thyroid action within the physiological limit of restoration is a valid approach to explain the role of thyroid hormones in male zebrafish reproduction. Interestingly, Houbrechts et al. (2019) demonstrated the Dio2-knockout (KO) zebrafish ($dio2^{-/-}$) significantly reduced androgen (11-KT and testosterone) levels in the testis, and steroidogenesis and steroid signaling were similarly disturbed when compared with control group. This indicates that absence of thyroid hormones by goitrogen treatment or DIO2 KO, which suppresses thyroid hormone production, may act directly on the testis to repress steroidogenesis. These data also reveal that normal thyroid hormone levels are fundamental to normal reproduction in zebrafish. On the other hand, Song et al. (2021) have recently reported that knockout of *tshba* in zebrafish resulted in defective development of secondary sex characteristics, but did not affect the spermatogenesis, indicating that thyroid hormones may be not necessary to male germ cell development. According to our knowledge, we cannot compare the methimazole exposure with the knockout of *tshba* in zebrafish. These two models represent thyroid loss of function in different stages of life of zebrafish. Our model is a chronic exposure (21 days) in sexually mature males (3 months of age), while *tshb* knockout took place from fertilization until sexual maturation, i.e., along the entire development of zebrafish. In addition to that, we believe that our results are similar to the ones obtained in the knockout of *tshb* in zebrafish. Song and collaborators (2021) reported reproductive performance defects, but normal gonadal histology. However, no histomorphometry data (e.g., germ cell cyst composition) was performed in their study, and detailed analysis of the gonadal histology (Song et al., 2021) showed a reduced testicular lumen and apparently less spermatozoa in the *tshba*−/− as compared to wild type (*tshba*+/+). Histomorphometric analysis of zebrafish *tshba*−/− testis should be investigated to address whether thyroid hormones are necessary for zebrafish spermatogenesis.

To address whether thyroid hormones can affect the expression of regulatory players of HPG axis in long-term or acute treatments, we performed two experiments: experiment 1 (methimazole exposure for 21 days—lowering of thyroid hormones) and experiment 2 (intracoelomic injection of T3 for 12 h) (**Figure 5**). In experiment 1, while transcript levels of gonadotropin-releasing hormones, *gnrh2* and *gnrh3* did not change, *gnih* mRNA levels were significantly elevated in the brain of animals after methimazole exposure. GnIH is a gonadotropin-inhibitory hormone and it has been shown to block gonadotropin secretion and reduce its plasma levels, therefore affecting reproduction (Tsutsui et al., 2017). In fish, GnIH orthologs have been described to exert either stimulatory or inhibitory actions on gonadotropin secretion depending on the species studied, season, and mode of treatment (Amano et al., 2006; Zhang et al., 2010; Moussavi et al., 2012; 2013; 2014; Branco et al., 2018; Fallah et al., 2019; Ma et al., 2020a, Ma et al., 2020b). In cyprinids, Zhang and collaborators (2010) have shown that zebrafish GnIH decreases plasma gonadotropin levels in goldfish. In mammals, Tsutsui et al. (2017) remarkably showed that hypothyroidism induced by PTU increases GnIH expression and reduces gonadotropins and plasma steroid levels in female mice. Altogether, this evidence can support that the decrease in plasma androgen level observed after methimazole treatment might be mediated by GnIH. As shown previously in goldfish, GnIH mediated inhibition of reproduction does not always correlate closely by inhibition of gonadotropin transcript levels due to uncoupling of release and synthesis. In this context, it was demonstrated that GnIH can increase gonadotropin subunit mRNA levels while reducing secretion of the hormones (Moussavi et al., 2012; Moussavi et al., 2013; Moussavi et al., 2014; Ma et al., 2020a, Ma et al., 2020b). Thus, the inhibition may be at the protein level, since *fshb* transcript level was increased in the pituitary of the methimazole-treated group as a compensatory/feedback mechanism. Similarly, Yoshiura et al. (1999) showed in goldfish that thiourea exposure for 2 weeks increased Fsh mRNA levels. A contributing factor could be due to feedback exerted by lower plasma 11-KT levels seen in these animals (Rojdmark et al., 1988; Trudeau et al., 1993; Habibi and Huggard-Nelson, 1998; Huggard-Nelson et al., 2002). There is increasing evidence that the effects of thyroid hormones as well as brain-pituitary-gonadal hormones are diverse, and change with season, mode of action, time-course, and concentration (Nelson and Habibi 2006, Nelson and Habibi 2008, Nelson and Habibi 2009; Nelson et al., 2011; Habibi et al., 2012; Moussavi et al., 2012, Moussavi et al., 2013, Moussavi et al., 2014; Nelson and Habibi 2016; Ma et al., 2020a, Ma et al., 2020b). This is reflected in the experiment 2 in which the acute treatment for 12 h with T3 injection resulted in a different effect than the ones observed

in the chronic treatment with methimazole. In Experiment 2, injection of T3 increases *gnrh3* mRNA levels, which indicates that the HPG axis is stimulated/activated. As a consequence of the BPG stimulation, a negative feedback on gonadotropin mRNA levels is expected. This explains the reduced *lh* levels following T3 injection in Experiment 2. This is coherent with earlier study in goldfish showing reduction in gonadotropins and synthesis of gonadal steroids following 12 h injection with T3 (Nelson et al., 2010). Altogether these results demonstrate that the HPG axis is affected when altering thyroid hormone levels in long or acute treatments. However, we were not able to explain the differences of *lh* and *fsh* expression between the two Experiments/conditions. We believe that this difference might be due to distinct regulatory mechanisms between the two gonadotropins.

In addition to these data, we examined the actions of thyroid hormones on zebrafish spermatogenesis. Histomorphometrical analysis revealed an increase of type A undifferentiated spermatogonia (A_{und}) proportion in T3 *in vitro* exposure (100 nM), which may reflect the up-regulation of *nanos2* (marker of type A undifferentiated spermatogonia) (100 and 1,000 nM of T3). The number of spermatozoa also increased. This data corroborates the histomorphometry of the zebrafish testes from *in vivo* exposures using methimazole and methimazole co-treated with T4, indicating, therefore, a direct action of thyroid hormones in the zebrafish spermatogenesis. Previously, Morais et al. (2013) reported that the mitotic indices of A_{und} and Sertoli cells were stimulated after T3 treatment. Likewise, Safian and collaborators (2016) reported that T3 improved the formation of new cysts of A_{und}, accumulation of differentiated spermatogonia (A_{diff}) and reduction of spermatogonia Morais et al. (2013) using lower dose of T3 (50 ng/ml) also demonstrated an increase of type A undifferentiated spermatogonia, which was corroborated by higher BrdU mitotic index of this cell type in T3-treated tissue. In this study, we also investigated the effects of T3 and T4 on gene expression. Several concentrations of T3 and T4 (10, 100 and 1,000 nM) were tested in zebrafish testis. Interestingly, T3 also stimulated *sycp3l* (meiotic marker) mRNA levels at 100 nM. Levels of *3β-HSD* and *cyp17a1* were also quantified and did not change within any level of T3 exposure. Another interesting result is that T4 does not exert any change on testicular gene expression, indicating that thyroid hormones act via T3 in zebrafish testis. In sum, this data support that thyroid hormone T3 stimulates zebrafish spermatogenesis by proliferation, differentiation, and meiosis. These results provide important data about the roles of thyroid hormones on brain-pituitary-testis and reinforce the interaction between reproductive and thyroid axes.

5 CONCLUSION

The present study clearly demonstrated that hypothyroidism induced by methimazole significantly impair zebrafish germ cell development by delaying differentiation and meiosis, and decreasing the number of spermatozoa as well as impairing the hypothalamic–pituitary axis. We also provide evidence that testicular function is dependent on thyroid hormones. Taken together, these results provide support for the hypothesis that thyroid hormones are essential for spermatogenesis and maintaining normal function of the hypothalamic–pituitary-gonadal axis in adult zebrafish.

DATA AVAILABILITY STATEMENT

The original contributions presented in the study are included in the article/**Supplementary Material**, further inquiries can be directed to the corresponding author.

ETHICS STATEMENT

The animal study was reviewed and approved by the Handling and experimentation were performed according to the Brazilian legislation regulated by National Council for the Control of Animal Experimental (CONCEA) and Ethical Principles in Animal Research (Protocol n. 1031-CEUA) and University of Calgary animal care committee and in accordance with the guidelines of the Canadian Council of Animal Care (Protocol #AC19-0161).

AUTHOR CONTRIBUTIONS

RN, MR, AT-N, and HH designed the study. MR, AT-N, IR, LD, and HF performed the experiments. All authors analyzed the data; RN, MR, AT-N and HH wrote the paper. All authors edited the article.

FUNDING

This work was supported by the São Paulo Research Foundation (Nos. FAPESP 2017/15793-7 and 2018/15319-6) to MR, (Nos. FAPESP 2014/07620-7 and 2020/03569-8) to RN and Natural Sciences and Engineering Research Council of Canada to HH (NSERC Discovery Grant; project no. 1021837).

SUPPLEMENTARY MATERIAL

The Supplementary Material for this article can be found online at: https://www.frontiersin.org/articles/10.3389/fcell.2022.865948/full#supplementary-material

Supplementary Figure S1 | (A) Relative mRNA levels of selected genes expressed in zebrafish testis after incubated for 7 days to different concentrations of T4 (0, 10, 100 e 1,000 nM). The following genes were evaluated: *nanos2* **(B)**, *sycp3l* (synaptonemal complex protein 3) **(C)**, *3β-HSD* (3-beta (β)-hydroxysteroid dehydrogenase) **(D)**, and *cyp17a1* (17α-hydroxylase/17,20 lyase/17,20 desmolase) **(E)**. Ct values were normalized with *β-actin* and expressed as relative values of basal levels of expression. Bars represent the mean ± SEM fold change (n = 8), relative to the control (basal), which is set at 1. Paired *t -test*,

Supplementary Table S1 | Primers used for gene expression studies (qPCR) (FW = Forward; RV = Reverse).

REFERENCES

Abraham, P., and Acharya, S. (2010). Current and Emerging Treatment Options for Graves’ Hyperthyroidism. *Tcrm* 6, 29–40. doi:10.2147/tcrm.s5229

Allan, E. R. O., and Habibi, H. R. (2012). Direct Effects of Triiodothyronine on Production of Anterior Pituitary Hormones and Gonadal Steroids in Goldfish. *Mol. Reprod. Dev.* 79, 592–602. doi:10.1002/mrd.22066

Amano, M., Moriyama, S., Iigo, M., Kitamura, S., Amiya, N., Yamamori, K., et al. (2006). Novel Fish Hypothalamic Neuropeptides Stimulate the Release of Gonadotrophins and Growth Hormone from the Pituitary of Sockeye Salmon. *J. Endocrinol.* 188, 417–423. doi:10.1677/joe.1.06494

Amin, S. O., and El-Sheikh, A. S. (1977). Pituitary-testicular Function Changes in Hypo-And Hyperthyroid Male Rats. *Cells Tissues Organs* 98, 121–129. doi:10.1159/000144788

Aoki, Y., Nakamura, S., Ishikawa, Y., and Tanaka, M. (2009). Expression and Syntenic Analyses of FournanosGenes in Medaka. *Zoological Sci.* 26, 112–118. doi:10.2108/zsj.26.112

Blanton, M. L., and Specker, J. L. (2007). The Hypothalamic-Pituitary-Thyroid (HPT) axis in Fish and its Role in Fish Development and Reproduction. *Crit. Rev. Toxicol.* 37, 97–115. doi:10.1080/10408440601123529

Branco, G. S., Melo, A. G., Ricci, J. M. B., Digmayer, M., De Jesus, L. W. O., Habibi, H. R., et al. (2019). Effects of GnRH and the Dual Regulatory Actions of GnIH in the Pituitary Explants and Brain Slices of *Astyanax Altiparanae* Males. *General Comp. Endocrinol.* 273, 209–217. doi:10.1016/j.ygcen.2018.08.006

Bruni, J. F., Dibbet, J. A., Meites, J., and Meites, J. (1975). Effects of Hyper- and Hypothyroidism on Serum LH and FSH Levels in Intact and Gonadectomized Male and Female Rats. *Endocrinology* 97, 558–563. doi:10.1210/endo-97-3-558

Campbell, B., Dickey, J. T., and Swanson, P. (2003). Endocrine Changes during Onset of Puberty in Male Spring Chinook Salmon, *Oncorhynchus tshawytscha*1. *Biol. Reprod.* 69, 2109–2117. doi:10.1095/biolreprod.103.020560

Carr, J. A., and Patiño, R. (2011). The Hypothalamus-Pituitary-Thyroid axis in Teleosts and Amphibians: Endocrine Disruption and its Consequences to Natural Populations. *General Comp. Endocrinol.* 170, 299–312. doi:10.1016/j.ygcen.2010.06.001

Carvalho, D. P., and Dupuy, C. (2017). Thyroid Hormone Biosynthesis and Release. *Mol. Cell. Endocrinol.* 458, 6–15. doi:10.1016/j.mce.2017.01.038

CastaÃ±eda CortÃ©s, D. C., Langlois, V. S., and Fernandino, J. I. (2014). Crossover of the Hypothalamic Pituitaryâ€"Adrenal/Interrenal, â€"Thyroid, and â€"Gonadal Axes in Testicular Development. *Front. Endocrinol.* 5, 1–11. doi:10.3389/fendo.2014.00139

Chen, S. X., Bogerd, J., Schoonen, N. E., Martijn, J., De Waal, P. P., and Schulz, R. W. (2013). A Progestin (17α,20β-Dihydroxy-4-Pregnen-3-One) Stimulates Early Stages of Spermatogenesis in Zebrafish. *General Comp. Endocrinol.* 185, 1–9. doi:10.1016/j.ygcen.2013.01.005

Chiao, Y.-C., Cho, W.-L., and Wang, P. S. (2002). Inhibition of Testosterone Production by Propylthiouracil in Rat Leydig Cells1. *Biol. Reprod.* 67, 416–422. doi:10.1095/biolreprod67.2.416

Chiao, Y.-C., Lin, H., Wang, S.-W., and Wang, P. S. (2000). Direct Effects of Propylthiouracil on Testosterone Secretion in Rat Testicular Interstitial Cells. *Br. J. Pharmacol.* 130, 1477–1482. doi:10.1038/sj.bjp.0703444

Chiba, H., Amano, M., Yamada, H., Fujimoto, Y., Ojima, D., Okuzawa, K., et al. (2004). Involvement of Gonadotropin-Releasing Hormone in Thyroxine Release in Three Different Forms of Teleost Fish: Barfin Founder, Masu Salmon and Goldfish. *Fish. Physiol. Biochem.* 30, 267–273. doi:10.1007/s10695-005-8676-y

Cooke, P. S., Holsberger, D. R., Witorsch, R. J., Sylvester, P. W., Meredith, J. M., TreinenChapin, K. A. R. E., et al. (2004). Thyroid Hormone, Glucocorticoids, and Prolactin at the Nexus of Physiology, Reproduction, and Toxicology. *Toxicol. Appl. Pharmacol.* 194, 309–335. doi:10.1016/j.taap.2003.09.016

Cooke, P. S., and Meisami, E. (1991). Early Hypothyroidism in Rats Causes Increased Adult Testis and Reproductive Organ Size but Does Not Change Testosterone Levels*. *Endocrinology* 129, 237–243. doi:10.1210/endo-129-1-237

Cooke, P. S., Zhao, Y.-D., and Bunick, D. (1994). Triiodothyronine Inhibits Proliferation and Stimulates Differentiation of Cultured Neonatal Sertoli Cells: Possible Mechanism for Increased Adult Testis Weight and Sperm Production Induced by Neonatal Goitrogen Treatment1. *Biol. Reprod.* 51, 1000–1005. doi:10.1095/biolreprod51.5.1000

Cyr, D., and Eales, J. G. (1996). Interrelationships between Thyroidal and Reproductive Endocrine Systems in Fish. *Rev. Fish. Biol. Fish.* 6, 165–200. doi:10.1007/BF00182342

de Franca, L. R., Hess, R. A., Cooke, P. S., and Russell, L. D. (1995). Neonatal Hypothyroidism Causes Delayed Sertoli Cell Maturation in Rats Treated with Propylthiouracil: Evidence that the Sertoli Cell Controls Testis Growth. *Anat. Rec.* 242, 57–69. doi:10.1002/ar.1092420108

De Oña, C. R., Obregón, M. J., Del Rey, F. E., and De Escobar, G. M. (1988). Developmental Changes in Rat Brain 5′-Deiodinase and Thyroid Hormones during the Fetal Period: The Effects of Fetal Hypothyroidism and Maternal Thyroid Hormones. *Pediatr. Res.* 24, 588–594. doi:10.1203/00006450-198811000-00010

Dittrich, R., Beckmann, M. W., Oppelt, P. G., Hoffmann, I., Lotz, L., Kuwert, T., et al. (2011). Thyroid Hormone Receptors and Reproduction. *J. Reproductive Immunol.* 90, 58–66. doi:10.1016/j.jri.2011.02.009

Duarte-Guterman, P., Navarro-Martín, L., and Trudeau, V. L. (2014). Mechanisms of Crosstalk between Endocrine Systems: Regulation of Sex Steroid Hormone Synthesis and Action by Thyroid Hormones. *General Comp. Endocrinol.* 203, 69–85. doi:10.1016/j.ygcen.2014.03.015

Fallah, H. P., Rodrigues, M. S., Corchuelo, S., Nóbrega, R. H., and Habibi, H. R. (2020). Role of GnRH Isoforms in Paracrine/autocrine Control of Zebrafish (*Danio rerio*) Spermatogenesis. *Endocrinology* 161, 1–16. doi:10.1210/endocr/bqaa004

Fallah, H. P., Tovo-Neto, A., Yeung, E. C., Nóbrega, R. H., and Habibi, H. R. (2019). Paracrine/autocrine Control of Spermatogenesis by Gonadotropin-Inhibitory Hormone. *Mol. Cell. Endocrinol.* 492, 110440. doi:10.1016/j.mce.2019.04.020

Figueiredo, A. F. A., Wnuk, N. T., Tavares, A. O., Miranda, J. R., Hess, R. A., de França, L. R., et al. (2019). Prepubertal PTU Treatment in Rat Increases Sertoli Cell Number and Sperm Production. *Reproduction* 158, 201–211. doi:10.1530/REP-19-0127

Flood, D. E. K., Fernandino, J. I., and Langlois, V. S. (2013). Thyroid Hormones in Male Reproductive Development: Evidence for Direct Crosstalk between the Androgen and Thyroid Hormone Axes. *General Comp. Endocrinol.* 192, 2–14. doi:10.1016/j.ygcen.2013.02.038

García-López, A., de Jonge, H., Nóbrega, R. H., de Waal, P. P., Van Dijk, W., Hemrika, W., et al. (2010). Studies in Zebrafish Reveal Unusual Cellular Expression Patterns of Gonadotropin Receptor Messenger Ribonucleic Acids in the Testis and Unexpected Functional Differentiation of the Gonadotropins. *Endocrinology* 151, 2349–236060. doi:10.1210/en.2009-1227

Gautier, A., Sohm, F., Joly, J.-S., Le Gac, F., and Lareyre, J.-J. (2011). The Proximal Promoter Region of the Zebrafish Gsdf Gene Is Sufficient to Mimic the Spatio-Temporal Expression Pattern of the Endogenous Gene in Sertoli and Granulosa Cells1. *Biol. Reprod.* 85, 1240–1251. doi:10.1095/biolreprod.111.091892

Gilleron, J., Nebout, M., Scarabelli, L., Senegas-Balas, F., Palmero, S., Segretain, D., et al. (2006). A Potential Novel Mechanism Involving Connexin 43 Gap Junction for Control of Sertoli Cell Proliferation by Thyroid Hormones. *J. Cell. Physiol.* 209, 153–161. doi:10.1002/jcp.20716

Habibi, H. R., and Huggard, D. L. (1998). Testosterone Regulation of Gonadotropin Production in Goldfish. *Comp. Biochem. Physiology Part C Pharmacol. Toxicol. Endocrinol.* 119, 339–344. doi:10.1016/s0742-8413(98)00022-x

Habibi, H. R., Nelson, E. R., and Allan, E. R. O. (2012). New Insights into Thyroid Hormone Function and Modulation of Reproduction in Goldfish. *General Comp. Endocrinol.* 175, 19–26. doi:10.1016/j.ygcen.2011.11.003

Heidari, R., Niknahad, H., Jamshidzadeh, A., Eghbal, M. A., and Abdoli, N. (2015). An Overview on the Proposed Mechanisms of Antithyroid Drugs-Induced Liver Injury. *Adv. Pharm. Bull.* doi:10.5681/apb.2015.001

Hernandez, A. (2018). Thyroid Hormone Role and Economy in the Developing Testis. *Vitam. Horm.* 106, 473–500. doi:10.1016/bs.vh.2017.06.005

Hess, R. A., Cooke, P. S., Bunick, D., and Kirby, J. D. (1993). Adult Testicular Enlargement Induced by Neonatal Hypothyroidism Is Accompanied by Increased Sertoli and Germ Cell Numbers. *Endocrinology* 132, 2607–2613. doi:10.1210/endo.132.6.8504761

Holsberger, D. R., and Cooke, P. S. (2005). Understanding the Role of Thyroid Hormone in Sertoli Cell Development: a Mechanistic Hypothesis. *Cell. Tissue Res.* 322, 133–140. doi:10.1007/s00441-005-1082-z

Houbrechts, A. M., Van houcke, J., and Darras, V. M. (2019). Disruption of Deiodinase Type 2 in Zebrafish Disturbs Male and Female Reproduction. *J. Endocrinol.* 241, 111–123. doi:10.1530/JOE-18-0549

Huggard-Nelson, D. L., Nathwani, P. S., Kermouni, A., and Habibi, H. R. (2002). Molecular Characterization of LH-β and FSH-β Subunits and Their Regulation by Estrogen in the Goldfish Pituitary. *Mol. Cell. Endocrinol.* 188, 171–193. doi:10.1016/s0303-7207(01)00716-x

Huhtaniemi, I. T., and Themmen, A. P. N. (2005). Mutations in Human Gonadotropin and Gonadotropin-Receptor Genes. *Endo* 26, 207–218. doi:10.1385/ENDO:26:3:207

Jacobs, G. F. M., Michielsen, R. P. A., and Kühn, E. R. (1988). Thyroxine and Triiodothyronine in Plasma and Thyroids of the Neotenic and Metamorphosed Axolotl *Ambystoma mexicanum*: Influence of TRH Injections. *General Comp. Endocrinol.* 70, 145–151. doi:10.1016/0016-6480(88)90103-7

Jansen, H. T., Kirby, J. D., Cooke, P. S., Arambepola, N., and Iwamoto, G. A. (2007). Impact of Neonatal Hypothyroidism on Reproduction in the Male Hamster, *Mesocricetus auratus*. *Physiology Behav.* 90, 771–781. doi:10.1016/j.physbeh.2006.12.017

Kang, H., Kenealy, T. M., and Cohen, R. E. (2020). The Hypothalamic-Pituitary-Gonadal axis and Thyroid Hormone Regulation Interact to Influence Seasonal Breeding in Green Anole Lizards (*Anolis carolinensis*). *General Comp. Endocrinol.* 292, 113446. doi:10.1016/j.ygcen.2020.113446

Larsen, D. A., Swanson, P., Dickey, J. T., Rivier, J., and Dickhoff, W. W. (1998). In VitroThyrotropin-Releasing Activity of Corticotropin-Releasing Hormone-Family Peptides in Coho Salmon,*Oncorhynchus kisutch*. *General Comp. Endocrinol.* 109, 276–285. doi:10.1006/gcen.1997.7031

Leal, M. C., De Waal, P. P., García-López, Á., Chen, S. X., Bogerd, J., and Schulz, R. W. (2009). Zebrafish Primary Testis Tissue Culture: An Approach to Study Testis Function *Ex Vivo*. *General Comp. Endocrinol.* 162, 134–138. doi:10.1016/j.ygcen.2009.03.003

Lema, S. C., Dickey, J. T., Schultz, I. R., and Swanson, P. (2009). Thyroid Hormone Regulation of mRNAs Encoding Thyrotropin β-subunit, Glycoprotein α-subunit, and Thyroid Hormone Receptors α and β in Brain, Pituitary Gland, Liver, and Gonads of an Adult Teleost, *Pimephales promelas*. *J. Endocrinol.* 202, 43–54. doi:10.1677/JOE-08-0472

Ma, Y., Ladisa, C., Chang, J. P., and Habibi, H. R. (2020a). Multifactorial Control of Reproductive and Growth axis in Male Goldfish: Influences of GnRH, GnIH and Thyroid Hormone. *Mol. Cell. Endocrinol.* 500, 110629. doi:10.1016/j.mce.2019.110629

Ma, Y., Ladisa, C., Chang, J. P., and Habibi, H. R. (2020b). Seasonal Related Multifactorial Control of Pituitary Gonadotropin and Growth Hormone in Female Goldfish: Influences of Neuropeptides and Thyroid Hormone. *Front. Endocrinol.* 11, 175. doi:10.3389/fendo.2020.00175

Mackenzie, D. S., Sokolowska, M., Peter, R. E., and Breton, B. (1987). Increased Gonadotropin Levels in Goldfish Do Not Result in Alterations in Circulating Thyroid Hormone Levels. *General Comp. Endocrinol.* 67, 202–213. doi:10.1016/0016-6480(87)90149-3

Mackenzie, D. S. (1982). Stimulation of the Thyroid Gland of a Teleost Fish, Gillichthys Mirabilis, by Tetrapod Pituitary Glycoprotein Hormones. *Comp. Biochem. Physiology Part A Physiology* 72, 477–482. doi:10.1016/0300-9629(82)90111-6

Matta, S. L. P., Vilela, D. A. R., Godinho, H. P., and França, L. R. (2002). The Goitrogen 6-N-Propyl-2-Thiouracil (PTU) Given during Testis Development Increases Sertoli and Germ Cell Numbers Per Cyst in Fish: the tilapia (*Oreochromis niloticus*) Model. *Endocrinology* 143, 970–978. doi:10.1210/endo.143.3.8666

Mendis-Handagama, S. M., and Siril Ariyaratne, H. B. (2005). Leydig Cells, Thyroid Hormones and Steroidogenesis. *Indian J. Exp. Biol.* 43, 939–962.

Miura, T., Miura, C., Konda, Y., and Yamauchi, K. (2002). Spermatogenesis-preventing Substance in Japanese Eel. *Development* 129, 2689–2697. doi:10.1242/dev.129.11.2689

Morais, R. D. V. S., Nóbrega, R. H., Gómez-González, N. E., Schmidt, R., Bogerd, J., França, L. R., et al. (2013). Thyroid Hormone Stimulates the Proliferation of Sertoli Cells and Single Type A Spermatogonia in Adult Zebrafish (*Danio rerio*) Testis. *Endocrinology* 154, 4365–4376. doi:10.1210/en.2013-1308

Moussavi, M., Wlasichuk, M., Chang, J. P., and Habibi, H. R. (2012). Seasonal Effect of GnIH on Gonadotrope Functions in the Pituitary of Goldfish. *Mol. Cell. Endocrinol.* 350, 53–60. doi:10.1016/j.mce.2011.11.020

Moussavi, M., Wlasichuk, M., Chang, J. P., and Habibi, H. R. (2013). Seasonal Effect of Gonadotrophin Inhibitory Hormone on Gonadotrophin-Releasing Hormone-Induced Gonadotroph Functions in the Goldfish Pituitary. *J. Neuroendocrinol.* 25, 506–516. doi:10.1111/jne.12024

Moussavi, M., Wlasichuk, M., Chang, J. P., and Habibi, H. R. (2014). Seasonal Effects of GnIH on Basal and GnRH-Induced Goldfish Somatotrope Functions. *J. Endocrinol.* 223, 191–202. doi:10.1530/joe-14-0441

Mukhi, S., Torres, L., and Patiño, R. (2007). Effects of Larval-Juvenile Treatment with Perchlorate and Co-treatment with Thyroxine on Zebrafish Sex Ratios. *General Comp. Endocrinol.* 150, 486–494. doi:10.1016/j.ygcen.2006.11.013

Nelson, E. R., Allan, E. R. O., Pang, F. Y., and Habibi, H. R. (2011). Auto-regulation of Thyroid Hormone Receptors in the Goldfish Ovary and Testis. *General Comp. Endocrinol.* 172, 50–55. doi:10.1016/j.ygcen.2010.12.017

Nelson, E. R., Allan, E. R. O., Pang, F. Y., and Habibi, H. R. (2010). Thyroid Hormone and Reproduction: Regulation of Estrogen Receptors in Goldfish Gonads. *Mol. Reprod. Dev.* 77, 784–794. doi:10.1002/mrd.21219

Nelson, E. R., and Habibi, H. R. (2006). Molecular Characterization and Sex-Related Seasonal Expression of Thyroid Receptor Subtypes in Goldfish. *Mol. Cell. Endocrinol.* 253, 83–95. doi:10.1016/j.mce.2006.05.003

Nelson, E. R., and Habibi, H. R. (2008). Seasonal-related Homologous Regulation of Goldfish Liver Estrogen Receptor Subtypes. *Cybium* 32, 248–249. doi:10.26028/cybium/2008-322SP-124

Nelson, E. R., and Habibi, H. R. (2016). Thyroid Hormone Regulates Vitellogenin by Inducing Estrogen Receptor Alpha in the Goldfish Liver. *Mol. Cell. Endocrinol.* 436, 259–267. doi:10.1016/j.mce.2016.08.045

Nelson, E. R., and Habibi, H. R. (2009). Thyroid Receptor Subtypes: Structure and Function in Fish. *General Comp. Endocrinol.* 161, 90–96. doi:10.1016/j.ygcen.2008.09.006

Nóbrega, R. H., Greebe, C. D., Van De Kant, H., Bogerd, J., de França, L. R., and Schulz, R. W. (2010). Spermatogonial Stem Cell Niche and Spermatogonial Stem Cell Transplantation in Zebrafish. *PLoS One* 5, e12808. doi:10.1371/journal.pone.0012808

Orozco, A., Valverde-R, C., Olvera, A., and García-G, C. (2012). Iodothyronine Deiodinases: a Functional and Evolutionary Perspective. *J. Endocrinol.* 215, 207–219. doi:10.1530/JOE-12-0258

Pankhurst, N. W. (2016). "Reproduction and Development," in *Fish Physiology – Biology of Stress in Fish*. Editors C. B. Schreck, L. Tort, A. Farrell, and C. Brauner (San Diego, CA: Academic Press), 295–331. doi:10.1016/b978-0-12-802728-8.00008-4

Patiño, R., Wainscott, M. R., Cruzli, E. I., Balakrishnan, S., Mcmurry, C., Blazer, V. S., et al. (2003). Effects of Ammonium Perchlorate on the Reproductive Performance and Thyroid Follicle Histology of Zebrafish. *Environ. Toxicol. Chem.* 22, 1115–1121.

Planas, J. V., Swanson, P., and Dickhoff, W. W. (1993). Regulation of Testicular Steroid Production *In Vitro* by Gonadotropins (GTH I and GTH II) and Cyclic AMP in Coho Salmon (*Oncorhynchus kisutch*). *General Comp. Endocrinol.* 91, 8–24. doi:10.1006/gcen.1993.1099

Poguet, A.-L., Legrand, C., Feng, X. u., Yen, P. M., Meltzer, P., Samarut, J., et al. (2003). Microarray Analysis of Knockout Mice Identifies Cyclin D2 as a Possible Mediator for the Action of Thyroid Hormone during the Postnatal Development of the Cerebellum. *Dev. Biol.* 254, 188–199. doi:10.1016/s0012-1606(02)00039-8

Rao, J. N., Liang, J. Y., Chakraborti, P., and Feng, P. (2003). Effect of Thyroid Hormone on the Development and Gene Expression of Hormone Receptors in Rat Testes *In Vivo*. *J. Endocrinol. Investig.* 26, 435–443. doi:10.1007/BF03345199

Rodrigues, M. S., Fallah, H. P., Zanardini, M., Malafaia, G., Habibi, H. R., and Nóbrega, R. H. (2021). Interaction between Thyroid Hormones and Gonadotropin Inhibitory Hormone in *Ex Vivo* Culture of Zebrafish Testis: An Approach to Study Multifactorial Control of Spermatogenesis. *Mol. Cell. Endocrinol.* 532, 111331. doi:10.1016/j.mce.2021.111331

Röjdmark, S., Berg, A., and Kallner, G. (1988). Hypothalamic-pituitary-testicular axis in Patients with Hyperthyroidism. *Horm. Res.* 29, 185–190. doi:10.1159/000181000

Roy, P., Datta, M., Dasgupta, S., and Bhattacharya, S. (2000). Gonadotropin-Releasing Hormone Stimulates Thyroid Activity in a Freshwater Murrel, *Channa gachua* (Ham.), and Carps, Catla Catla (Ham.) and Cirrhinus Mrigala (Ham.). *General Comp. Endocrinol.* 117, 456–463. doi:10.1006/gcen.1999.7432

Safian, D., Morais, R. D. V. S., Bogerd, J., and Schulz, R. W. (2016). Igf Binding Proteins Protect Undifferentiated Spermatogonia in the Zebrafish Testis against Excessive Differentiation. *Endocrinology* 157, 4423–4433. doi:10.1210/en.2016-1315

Schulz, R. W., de França, L. R., Lareyre, J.-J., Legac, F., Chiarini-Garcia, H., Nobrega, R. H., et al. (2010). Spermatogenesis in Fish. *General Comp. Endocrinol.* 165, 390–411. doi:10.1016/j.ygcen.2009.02.013

Sharma, P., and Patiño, R. (2013). Regulation of Gonadal Sex Ratios and Pubertal Development by the Thyroid Endocrine System in Zebrafish (*Danio rerio*). *General Comp. Endocrinol.* 184, 111–119. doi:10.1016/j.ygcen.2012.12.018

Sharma, P., Tang, S., Mayer, G. D., and Patiño, R. (2016). Effects of Thyroid Endocrine Manipulation on Sex-Related Gene Expression and Population Sex Ratios in Zebrafish. *General Comp. Endocrinol.* 235, 38–47. doi:10.1016/j.ygcen.2016.05.028

Siril Ariyaratne, H. B., Ian Mason, J., and Mendis-Handagama, S. M. L. C. (2000). Effects of Thyroid and Luteinizing Hormones on the Onset of Precursor Cell Differentiation into Leydig Progenitor Cells in the Prepubertal Rat Testis1. *Biol. Reprod.* 63, 898–904. doi:10.1095/biolreprod63.3.898

Song, J., Lu, Y., Cheng, X., Shi, C., Lou, Q., Jin, X., et al. (2021). Functions of the Thyroid-Stimulating Hormone on Key Developmental Features Revealed in a Series of Zebrafish Dyshormonogenesis Models. *Cells*. doi:10.3390/cells10081984

Swapna, I., Rajasekhar, M., Supriya, A., Raghuveer, K., Sreenivasulu, G., Rasheeda, M. K., et al. (2006). Thiourea-induced Thyroid Hormone Depletion Impairs Testicular Recrudescence in the Air-Breathing Catfish, *Clarias gariepinus*. *Comp. Biochem. Physiology Part A Mol. Integr. Physiology* 144, 1–10. doi:10.1016/j.cbpa.2006.01.017

Swapna, I., and Senthilkumaran, B. (2007). Thyroid Hormones Modulate the Hypothalamo-Hypophyseal-Gonadal axis in Teleosts: Molecular Insights. *Fish. Physiol. Biochem.* 33, 335–345. doi:10.1007/s10695-007-9165-2

Teerds, K. J., de Rooij, D. G., De Jong, F. H., and Van Haaster, L. H. (1998). Development of the Adult-type Leydig Cell Population in the Rat Is Affected by Neonatal Thyroid Hormone Levels1. *Biol. Reprod.* 59, 344–350. doi:10.1095/biolreprod59.2.344

Tousson, E., Ali, E. M. M., Ibrahim, W., and Mansour, M. A. (2011). Proliferating Cell Nuclear Antigen as a Molecular Biomarker for Spermatogenesis in PTU-Induced Hypothyroidism of Rats. *Reprod. Sci.* 18, 679–686. doi:10.1177/1933719110395401

Tovo-Neto, A., da Silva Rodrigues, M., Habibi, H. R., and Nóbrega, R. H. (2018). Thyroid Hormone Actions on Male Reproductive System of Teleost Fish. *General Comp. Endocrinol.* 265, 230–236. doi:10.1016/j.ygcen.2018.04.023

Tovo-Neto, A., Martinez, E. R. M., Melo, A. G., Doretto, L. B., Butzge, A. J., Rodrigues, M. S., et al. (2020). Cortisol Directly Stimulates Spermatogonial Differentiation, Meiosis, and Spermiogenesis in Zebrafish (*Danio rerio*) Testicular Explants. *Biomolecules* 10, 429. doi:10.3390/biom10030429

Trudeau, V. L., Murthy, C. K., Habibi, H. R., Sloley, B. D., and Peter, R. E. (1993). Effects of Sex Steroid Treatments on Gonadotropin-Releasing Hormone-Stimulated Gonadotropin Secretion from the Goldfish Pituitary1. *Biol. Reprod.* 48, 300–307. doi:10.1095/biolreprod48.2.300

Tsutsui, K., Son, Y. L., Kiyohara, M., and Miyata, I. (2017). Discovery of GnIH and its Role in Hypothyroidism-Induced Delayed Puberty. *Endocrinology* 159, 62–68. doi:10.1210/en.2017-00300

ValadareS, N. F., Polikarpov, I., and Garratt, R. C. (2008). Ligand Induced Interaction of Thyroid Hormone Receptor Beta with its Coregulators. *J. Steroid Biochem. Mol. Biol.* 112, 205–212. doi:10.1016/j.jsbmb.2008.10.006

Van Der Ven, L. T. M., Van Den Brandhof, E.-J., Vos, J. H., Power, D. M., and Wester, P. W. (2006). Effects of the Antithyroid Agent Propylthiouracil in a Partial Life Cycle Assay with Zebrafish. *Environ. Sci. Technol.* 40, 74–81. doi:10.1021/es050972c

Wagner, M. S., Wajner, S. M., and Maia, A. L. (2009). Is There a Role for Thyroid Hormone on Spermatogenesis? *Microsc. Res. Tech.* 72, 796–808. doi:10.1002/jemt.20759

Wagner, M. S., Wajner, S. M., and Maia, A. L. (2008). The Role of Thyroid Hormone in Testicular Development and Function. *J. Endocrinol.* 199, 351–365. doi:10.1677/JOE-08-0218

Wajner, S. M., Wagner, M. S., and Maia, A. L. (2009). Clinical Implications of Altered Thyroid Status in Male Testicular Function. *Arq. Bras. Endocrinol. Metab.* 53, 976–982. doi:10.1590/S0004-27302009000800011

Wang, D.-S., Jiao, B., Hu, C., Huang, X., Liu, Z., and Cheng, C. H. K. (2008). Discovery of a Gonad-specific IGF Subtype in Teleost. *Biochem. Biophysical Res. Commun.* 367, 336–341. doi:10.1016/j.bbrc.2007.12.136

Weng, Q., Saita, E., Watanabe, G., Takahashi, S., Sedqyar, M., Suzuki, A. K., et al. (2007). Effect of Methimazole-Induced Hypothyroidism on Adrenal and Gonadal Functions in Male Japanese Quail (*Coturnix japonica*). *J. Reproduction Dev.* 53, 1335–1341. doi:10.1262/jrd.19081

Xie, X., Nóbrega, R., and Pšenička, M. (2020). Spermatogonial Stem Cells in Fish: Characterization, Isolation, Enrichment, and Recent Advances of *In Vitro* Culture Systems. *Biomolecules* 10, 644. doi:10.3390/biom10040644

Yan, Y.-L., Desvignes, T., Bremiller, R., Wilson, C., Dillon, D., High, S., et al. (2017). Gonadal Soma Controls Ovarian Follicle Proliferation through Gsdf in Zebrafish. *Dev. Dyn.* 246, 925–945. doi:10.1002/dvdy.24579

Yano, A., Suzuki, K., and Yoshizaki, G. (2008). Flow-cytometric Isolation of Testicular Germ Cells from Rainbow Trout (*Oncorhynchus mykiss*) Carrying the Green Fluorescent Protein Gene Driven by Trout Vasa Regulatory Regions. *Biol. Reprod.* 78, 151–158. doi:10.1095/biolreprod.107.064667

Yoshiura, Y., Sohn, Y. C., Munakata, A., Kobayashi, M., and Aida, K. (1999). Molecular Cloning of the cDNA Encoding the β Subunit of Thyrotropin and Regulation of its Gene Expression by Thyroid Hormones in the Goldfish, *Carassius auratus*. *Fish. Physiol. Biochem.* 21, 201–210. doi:10.1023/a:1007884527397

Zhang, Y., Li, S., Liu, Y., Lu, D., Chen, H., Huang, X., et al. (2010). Structural Diversity of the Gnih/gnih Receptor System in Teleost: Its Involvement in Early Development and the Negative Control of LH Release. *Peptides* 31, 1034–1043. doi:10.1016/j.peptides.2010.03.003

Conflict of Interest: The authors declare that the research was conducted in the absence of any commercial or financial relationships that could be construed as a potential conflict of interest.

Publisher's Note: All claims expressed in this article are solely those of the authors and do not necessarily represent those of their affiliated organizations, or those of the publisher, the editors and the reviewers. Any product that may be evaluated in this article, or claim that may be made by its manufacturer, is not guaranteed or endorsed by the publisher.

frontiers | Frontiers in Cell and Developmental Biology

ORIGINAL RESEARCH
published: 07 July 2022
doi: 10.3389/fcell.2022.829067

TFP5-Mediated CDK5 Activity Inhibition Improves Diabetic Nephropathy *via* NGF/Sirt1 Regulating Axis

*Shi-Lu Cao[1,2†], Hong-Yan Luo[1,2†], Yong-Cai Gao[1†], Xiao-Mei Lan[3,4], Shun-Yao Liu[1,2], Bo Li[1,4], Li Bao[1,2], Jing E.[1,5], Danna Ma[1,5], Guo-Qing Zhang[1], Li-Rong Yang[1], Xi Bao[1,2] and Ya-Li Zheng[1,2]**

[1]Department of Nephrology, Ningxia Medical University Affiliated People's Hospital of Autonomous Region of Yinchuan, Yinchuan, China, [2]The Third Clinical Medical College of Ningxia Medical University, Yinchuan, China, [3]Department of Geriatrics, Ningxia Medical University Affiliated People's Hospital of Autonomous Region of Yinchuan, Yinchuan, China, [4]Dialysis Department of Nephrology Hospital, The First Affiliated Hospital of Xi'an Jiaotong University, Xi'an, China, [5]Department of Nephrology, The Second Affiliated Hospital of Xi'an Jiaotong University, Xi'an, China

OPEN ACCESS

Edited by:
Natalia Martins Feitosa, Federal University of Rio de Janeiro, Brazil

Reviewed by:
Christopher Wilcox, Georgetown University, United States
Jackson De Souza-Menezes, Federal University of Rio de Janeiro, Brazil

***Correspondence:**
Ya-Li Zheng
zhengyali@nxrmyy.com

[†]These authors have contributed equally to this work

Specialty section:
This article was submitted to Molecular and Cellular Pathology, a section of the journal Frontiers in Cell and Developmental Biology

Received: 04 December 2021
Accepted: 27 May 2022
Published: 07 July 2022

Citation:
Cao S-L, Luo H-Y, Gao Y-C, Lan X-M, Liu S-Y, Li B, Bao L, E. J, Ma D, Zhang G-Q, Yang L-R, Bao X and Zheng Y-L (2022) TFP5-Mediated CDK5 Activity Inhibition Improves Diabetic Nephropathy via NGF/Sirt1 Regulating Axis. Front. Cell Dev. Biol. 10:829067. doi: 10.3389/fcell.2022.829067

Diabetic nephropathy (DN) is one of the leading causes of chronic kidney disease (CKD), during which hyperglycemia is composed of the major force for the deterioration to end-stage renal disease (ESRD). However, the underlying mechanism triggering the effect of hyperglycemia on DN is not very clear and the clinically available drug for hyperglycemia-induced DN is in need of urgent development. Here, we found that high glucose (HG) increased the activity of cyclin-dependent kinase 5 (CDK5) dependent on P35/25 and which upregulated the oxidative stress and apoptosis of mouse podocytes (MPC-5). TFP5, a 25-amino acid peptide inhibiting CDK5 activity, decreased the secretion of inflammation cytokines in serum and kidney, and effectively protected the kidney function in *db/db* mouse from hyperglycemia-induced kidney injuries. In addition, TFP5 treatment decreased HG-induced oxidative stress and cell apoptosis in MPC-5 cells and kidney tissue of *db/db* mouse. The principal component analysis (PCA) of RNA-seq data showed that MPC-5 cell cultured under HG, was well discriminated from that under low glucose (LG) conditions, indicating the profound influence of HG on the properties of podocytes. Furthermore, we found that HG significantly decreased the level of NGF and Sirt1, both of which correlated with CDK5 activity. Furthermore, knockdown of NGF was correlated with the decreased expression of Sirt1 while NGF overexpression leads to upregulated Sirt1 and decreased oxidative stress and apoptosis in MPC-5 cells, indicating the positive regulation between NGF and Sirt1 in podocytes. Finally, we found that K252a, an inhibitor of NGF treatment could undermine the protective role of TFP5 on hyperglycemia-induced DN in *db/db* mouse model. In conclusion, the CDK5-NGF/Sirt1 regulating axis may be the novel pathway to prevent DN progression and TFP5 may be a promising compound to improved hyperglycemia induced DN.

Keywords: TFP5, diabetic nephropathy, CDK5, NGF, Sirt1

INTRODUCTION

Chronic kidney disease (CKD) is a prevalent and irreversible syndrome of kidney disease (Ammirati, 2020). Clinically, CKD patients present a reduced glomerular filtration rate (GFR), increased urinary albumin excretion, and creatinine (Vega and Huidobro E., 2019). Usually, the patient was diagnosed as CKD when GFR <60 ml/min/1.73 m^2, and the content of albumin was >30 mg in the 24 h urine, or isolated urine sample, rectified by urinary creatinine (Ammirati, 2020).

CKD often results in a sustained damage of renal parenchyma, and finally promotes deterioration of renal function (Akchurin, 2019). Among the pathogenic factors, diabetic nephropathy (DN) is one of the primary causes of end-stage renal disease (ESRD) world-wide (Lo et al., 2018). Fifty percent of type 2 diabetes (T2D) patients and 33% of type 1 diabetes (T1D patients) finally develop CKD (Thomas et al., 2015). The different morbidity may result from different causes, such as obesity, intrarenal vascular disease, atherosclerosis, or renal ischemia in T2D (Anders et al., 2018). CKD is correlated with the dysfunction of glomerular basement membrane composed of fenestrated endothelial cells and interdigitating cell derived from podocytes. The filtration barrier exerts its function by allowing just small molecules that are without a high negative charge to pass through (Jefferson et al., 2008). Evidence showed that excessive podocyte damage will eventually result in extensive podocyte loss, and the number of podocytes exhibited a gradual decrease as the disease deteriorated. Podocytes lacked the ability to renew, and excessive loss of podocytes will finally leads to large-scale replacement of glomerular basement membrane by the parietal epithelial cells and the Bowman capsule, which accelerates the progression segmental glomerulosclerosis (Nakamura et al., 2000; Langham et al., 2002). Therefore, the intact podocytes are necessary for the renal function in diabetic kidney disease. A number of studies showed that high intracellular glucose level could produces advanced glycation end products which could result in the expression of transforming growth factor (TGFβ1) in podocytes, promoting apoptosis and GBM thickening by stimulating extracellular matrix production (Nowotny et al., 2015; Rabbani and Thornalley, 2018). Furthermore, TGFβ inhibited the expression of integrin in podocytes, leading to podocyte detachment and podocytopenia under hyperglycemia. Except for podocytes, the increased oxidative stress and inflammation caused by hyperglycemia were also reported for its contribution to DN (Elmarakby and Sullivan, 2012; Yaribeygi et al., 2019).

CDK5 is a proline-directed Ser/Thr protein kinase that plays an important role in many cellular functions including cell motility and survival which could be activated by binding to regulatory subunit, p35, p39, or p25 (a proteolytic fragment of p35) (Lew et al., 1994). CDK5 phosphorylation regulates the function of various regulatory proteins, including members of the Bcl-2 family of pro- and anti-apoptotic proteins. Previous evidence showed that p35 and p39 are thought to be necessary and sufficient for both CDK5 activities (Ko et al., 2001). CDK5 activity can also be inhibited by the purine-based compounds Olomoucine and Roscovitine (Vesely et al., 1994; Meijer et al., 1997). However, neither of the two compounds are selective inhibitors of CDK5. For example, CDK1/2/5 and Erk1/2 could be inhibited by Olomoucine and Roscovitine, and Roscovitine could also inhibit pyridoxal kinase (Meijer et al., 1997; Knockaert et al., 2002; Bach et al., 2005). Currently, Liebl et al. (2011) are developing more specific CDK5 inhibitors. Furthermore, diabetes-associated hyperglycemia increased the CDK5 levels (Cai et al., 2020). Recent studies suggest that CDK5 plays crucial roles in physiological functions in glucose-stimulated insulin secretion in pancreatic cells, indicating that CDK5 might be a potential drug target for diabetes mellitus and subsequent DN progression (Wei and Tomizawa, 2007). Therefore, specific CDK5 inhibitor and the effect of CDK5 on DN is urgently required to be explored.

Podocytes are highly specialized cells with a key role in kidney physiology. Destruction of their structure caused by injury could result in severe renal diseases. Previous study reported the capability of podocytes to produce and secrete the nerve growth factor (NGF) in an *in vitro* model (Caroleo et al., 2015). Studies have found that the increased secretion of NGF in a high glucose (HG) environment can protect nerve cells and pancreatic islet β cells from HG-induced oxidative stress and inflammatory factors damage, confirming that NGF is a new biological target for podocyte regulation (Guo et al., 2011; Caroleo et al., 2015; Skaper, 2017). However, the role of NGF in diabetes-induced CKD is not very clear. In diabetics, there was an early length-dependent dysfunction of small-diameter sensory fibers, with depletion of skin NGF and the sensory neuropeptide substance P (Anand, 1996).

Sirt1 has been reported to affect oxidative stress and apoptosis *via* deacetylation of its substrates (Yu and Auwerx, 2010). Intriguingly, the inhibition of Sirt1 with pharmacological agents leads to an elevation of ROS levels and NOX production (Wosniak et al., 2009; Benard et al., 2014). It was demonstrated that Sirt1 agonist SRT1720 upregulated eNOs and superoxide dismutase (SOD) levels to ameliorate endothelial oxidative stress (Chen et al., 2012). Previous studies showed that HG stress triggers the initial changes in proximal tubules and subsequent epigenetically irreversible glomerular damages which could be rescued by proximal tubular Sirt1 overexpression. Reduction of Sirt1 expression in proximal tubules leads to the decrease of glomerular Sirt1, and affects Sirt1 expression in podocytes (Hasegawa et al., 2016). Studies on diabetic animals had shown overexpression of Sirt1 in both podocytes and renal tubular cells attenuated proteinuria and kidney injury in the animal model of diabetic nephropathy through deacetylation of NF-κB, Smad3, FOXO, and p53 (Ji et al., 2021).

Furthermore Sirt1 is one of the substrates of CDK5 (Bai et al., 2012), which plays an important protective role in cell differentiation, survival, and anti-oxidation in diabetic nephropathy (Dong et al., 2014; Kong et al., 2015). Especially in a HG environment, CDK5 has a protective effect on the structure, function, and apoptosis of podocytes (Nakatani and Inagi, 2016; Chuang et al., 2017; Rogacka et al., 2018). The hyperphosphorylation of Sirt1 by CDK5 in HG environment makes it lose the above effect (Bai et al., 2014). The latest study revealed that the NGF/Sirt1 axis may become a new therapeutic

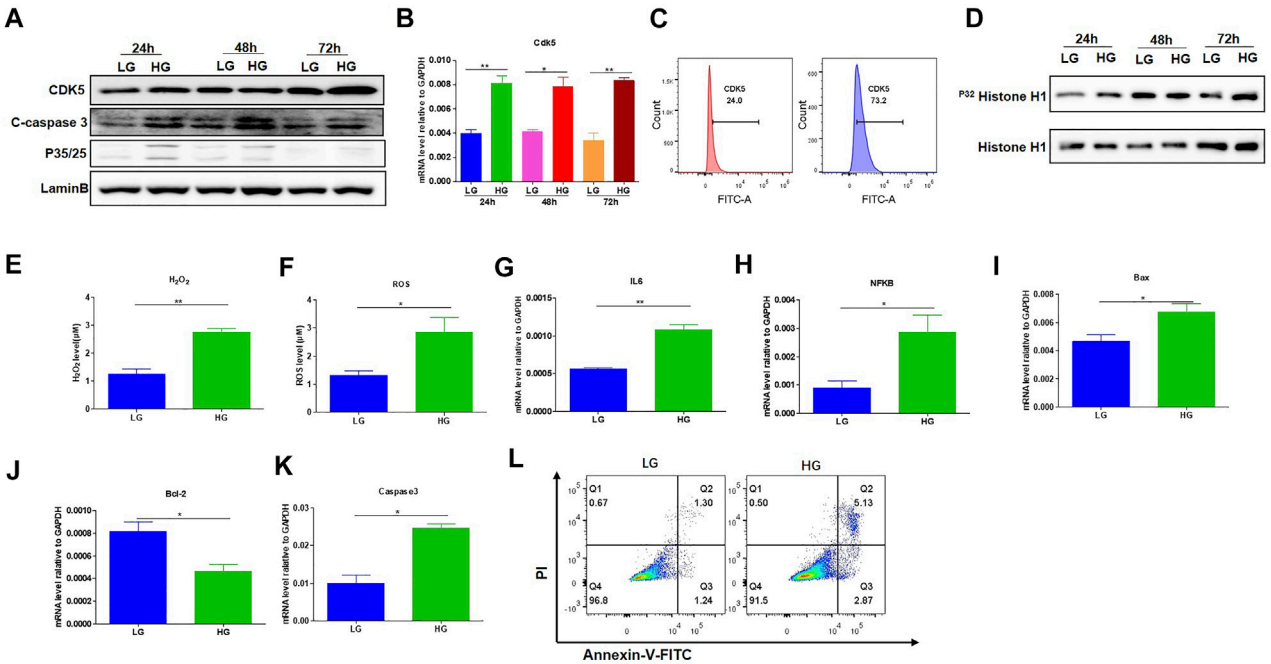

FIGURE 1 | HG-promoted oxidative stress-induced apoptosis in podocytes. **(A)** The effect of HG treatment on protein level of CDK5, p35/25 and apoptosis-related cleaved caspase-3 in MPC-5 cell lines. The cells were treated for 24, 48, and 72 h with LG and HG conditions, respectively. LaminB was regarded as the loading control. **(B)** The change of mRNA of CDK5 after 24, 48, and 72 h treatment with LG and HG in MPC-5 cells. **(C)** The detection of CDK5 expression in MPC-5 cells after HG treatment by flow cytometry. The cells were treated for 24 h under HG and LG conditions, and the goat anti-rabbit 488 secondary antibody was used. **(D)** The effect of HG treatment on the activity of CDK5 at different timepoints. Cdk5 was harvested by C-8 antibody by immunoprecipitation. The immunoprecipitate was then subjected to *in vitro* histone H1 kinase assays. **(E,F)** The effect of HG treatment on the level of **(E)** H_2O_2 and **(F)** ROS after 24 h culture. H_2O_2 was measured by hydrogen peroxide test kit, and ROS level was assessed using the probe 2′,7′-dichlorodihydrofluorescein diacetate (DCFH-DA) following TFP5 treatment. **(G,H)** The change of the mRNA level of IL-6 **(G)** and NFKB **(H)** expression in MPC-5 under HG culture condition. The cells were treated for 24 h under LG and HG conditions. GAPDH was regarded as the reference gene. **(I–K).** The mRNA level of Bax **(I)**, Bcl-2 **(J)** and caspase 3 **(K)** under HG treatment in MPC-5 cells. The cells were treated for 24 h under LG and HG conditions. GAPDH was regarded as the reference gene. **(L)** The effect of TFP5 treatment on the HG-induced apoptosis in MPC-5 cell lines. Propidium Iodide (PI) was used to separate the viable cells, and Annexin-FITC was used to identify the apoptotic cells. $^{*}p < 0.05$, $^{**}p < 0.01$. A p value less than 0.05 was considered as statistically significant.

target for intervening cell damage (Tsai et al., 2018). Therefore, we propose the scientific hypothesis: The CDK5 activity in diabetic nephropathy causes podocyte injury and apoptosis by regulating the NGF/Sirt1 axis and oxidative stress inflammatory factors in podocytes.

Previous study has reported a 24-aa peptide (termed P5), which has shown the ability to inhibit CDK5/p25 activity in transfected human embryonic kidney 293 cells. Thereafter, TFP5 (modified as P5) was designed to penetrate the blood–brain barrier after intraperitoneal injections, which inhibited abnormal Cdk5/p25 hyperactivity and significantly rescued AD pathology in AD model mice (Shukla et al., 2013). In this study, we found that TFP5, a specific inhibitor of CDK5, efficiently protected the kidney function from the damage of diabetes. TFP5 promoted the survival of podocytes by inhibiting apoptosis and oxidation caused by hyperglycemia in *db/db* mice. TFP5-mediated CDK5 inhibition upregulated Sirt1 expression, and NGF was necessary for the regulating axis. In conclusion, TFP5 treatment protects the kidney from hyperglycemia-induced damage by CDK5-NGF-Sirt1 regulation axis, and NGF and Sirt1 may be the novel target for DN.

MATERIALS AND METHODS

Animal

The male C57BLKS/J *db/db* diabetic mice at the age of 7 weeks and age-matched *db/m* mice were purchased from Southern Model Animal Co., Ltd. (Nanjing, China). All mice were raised in a SPF IVC cage with a 12 h light–dark cycle at a temperature of 25°C. Before treatment, all mice were acclimatized to the raising environment for 1 week, and the glucose level and urinary albumin level were measured and all mice were randomly divided into different groups. The mice were administrated with 150 μl TFP5 peptide (200 μM) or 150 μl scramble peptide (200 μM) by intraperitoneal injection every 3 days. Totally, the mice were treated for 16 times (from week 8 to week 16). All the experimental procedures were approved by the Institutional Animal Care and Use Committee of Ningxia Medical University (NO. 2018-026).

Biochemistry Analysis

The level of fasting blood glucose of all mice was monitored 4 h post feeding by using blood glucose meter (Roche, Basel,

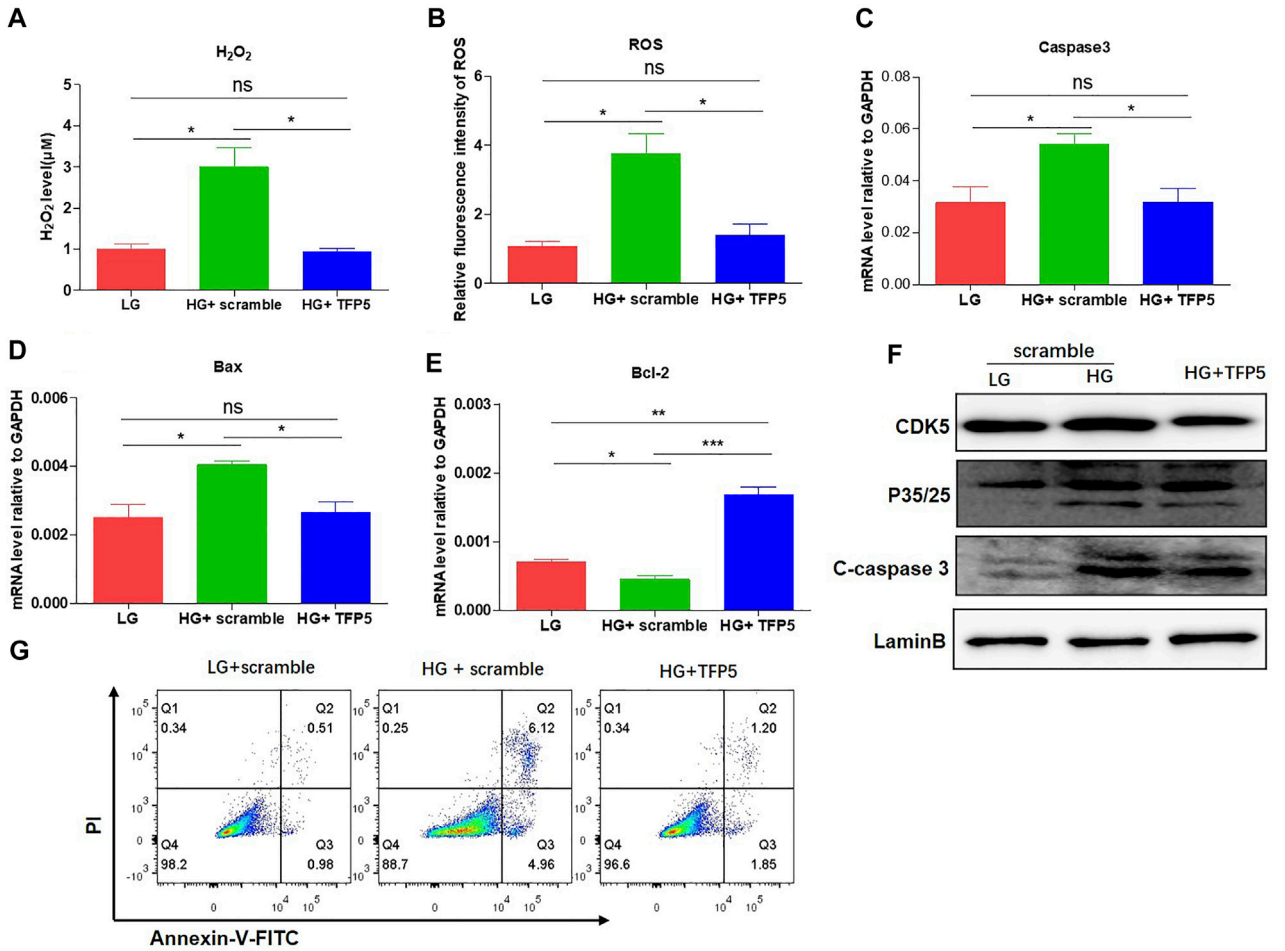

FIGURE 2 | TFP5-mediated CDK5 suppression reduces HG-induced oxidative stress, inflammatory cytokines, and apoptosis in podocytes. **(A)** The effect of TFP5 on the level of H_2O_2 under 24 h HG treatment. H_2O_2 was measured by hydrogen peroxide test kit. **(B)** The detection of ROS after TFP5 treatment. ROS Level was assessed using the probe 2′,7′-dichlorodihydrofluorescein diacetate (DCFH-DA) following TFP5 treatment. **(C–E)** The effect of TFP5 of the mRNA level of **(A)** H_2O_2, **(B)** ROS, **(C)** Caspase-3, **(D)** Bax, and **(E)** Bcl-2 expression of MPC-5 after 24 h HG treatment. **(F)** The effect of TFP5 on the protein level of CDK5, p35/25 and apoptosis-related cleaved caspase-3 in MPC-5 after 24 h HG treatment. **(G)** The effect of TFP5 on HG-induced apoptosis of MPC-5 cells. PI was used to separate the viable cells and Annexin-FITC was used to identify the apoptotic cells. $^{*}p < 0.05$, $^{**}p < 0.01$, $^{***}p < 0.001$. A p value less than 0.05 was considered as statistically significant.

Switzerland). Urinary albumin excretion was detected by the enzyme-linked immunosorbent assay (Bethyl Laboratories, Montgomery, United States) according to the manufacturer's instructions.

Plasmids and Cell Lines

MPC-5 cell line was purchased from ATCC. NGF overexpressed MPC-5 cells were constructed by pHBLV-CMV-MCS plasmid purchased from Hanheng biology. SiRNAs of NGF were purchased from Hanheng biology.

Antibodies and Inhibitors

Antibodies for P35/P25 (#2680S, Clone: C64B10; Cell signaling technology), CDK5 (#14145; Clone: D1F7M; Cell signaling technology). Anti-NGF, (#ab52918; clone: EP1320Y; abcam). Anti-Sirt1 (#ab189494; clone: EPR18239; abcam). Anti-Cleaved Caspase-3 (#ab32042: clone: E83-77, abcam). Anti-Sirt1 (#ab76039, EPR2849Y, abcam). K252a (MedChemExpress; CAS No.: 99533-80-9). TFP5 and scrambled peptide (SCB) were produced by Nanjing Peptide Industry Biotechnology Co., LTD. (Sequences: TFP5, FITCGGGKEAFWDRCLSVINLM SSKMLQINAYARAARRAARR;
SCB: FITCGGGGGGFWDRC LSGKGKMSSKGGGINAYARAARRAARR). SCB peptide was a designed peptide without specific effect on physiological function as we identified previously.

Cell Culture

Immortalized mouse podocytes MPC-5 were cultured in Dulbecco's modified Eagle medium (DMEM) composed of 10% fetal bovine serum, 2 mmol/L glutamine, 1 mmol/L sodium pyruvate, 1% penicillin and streptomycin in 37°C with

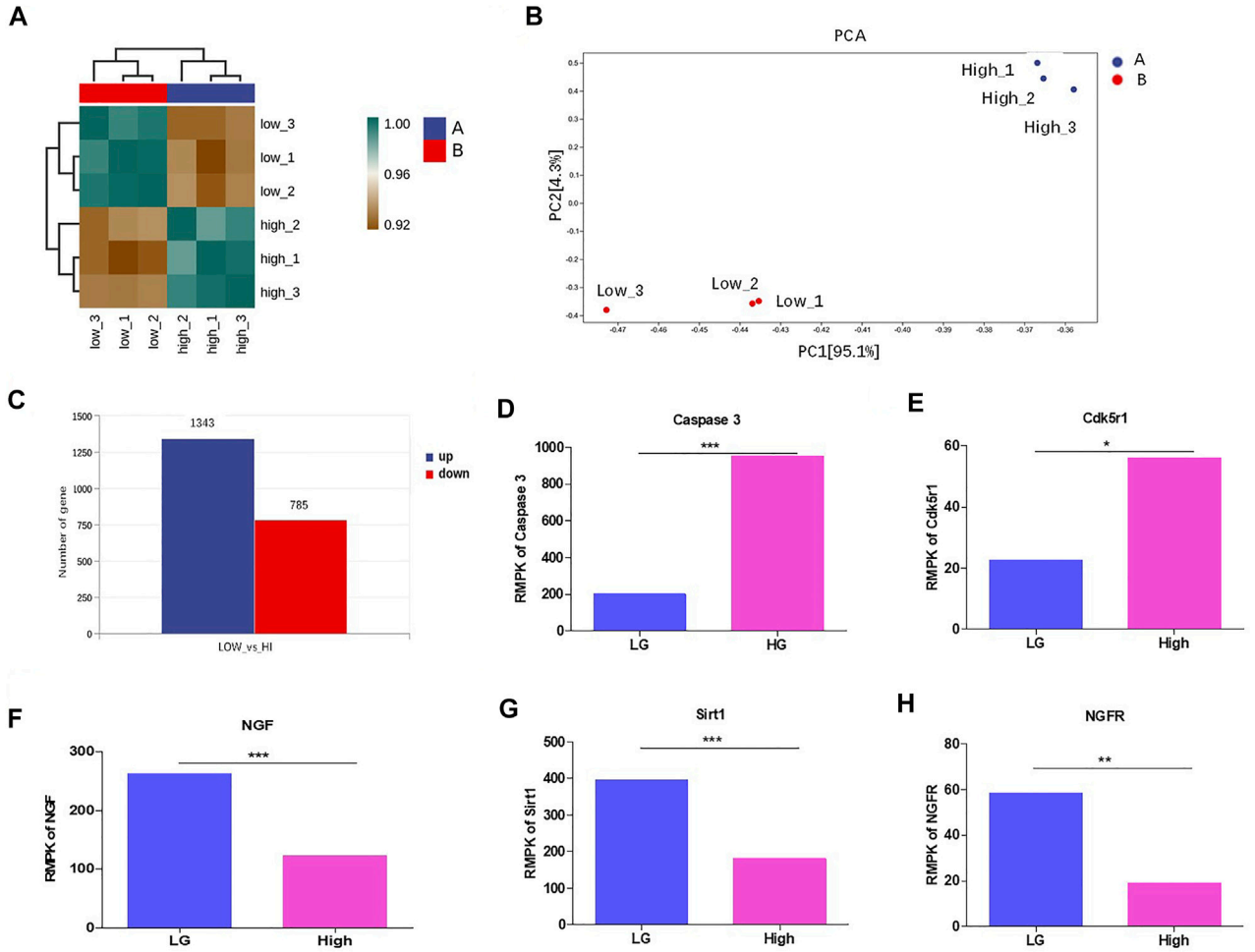

FIGURE 3 | HG altered the transcriptome and suppressed Sirt1 and NGF levels in podocytes. **(A)** The correlation analysis between MPC-5 cells treated with 24 h HG and LG treatments. $n = 3$. The clustering analyses were evaluated by the gene expression condition of mRNA level. **(B)** PCA analysis of MPC-5 cells treated under HG and LG conditions $n = 3$. **(C)** The number of differentially expressed genes between HG and LG groups. The threshold was set as the fold change ≥2. **(D–H)** The effect of 24 h HG treatment on the mRNA level of **(D)** caspase-3 **(E)** Cdk5r, **(F)** NGF, **(G)** Sirt1, **(H)** NGFR. FPKM: fragments per kilobase of transcript per Million reads. $^{*}p < 0.05$, $^{**}p < 0.01$. A p value less than 0.05 was considered as statistically significant.

5% carbon dioxide (CO2) incubator and 95% air. The concentration of glucose in LG and HG mediums, respectively, were 1 g/L and 4.5 g/L.

RNA Extraction and Real-Time PCR

In cell lines, the total RNA was extracted by TRIzol reagent according to established protocol. Briefly, 2×10^6 cells were washed by 5 ml ice-cold PBS. 1 ml TRIzol was added and sufficiently pipetted with the cell pellet. 200 µl Chloroform was added and immediately shaken for 45 s, and then, the samples were centrifuged at 12,000 g for 15 min at 4°C. The top layer was collected into RNase free tube, and equal volume of isopropanol were added and mixed sufficiently. The samples were centrifuged at 12,000 g for 50 min. The RNA pellet was washed twice with RNase-free 75% ethanol. RNA was suspended in diethyl pyrocarbonate-treated (DEPC) water. For tissue, a 0.2 g tissue was cut off from the frozen sample, and was homogenized in liquid nitrogen. The sample was then crushed with a mortar, and the RNA extraction was continued as that for cell line. 1 µg mRNA was used for cDNA synthesis with PrimeScript RT reagent Kit (Takara, Cat. No., RR037A). Quantitative-PCR was performed in triplicates with SYBR Green Master Mix (Applied Biosystems, Carlsbad, CA, United States), with ABI PRISM 7500 facility. The expression of target genes was normalized to GAPDH expression. The $2^{-\Delta CT}$ method was used to calculate the relative expression of targeted genes. All experiments were performed in triplicate. Primer sequences were as follows: NGF-F: 5′-CCAGTGAAATTAGGCTCCCTG-3′, NGF-R: 5′-CCTTGG CAAAACCTTTATTGGG-3′; CDK5-F: 5′-CTGTCCCTATCC CCCAGCTAT-3′, CDK5-R: 5′-GGCAGCACCGAGATGATG G-3′; Sirt1-F: 5′-TGATTGGCACCGATCCTCG-3′, Sirt1-R: 5′-CCACAGCGTCATATCATCCAG-3′; Caspase 3-F: 5′-TGG TGATGAAGGGGTCATTTATG-3′, Caspase 3-F: 5′-TTCGGC TTTCCAGTCAGACTC-3′; Bax-F: 5′-AGACAGGGGCCTTTT

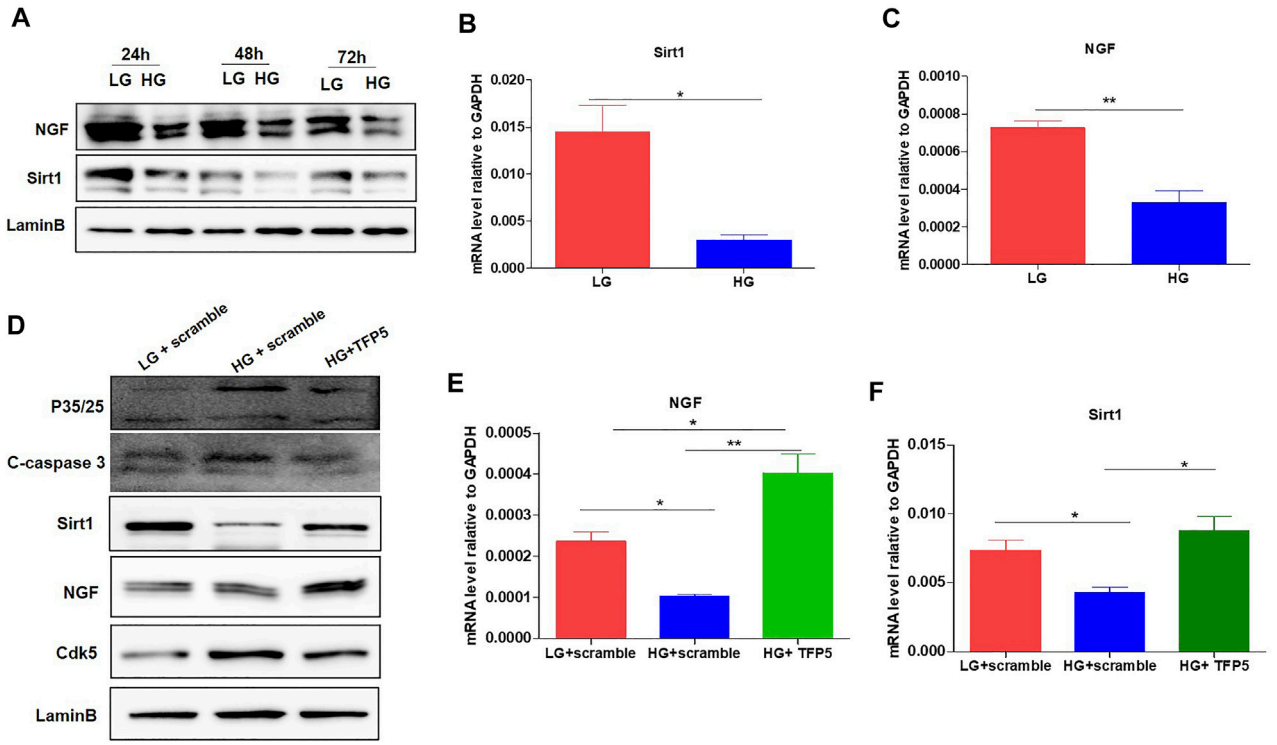

FIGURE 4 | The effect of TFP5 on the oxidative stress and apoptosis resulted from HG treatment in podocytes. **(A)** The effect of HG treatment on the protein level of NGF of MPC-5 cell lines. The cells were treated for 24, 48, and 96 h, respectively. LaminB was regarded as the loading control. **(B,C)** The effect of 24 h HG treatment on the mRNA level of Sirt1 **(B)** and NGF **(C)** in MPC-5 cell lines. GAPDH was regarded as the reference gene. **(D)** The effect of TFP5 treatment on the protein level of P35/25, cleaved-caspase 3, Cdk5, NGF, and Sirt1 under 24 h LG and HG in podocytes. **(E,F)** The effect of TFP5 treatment on the mRNA level of NGF **(E)** and Sirt1 **(F)** under 24 h LG and HG in MPC-5 cell lines. *$p < 0.05$, **$p < 0.01$. A p value less than 0.05 was considered as statistically significant.

TGCTAC-3′, Bax-R: 5′-AATTCGCCGGAGACACTCG-3′; Bcl-2-F:5′-GAGAGCGTCAACAGGGAGATG-3′, Bcl-2-R: 5′-CCA GCCTCCGTTATCCTGGA-3′.

RNA Sequence

MPC-5 cells cultured under LG and HG were collected. RNA was extracted and cDNA was then produced by Takara's Reverse Transcriptase kit. Then, the amplification of all cDNA samples was performed with the KAPA Library Quantification kit for 22–25 cycles. The samples were sequenced on the computer to obtain image files, which were converted by the software of the sequencing platform to generate the raw data of FASTQ. We counted the raw data of each sample separately, used Cutadapt to remove the linker at the 3′ end, and removed the Reads with an average quality score lower than Q20. Then, we assessed sequencing data quality by taking base quality distribution, base content distribution, and reads average quality distribution. Finally, the amplified cDNA library was sequenced and analyzed. The FPKM (fragments per kilobase of transcript per M) was calculated and used to estimate the abundance of gene expression.

Flow Cytometry

We detected the expression of CDK5 (Second antibody goat anti-mouse Alexa Fluor 488) on MPC-5 cells under HG and TFP5 treatment. Annexin V (AV) and propidium Iodide (PI) were used to detect the apoptosis by flow cytometry. Briefly, MPC-5 cells were washed with ice cold PBS twice. We then added PI (10 μl) and AV-FITC (AV-FITC, 10 μl) to a cell suspension of 100 μl and incubated them at room temperature in the dark for 15 min. For CDK5 staining, 2×10^6 MPC-5 cells were resuspended by staining buffer, and 5 μl antibodies were added to the sample. The cells were incubated at 4°C for 30 min in darkness. Then, 5 μl goat anti-mouse Alexa Fluor 488 was added and incubated at 4°C for another 30 min in darkness. Finally, the cells were washed with PBS twice and analyzed with BD Fortessa equipment. Finally, the data was analyzed by FlowJo software (V10).

ROS Detection

Intracellular ROS production was measured using 2′,7′-dichlorodihydrofluorescein diacetate (DCFH-DA) (Beyotime, Shanghai, China). Seed fibroblasts were kept in 60 mm dishes. After incubation, cells were harvested using trypsin-EDTA solution. The cell suspension was then centrifuged at room temperature for 5 min and the supernatant was removed. The fluorescence intensity of DCFH-DA was measured and calculated using a flow cytometer (Fortessa, BD).

H_2O_2 Detection

The cells were collected in a centrifuge tube and the supernatant was discarded. 100–200 μl hydrogen peroxide detection lysis

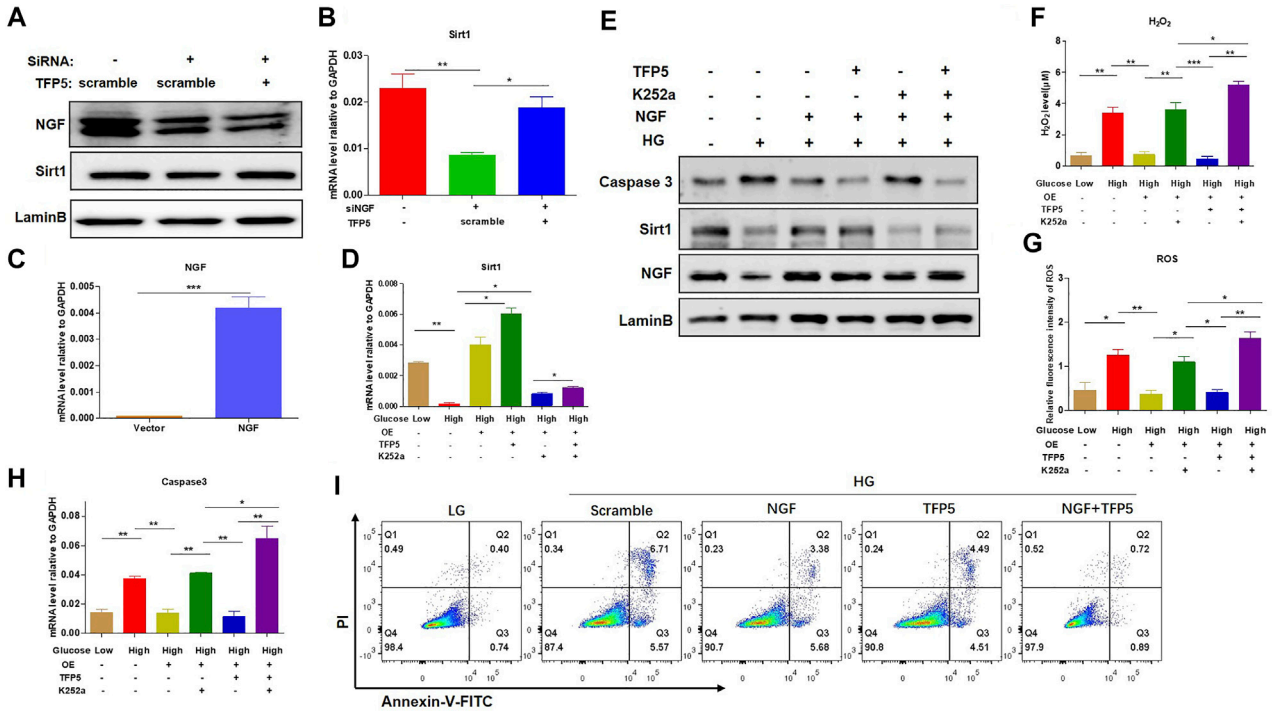

FIGURE 5 | NGF overexpression overcame the HG-induced oxidative stress and apoptosis in podocytes. **(A)** The effect of NGF knockdown on Sirt1 expression level under 24 h HG treatment in mouse podocytes. LaminB was regarded as the loading control. **(B)** The effect of NGF knockdown on the mRNA level of Sirt1 and in mouse podocytes. GAPDH was regarded as the reference gene. **(C)** The verification of NGF mRNA level in NGF overexpressed MPC-5 cells. **(D)** The effect of NGF expression and TFP5 treatment on the mRNA level of Sirt1 in MPC-5 cells. **(E)** The effect of NGF expression on the protein level of caspase-3 and Sirt1 MPC-5 cells. **(F)** The effect of NGF overexpression and TFP5 treatment on the level of H_2O_2. **(G)** The effect of NGF overexpression and TFP5 treatment on the level ROS. ROS level was assessed using the probe 2′,7′-dichlorodihydrofluorescein diacetate (DCFH-DA) following TFP5 treatment. **(H)** The effect of NGF overexpression on the mRNA level of caspase-3 after 24 h HG treatment. **(I)** The detection of MPC-5 cells apoptosis under NGF overexpression and TFP5 treatments by C-flow cytometry. PI was used to separate the viable cells and Annexin-FITC was used to identify the apoptotic cells. $^*p < 0.05$, $^{**}p < 0.01$, $^{***}p < 0.001$. A p value less than 0.05 was considered as statistically significant.

solution was added into per 1 × 10^7 cells and then fully homogenized to disrupt and lyse the cells. Centrifuge was at about 12,000 g for 3–5 min at 4°C, and the supernatant was taken for subsequent determination by using hydrogen peroxide test kit (Beyotime, cata# S0038).

Evaluation of CDK5 Activity

CDK5 activity were measured according to a previous study (Zheng et al., 2016). Briefly, the CDK5 complex was obtained by immunoprecipitation from tissue lysates. Then, the extracted CDK5 complex was incubated with histone H1 for 1 h at a temperature of 30°C. After the incubation was completed, a moderate volume of SDS loading buffer was added and then boiled for 5 min. The phosphorylation levels of histone H1 were regarded as a reflection of CDK5 kinase activity.

Immunocytochemistry

The mouse kidney was harvested and fixed with 4% paraformaldehyde overnight. The fixed tissues were cut into 4 μm sections. The sections were warmed at 80°C for 2 h and immediately dewaxed in xylene. Then, the sections were serially rehydrated with 100% ethanol, 85% ethanol, 75% ethanol, and 50% ethanol. The samples were incubated by target primary antibody at 4°C for 12 h. After the antigen retrieval with pH = 6.0 sodium citrate buffer in microwave oven, the sections were incubated in 3% H_2O_2 (diluted with methanol) to block endogenous peroxidases and was blocked in normal goat serum. The sections were then incubated with CDK5, Sirt1, NGF, P35/25 overnight at 4°C, followed by incubation with an instant biotinylated corresponding lgG antibodies. Finally, the sections were incubated with SABC reagents and staining with DAB and hematoxylin. Finally, sections were imaged under a microscope and six different fields were randomly captured to evaluate the intensity of staining. Expression of the CDK5, NGF, Sirt1, and P35/25 proteins was assessed by the positive signal for the staining intensity (0, negative; 1, light; 2, moderate; 3, strong). The representative pictures are shown in the figures.

Histological Evaluation Score

The fresh renal tissue specimens isolated from mice were fixed and cut in 4 μm, and was stained with HE according to standard procedures. Three sections per kidney were evaluated under a light microscope. All samples were independently calculated by at least two experienced renal pathologists in a blinded method. Pathological scoring (0–5) was used to assess the degree of glomerulosclerosis scores. Eight random areas were selected.

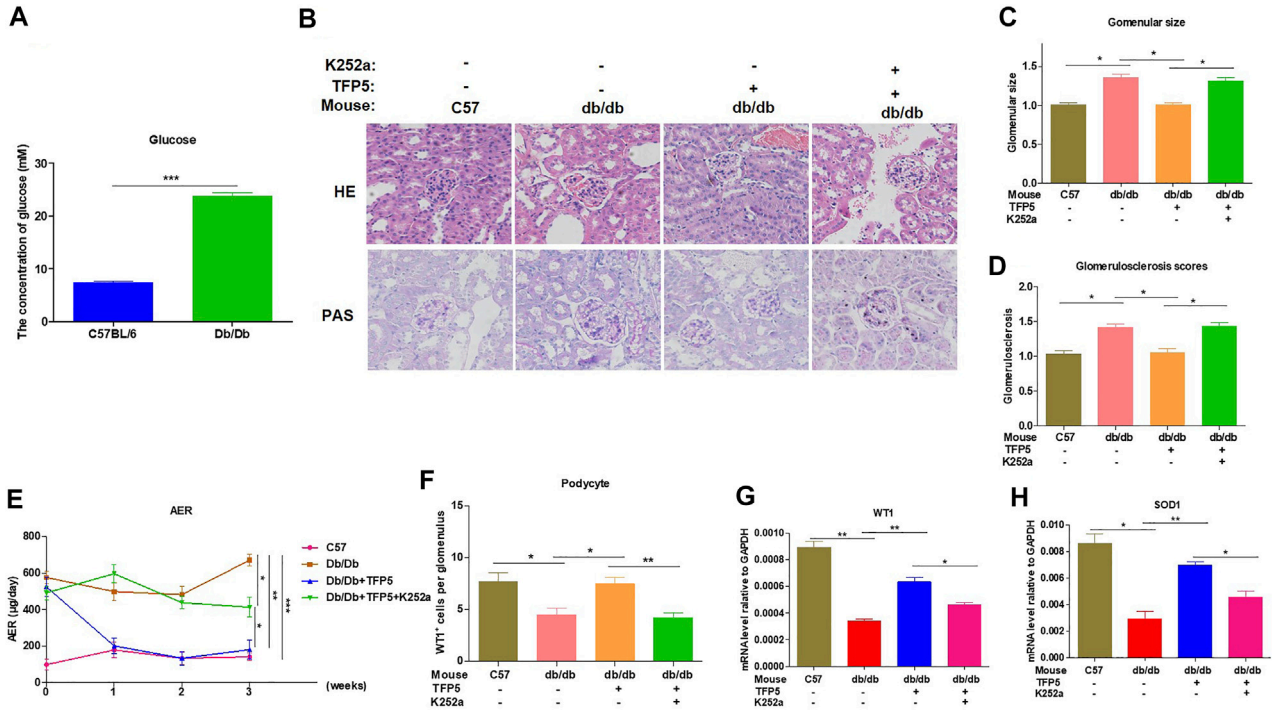

FIGURE 6 | TFP5 treatment alleviated renal function in *db/db* mouse with diabetic nephropathy. **(A)** The detection of serum glucose level in C57/BL6J and *db/db* mouse model, $n = 5$. **(B)** HE staining and PAS staining were performed in all four groups. The C57BL/6J mouse was used as control group. C57BL/6J, $n = 5$; *db/db*, $n = 5$; *db/db* + TFP5, $n = 5$; *db/db* + TFP5 + K252a, $n = 5$. **(C)** The glomerular size was measured and analyzed for all four groups. C57BL/6J, $n = 5$; *db/db*, $n = 5$; *db/db* + TFP5, $n = 5$; *db/db* + TFP5 + K252a, $n = 5$. **(D)** The glomerulosclerosis score was evaluated in all four groups. C57BL/6J, $n = 5$; *db/db*, $n = 5$; *db/db* + TFP5, $n = 5$; *db/db* + TFP5 + K252a, $n = 5$. **(E)** The detection of urinary albumin excretion rate (AER) over 24 h in all four groups. C57BL/6J, $n = 5$; *db/db*, $n = 5$; *db/db* + TFP5, $n = 5$; *db/db* + TFP5 + K252a, $n = 5$. **(F)** The counting of renal podocyte number in four groups. WT1 was used as the positive marker of podocytes by IHC staining. C57BL/6J, $n = 4$; *db/db*, $n = 4$; *db/db* + TFP5, $n = 4$; *db/db* + TFP5 + K252a, $n = 4$. **(G)** The mRNA level of WT1 gene in kidney. C57BL/6J, $n = 4$; *db/db*, $n = 4$; *db/db* + TFP5, $n = 4$; *db/db* + TFP5 + K252a, $n = 4$. **(H)** The mRNA level of SOD1 gene in the kidney of four groups. C57BL/6J, $n = 4$; *db/db*, $n = 4$; *db/db* + TFP5, $n = 4$; *db/db* + TFP5 + K252a, $n = 4$. $^{*}p < 0.05$, $^{**}p < 0.01$. A p value less than 0.05 was considered as statistically significant.

Pathological scoring ranged from 0 to 5 points of injury area (IA): 0, normal; 1, IA < 10%; 2, 10% < IA < 25%; 3, 25% < IA < 50%; 4, 50% < IA < 75%; 5, IA > 75%.

Statistical Analysis

The unpaired Student's t-test (two-sided) was used to calculate the statistical difference of two groups, and two-way ANOVA analysis was performed for multiple comparisons. All results in figures are the representative results of at least three independent experiments. The values in graphs are exhibited as mean ± SD. Analyses and figures were obtained by using GraphPad 7.0 software.

RESULTS

HG Increased the Expression and Activity of CDK5 and in Mouse Podocytes

To investigate the effects of HG treatment on CDK5 expression and activity, we cultured the mouse podocytes MPC-5 cells, respectively, under LG and HG conditions at multiple timepoints. We found that MPC-5 cells treated with HG exhibited higher level of CDK5 expression in transcriptional and translational levels compared with that under LG (**Figures 1A,B**). Consistently, we also detected the higher CDK5 expression under HG by flow cytometry (**Figure 1C**; **Supplementary Figure S1**). Furthermore, we measured the effect of HG on CDK5 activity, and we found CDK5 activity significantly increased under HG culture conditions (**Figure 1D**). Taken together, HG upregulates CDK5 activity and expression levels in mouse podocytes.

HG Leads to High Oxidative Stress, Inflammatory Cytokines, and Apoptosis of Podocytes

Previous studies have closely correlated CDK5 activity with oxidative stress-induced cell death (Sahlgren et al., 2006; Guo et al., 2018). To investigate the influence of HG treatment on the properties of MPC-5 cells, we conducted the detection of the oxidative stress, and apoptosis-related genes in MPC-5 cells under HG condition. HG treatment significantly upregulated the levels of H_2O_2 and ROS compared to that under LG condition, indicating the enhanced oxidative stress after HG treatment (**Figures 1E,F**). Furthermore, IL-6 and NFKB, two important inflammatory cytokines, exhibited obvious increases

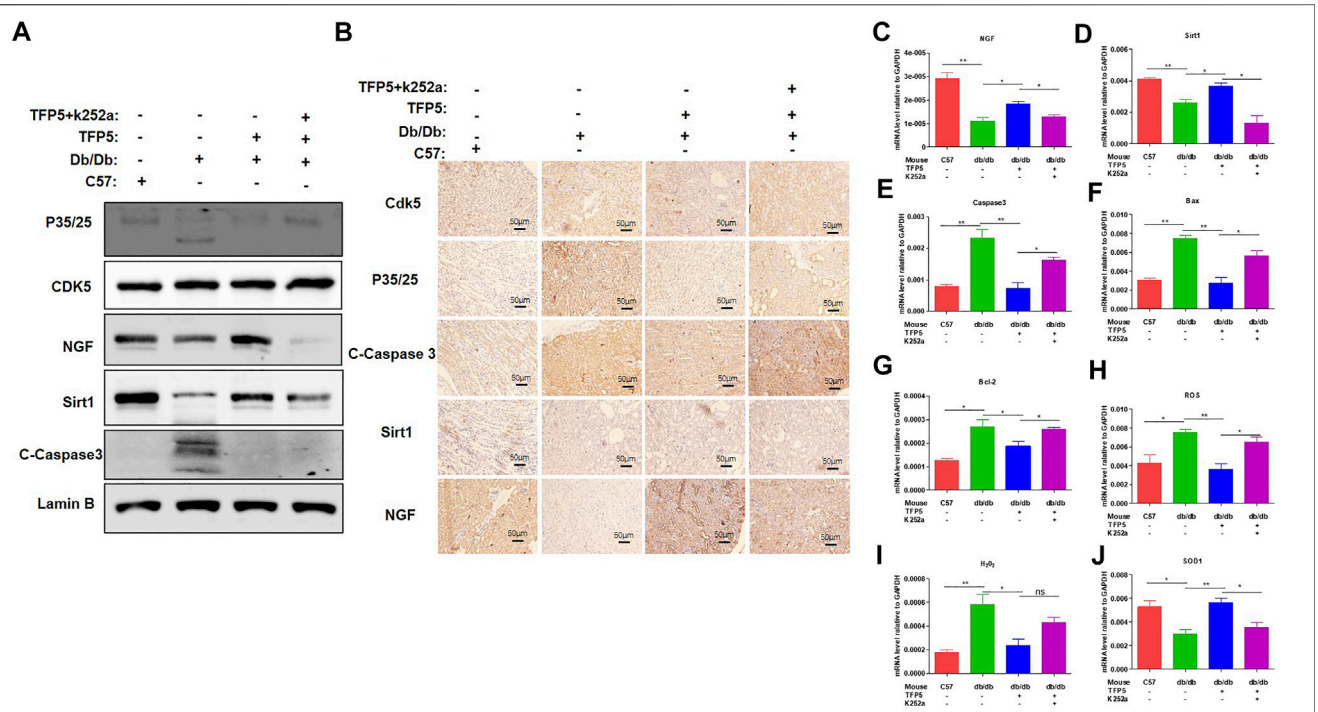

FIGURE 7 | NGF inhibitor undermined the function of TFP5 on diabetic nephropathy in *db/db* mouse model. **(A)** The level of P35/25, CDK5, NGF and Sirt1 in kidney tissue after TFP5 treatment or NGF inhibition by Western blot. **(B)** IHC staining of P35/25, CDK5, NGF and Sirt1 in kidney tissue after TFP5 treatment or NGF inhibition. **(C–J)** The mRNA level of **(C)** NGF, **(D)** Sirt1, **(E)** caspase 3, **(F)** Bax, **(G)** Bcl-2, **(H)** ROS, **(I)** H_2O_2, **(J)** SOD1 in kidney tissue after TFP5 treatment, or NGF inhibition, or both. $^*p < 0.05$, $^{**}p < 0.01$. A p value less than 0.05 was considered as statistically significant.

after 48 h under HG condition (**Figures 1G,H**). Finally, HG led to higher Bax and caspase 3 and decreased Bcl-2 level (**Figures 1I–K**). Consistently, the apoptosis staining with PI and Annexin assay exhibited the higher MPC-5 apoptosis under HG conditions (**Figure 1L**). Therefore, the increased expression level of CDK5 induced by HG may be correlated with podocyte injury in diabetes.

TFP5-Mediated CDK5 Activity Suppression Reduced HG-Induced Oxidative Stress, Inflammatory Cytokines, and Podocyte Apoptosis

To demonstrate whether CDK5 is necessary for the podocyte injury under HG, we suppressed CDK5 activity and expression by TFP5, a truncated 24 amino acid peptide derived from the p35 protein. TFP5 significantly decreased the level of H_2O_2 (**Figure 2A**) and ROS (**Figure 2B**) level, indicating the reduced oxidative stress in MPC-5 cells after TFP5 treatment under HG treatment. In addition, we also detected the decreased cleaved-caspase-3 (**Figure 2C**) and Bax (**Figure 2D**) and increased Bcl-2 (**Figure 2E**) level after TFP5 treatment, indicating the decreased apoptotic MPC-5 cell after TFP5 treatment under HG. The western blot assay showed that HG significantly increased the levels of P35, P25, and C-caspase 3, and TFP5 treatment decreased the levels of CDK5, p35, P25, and cleaved-caspase 3 under HG condition (**Figure 2F**). Furthermore, TFP5 treatment strongly inhibited MPC-5 apoptosis under HG culture condition (**Figure 2G**). Taken together, TFP5 may be a novel CDK5 inhibitor, and attenuates podocytes injury under HG condition.

HG Altered the Transcriptome and Suppresses Sirt1 and NGF Levels in Mouse Podocytes

To study the underlying mechanism, we performed RNA sequencing for MPC-5 cell cultured under LG and HG condition. The results showed that the three repeats in low or high group exhibited good intra-clustering. Meanwhile, the LG and HG groups have different expression panels (**Figure 3A**). The Principal Component Analysis (PCA) showed that LG- and HG-treated MPC-5 cells showed statistically different expression spectrums (**Figure 3B**). Totally, 1,343 genes increased and 785 genes decreased with the change threshold of 1.5 times compared with the LG group (**Figure 3C**). In the differentially expressed genes, we indeed observed the upregulation of casepases-3 (**Figure 3D**) and CDK5r1 (**Figure 3E**) under HG condition. Meanwhile, NGF, Sirt1 and NGFR were significantly decreased after HG treatment (**Figures 3E,F,G**). Interestingly Sirt1 is one of the most important substrates of CDK5. Taken together, HG alters the transcriptome of mouse podocytes.

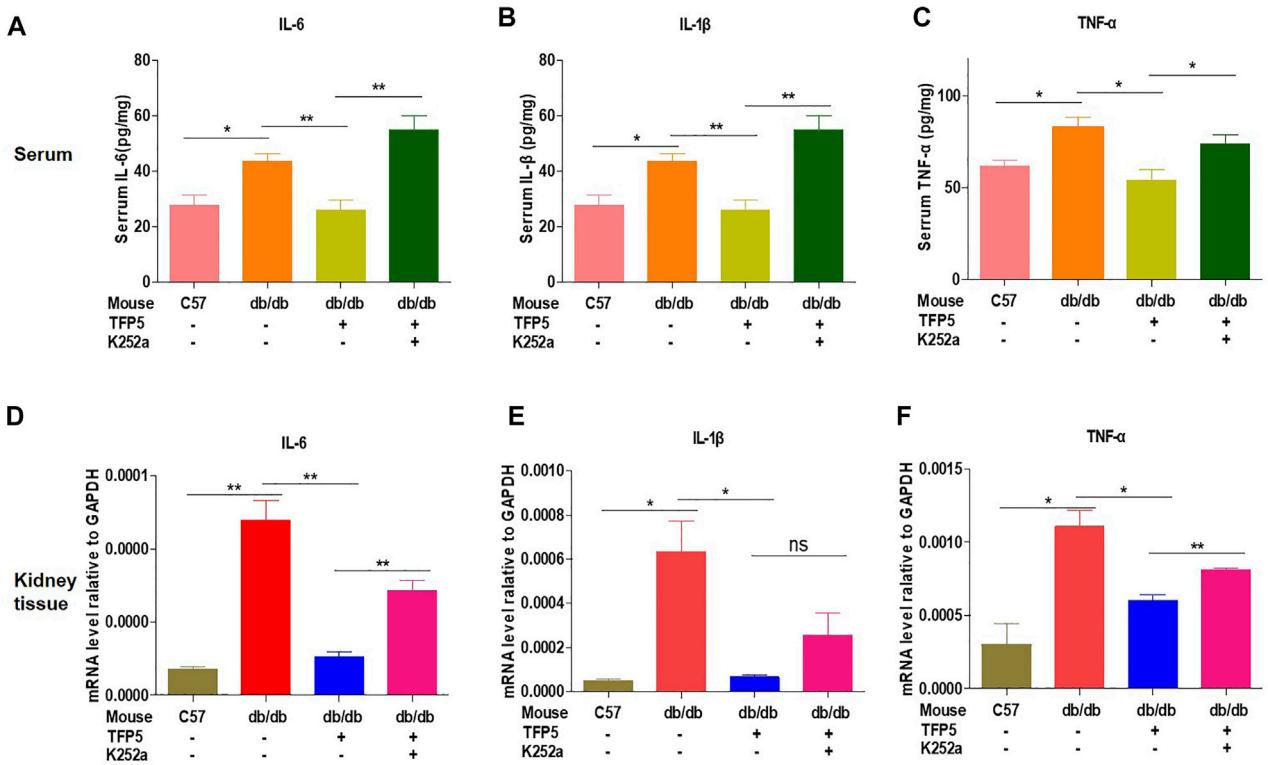

FIGURE 8 | TFP5 treatment decreased the level of proinflammatory factor levels in *db/db* mouse. **(A–C)** The detection of the level of IL-6, **(A)** IL1-β, **(B)** TNFα **(C)** by Elisa in the plasma of *db/db* mice treated with TFP5, or K252a, or both. C57BL/6J, $n = 4$; *db/db*, $n = 4$; *db/db* + TFP5, $n = 4$; *db/db* + TFP5 + K252a, $n = 4$. **(D–F)** The detection of mRNA level of IL-6, **(D)** IL1-β, **(E)** TNFα **(F)** by RT-PCR in the kidney tissue of *db/db* mice treated with TFP5 or K252a or both. C57BL/6J, $n = 3$; *db/db*, $n = 3$; *db/db* + TFP5, $n = 3$; *db/db* + TFP5 + K252a, $n = 3$. $^{*}p < 0.05$, $^{**}p < 0.01$. A p value less than 0.05 was considered as statistically significant.

TFP5 Counteracted HG Induced Sirt1 and NGF Decrease in Mouse Podocytes

To confirm the correlation between TFP5 treatment and Sirt1 and NGF expressions, we detected the expression of NGF and Sirt1 after TFP5 treatment. The Western blot showed that HG decreases the expression level of NGF and Sirt1 at 24, 48, and 72 h (**Figure 4A**). Consistently, we observed the significant decrease of Sirt1 and NGF at transcriptional level (**Figures 4B,C**). TFP5 treatment significantly inhibited the expression of C-caspase-3 and CDK5 and increased Sirt1 and NGF levels (**Figures 4D,E,F**). Taken together, TFP5 could rescue HG-induced decrease of Sirt1 and NGF in mouse podocytes.

NGF Overexpression Overcomes the Oxidative Stress and Apoptosis Under HG in Mouse Podocytes

To identify the necessity of NGF in HG-induced podocytes apoptosis, we knockdown NGF by siRNA. We found that NGF knockdown significantly decreased the mRNA and protein level of Sirt1 (**Figures 5A,B**). Furthermore, TFP5 treatment-rescued NGF knockdown induced Sirt1 decrease (**Figures 5A,B**). On the other hand, we overexpressed NGF in MPC-5 cell (**Figure 5C**). We found that NGF overexpression significantly upregulated Sirt1 expression level and under HG condition (**Figures 5D,E**). Furthermore, the combination of TFP5 and NGF overexpression exhibited even higher Sirt1 expression than NGF overexpression alone under HG treatment (**Figures 5D,E**). k252a, an NGF-specific inhibitor, significantly decreased Sirt1 expression in TFP5 treatment and NGF overexpressed MPC-5 under HG condition, indicating the dominant role of NGF on the regulation of Sirt1. Meanwhile, we found that NGF overexpression and TFP5 treatment decreased the expression level of cleaved caspase-3 which was upregulated by K252a treatment (**Figures 5D,E**). In addition, we also observed the obvious decrease of H_2O_2 and ROS after NGF overexpression, and k252a treatment counteracted the function of NGF overexpression and TFP5 treatment (**Figures 5F,G**). Finally, we found that NGF overexpression inhibited HG-induced MPC-5 cell apoptosis, and TFP5 exhibited the synergistic effect with NGF overexpression (**Figures 5H,I**). In conclusion, NGF plays an important role in HG-induced MPC-5 apoptosis.

NGF Inhibitor Undermines the Function of TFP5 on Diabetic Nephropathy in *db/db* Mouse Model

To identify the effect of TFP5 and NGF on renal function damage caused by hyperglycemia in *db/db* mouse model, we treated mice with TFP5 peptides, K252a, or both. Firstly, we observed that the *db/db* mice showed a higher level of glucose level in serum

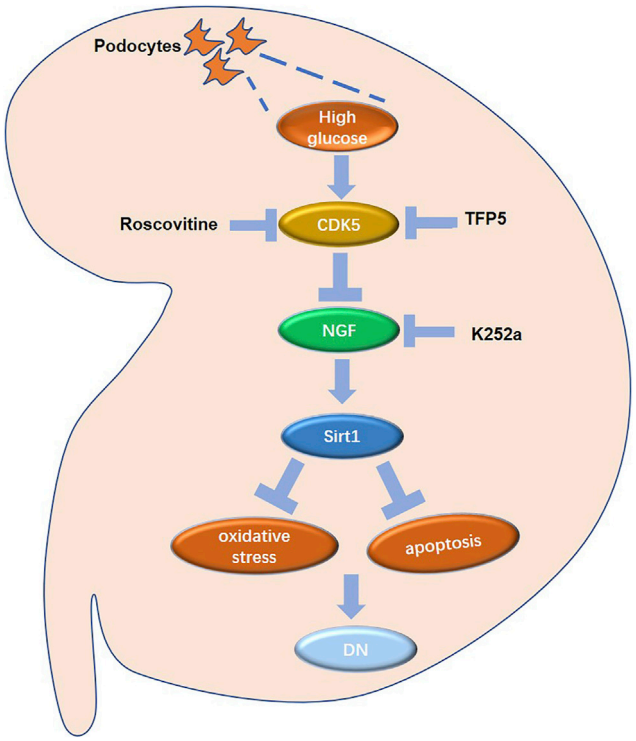

FIGURE 9 | The regulatory network in mouse renal podocytes. Roscovitine: CDK5 inhibitor; TFP5: a 25 amino acid peptide that inhibiting CDK5 activity; K252a: NGF inhibitor; DN: diabetic nephropathy.

compared to the control group (**Figure 6A**). As TFP5 and K252a had a profound effect on podocytes survival, we subsequently explored its influence upon glomerulus using histological staining. HE and Periodic acid–Schiff staining of kidney showed that hyperglycemia increased the glomerular size and glomerulosclerosis scores (**Figures 6B–D**). TFP5 treatment efficiently decreased the glomerular size and glomerulosclerosis scores which was upregulated by K252a treatment (**Figures 6B–D**). We also measured the urinary albumin excretion rate (AER) during the experiment. We found that hyperglycemia led to increased AER while TFP5 treatment led to decreased AER in *db/db* mouse. In addition, K252a reversed the function of TFP5 and led to severe AER (**Figure 6E**). In addition, we counted the number of podocytes under different treatments. We observed the decreased podocytes and TFP5 counteract hyperglycemia-induced podocytopenia (**Figure 6F**). Meanwhile, we used the podocytes-specific marker, WT1, by IHC assay. Consistently, WT1 positive podocytes decreased under hyperglycemia, which increased after TFP5 treatment (**Figure 6G**). We also measured the oxidative stress in kidney under different treatments. The results showed that the SOD1 decreased under hyperglycemia in *db/db* mouse (**Figure 6H**). TFP5 treatment upregulated SOD1, which was decreased by K252a treatment (**Figure 6H**). In addition, we also detected the expression level of P35/25, NGF, Sirt1, apoptosis and oxidative stress-related gene in the tissue after TFP5 or K252a treatment. We found that TFP5 treatment obviously decreased apoptosis (**Figures 7A,B,E–G**; **Supplementary Figure S2**) and oxidative stress- (**Figures 7H,I**) related genes while significantly upregulated NGF (**Figures 7A–C**; **Supplementary Figure S2**), Sirt1(**Figures 7A,B,D**; **Supplementary Figure S2**), Bcl-2 (**Figure 7G**) and SOD1 (**Figure 7J**) level in the kidney tissue of *db/db* mouse, which was undermined by k252a treatment (**Figures 7A–J**). In conclusion, NGF inhibitor undermines the function of TFP5 on DN in *db/db* mouse model.

TFP5 Improved the Inflammatory Cytokines Under Hyperglycemia

To investigated the effect of TFP5 on the inflammatory cytokines in serum and kidney of *db/db* mice. We found that TFP5 significantly upregulated IL-6, IL-1β, and tumor necrosis factor (TNF-α) in serum (**Figures 8A–C**) and kidney tissue (**Figures 8D–F**). TFP5 treatment decreased hyperglycemia-induced IL-6, IL-1β, and TNF-α upregulation. Furthermore, K252a treatment counteracted the effect of TFP5 and led to the upregulation of IL-6, IL-1β, and TNF-α in the serum and kidney of *db/db* model mice.

DISCUSSION

DN is a major long-term complication, which affects about 30% of patients with T1D, and 40% of patients with T1D (Alicic et al., 2017), is the major cause of kidney failure worldwide and the single strongest predictor of mortality in diabetic patients. Today, about 40% of patients need renal replacement therapy (Ritz et al., 2011). These classic descriptions indicate that patients with T1D develop DN within 10 years after the onset of diabetes.

Previous evidence has shown that strict glycemic control could improve the progression of DN. Although DN is considered to be a microvascular complication of diabetes, there is increasing evidence that podocyte loss and epithelial dysfunction play an important role. White et al. (2002) demonstrated that although mesangial dilatation and GBM thickening are the most common DN lesions, careful cell analysis using samples from patients with T1D and T2D showed that the number of podocytes is highly correlated with proteinuria and seems to be one of the best predictors of disease. Podocyte loss may be due to apoptosis or abscission of podocytes caused by hyperglycemia-induced ROS production (Susztak et al., 2006), indicating podocytes may be the "weakest link" in DN development. Here, we found that MPC-5 cells presented obvious apoptosis induced by oxidative stress under HG condition. TFP5, a peptide-inhibiting CDK5, efficiently inhibited HG-induced podocytes cells apoptosis and DN in the mouse model by decreasing NGF level and upregulating Sirt1 level. Therefore, our work illuminated a novel and targetable TFP5-CDK5-NGF-Sirt1 regulating axis, which may be the promising targets for diabetic kidney disease therapy in future.

TFP5 may be a promising oligopeptide drugs for diabetic kidney disease. Our previous study showed depletion of CDK5 causes significant depressed expression of WT1 and apoptosis of podocytes. Reducing ciliary body length by drug or gene inhibition of CDK5 can reduce polycystic kidney disease in renal tuberculosis model (Husson et al., 2016). Guevara et al. (2014) found that CDK5 and its regulator p35/P25 and cyclin I

were also expressed in renal tubular cells. We show that treatment with CDK5 inhibitors can promote the formation of survival-promoting CDK5/cyclin I complex and improve cell survival in the case of ischemia-reperfusion Pro apoptotic injury, support the benefits of renal preservation treated with CDK5 inhibitors, and contribute to renal tubular protection. Although we previously reported that CDK5 deletion resulted in decreased WT1 expression and podocyte apoptosis, the CDK5 activity down regulated by p35 had no effect on the expression of cleaved caspase 3. On the contrary, increased apoptosis can be detected in p35 deregulated podocytes by TUNEL analysis and immunofluorescence staining of cleaved caspase 3 antibody. Podocyte viability of CDK5 and p35 knockout cells decreased (Zheng et al., 2016). In addition, Liu, 2013. reported that intermediate filament protein nestin is related to the occurrence of DN. Blocking CDK5 can increase nestin level and reduce renal damage, which will provide a useful target for the treatment of DN, indicating the crucial role of CDK5 activity on the treatment of diabetic kidney disease. In this study, we found that TFP5 effectively rescued HG-induced MPC-5 cells apoptosis and oxidative stress. In hyperglycemia-caused kidney function damage of *db/db* mouse model, TFP5 treatment increased the number of podocytes and improved the kidney function indexes.

TFP5 may regulate kidney function by effect of Sirt1 activity. Zhang et al. (2018) reported that CDK was also involved in the ubiquitin-proteasome pathway-mediated degradation of Sirt1 expression in Parkinson's disease models, which could be efficiently blocked by the inhibition of CDK5. The phosphorylation of S47 is closely related to the nuclear retention of Sirt1, but not to telomere repeat binding factor 2-interacting protein 1. CDK5 was identified as a Sirt1 kinase that regulates s47 phosphorylation. Knockout, or inhibition of CDK5, can reduce the number of aging endothelial cells, promote the nuclear output of Sirt1, and reduce the expression of inflammatory genes in porcine aortic endothelial cells, accompanied by the accumulation of truncated regulatory subunits of CDK5, and P25 in aging porcine aortic endothelial cells and active arteries of atherosclerosis. Long-term treatment with Roscovitine blocked the development of cell senescence and atherosclerosis in the aorta of hypercholesterolemic apolipoprotein E-deficient mice (Bai et al., 2012). *In vivo* and *in vitro*, inhibition of CDK5 can reverse sevoflurane-induced neuronal apoptosis, while inhibition of CDK5 activity can promote the expression of Sirt1, which plays an important role in inducing autophagy activation. Yang et al. (2020) found that Sirt1 inhibition inhibited the protective effect of ROSC on sevoflurane-induced nerve injury by inhibiting autophagy activation. In addition, CDK5 is responsible for the phosphorylation of Sirt1 on serine 47 residue. This modification blocks the anti-aging activity of Sirt1 and plays a key role in the loss of Sirt1 function during vascular aging. Therefore, Sirt1 function can be improved by inhibiting CDK5 so as to prevent the development of atherosclerosis and slow down the process of vascular aging (Bai et al., 2012; Bai et al., 2014). Conversely, Sirt1 also regulates the expression of CDK5 through epigenetic modification. Acetylation of CDK5 at k33 (ac-CDK5) resulted in loss of ATP binding and impaired kinase activity. We identified GCN5 and Sirt1 as key factors controlling ac-CDK5 levels. Ac-CDK5 reached the lowest level in rat fetal brain, but increased significantly after birth. Interestingly, nuclear ac-CDK5 levels were negatively correlated with neurite length in embryonic hippocampal neurons, which was inhibited by Sirt1 inhibitor EX527 or acetyl simulant. The ectopic expression of (K33Q) CDK5 is inhibited, indicating that the positive regulation of Sirt1 is positively regulating the growth of neurite through the deacetylation of nuclear CDK5 (Lee et al., 2018). Consistently, we observed the significant decrease of Sirt1 under HG condition in MPC-5 cells, which was reversed by TFP5 treatment. Therefore, TFP5 may protect podocytes and improve diabetes nephropathy *via* affecting the level of Sirt1.

NGF may mediate the upregulation of Sirt1 after TFP5 treatment. NGF is one of the most common neurotrophic factors. It is found that neuronal apoptosis induced by the decline of NGF secretion ability of brain neuronal cells leads to neurodegenerative diseases. Previous evidence showed that during the process of apoptosis of PC12 cells (Rat neuronal cell) induced by NGF withdrawal, the activation of CDK5/p35, the protein catalyzing the phosphorylation of Sirt1, plays an important mediating role. Furthermore, Roscovitine, a specific inhibitor of CDK5, had the potential to protect neuronal cells. Apart from the regulation of the neuronal cell of NGF, Tatsuo Hata et al. reported that NGF is closely related to diabetic pathology and insulin homeostasis, indicating the potential role of NGF in hyperglycemia-induced diseases (Hata et al., 2015). Similarly, NGF withdrawal resulted in pancreatic cancer β Cell apoptosis. Recent studies on podocyte model *in vitro* found that podocytes, like neurons, have the ability to synthesize and secrete NGF, suggesting that NGF may be a novel target of glomerular podocytes (Caroleo et al., 2015). In our study, we found that NGF positively regulated the expression of Sirt1 in MPC-5 cells, and TFP5 significantly upregulated NGF expression. The overexpression of NGF effectively rescued HG-induced decrease of Sirt1. In addition, the k252a, the inhibitor of NGF, blocked the function of TFP5 on Sirt1 regulation (**Figure 9**). In conclusion, CDK5-NGF-Sirt1 axis may be a novel regulating mechanism in podocytes and *db/db* mouse models.

DATA AVAILABILITY STATEMENT

Raw data and processed data of RNA-seq are available at the NCBI repository (SUB11139134; https://www.ncbi.nlm.nih.gov/sra/PRJNA811338).

ETHICS STATEMENT

The animal study was reviewed and approved by the Institutional Animal Care and Use Committee of Ningxia Medical University (NO. 2018-026).

AUTHOR CONTRIBUTIONS

All authors participated in the design, interpretation, data analysis, and manuscript review of the study; S-LC, H-YL

and YC-G contributed to conception and design, data collection, drafting articles, and final approval of the forthcoming version; X-ML, BL, and LB contributed to concept and design, data analysis and interpretation, and drafting articles; JE, DM, G-QZ, S-YL, L-RL, and XB drafted articles or critically revised important knowledge contents; Y-LZ drafted this article or critically revised important intellectual content.

FUNDING

This work was funded by the following grant sponsors: National Natural Science Foundation of China, Grant No. 81860136 and No. 81460161; Natural Science Foundation of Ningxia Province, Grant No. 2022AAC02059, No. NZ17186, and No. 2021AAC03311. The Key Research and Development Program of Ningxia Province Region projects, Grants No. 2022BEG03121 and No. 2018BFG0210 (Eastern and Western collaboration program). This research supporter had no role in the study design.

SUPPLEMENTARY MATERIAL

The Supplementary Material for this article can be found online at: https://www.frontiersin.org/articles/10.3389/fcell.2022.829067/full#supplementary-material

REFERENCES

Akchurin, O. M. (2019). Chronic Kidney Disease and Dietary Measures to Improve Outcomes. *Pediatr. Clin. N. Am.* 66 (1), 247–267. doi:10.1016/j.pcl.2018.09.007

Alicic, R. Z., Rooney, M. T., and Tuttle, K. R. (2017). Diabetic Kidney Disease Challenges, Progress, and Possibilities [J]. *Clin. J. Am. Soc. Nephrol.* 12 (12), 2032–2045. doi:10.2215/cjn.11491116

Ammirati, A. L. (2020). Chronic Kidney Disease [J]. *Rev. Assoc. Med. Bras.* 66 (Suppl. 1), s03–s9. Suppl 1. doi:10.1590/1806-9282.66.s1.3

Anand, P. (1996). Neurotrophins and Peripheral Neuropathy. *Philos. Trans. R. Soc. Lond B Biol. Sci.* 351 (1338), 449–454. doi:10.1098/rstb.1996.0041

Anders, H.-J., Huber, T. B., Isermann, B., and Schiffer, M. (2018). CKD in Diabetes: Diabetic Kidney Disease versus Nondiabetic Kidney Disease. *Nat. Rev. Nephrol.* 14 (6), 361–377. doi:10.1038/s41581-018-0001-y

Bach, S., Knockaert, M., Reinhardt, J., Lozach, O., Schmitt, S., Baratte, B., et al. (2005). Roscovitine Targets, Protein Kinases and Pyridoxal Kinase. *J. Biol. Chem.* 280 (35), 31208–31219. doi:10.1074/jbc.m500806200

Bai, B., Liang, Y., Xu, C., Lee, M. Y. K., Xu, A., Wu, D., et al. (2012). Cyclin-Dependent Kinase 5-Mediated Hyperphosphorylation of Sirtuin-1 Contributes to the Development of Endothelial Senescence and Atherosclerosis. *Circulation* 126 (6), 729–740. doi:10.1161/circulationaha.112.118778

Bai, B., Vanhoutte, P. M., and Wang, Y. (2014). Loss-of-SIRT1 Function during Vascular Ageing: Hyperphosphorylation Mediated by Cyclin-dependent Kinase 5. *Trends Cardiovasc. Med.* 24 (2), 81–84. doi:10.1016/j.tcm.2013.07.001

Benard, V. B., Thomas, C. C., King, J., Massetti, G. M., Doria-Rose, V. P., and Saraiya, M. (2014). Vital Signs: Cervical Cancer Incidence, Mortality, and Screening - United States, 2007-2012. *MMWR Morb. Mortal. Wkly. Rep.* 63 (44), 1004–1009.

Cai, H. B., Fan, Z. Z., Tian, T., Li, Z. C., Zhao, C. C., Guo, W. T., et al. (2020). Diabetes-Induced H3K9 Hyperacetylation Promotes Development of Alzheimer's Disease through CDK5. *J. Alzheimers Dis.* 77 (1), 75–84. doi:10.3233/JAD-200163

Caroleo, M. C., Carito, V., Pingitore, A., Perrotta, I. D., Perri, M., Mancuso, D., et al. (2015). Human Kidney Podocyte Cell Population as a Novel Biological Target of Nerve Growth Factor. *Growth factors.* 33 (1), 14–22. doi:10.3109/08977194.2014.975799

Chen, H., Wan, Y., Zhou, S., Lu, Y., Zhang, Z., Zhang, R., et al. (2012). Endothelium-specific SIRT1 Overexpression Inhibits Hyperglycemia-Induced Upregulation of Vascular Cell Senescence. *Sci. China Life Sci.* 55 (6), 467–473. doi:10.1007/s11427-012-4329-4

Chuang, P. Y., Cai, W., Li, X., Fang, L., Xu, J., Yacoub, R., et al. (2017). Reduction in Podocyte SIRT1 Accelerates Kidney Injury in Aging Mice. *Am. J. Physiology-Renal Physiology* 313 (3), F621–F628. doi:10.1152/ajprenal.00255.2017

Dong, Y. J., Liu, N., Xiao, Z., Sun, T., Wu, S. H., Sun, W. X., et al. (2014). Renal Protective Effect of Sirtuin 1. *J. Diabetes Res.* 2014, 843786. doi:10.1155/2014/843786

Elmarakby, A. A., and Sullivan, J. C. (2012). Relationship between Oxidative Stress and Inflammatory Cytokines in Diabetic Nephropathy. *Cardiovasc Ther.* 30 (1), 49–59. doi:10.1111/j.1755-5922.2010.00218.x

Guevara, T., Sancho, M., Pérez-Payá, E., and Orzáez, M. (2014). Role of CDK5/cyclin Complexes in Ischemia-Induced Death and Survival of Renal Tubular Cells. *Cell Cycle* 13 (10), 1617–1626. doi:10.4161/cc.28628

Guo, D., Xie, W., Xiong, P., Li, H., Wang, S., Chen, G., et al. (2018). Cyclin-dependent Kinase 5-mediated Phosphorylation of Chloride Intracellular Channel 4 Promotes Oxidative Stress-Induced Neuronal Death. *Cell Death Dis.* 9 (10), 951. doi:10.1038/s41419-018-0983-1

Guo, T., Mandai, K., Condie, B. G., Wickramasinghe, S. R., Capecchi, M. R., and Ginty, D. D. (2011). An Evolving NGF-Hoxd1 Signaling Pathway Mediates Development of Divergent Neural Circuits in Vertebrates. *Nat. Neurosci.* 14 (1), 31–36. doi:10.1038/nn.2710

Hasegawa, K., Wakino, S., Sakamaki, Y., Muraoka, H., Umino, H., Minakuchi, H., et al. (2016). Communication from Tubular Epithelial Cells to Podocytes through Sirt1 and Nicotinic Acid Metabolism. *Chyr* 12 (2), 95–104. doi:10.2174/1573402112666160302102217

Hata, T., Sakata, N., Yoshimatsu, G., Tsuchiya, H., Fukase, M., Ishida, M., et al. (2015). Nerve Growth Factor Improves Survival and Function of Transplanted Islets via TrkA-Mediated β Cell Proliferation and Revascularization. *Transplantation* 99 (6), 1132–1143. doi:10.1097/tp.0000000000000655

Husson, H., Moreno, S., Smith, L. A., Smith, M. M., Russo, R. J., Pitstick, R., et al. (2016). Reduction of Ciliary Length through Pharmacologic or Genetic Inhibition of CDK5 Attenuates Polycystic Kidney Disease in a Model of Nephronophthisis. *Hum. Mol. Genet.* 25 (11), 2245–2255. doi:10.1093/hmg/ddw093

Jefferson, J. A., Shankland, S. J., and Pichler, R. H. (2008). Proteinuria in Diabetic Kidney Disease: A Mechanistic Viewpoint. *Kidney Int.* 74 (1), 22–36. doi:10.1038/ki.2008.128

Ji, J., Tao, P., Wang, Q., Li, L., and Xu, Y. (2021). SIRT1: Mechanism and Protective Effect in Diabetic Nephropathy. *Emiddt* 21 (5), 835–842. doi:10.2174/1871530320666201029143606

Knockaert, M., Greengard, P., and Meijer, L. (2002). Pharmacological Inhibitors of Cyclin-dependent Kinases. *Trends Pharmacol. Sci.* 23 (9), 417–425. doi:10.1016/s0165-6147(02)02071-0

Ko, J., Humbert, S., Bronson, R. T., Takahashi, S., Kulkarni, A. B., Li, E., et al. (2001). p35 and P39 Are Essential for Cyclin-dependent Kinase 5 Function during Neurodevelopment. *J. Neurosci.* 21 (17), 6758–6771. doi:10.1523/jneurosci.21-17-06758.2001

Kong, L., Wu, H., Zhou, W., Luo, M., Tan, Y., Miao, L., et al. (2015). Sirtuin 1: A Target for Kidney Diseases. *Mol. Med.* 21, 87–97. doi:10.2119/molmed.2014.00211

Langham, R. G., Kelly, D. J., Cox, A. J., Thomson, N. M., Holthöfer, H., Zaoui, P., et al. (2002). Proteinuria and the Expression of the Podocyte Slit Diaphragm Protein, Nephrin, in Diabetic Nephropathy: Effects of Angiotensin Converting Enzyme Inhibition. *Diabetologia* 45 (11), 1572–1576. doi:10.1007/s00125-002-0946-y

Lee, J., Ko, Y. U., Chung, Y., Yun, N., Kim, M., Kim, K., et al. (2018). The Acetylation of Cyclin-dependent Kinase 5 at Lysine 33 Regulates Kinase Activity and Neurite Length in Hippocampal Neurons. *Sci. Rep.* 8 (1), 13676. doi:10.1038/s41598-018-31785-9

Lew, J., Huang, Q.-Q., Qi, Z., Winkfein, R. J., Aebersold, R., Hunt, T., et al. (1994). A Brain-specific Activator of Cyclin-dependent Kinase 5. *Nature* 371 (6496), 423–426. doi:10.1038/371423a0

Liebl, J., Fürst, R., Vollmar, A. M., and Zahler, S. (2011). Twice Switched at Birth: Cell Cycle-independent Roles of the "Neuron-specific" Cyclin-dependent Kinase 5 (Cdk5) in Non-neuronal Cells. *Cell. Signal.* 23 (11), 1698–1707. doi:10.1016/j.cellsig.2011.06.020

Liu, W. (2013). The expression of intermediate filament protein nestin and its association with cyclin-dependent kinase 5 in the glomeruli of rats with diabetic nephropathy. *The American journal of the medical sciences* 345 (6), 470–477.

Lo, C., Toyama, T., Wang, Y., Lin, J., Hirakawa, Y., Jun, M., et al. (2018). Insulin and Glucose-Lowering Agents for Treating People with Diabetes and Chronic Kidney Disease. *Cochrane Database Syst. Rev.* 9, CD011798. doi:10.1002/14651858.CD011798.pub2

Meijer, L., Borgne, A., Mulner, O., Chong, J. P., Blow, J. J., Inagaki, N., et al. (1997). Biochemical and Cellular Effects of Roscovitine, a Potent and Selective Inhibitor of the Cyclin-dependent Kinases Cdc2, Cdk2 and Cdk5. *Eur. J. Biochem.* 243 (1-2), 527–536. doi:10.1111/j.1432-1033.1997.t01-2-00527.x

Nakamura, T., Ushiyama, C., Suzuki, S., Hara, M., Shimada, N., Ebihara, I., et al. (2000). Urinary Excretion of Podocytes in Patients with Diabetic Nephropathy. *Nephrol. Dial. Transpl.* 15 (9), 1379–1383. doi:10.1093/ndt/15.9.1379

Nakatani, Y., and Inagi, R. (2016). Epigenetic Regulation through SIRT1 in Podocytes. *Chyr* 12 (2), 89–94. doi:10.2174/1573402112666160302102515

Nowotny, K., Jung, T., Höhn, A., Weber, D., and Grune, T. (2015). Advanced Glycation End Products and Oxidative Stress in Type 2 Diabetes Mellitus. *Biomolecules* 5 (1), 194–222. doi:10.3390/biom5010194

Rabbani, N., and Thornalley, P. J. (2018). Advanced Glycation End Products in the Pathogenesis of Chronic Kidney Disease. *Kidney Int.* 93 (4), 803–813. doi:10.1016/j.kint.2017.11.034

Ritz, E., Zeng, X.-X., and Rychlík, I. (2011). Clinical Manifestation and Natural History of Diabetic Nephropathy. *Contrib. Nephrol.* 170, 19–27. doi:10.1159/000324939

Rogacka, D., Audzeyenka, I., Rychłowski, M., Rachubik, P., Szrejder, M., Angielski, S., et al. (2018). Metformin Overcomes High Glucose-Induced Insulin Resistance of Podocytes by Pleiotropic Effects on SIRT1 and AMPK. *Biochimica Biophysica Acta (BBA) - Mol. Basis Dis.* 1864 (1), 115–125. doi:10.1016/j.bbadis.2017.10.014

Sahlgren, C. M., Pallari, H.-M., He, T., Chou, Y.-H., Goldman, R. D., and Eriksson, J. E. (2006). A Nestin Scaffold Links Cdk5/p35 Signaling to Oxidant-Induced Cell Death. *EMBO J.* 25 (20), 4808–4819. doi:10.1038/sj.emboj.7601366

Shukla, V., Zheng, Y. L., Mishra, S. K., Amin, N. D., Steiner, J., Grant, P., et al. (2013). A Truncated Peptide from P35, a Cdk5 Activator, Prevents Alzheimer's Disease Phenotypes in Model Mice. *FASEB J.* 27 (1), 174–186. doi:10.1096/fj.12-217497

Skaper, S. D. (2017). Nerve Growth Factor: a Neuroimmune Crosstalk Mediator for All Seasons. *Immunology* 151 (1), 1–15. doi:10.1111/imm.12717

Susztak, K., Raff, A. C., Schiffer, M., and Bottinger, E. P. (2006). Glucose-Induced Reactive Oxygen Species Cause Apoptosis of Podocytes and Podocyte Depletion at the Onset of Diabetic Nephropathy. *Diabetes* 55 (1), 225–233. doi:10.2337/diabetes.55.01.06.db05-0894

Thomas, M. C., Brownlee, M., Susztak, K., Sharma, K., Jandeleit-Dahm, K. A. M., Zoungas, S., et al. (2015). Diabetic Kidney Disease. *Nat. Rev. Dis. Prim.* 1, 15018. doi:10.1038/nrdp.2015.18

Tsai, M.-S., Lee, P.-H., Sun, C.-K., Chiu, T.-C., Lin, Y.-C., Chang, I.-W., et al. (2018). Nerve Growth Factor Upregulates Sirtuin 1 Expression in Cholestasis: a Potential Therapeutic Target. *Exp. Mol. Med.* 50 (1), e426. doi:10.1038/emm.2017.235

Vega, J., and Huidobro E., J. P. (2019). Efectos en la función renal de la suplementación de creatina con fines deportivos. *Rev. Méd. Chile* 147 (5), 628–633. doi:10.4067/s0034-98872019000500628

Vesely, J., Havlicek, L., Strnad, M., Blow, J. J., Donella-Deana, A., Pinna, L., et al. (1994). Inhibition of Cyclin-dependent Kinases by Purine Analogues. *Eur. J. Biochem.* 224 (2), 771–786. doi:10.1111/j.1432-1033.1994.00771.x

Wei, F.-Y., and Tomizawa, K. (2007). Cyclin-Dependent Kinase 5 (Cdk5): A Potential Therapeutic Target for the Treatment of Neurodegenerative Diseases and Diabetes Mellitus. *Mrmc* 7 (10), 1070–1074. doi:10.2174/138955707782110114

White, K. E., Bilous, R. W., Marshall, S. M., El Nahas, M., Remuzzi, G., Piras, G., et al. (2002). Podocyte Number in Normotensive Type 1 Diabetic Patients with Albuminuria. *Diabetes* 51 (10), 3083–3089. doi:10.2337/diabetes.51.10.3083

Wosniak, J., Jr., Santos, C. X. C., Kowaltowski, A. J., and Laurindo, F. R. M. (2009). Cross-Talk between Mitochondria and NADPH Oxidase: Effects of Mild Mitochondrial Dysfunction on Angiotensin II-Mediated Increase in Nox Isoform Expression and Activity in Vascular Smooth Muscle Cells. *Antioxidants Redox Signal.* 11 (6), 1265–1278. doi:10.1089/ars.2009.2392

Yang, X., Zhang, W., Wu, H., Fu, S., Yang, J., Liu, S., et al. (2020). Downregulation of CDK5 Restores Sevoflurane-Induced Cognitive Dysfunction by Promoting SIRT1-Mediated Autophagy. *Cell Mol. Neurobiol.* 40 (6), 955–965. doi:10.1007/s10571-020-00786-6

Yaribeygi, H., Atkin, S. L., and Sahebkar, A. (2019). Interleukin-18 and Diabetic Nephropathy: A Review. *J. Cell. Physiology* 234 (5), 5674–5682. doi:10.1002/jcp.27427

Yu, J., and Auwerx, J. (2010). Protein Deacetylation by SIRT1: An Emerging Key Post-translational Modification in Metabolic Regulation. *Pharmacol. Res.* 62 (1), 35–41. doi:10.1016/j.phrs.2009.12.006

Zhang, Q., Zhang, P., Qi, G.-J., Zhang, Z., He, F., Lv, Z.-X., et al. (2018). Cdk5 Suppression Blocks SIRT1 Degradation via the Ubiquitin-Proteasome Pathway in Parkinson's Disease Models. *Biochimica Biophysica Acta (BBA) - General Subj.* 1862 (6), 1443–1451. doi:10.1016/j.bbagen.2018.03.021

Zheng, Y.-L., Zhang, X., Fu, H.-X., Guo, M., Shukla, V., Amin, N. D., et al. (2016). Knockdown of Expression of Cdk5 or P35 (A Cdk5 Activator) Results in Podocyte Apoptosis. *PLoS One* 11 (8), e0160252. doi:10.1371/journal.pone.0160252

Conflict of Interest: The authors declare that the research was conducted in the absence of any commercial or financial relationships that could be construed as a potential conflict of interest.

frontiers | Frontiers in Cell and Developmental Biology

ORIGINAL RESEARCH
published: 12 August 2022
doi: 10.3389/fcell.2022.908045

Caffeine Restores Neuronal Damage and Inflammatory Response in a Model of Intraventricular Hemorrhage of the Preterm Newborn

Pilar Alves-Martinez[1,2], Isabel Atienza-Navarro[1,2], Maria Vargas-Soria[1,2], Maria Jose Carranza-Naval[1,2,3], Carmen Infante-Garcia[1,2], Isabel Benavente-Fernandez[2,4,5], Angel Del Marco[1,2], Simon Lubian-Lopez[2,5] and Monica Garcia-Alloza[1,2]**

[1]Division of Physiology, School of Medicine, Universidad de Cadiz, Cadiz, Spain, [2]Biomedical Research and Innovation Institute of Cádiz Cadiz (INiBICA) Research Unit, Puerta del Mar University Hospital University of Cadiz, Cadiz, Spain, [3]Salus-Infirmorum, University of Cadiz, Cadiz, Spain, [4]Area of Pediatrics, Department of Child and Mother Health and Radiology, Medical School, University of Cadiz, Cadiz, Spain, [5]Section of Neonatology, Division of Pediatrics, Hospital Universitario Puerta del Mar, Cadiz, Spain

OPEN ACCESS

Edited by:
Natalia Martins Feitosa,
Federal University of Rio de Janeiro, Brazil

Reviewed by:
Leticia De Pontes,
University of São Paulo, Brazil
Fernanda Crunfli,
State University of Campinas, Brazil

***Correspondence:**
Simon Lubian-Lopez
simonlubian@sspa.juntadeandalucia.es
Monica Garcia-Alloza
monica.garcia@uca.es

Specialty section:
This article was submitted to Molecular and Cellular Pathology, a section of the journal Frontiers in Cell and Developmental Biology

Received: 30 March 2022
Accepted: 30 May 2022
Published: 12 August 2022

Citation:
Alves-Martinez P, Atienza-Navarro I, Vargas-Soria M, Carranza-Naval MJ, Infante-Garcia C, Benavente-Fernandez I, Del Marco A, Lubian-Lopez S and Garcia-Alloza M (2022) Caffeine Restores Neuronal Damage and Inflammatory Response in a Model of Intraventricular Hemorrhage of the Preterm Newborn. Front. Cell Dev. Biol. 10:908045. doi: 10.3389/fcell.2022.908045

Germinal matrix-intraventricular hemorrhage (GM-IVH) is the most frequent intracranial hemorrhage in the preterm infant (PT). Long-term GM-IVH-associated sequelae include cerebral palsy, sensory and motor impairment, learning disabilities, or neuropsychiatric disorders. The societal and health burden associated with GM-IVH is worsened by the fact that there is no successful treatment to limit or reduce brain damage and neurodevelopment disabilities. Caffeine (Caf) is a methylxanthine that binds to adenosine receptors, regularly used to treat the apnea of prematurity. While previous studies support the beneficial effects at the brain level of Caf in PT, there are no studies that specifically focus on the role of Caf in GM-IVH. Therefore, to further understand the role of Caf in GM-IVH, we have analyzed two doses of Caf (10 and 20 mg/kg) in a murine model of the disease. We have analyzed the short (P14) and long (P70) effects of the treatment on brain atrophy and neuron wellbeing, including density, curvature, and phospho-tau/total tau ratio. We have analyzed proliferation and neurogenesis, as well as microglia and hemorrhage burdens. We have also assessed the long-term effects of Caf treatment at cognitive level. To induce GM-IVH, we have administered intraventricular collagenase to P7 CD1 mice and have analyzed these animals in the short (P14) and long (P70) term. Caf showed a general neuroprotective effect in our model of GM-IVH of the PT. In our study, Caf administration diminishes brain atrophy and ventricle enlargement. Likewise, Caf limits neuronal damage, including neurite curvature and tau phosphorylation. It also contributes to maintaining neurogenesis in the subventricular zone, a neurogenic niche that is severely affected after GM-IVH. Furthermore, Caf ameliorates small vessel bleeding and inflammation in both the cortex and the subventricular zone. Observed mitigation of brain pathological features commonly associated with GM-IVH also results in a significant improvement of learning and memory abilities in the long term. Altogether, our data support the promising effects of Caf to reduce central nervous system complications associated with GM-IVH.

Keywords: preterm infant, germinal matrix-intraventricular hemorrhage, caffeine, atrophy, microglia, hemorrhage, cognition

1 INTRODUCTION

Very low birth weight infants (VLBWIs) are those preterm infants (PT) born at or under 32 weeks of gestational age. There are more than 15 million premature births worldwide every year, and preterm birth is the leading cause of death in children (Walani, 2020). Although in recent years survival rates of PT have increased due to advances in neonatal intensive care and perinatal medicine, this is also accompanied by an increase in morbidities associated with prematurity (for review (Atienza-Navarro et al., 2020)). Therefore, this preterm population is at high risk for complications such as germinal matrix-intraventricular hemorrhage (GM-IVH), which is not only one of the most common pathologies associated with prematurity but also the most frequent intracranial hemorrhage in the PT (da Silva et al., 2018). Although incidences may vary depending on the studies and populations assessed, approximately 20%–30% of all PT may suffer GM-IVH of any grade, and severe GM-IVH may affect between 6% and 16% of all PT (Stoll et al., 2010; Bolisetty et al., 2014; Radic et al., 2015a; Khanafer-Larocque et al., 2019). Moreover, severe GM-IVH is the leading cause of death in PT with a gestational age at birth under 28 weeks (Harkin et al., 2019).

The germinal matrix (GM) is a highly vascularized region that fully covers the ventricle. It is also a source of neuronal and glial cells in the immature brain that will maturate and migrate to their final destinations along development (Segado-Arenas et al., 2017; Cerisola et al., 2019). The immaturity of the central nervous system (CNS) of the PT, its hemodynamic instability (Szpecht et al., 2016), and the difficulty to autoregulate cerebral blood flow (Rellan Rodríguez et al., 2008) make the fragile GM vasculature prone to bleed (Atienza-Navarro et al., 2020; Lampe et al., 2020). Since GM commences to involute by 28 gestational weeks until it disappears in full-term kids (Mukerji et al., 2015; Segado-Arenas et al., 2017), GM-IVH affects almost exclusively VLBWIs (da Silva et al., 2018). GM-IVH–associated morbidities (Christian et al., 2016) include cerebral palsy, sensory and motor impairment, and learning disabilities among others (for review (Atienza-Navarro et al., 2020)). Although the harmful effects of severe GM-IVH seem unquestionable (Bolisetty et al., 2014; Mukerji et al., 2015), previous studies have also reported that any degree of GM-IVH may predispose to suffer these complications (Radic et al., 2015b; Iyer et al., 2015). GM-IVH patients also have a higher risk to develop psychiatric disorders such as autism spectrum disorders, anxiety, depression, or altered social behaviors (You et al., 2019; Chung et al., 2020).

The societal and health burden associated with prematurity and GM-IVH concretely, is worsened by the fact that there is no successful treatment to limit or reduce brain damage and neurodevelopment disabilities. Different options, such as prophylactic vitamin K, coagulating factors, angiogenic inhibitors, COX-2 inhibitor celecoxib, or endothelial growth factor R2 inhibitors, might have beneficial effects in the GM-IVH management by stabilizing the GM at different levels, but more studies are required before use in clinical care (for review (Deger et al., 2021)). Other approaches have focused on caffeine (Caf), regularly used to treat the apnea of prematurity (Long et al., 2021). Caf has antioxidant, neuroprotective, and anti-inflammatory properties, and studies in newborn and young animals have shown its capacity to reduce brain hypoxic damage (Yang et al., 2021). Similarly, studies in patients have reported that Caf treatment in VLBWI with apnea of prematurity may improve neurodevelopmental outcomes (Schmidt et al., 2007; Maitre et al., 2015). Nevertheless, to our knowledge, the direct effect of Caf on GM-IVH remains undetermined, and there is only one study assessing the role of Caf in GM-IVH (MRI and Neurodevelopment in PT Following Administration of High-Dose of Caf. ClinicalTrials.gov. Identifier: NCT00809055) reporting beneficial long-term effects of Caf treatment (Mürner-Lavanchy et al., 2018). Therefore, we have used an animal model of GM-IVH to specifically assess the effect of two doses of Caf (10 and 20 mg/kg/day) on brain pathology and cognitive performance. We have observed that both in the short term (P14) and in the long term (P70), Caf reduces brain atrophy. Also, mature neurons population and neuron curvature are significantly improved. Likewise, reduced proliferation and neurogenesis in the subventricular zone (SVZ) are ameliorated by Caf treatment. Furthermore, cortical and SVZ bleeding and inflammation are reduced, altogether resulting in better learning and memory capabilities in the long term, in line with previous observations in other models of perinatal insult (Endesfelder et al., 2017a; Yang et al., 2022). Ultimately, our results may help better understand the pathological features associated with GM-IVH in the PT and to elucidate the beneficial effects associated with Caf treatment.

2 METHODS

2.1 Animals and Treatments

For the experiment, 7-day-old (P7) CD1 mice received 0.3 IU of collagenase (Col) (purified collagenase VII, batch SLBG8830V, Sigma-Aldrich, St Louis, MO, United States) in 1 µl of TESCA (TES buffer 50mM and calcium chloride anhydrous 0.36 mM) administered intracerebroventricularly, as previously described (Segado-Arenas et al., 2017). Briefly, mice were anesthetized with isoflurane, immobilized in a stereotactic frame (David-Kopf, CA, United States), and Col was administered at 0.1 µl/min for 10 min using a 10-µl Hamilton syringe (Hamilton Company, United States) in the right ventricle (AP −3 mm, ML −1 mm, and DV +4 mm, using Bregma as reference). The needle was left in the lesion site for 5 min after completing the injection. Sham animals underwent the same surgical procedures but received 1 µl of TESCA. Animals were allowed to recover and were returned to the home cages with their mothers. A naïve group of animals did not undergo any surgical procedures. Animals were treated with

Caf (Sigma-Aldrich, St Louis, MO, United States) (10 or 20 mg/kg/day) intraperitoneally (i.p.) (Kaindl et al., 2008; Fan et al., 2011) for 3 consecutive days, commencing immediately after the lesions (P7–P9), and untreated animals received filtered phosphate buffer (PBS) instead. A first set of animals were analyzed at P14, and a second set of mice were analyzed at P70 to assess the effects of Caf in the short and long terms.

Body weight was measured before the lesions and before sacrifice at P14 and P70. All experimental procedures were approved by the Animal Care and Use Committee of the University of Cadiz, in accordance with the guidelines for care and use of experimental animals (European Commission Directive 2010/63/UE and Spanish Royal Decree 53/2013).

2.2 Morris Water Maze (MWM)

The MWM test commenced at P56, and it was performed as previously described (Segado-Arenas et al., 2017). Briefly, the pool consisted of a round tank 90 cm in diameter surrounded by external clues, with a platform hidden under the water. Water temperature was 21 ± 2 °C. The acquisition phase included four trials per day for 4 consecutive days. The time limit was 60 s/trial, with a 10-min inter-trial interval. If the animal did not find the platform, it was placed on the platform for 10 s. The retention phase was performed 24 and 72 h after the completion of the acquisition phase and consisted in a single trial with the platform removed. Time required to locate the platform in the acquisition phase, the number of entrances in quadrant 2, where the platform was located, during the retention phase, and swimming speed were analyzed by Smart software (Panlab, Barcelona, Spain).

2.3 Actimetry and the New Object Discrimination (NOD) Test

Spontaneous motor activity was analyzed the day after completing the MWM test by measuring the walking distance for 30 min in a rectangular box (44 cm long × 22 cm width × 40 cm high). The NOD test was commenced 24 hours later to analyze episodic memory. Animals were exposed to two objects for 5 min for habituation purposes, which were not used again during the test. The next day each mouse received two sample trials and a test trial. On the first sample trial, mice were allowed to explore for 5 min, with four copies of a novel object (navy balls) arranged in a triangle-shaped spatial configuration. After a 30-min delay, mice received a second sample trial with four novel objects (red cones) arranged in a quadratic-shaped spatial configuration, for 5 min. After 30 min, the mice received a test trial with two copies of the object from sample trial 2 ("recent" objects) placed at the same position, and two copies of the object from sample trial 1 ("familiar" objects) with one of them being placed at the same position ("old non displaced" object) and the other in a new position ("familiar displaced" object). An integrated episodic memory for "what," "where," and "when" paradigms were analyzed are shown, as previously described (Dere et al., 2005). "What" was defined as the difference in time exploring familiar and recent objects, "where" was defined as the difference in time exploring displaced and nondisplaced objects, and "when" was defined as the difference between time exploring familiar nondisplaced and recent nondisplaced objects.

2.4 Rotarod

Motor skills and motor coordination were also evaluated by the rotarod (Panlab Harvard Apparatus, Barcelona, Spain), as described (Segado-Arenas et al., 2017). The animal was placed for 3 min at 4 rpm for habituation purposes on the horizontal rod (3 cm in diameter and 5.7 cm wide). During the test, the speed was increased from 4 to 40 rpm within 1 min. The time spent on the rod and the velocity when the animal fell were recorded.

2.5 Tissue Processing

Animals were sacrificed by an overdose of pentobarbital (Richter Pharma, Wels, Austria) (120 mg/kg) administered i.p. Brains were harvested and weighed. While the ventricle provides complete access to the brain, our previous characterization of the model revealed that the right hemisphere was more severely affected after Col administration in the right ventricle (Segado-Arenas et al., 2017). Therefore, all of our *postmortem* analyses were performed on the brain structures of the right hemisphere (the cortex, SVZ, and hippocampus), as described (Segado-Arenas et al., 2017). The brains from half of the animals were fixed in 4% paraformaldehyde (PFA) for 3 weeks and cryoprotected in 30% sucrose, and serial coronal sections of 30 μm were cut on a cryostat (Thermo-Scientific, Microm HM 525, Germany). The sections were stored at −20°C in PBS and glycerol (1:1) until ipsilateral hemispheres were used. The brains from the remaining animals were dissected, and the ipsilateral cortex, striatum, and hippocampus were immediately frozen at −80°C for biochemical studies.

2.6 Cresyl Violet Staining

Six coronal sections of 30 μm at 1.5, 0.5, −0.5, −1.5, −2.5, and −3.5 mm from Bregma were selected (Segado-Arenas et al., 2017; Infante-Garcia et al., 2018). Sections were mounted on Superfrost™ slides (Thermo-Fisher Scientific, Waltham, MA, United States), dehydrated in 70% ethanol for 15 min, and incubated in 0.5% cresyl violet solution for 10 min. Tissues were fixed in 0.25% acetic acid in ethanol for 7 min, followed by ethanol for 2 min and xylol for 2 more minutes. Sections were mounted with DPX medium (Sigma Aldrich, St Louis, MO, United States). Images were photographed with a ×4 objective on an Olympus B×60 fluorescence microscope (Olympus, Tokyo, Japan) coupled to an Olympus DP71 camera, by MMIcellTools software (Olympus, Hamburg, Germany). Adobe Photoshop Elements software was used to photomerge all images and build complete sections. ImageJ was used to measure the total hemisection size, cortex, hippocampus, and ventricle areas. Quantifications were carried out in blind experiments for the person performing the measurements.

2.7 Prussian Blue Staining

Contiguous sections to those used for cresyl violet staining were selected to analyze small vessel bleeding, as described (Desestret et al., 2009) with minor modifications. Sections were dehydrated and incubated in Prussian blue solution (20% HCl and 10%

potassium ferrocyanide) for 30 min. They were rinsed with distilled water and rehydrated in PBS for 5 min. Sections were counterstained with neutral red (1% neutral red, 1% acetic acid) for 5 min. Sections were washed and dehydrated for 2 min with increasing concentrations of ethanol (95%, 99% + 1% of acetic acid, and 100%) and xylol. Sections were covered with DPX and photographed with an Olympus DP71 camera attached to an Olympus Bx60 microscope (Olympus, Tokyo, Japan) with a ×6.4 objective. Adobe Photoshop Elements software was used to photomerge all images and build complete sections. ImageJ software was used to quantify the hemorrhage burden (area occupied by hemorrhages) in the cortex and the SVZ.

2.8 NeuN/DAPI/Iba-1 Staining

Six coronal sections of 30 μm contiguous to those previously used were selected and incubated overnight at 4 °C with the anti-NeuN antibody (MAB377, Sigma, St. Louis, MO, United States) (1:200) to label mature neurons, and anti-Iba-1 (019-19741, Wako, Osaka, Japan) (1:1,000) as a microglia marker (Infante-Garcia et al., 2017a). Sections were incubated with anti-IgG-mouse Alexa Fluor 488 (1:1,000) (Thermo Fisher Scientific, Waltham, MA, United States) and anti-IgG-goat Alexa Fluor 594 (1:1,000) (Thermo Fisher Scientific, Waltham, MA, United States) for 1 h, followed by counterstaining with DAPI 1 mg/ml (Sigma, St. Louis, MO, United States) (1:3,000) for 10 min. Sections were photographed using an Olympus Bx60 fluorescence microscope (Olympus, Tokyo, Japan) coupled to an Olympus DP71 camera with a ×16 objective.

Twenty ROIs (7,451.062 μm^2/ROI) were selected in each cortical section, and eight ROIs were also selected in three sections 1 mm apart (1.5 to −0.5 mm from Bregma) which comprised the SVZ. The percentage of NeuN-positive cells (normalized by total cells stained with DAPI) was quantified in the cortex and the SVZ by ImageJ software (Ramos-Rodriguez et al., 2017).

Microglia burden (% covered area by Iba-1 immunostaining) in the cortex and the SVZ was also quantified by analyzing 20 ROIs/section in the cortex and eight ROIs/section in the SVZ by ImageJ software, as described (Infante-Garcia et al., 2016).

2.9 SMI-312 Immunostaining

The axonal curvature was analyzed with the anti-neurofilament marker SMI-312 antibody (Infante-Garcia et al., 2017b) in contiguous sections to those previously used. Sections were pretreated with 3% hydrogen peroxide and 0.5% Triton-X for 10 min and blocked with 3% bovine serum albumin (BSA) for 3 h. Thereafter, the sections were incubated with anti-SMI-312 (1:1,000) (837904, BioLegend, San Diego, CA, United States) overnight at 4°C. Anti-IgG-mouse Alexa Fluor 594 was used as a secondary antibody (Thermo Fisher Scientific, Waltham, MA, United States) (1:200). Images were acquired with an Olympus Bx60 fluorescence microscope (Olympus, Tokyo, Japan) coupled to an Olympus DP71 camera with a 40X objective and MMIcellTools software. The axon curvature ratio was calculated by dividing the end-to-end distance of a neurite segment by the total length between the two segment ends. Neurites had at least 20 μm of length (Infante-Garcia et al., 2017b). At least 150 neurites in the cortex and 45 neurites in the SVZ of each animal were analyzed by ImageJ software.

2.10 Ki67 and Doublecortin (DCX) Immunostaining

Proliferation and neurogenesis were analyzed in the SVZ. Three sections 1 mm apart (1.5 to −0.5 mm from Bregma) were selected. To analyze proliferation and neurogenesis, the anti-Ki67 antibody (ab15580, Abcam, Amsterdam, Netherlands) (1:200) and anti-DCX antibody (sc-271390, Santa Cruz Biotechnology, Inc., Texas, United States) (1:50) were used as described in Hierro-Bujalance et al. (2020a). Sections were pretreated with citrate formamide (1:1) for 2 h at 65°C. Thereafter, sections were incubated in 2N HCL for 30 min at 37°C and placed in a 0.1M borate buffer at pH 8.5. After blocking with 3% BSA and 0.5% TritonX-100 for 1 h, sections were incubated with primary antibodies overnight at 4 °C. Secondary antibodies anti-IgG-rabbit Alexa Fluor 488 (Thermo Fisher Scientific, Waltham, MA, United States) (1:1,000) and anti-IgG-mouse Alexa Fluor 594 (Thermo Fisher Scientific, Waltham, MA, United States) (1:1,000) were used. Confocal images of 30 μm in depth were acquired with a Z-step size of 2 μm. A ×20 objective on a Zeiss LSM 900 Airyscam 2 confocal microscope (Zeiss, Oberkochen, Germany) was used.

ImageJ software was used to analyze DCX burden (percentage of area covered by DCX^+ cells), density of $Ki67^+$ cells, and overlapping DCX^+ area/$Ki67^+$ cells in the SVZ, as described in Ramos-Rodriguez et al. (2014), considering the SVZ area comprised in the first 100 μm adjacent to the ventricle lumen.

2.11 Total-Tau and Phospho-Tau Levels

Total-tau (10736333, Invitrogen, Thermo-Fisher Scientific, Waltham, MA, United States) and phospho-tau levels [pS199] (10272883, Invitrogen, Thermo-Fisher Scientific, Waltham, MA, United States) were measured in the cortex and striatum samples by colorimetric ELISA kits, following the manufacturer's instructions. Briefly, 10 mg of tissue were homogenized in 50 μl of homogenization buffer (5 M guanidine-HCl diluted in 50 mM Tris) with protease and phosphatase inhibitor cocktail for 20 min on ice. The homogenate was centrifuged at 14,500×g for 5 min at 4 °C, and the supernatant was collected for ELISA assay. Absorbances were measured at 450 nm in a spectrophotometer (MQX200R2, BioTek Instruments, Burlington VT, United States). Phospho-tau/total-tau ratios in pmol/g tissue were calculated, and results are expressed as a percentage of control values.

2.12 Statistical Analysis

Two-way ANOVA (group × treatment) followed by the *post hoc* Tukey b test was used. No statistical differences were detected between sham and naïve groups, and therefore, these animals were combined in a single control group. Three-way ANOVA (group × treatment × day) was used to analyze the acquisition phase of the MWM test. Statistical data are collected in **Supplementary Table S1**. SPSS v.24 software was used for all statistical analyses.

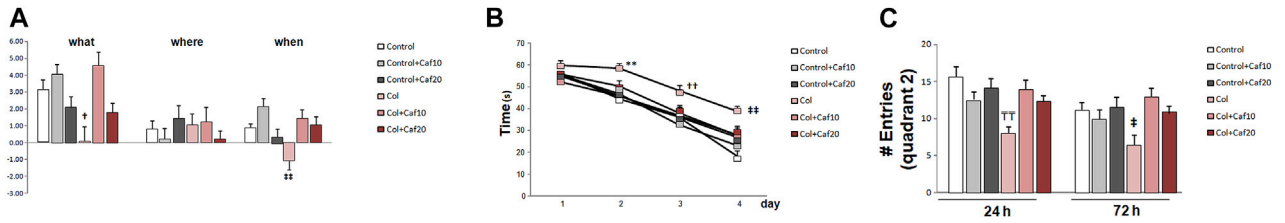

FIGURE 1 | Caf treatment limits cognitive impairment after GM-IVH. **(A)** Col-treated mice were compromised in the NOD test for "what" and "when" paradigms. Caf treatment reverted this situation ("what" [$F_{(2,200)} = 2.32$ and $p = 0.038$; †$p = 0.014$ vs. Control + Caf10, Control + Caf20, and Col + Caf10]; "where" [$F_{(2,213)} = 1.28$ and $p = 0.278$]; "when" [$F_{(2,209)} = 3.97$ and $p = 0.002$; ‡‡$p < 0.001$ vs. Control, Control+ Caf10, Col + Caf10, and Col + Caf20]. Data are representative of 10–16 animals (Control n = 16, Control + Caf10 n = 15, Control + Caf20 n = 15, Col n = 10, Col + Caf10 n = 10, and Col + Caf20 n = 13). **(B)** Individual day assessment in the acquisition phase of the MWM revealed that GM-IVH impairs learning in the acquisition phase while Caf treatment limits this situation (day 1 [$F_{(5,305)} = 1.72$ and $p = 0.128$], day 2 [$F_{(5,307)} = 0.315$ and $^{**}p = 0.009$ vs. rest of the groups], day 3 [$F_{(5,310)} = 2.52$ and ††$p = 0.029$ vs. Control, Control + Caf10, and Control+ Caf20], day 4 [$F_{(5,270)} = 5.050$ and ‡‡$p < 0.01$ vs. Control and Control+ Caf10]. Data are representative of 10–16 animals (Control n = 16, Control + Caf10 n = 16, control + Caf20 n = 16, Col n = 10, Col + Caf10 n = 10, and Col + Caf20 n = 12). **(C)** In the retention phase of the MWM, we analyzed the number of times that mice entered the quadrant where the platform used to be located (quadrant 2), and we observed that Col-injured mice entered a significantly lower number of times, while Caf reversed this situation during retention 1 (24 h) [$F_{(2,67)} = 5.88$ and $p = 0.004$; $\overline{\text{TT}}p = 0.003$ vs. Control, Control + Caf10, Control + Caf20, and Col + Caf10]. A similar profile was observed in retention 2 (72 h) [$F_{(2,65)} = 4.60$ and $p = 0.013$; ‡$p = 0.047$ vs. Control + Caf10 and Control + Caf20]. Data are representative of 9–16 animals (Control n = 16, Control + Caf10 n = 15, Control + Caf20 n = 15, Col n = 9, Col + Caf10 n = 9, and Col + Caf20 n = 13).

TABLE 1 | Motor activity was not affected in any of the groups under study.

Treatment	Distance travelled (cm)	Time rotarod (s)	Speed rotarod (rpm)	Swimming velocity (cm/s)
Control	11,487.05 ± 865.02	14.06 ± 2.30	19.12 ± 2.02	27.53 ± 2.80
Control + Caf10	14,100.55 ± 840.67	12.73 ± 2.58	15.00 ± 1.72	22.79 ± 1.28
Control + Caf20	13,996.44 ± 1,688.70	13.66.1.80	20.13 ± 2.33	23.71 ± 1.03
Col	9,081.58 ± 1,085.24	10.37 ± 1.68	14.50 ± 2.40	25.57 ± 1.14
Col + Caf10	10,102.61 ± 1737.52	13.50 ± 2.70	17.80 ± 1.89	28.06 ± 2.95
Col + Caf20	11,489.95 ± 1,502.97	15.25 ± 1.54	20.07 ± 1.40	26.30 ± 2.92

Distance travelled in the motor activity test was not affected in any of the groups under study [$F_{(2,70)} = 1.59$; p = 0.211]. Similarly, time [$F_{(2,73)} = 1.60$; p = 0.209] and speed [$F_{(5,72)} = 0.906$; p = 0.482] in the rotarod test were similar in all groups under study. No differences were observed in the swimming velocity in the MWM test [$F_{(2,73)} = 2.70$; p = 0.074].

3 RESULTS

3.1 Caf Treatment Restores Cognitive Deficits in Mice With GM-IVH

We analyzed episodic memory in the NOD test and while we did not detect significant differences among groups for "where" paradigm, we observed a compromise for "what" and "when" paradigms in animals with GM-IVH. Nevertheless, Caf treatment (10 mg/Kg/day) significantly improved the performance in the "what" paradigm, while both doses of Caf (10 and 20 mg/Kg/day) restored the impairment observed for "when" paradigm (**Figure 1A**).

When analyzing learning and memory in the MWM, we did not detect a significant group × treatment × day effect in the acquisition phase [$F_{(61,196)} = 1.18$; $p = 0.350$]. However, the individual day assessment revealed a progressive compromise in mice with GM-IVH that was partially restored by Caf treatment. On day 2, both doses of Caf under study (10 and 20 mg/kg/day) significantly improved the performance in the MWM, and no differences were detected on the following days between control animals and animals with GM-IVH treated with Caf (**Figure 1B**). Memory impairment was also observed in animals with GM-IVH when the numbers of entrances in quadrant 2, where the platform was located along the acquisition phase, were compared. Animals treated with both doses of Caf treatment (10 and 20 mg/kg/day) reached control values 24 and 72 h after completing the acquisition phase, and Caf (10 mg/Kg/day) significantly improved the performance 24 h after completing the acquisition phase (**Figure 1C**).

The motor activity was not affected in any of the groups under study when we compared the total distance traveled in the open field, swimming speed in the MWM, time, and speed in the rotarod test (**Table 1**), suggesting that all observed behavioral outcomes are indeed due to learning and memory alterations and not due to motor alterations.

3.2 Brain Atrophy Is Reduced in GM-IVH Animals After Caf Treatment

When we compared brain/body weight in all groups under study, we observed a significant reduction of this ratio in mice with GM-IVH in both the short (P14) and the long (P70) term. Our observations are in accordance with previous studies in a similar model (Jinnai et al., 2020), and also, patients with GM hemorrhage showed ventriculomegaly on the side of the hemorrhage with mild atrophy (Fusch et al., 1997). By P14, no differences were observed between control animals and those with GM-IVH treated with Caf. In the long term (P70), brain/

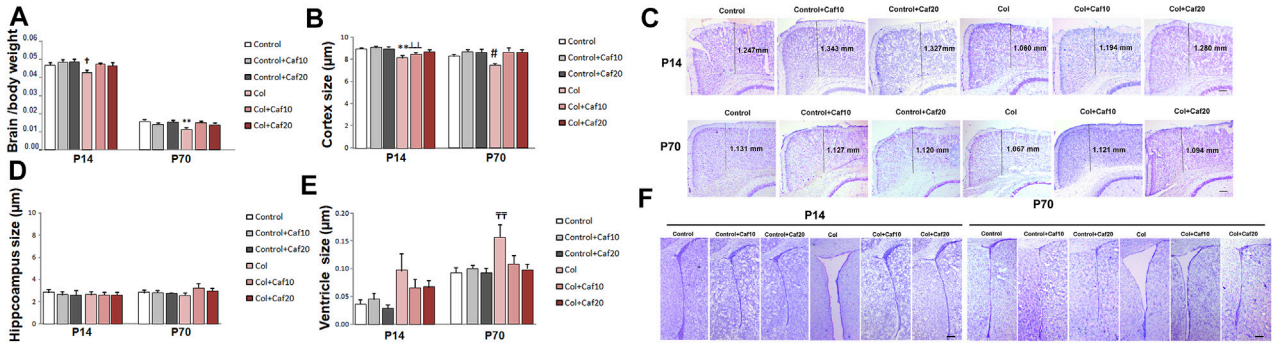

FIGURE 2 | Brain atrophy was improved by Caf treatment. **(A)** Brain/body weight ratio was reduced in mice with GM-IVH, and this effect was limited by Caf treatment, at both 10 and 20 mg/kg/day in the short term [$F_{(2,87)} = 4.24$ and †$p = 0.017$ vs. Control, Control + Caf10 and Control + Caf20]. Data are representative of 9–21 mice (Control n = 16, Control + Caf10 n = 19, Control + Caf20 n = 18, Col n = 13, Col + Caf10 n = 13, and Col + Caf20 n = 17). Brain/body weight ratio was still reduced at P70 and Caf treatment restored this situation [$F_{(2,93)} = 8.38$ and $^{**}p < 0.01$ vs. rest of the groups]. Data are representative of 10–21 mice (Control n = 21, Control + Caf10 n = 17, Control + Caf20 n = 19, Col n = 10, Col + Caf10 n = 15, and Col + Caf20 n = 17). **(B)** At P14, we detected a reduction of cortical size after Col lesions [$F_{(2,236)} = 3.30$ and $p = 0.038$, $^{**}p < 0.001$ vs. rest of the groups, and $\perp\!\!\perp p < 0.001$ vs. Control + Caf10], which was limited by Caf treatment, and a similar profile was observed at P70 [$F_{(2,187)} = 3.32$ and $p = 0.038$, #$p = 0.007$ vs. Control + Caf20, Col + Caf10, and Col + Caf20]. Data are representative of 6–8 mice (Control n = 8, Control + Caf10 n = 7, Control + Caf20 n = 6, Col n = 7, Col + Caf10 n = 7, and Col + Caf20 n = 8). **(C)** Representative cresyl violet staining images showing cortical size reduction after inducing GM-IVH and the restorative effect of Caf treatment at P14 and P70. Scale bar = 100 µm. **(D)** We did not observe any significant differences among groups when we compared the hippocampus size at P14 [$F_{(2,117)} = 0.117$ and $p = 0.890$]. Data are representative of 5–8 mice (Control n = 8, Control + Caf10 n = 7, Control + Caf20 n = 5, Col n = 7, Col + Caf10 n = 7, and Col + Caf20 n = 8). Differences did not reach statistical significance at P70 either [$F_{(2,83)} = 0.779$ and $p = 0.453$]. Data are representative of 4–7 mice (Control n = 6, Control + Caf10 n = 7, Control + Caf20 n = 4, Col n = 6, Col + Caf10 n = 4, and Col + Caf20 n = 7). **(E)** We detected ventricle enlargement after Col lesions, and Caf treatment limited this situation, reaching statistical significance in the long term: P14 [$F_{(2,107)} = 0.198$ and $p = 0.5$]. Data are representative of 6–8 mice (Control n = 8, Control + Caf10 n = 6, Control + Caf20 n = 6, Col n = 7, Col + Caf10 n = 7, and Col + Caf20 n = 8); P70 [$F_{(2,163)} = 3.12$ and $p = 0.046$; $\overline{\top\top} p = 0.005$ vs. Control, Control + Caf10, Control + Caf20, and Col + Caf20]. Data are representative of 4–7 mice (Control n = 6, Control + Caf10 n = 7, Control + Caf20 n = 4, Col n = 6, Col + Caf10 n = 4, and Col + Caf20 n = 7). **(F)** Representative cresyl violet staining images showing ventricle enlargement after inducing GM-IVH and the restorative effect of Caf treatment at P14 and P70. Scale bar = 100 µm.

body ratios were significantly improved by Caf (10 and 20 mg/Kg/day) when treated animals were compared with untreated GM-IVH mice (**Figure 2A**).

Further assessment of brain morphology revealed a compromise in animals with GM-IVH when we analyzed the cortical size. A significant reduction of the cortex size was observed, and Caf treatment limited this effect when animals were analyzed at P14. By P70, Caf treatment (10 and 20 mg/kg/day) significantly improved the cortical size when compared with those from untreated animals (**Figures 2B,C**). No significant differences among groups were observed when we compared the hippocampus size (**Figure 2D**). Nevertheless, brain atrophy was also supported by a significant ventricle enlargement detected in mice with GM-IVH both in the short (P14) and in the long term (P70), as previously described (Segado-Arenas et al., 2017). No differences were observed between control animals and GM-IVH mice treated with Caf in the short term (P14). Also, Caf 10 and 20 mg/kg/day significantly reduced ventricle enlargement at P70, when treated mice were compared with animals with GM-IVH, supporting the neuroprotective effect of the treatment (**Figures 2E,F**).

3.3 Caf Treatment Restores Neuron Density and Curvature

We also characterized the neuron density and neuritic curvature as a marker of neuron wellbeing, as previously described (Stern et al., 2004; Meyer-Luehmann et al., 2008). Mature neuron density was quantified by measuring the NeuN/DAPI ratio. We observed that this ratio was significantly compromised in the cortex both in the short (P14) and the long (P70) term, after inducing a GM-IVH, while Caf treatment (10 and 20 mg/kg/day) significantly improved this situation at both time points, reaching control values for both 10 and 20 mg/kg/day (**Figures 3A,B**) and suggesting a role in protecting neuronal integrity after the lesions. When we analyzed the SVZ, we observed a reduced NeuN/DAPI ratio in animals with a lesion that was significantly improved in the short term (P14) after 10 and 20 mg/kg/day Caf was administered. Differences were not statistically significant in the long term (P70) (**Figure 3C**).

We also analyzed neuron wellbeing by measuring the neurite curvature since increased curvature ratios are observed in neurons under other insults (Meyer-Luehmann et al., 2008; Infante-Garcia et al., 2017b). At P14, the neurite curvature was severely compromised in the cortex from animals with GM-IVH when compared with the rest of the groups. A significant improvement was observed after Caf treatment at both doses under study (10 and 20 mg/kg/day) when compared with untreated mice with GM-IVH, although they did not reach control values (**Figures 3D,E**). Differences in the neurite curvature were no longer detected among groups when the cortex was analyzed in the long term (P70) (**Figures 3D,E**). At P14, neurite curvature was significantly affected in the SVZ from animals lesioned with Col, and Caf (10 and 20 mg/kg/day) completely reversed this limitation (**Figure 3F**). On the other hand, as observed in the cortex, differences among groups were

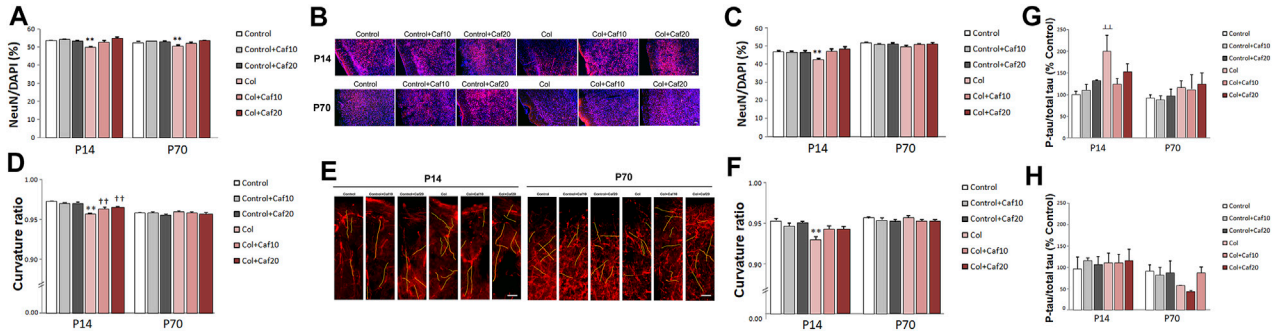

FIGURE 3 | Caf reduces neuronal compromise after GM-IVH. **(A)** NeuN/DAPI ratio was significantly reduced in the cortex from Col-treated mice, and Caf treatment reverted this situation at P14 [$F_{(2,271)} = 9.53$ and $p < 0.001$; $^{**}p < 0.01$ vs. rest of the groups]. Data are representative of 3–5 mice (Control n = 4, Control + Caf10 n = 5, Control + Caf20 n = 5, Col n = 3, Col + Caf10 n = 4, and Col + Caf20 n = 4). Similar differences were observed at P70 [$F_{(22,983)} = 4.45$ and $p = 0.012$; $^{**}p < 0.01$ vs. rest of the groups]. Data are representative of 3–6 mice (Control n = 6, Control + Caf10 n = 5, Control + Caf20 n = 5, Col n = 4, Col + Caf10 n = 4, and Col + Caf20 n = 3). **(B)** Representative images of cortical NeuN (red) and DAPI (blue) staining showing that the reduced NeuN/DAPI ratio in GM-IVH animals improves in Caf-treated animals at P14 and P70. Scale bar = 50 μm. **(C)** NeuN/DAPI ratio was affected in the SVZ at P14 [$F_{(2,420)} = 11.82$ and $p < 0.01$; $^{**}p < 0.01$ vs. rest of the groups]. Data are representative of 3–5 mice (Control n = 4, Control + Caf10 n = 5, Control + Caf20 n = 5, Col n = 3, Col + Caf10 n = 3, and Col + Caf20 n = 3). Differences were no longer detected at P70 [$F_{(2,559)} = 0.351$ and $p = 0.704$]. Data are representative of 3–6 mice (Control n = 6, Control + Caf10 n = 5, Control + Caf20 n = 5, Col n = 4, Col + Caf10 n = 4, and Col + Caf20 n = 3). **(D)** Cortical curvature ratio was significantly affected by Col lesions, and Caf treatment improved this situation at P14 [$F_{(24,048)} = 16.79$ and $p < 0.01$; $^{**}p < 0.01$ vs. rest of the groups, $\dagger\dagger p < 0.01$ vs. Control, Control + Caf10, and Control + Caf20]. Data are representative of 5–6 mice (Control n = 5, Control + Caf10 n = 5, Control + Caf20 n = 5, Col n = 6, Col + Caf10 n = 6, and Col + Caf20 n = 5). No differences were observed in any of the groups under study when the curvature ratio was analyzed in the cortex at P70 [$F_{(23,645)} = 2.65$, $p = 0.071$]. Data are representative of 4–5 mice (Control n = 5, Control + Caf10 n = 5, Control + Caf20 n = 4, Col n = 5, Col + Caf10 n = 5, and Col + Caf20 n = 5). **(E)** Illustrative example of cortical SMI-312 staining at P14 and P70. Representative neurites are labeled in yellow to highlight neuronal curvature in all groups under study. Scale bar = 15 μm. **(F)** Curvature ratio was also significantly affected in the SVZ at P14 [$F_{(21,129)} = 7.27$ and $p = 0.001$; $^{**}p < 0.01$ vs. rest of the groups]. Data are representative of 4–5 mice (Control n = 5, Control + Caf10 n = 5, Control + Caf20 n = 4, Col n = 5, Col + Caf10 n = 5, and Col + Caf20 n = 5). Neuron curvature ratio was no longer affected in the SVZ at P70 [$F_{(21,016)} = 0.269$ and $p = 0.765$]. Data are representative of 4–5 mice (Control n = 5, Control + Caf10 n = 5, Control + Caf20 n = 3, Col n = 5, Col + Caf10 n = 5, and Col + Caf20 n = 5). **(G)** Tau phosphorylation was significantly increased in the cortex from P14 mice after Col lesions, and Caf treatment improved this situation when compared with Control mice [$F_{(2,30)} = 3.33$ and $p = 0.49$; $\perp\!\!\!\perp p = 0.006$ vs. Control and Control + Caf10]. Data are representative of 5–7 animals (Control n = 7, Control + Caf10 n = 5, Control + Caf20 n = 5, Col n = 7, Col + Caf10 n = 6, and Col + Caf20 n = 6). Differences were no longer detected in the long term [$F_{(2,26)} = 0.016$ and $p = 0.984$]. Data are representative of 4–7 animals (Control n = 5, Control + Caf10 n = 5, Control + Caf20 n = 4, Col n = 7, Col + Caf10 n = 6, and Col + Caf20 n = 5). **(H)** Tau phosphorylation was not significantly affected in the striatum from P14 mice [$F_{(2,27)} = 0.031$ and $p = 0.970$]. Data are representative of 5–6 animals (Control n = 5, Control + Caf10 n = 5, Control + Caf20 n = 6, Col n = 6, Col + Caf10 n = 5, and Col + Caf20 n = 6). No differences were observed among groups at P70 [$F_{(2,25)} = 0.768$ and $p = 0.474$]. Data are representative of 5–6 animals (Control n = 5, Control + Caf10 n = 5, Control + Caf20 n = 5, Col n = 5, Col + Caf10 n = 5, and Col + Caf20 n = 6).

no longer observed when the neurite curvature was analyzed in the long term (P70) in the SVZ.

3.4 Caf Treatment Limits Cortical Tau Hyperphosphorylation

When we analyzed the cortex from GM-IVH, we observed an increase in [pS199] tau phosphorylation by 14 days of age. Abnormal tau phosphorylation is observed in different neuropathological situations as a marker of neuronal damage, and interestingly, even early tau alterations might significantly worsen cognitive function (Hochgräfe et al., 2013). The reduction observed in the phospho tau/total tau ratio after the Caf treatment was not statistically significant when compared with untreated animals, although differences were no longer detected when Caf-treated mice were compared with control animals (**Figure 3G**). By P70, tau hyperphosphorylation was no longer observed in the cortex from animals with a lesion, and no differences were detected among groups (**Figure 3G**). When we analyzed the striatum, we did not observe any significant differences in tau phosphorylation in the short (P14) or the long (P70) term (**Figure 3H**).

3.5 Neurogenesis Impairment Is Improved by Caf Treatment After Inducing GM-IVH

We analyzed proliferation and neurogenesis (by Ki67 and DCX immunostaining respectively) in the SVZ, a major neurogenic niche in the mouse. We detected an overall reduction in the number of $Ki67^+$ cells and DCX^+ area from P14 to P70, as previously described in other models (Hierro-Bujalance et al., 2020a), since both processes are reduced with age. We did not observe significant differences in the number of proliferating cells after GM-IVH lesions or after Caf treatment in the short (P14) or in the long (P70) term (**Figures 4A,D**). However, we observed a compromise in neurogenesis, and the DCX burden was severely reduced in the SVZ at P14 after Col lesions, probably as a consequence of the damage in the area induced by Col administration, as previously described (Segado-Arenas et al., 2017). Nevertheless, Caf treatment at the highest dose (20 mg/kg/day) improved this situation in the short term (P14) reaching control values, suggesting that beneficial effects mediated by Caf might be related to its capacity to preserve brain neurogenesis. While a similar profile was observed in the long term (P70), differences did not reach statistical significance (**Figures 4B,D**). We also observed a compromise when we analyzed DCX area/

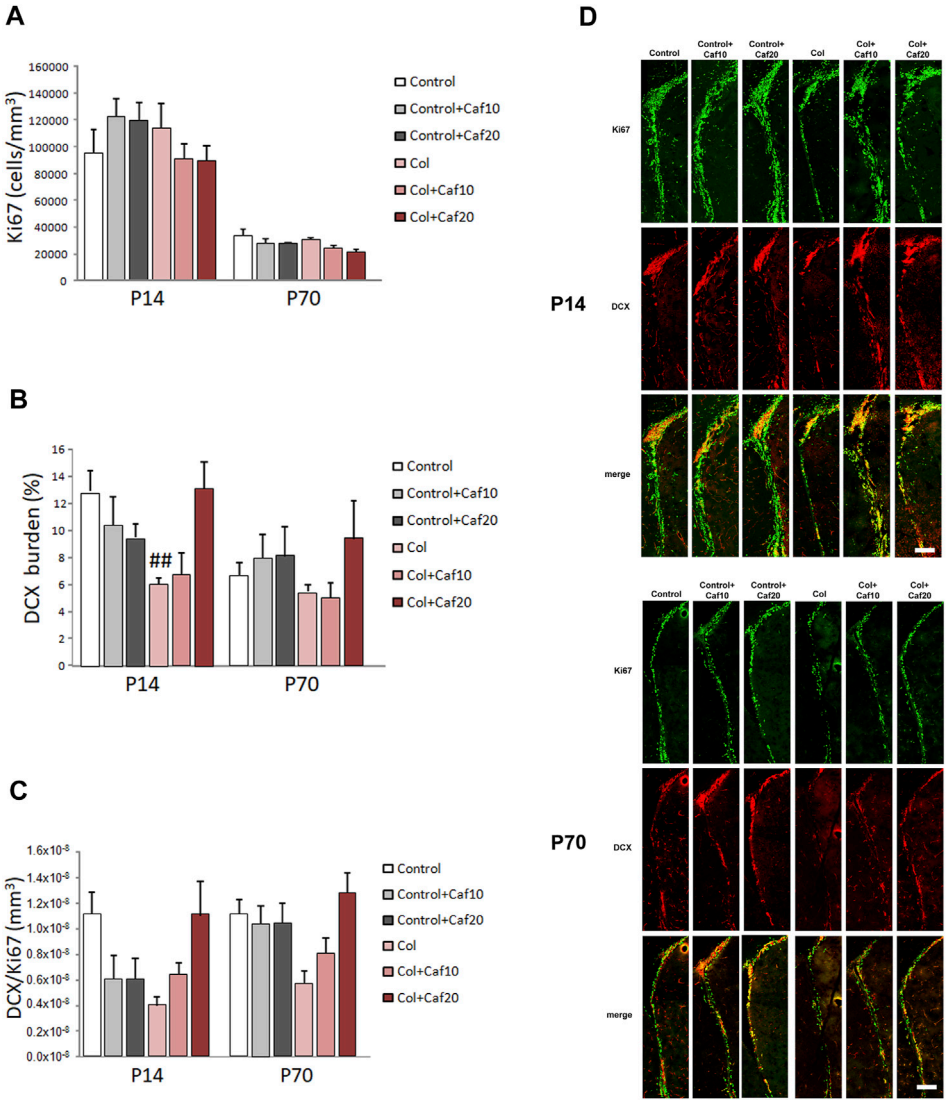

FIGURE 4 | Caf treatment improves neurogenesis in the SVZ after GM-IVH. **(A)** Proliferating cells were not significantly affected in the SVZ when we analyzed the density of Ki67$^+$ cells in the short (P14) [$F_{(2,94)} = 1.74$ and $p = 0.181$] or the long (P70) [$F_{(2,85)} = 0.023$ and $p = 0.977$] term. **(B)** DCX burden was significantly reduced in the SVZ after GM-IVH induction. The highest dose of Col (20 mg/kg/day) counterbalanced this situation at P14 [$F_{(2,95)} = 5.86$ and $p = 0.003$; ##$p = 0.004$ vs. Control and col + Caf20], and a similar profile was observed at P70, although differences were not statistically significant [$F_{(2,83)} = 0.694$ and $p = 0.503$]. **(C)** DCX area/Ki67$^+$ cell ratio was also reduced after Col lesions, although differences were not statistically significant at P14 [$F_{(2,96)} = 0.00$ and $p = 1.00$] or P70 [$F_{(2,84)} = 0.00$ and $p = 1.00$]. Data are representative of 6–7 animals (P14: Control n = 7, Control + Caf10 n = 6, Control + Caf20 n = 6, Col n = 7, Col + Caf10 n = 6, and Col + Caf20 n = 6. P70: Control n = 7, Control + Caf10 n = 6, Control + Caf20 n = 6, Col n = 7, Col + Caf10 n = 6, and Col + Caf20 n = 6). **(D)** Illustrative example of Ki67 (green) and DCX (red) immunostaining in the SVZ from mice with GM-IHV treated with Caf at P14 and P70. Scale bar = 125 μm.

Ki67$^+$ cells in the SVZ, although differences were not statistically significant (**Figures 4C,D**).

3.6 Bleeding Is Reduced by Caf Treatment After GM-IVH

As previously shown, induction of GM-IVH results in an overspread increase in small vessel bleeding in the brain (Segado-Arenas et al., 2017; Hierro-Bujalance et al., 2020b), supporting the idea that vascular damage is not only limited to the site of the injection but also showing alterations in more distant regions. In our hands, Caf reduced vascular damage analyzed by the presence of hemorrhages in the brain. When we analyzed the cortex, we observed that hemorrhage burden was significantly increased at P14, while no differences were observed when Caf-treated animals were compared with control mice. Cortical hemorrhage burden was also significantly increased in the long term (P70) in animals with GM-IVH, whereas Caf treatment effectively reduced the presence of cortical hemorrhages when administered at 10 and 20 mg/kg/day (**Figures 5A,B**). As expected, the SVZ was the most severely affected area due to its proximity to the

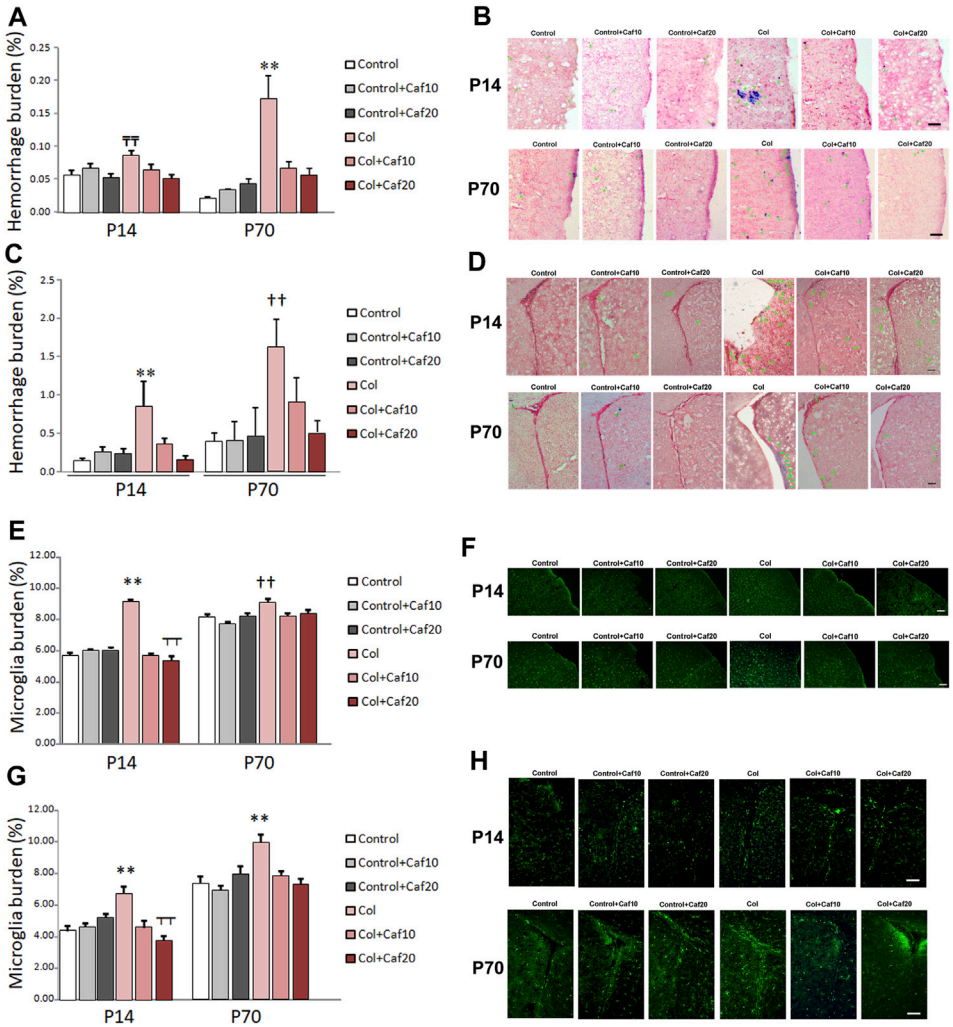

FIGURE 5 | Caf reduces bleeding and inflammation in the brain from animals with GM-IVH. **(A)** Hemorrhage burden was increased in the cortex from animals with Col lesions, and Caf treatment limited this situation in the short term (P14) [$F_{(2,150)} = 4.27$ and $p = 0.016$; $\top\top p = 0.001$ vs. Control, Control + Caf20, and Col + Caf20] and completely reversed it in the long term (P70) [$F_{(2,153)} = 12.02$ and $p < 0.001$; $^{**}p = 0.001$ vs. rest of the groups]). Data are representative of 4–6 animals (P14: Control n = 6, Control + Caf10 n = 5, Control + Caf20 n = 5, Col n = 6, Col + Caf10 n = 6, and Col + Caf20 n = 6. P70: Control n = 5, Control + Caf10 n = 5, Control + Caf20 n = 4, Col n = 6, Col + Caf10 n = 4, and Col + Caf20 n = 5). **(B)** Illustrative example of Prussian blue staining in the cortex from animals with GM-IVH lesions and after treatment with Caf. Green arrows point at hemorrhages. Scale bar = 100 μm. **(C)** Increased hemorrhage burden in the SVZ was also reduced after Caf treatment at P14 [$F_{(2,73)} = 5.93$ and $p = 0.004$; $^{**}p = 0.003$ vs. rest of the groups] and P70 [$F_{(2,71)} = 4.74$ and $p = 0.012$; $\dagger\dagger p = 0.010$ vs. Control, Control + Caf10, Control + Caf20, and Col + Caf20]. Data are representative of 4–6 animals (P14: Control n = 6, Control + Caf10 n = 5, Control + Caf20 n = 5, Col n = 6, Col + Caf10 n = 5, and Col + Caf20 n = 5. P70: Control n = 5, Control + Caf10 n = 5, Control + Caf20 n = 4, Col n = 6, Col + Caf10 n = 4, and Col + Caf20 n = 5). **(D)** Illustrative example of Prussian blue staining in the SVZ from animals with GM-IVH lesions and after treatment with Caf. Green arrows point at hemorrhages. Scale bar = 100 μm. **(E)** Microglial burden was significantly increased after Col lesions, and Caf treatment reverted this situation at P14 in the cortex [$F_{(21,814)} = 87.42$ and $p < 0.001$; $^{**}p < 0.01$ vs. rest of the groups and $\top\top p < 0.01$ vs. Control + Caf20]. A similar profile was observed at P70 in the cortex [$F_{(22,914)} = 6.22$ and $p = 0.002$; $\dagger\dagger p < 0.01$ vs. Control, Control + Caf10, Col + Caf10, and Col + Caf20]. Data are representative of 3–5 animals (P14: Control n = 3, Control + Caf10 n = 5, Control + Caf20 n = 5, Col n = 3, Col + Caf10 n = 3, and Col + Caf20 n = 4. P70: Control n = 5, Control + Caf10 n = 6, Control + Caf20 n = 5, Col n = 4, Col + Caf10 n = 4, and Col + Caf20 n = 3). **(F)** Illustrative images of cortical Iba-1 staining in the cortex from all groups under study at P14 and P70. Scale bar = 100 μm. **(G)** GM-IVH also increased microglial burden in the SVZ, and Caf reversed this situation at both P14 [$F_{(2,335)} = 12.11$ and $p < 0.001$; $^{**}p < 0.01$ vs. rest of the groups and $\top\top p < 0.01$ vs. Control + Caf20] and P70 [$F_{(2,547)} = 7.14$ and $p = 0.001$; $^{**}p < 0.01$ vs. rest of the groups]. **(H)** Illustrative images of cortical Iba-1 staining in the SVZ from all groups under study at P14 and P70. Scale bar = 100 μm.

ventricle, and Caf treatment successfully reduced hemorrhage burden at P14. A similar profile was observed at P70, although statistical differences with GM-IVH animals were only observed at the highest dose of Caf under study (20 mg/kg/day) (**Supplementary Table S2**) (**Figures 5C,D**).

3.7 Caf Treatment Reduces Inflammation in Animals With GM-IVH

Microglia burden, analyzed by Iba-1 staining, was significantly higher in the cortex from animals with GM-IVH, at both P14 and P70, and Caf (10 and 20 mg/kg/day) reduced cortical microglial

burden (**Figures 5E,F**). Similarly, microglial burden was also increased in the SVZ from animals with Col lesions in the short (P14) and the long (P70) term, and both doses of Caf effectively reduced the presence of activated microglia (**Figures 5G,H**). Our observations are in line with previous studies showing the Caf anti-inflammatory activity (Yang et al., 2022).

4 DISCUSSION

GM-IVH is one of the most relevant brain complications of the PT (Radic et al., 2015b; Valdez Sandoval et al., 2019), responsible for severe disabilities in the majority of these patients (Segado-Arenas et al., 2017), including cognitive and motor impairments (Morita et al., 2015; He et al., 2019), developmental delay (Bolisetty et al., 2014; Holwerda et al., 2016; Matijevic et al., 2019), or cerebral palsy (Bolisetty et al., 2014; da Silva et al., 2018). Even though the consequences are devastating GM-IVH has no successful treatment, and patients are in a tremendous need of new therapeutic opportunities.

Caf is commonly used in the clinic to treat the apnea of prematurity (Abdel-Hady et al., 2015), and previous studies have reported the beneficial effects of Caf treatment not only at the pulmonary level but also on the CNS. Caf treatment is not associated with improved survival rates without disabilities in VLBWI at 5 years (Schmidt et al., 2012). However, developmental coordination disorders are reduced by this age (Doyle et al., 2014). Also, Caf has been shown to have positive effects at an earlier age (18–21 months) with lower mean costs for these patients and better survival rates without neurodevelopmental disabilities, including reduced incidence of cerebral palsy and cognitive delay (Schmidt et al., 2007; Dukhovny et al., 2011). Moreover, long-term analysis reveals that by 11 years of age, kids treated with Caf for apnea of prematurity had better visuomotor, visuoperceptual, and visuospatial abilities or fine motor coordination (Maitre et al., 2015; Schmidt et al., 2017; Mürner-Lavanchy et al., 2018). In line with these observations, early Caf treatment to PT improves white matter microstructural development (Doyle et al., 2010; Liu et al., 2020). These data support that Caf has a direct neuroprotective effect apart from improving respiratory function (Yang et al., 2021). Since Caf is used to treat respiratory dysfunction, most of the studies focus on secondary outcomes, and the work specifically addressing the role of Caf on GM-IVH is limited in patients and animal models.

We have analyzed the direct effect of Caf in brain complications and cognitive function in a murine model of GM-IVH, generated by intracerebroventricular administration of 0.3 IU of Col. Previous studies have established this murine model of GM-IVH based on Col administration to P7 rodents (Lekic et al., 2015), and later studies have also used this approach (Segado-Arenas et al., 2017; Tang et al., 2017; Li et al., 2018; Scheuer et al., 2018; Almeida et al., 2019; Hierro-Bujalance et al., 2020b). Since P7 mice might be considered in the limit of prematurity (Semple et al., 2013), other approaches have also used younger mice (Alexander et al., 2014; Ko et al., 2018; Del Pozo et al., 2022) that might resemble a more severe aspect of prematurity, and therefore, it is also important to bear in mind that the actual outcomes might differ depending on the actual postnatal day in which the lesions are induced.

Earlier investigations have already shown that neonatal mice and PT express receptors for Caf (adenosine receptors 1 and 2) in the brain (Li et al., 2019), supporting the direct effect of Caf on the CNS (Li et al., 2019). We observed that Caf treatment, at both 10 and 20 mg/kg/day, had a neuroprotective effect in the short (P14) and the long (P70) term. The brain/body weight ratio was significantly reduced after Col administration, and Caf treatment restored control values in animals with GM-IVH. Direct brain examination revealed an overall compromise that preferentially affected the cortex at P14 and P70. Caf treatment successfully restored cortical atrophy and reduced ventricle enlargement, classically observed in GM-IVH patients (Goeral et al., 2021; Szentimrey et al., 2022), as well as in this (Segado-Arenas et al., 2017; Hierro-Bujalance et al., 2020b), and in other models resembling brain complications of the PT (Alexander et al., 2013; Di Martino et al., 2020).

Neuron wellbeing was further assessed by analyzing neurite curvature, as previously performed in other pathologies (Serrano-Pozo et al., 2010; Mizutani et al., 2021). Neurite curvature was significantly affected in the cortex and the SVZ at P14 in mice with GM-IVH, while both doses of Caf successfully limited this effect. We also observed an increase in tau phosphorylation in the cortex as it occurs in neurodegenerative disorders, indicative of alterations in the axonal microtubule assembly (Johnson and Stoothoff, 2004; Segado-Arenas et al., 2017; Trushina et al., 2019), and Caf treatment reduced tau hyperphosphorylation, in line with previous observations (Laurent et al., 2016; Zhao et al., 2017). Likewise, neuron population assessed by the NeuN/DAPI ratio was reduced after GM-IVH in the cortex and the SVZ from mice with GM-IVH, and Caf treatment counterbalanced this situation. These data support the capacity of Caf to limit neuronal loss, in line with previous studies showing that Caf may promote neuron survival after an hypoxic situation (Li et al., 2019; Soontarapornchai et al., 2021) or other insults (Stazi et al., 2021; Xie et al., 2021).

Since GM-IVH directly affects the SVZ, a main neurogenic niche in mice, we also analyzed cell proliferation and neurogenesis after Caf treatment. Previous studies have revealed a compromise in neurogenesis in this model (Segado-Arenas et al., 2017), and we also observed a reduction in DCX labeling in the SVZ. Interestingly, Caf treatment at the highest dose (20 mg/kg/day) successfully restored neurogenesis impairment, suggesting that Caf effects might not be circumscribed to limiting neuronal loss, but it may also promote neurogenesis. Whereas some studies have shown that Caf may compromise proliferation of human hippocampal progenitor cells (Houghton et al., 2020), neurogenesis seems to improve after Caf treatment in different animal models (Mao et al., 2020; Stazi et al., 2021).

We further analyzed the effect of Caf on small vessel bleeding observed after the induction of GM-IVH (Segado-Arenas et al., 2017; Hierro-Bujalance et al., 2020b). As expected, Col lesions increased the presence of hemorrhages in the cortex and more severely in the areas surrounding the injection site, as the SVZ. Previous studies in

patients have shown that early Caf administration improves hemodynamics (Katheria et al., 2015), and given the fragility of the preterm vasculature, this may account for the protective effects observed. While both doses of Caf reduced hemorrhage burden, Caf 20 mg/kg/day had a more robust effect. At this point, it should be taken into consideration that the doses used in this study (10 and 20 mg/kg/day) are in the range of previous studies using Caf in other models showing beneficial effects (Kaindl et al., 2008; Fan et al., 2011), but high-dose Caf treatment might have a negative impact on brain development and associated complications and therefore, Caf effects might entirely depend on the actual dose and pathologies under study (McPherson et al., 2015; Vesoulis et al., 2016; Saroha and Patel, 2020; Soontarapornchai et al., 2021). Importantly, Caf might not only have a positive effect in limiting the pathological complications associated, but it may also reduce the incidence of GM-IVH itself, when administered early to patients at risk (Borszewska-Kornacka et al., 2017; Helwich et al., 2017).

Antioxidant and anti-inflammatory properties of Caf have been largely addressed in different animal models, including neonatal hypoxia-ischemia or neonatal hyperoxia models (Endesfelder et al., 2017b; Di Martino et al., 2020), downregulating pro-inflammatory cytokines or limiting the presence of amoeboid microglia. Caf also suppresses pro-inflammatory mediators and their regulatory genes after lipopolysaccharide insult to microglial cells (Kang et al., 2012). However, to the best of our knowledge, no previous studies have addressed the anti-inflammatory effects of Caf after GM-IVH. Our study shows a significant increase in microglial burden in the cortex, and more importantly in the SVZ, after lesions, in both the short and the long term, whereas Caf treatment effectively counterbalances this inflammatory phenotype. In line with this, previous studies have reported that activation of adenosine A2a receptors might modulate microglial activation in animal models of perinatal brain injury (Colella et al., 2018). Following this idea, it is feasible that reduction of the inflammatory process might contribute to observed neuroprotection after Caf treatment, as previously described in hypoxic-ischemic damage in neonatal rats where Caf, through A2a receptors, inhibits the activation of NLRP3 inflammasome, reduces microglial activation, and regulates the release of inflammatory factors (Yang et al., 2022). However, we cannot exclude that other mechanisms may also contribute to the observed positive effects of Caf on neuron stability and wellbeing and previous studies in other models of neonatal insults have shown that Caf successfully reduces apoptosis markers (Endesfelder et al., 2017a; Soontarapornchai et al., 2021). On the other hand, other studies have pointed out that Caf neuroprotective effects might also be mediated by the regulation of autophagy in different models of neurodegeneration (Moon et al., 2014; Luan et al., 2018).

Cognitive impairments were observed in mice after GM-IVH. Although it might be possible that hippocampus is affected by Col administration, similar outcomes have been reported in other models of GM-IVH (Li et al., 2018), and our results are also in accordance with cognitive alterations observed in patients (Vohr, 2022). Episodic and spatial memory were improved after Caf treatment, and although no previous studies have addressed the role of Caf on cognitive impairment associated with GM-IVH lesions, our results are in line with other observations showing the beneficial effects of Caf and other methylxanthines after hypoxic-ischemic insults in newborn animals (Kumral et al., 2010; Potter et al., 2018). Although we cannot point toward a specific pathological feature responsible for cognitive impairment in our mouse model, it is feasible that the combination of all alterations might result in learning and memory disabilities observed since previous studies have shown independent beneficial effects for Caf that result in cognitive improvement after different insults (Alexander et al., 2013; Zhao et al., 2017; Potter et al., 2018).

Caf is a commonly used drug to treat the apnea of prematurity, and although it may also improve brain-associated complications to GM-IVH (Helwich et al., 2017), no previous study has addressed the role of Caf in brain pathology and cognitive impairment at this level. We showed that Caf counterbalances brain atrophy and neuronal damage while limiting small vessel bleeding and inflammation, ultimately ameliorating cognitive impairment and supporting a feasible role for Caf to reduce complications associated with GM-IVH of the VLBWI.

DATA AVAILABILITY STATEMENT

The raw data supporting the conclusion of this article will be made available by the authors, without undue reservation.

ETHICS STATEMENT

The animal study was reviewed and approved by the Animal Care and Use Committee of the University of Cadiz in accordance with the guidelines for care and use of experimental animals (European Commission Directive 2010/63/UE and Spanish Royal Decree 53/2013).

AUTHOR CONTRIBUTIONS

PA-M: experiment design, data acquisition, analysis, and interpretation. IA-N, MV-S, MJC-N, CI-G, and ADM: data acquisition and analysis. IB-F: design and analysis and critical revision of the manuscript for intellectual content. SL-L: study concept, design, and critical revision of the manuscript for intellectual content, MG-A: study concept and design and drafting and critical revision of the manuscript. All authors provided critical feedback and helped shape the research, analysis, and manuscript.

FUNDING

This study was supported by the following: PA-M: predoctoral fellowship. Instituto de Investigacion Biomedica de la Provincia de Cadiz (INIBICA). MG-A: Agencia Andaluza del Conocimiento. Proyectos I + D + I—Programa Operativo FEDER Andalucia 2014–2020 fondos FEDER (FEDER-UCA18-107189). Agencia Estatal de Investigacion. Ministerio de Educacion y Ciencia. Programa Estatal de Generacion de Conocimiento y Fortalecimiento Cientifico y Tecnologico del Sistema de I + D + i y del Programa Estatal de I + D + i Orientada a los Retos de la Sociedad, del Plan Estatal de Investigacion Cientifica y Tecnica y de Innovacion 2017–2020 (PID2020-115499RB-I00/AEI/10.13039/501100011033).

ACKNOWLEDGMENTS

The authors thank the animal facility (Servicio de Produccion y Experimentacion Animal) from the University of Cadiz for their technical support. They also thank "Servicios Centrales de Investigacion en Biomedicina" (SC-IBM) from the University of Cadiz for the resources and technical support.

SUPPLEMENTARY MATERIAL

The Supplementary Material for this article can be found online at: https://www.frontiersin.org/articles/10.3389/fcell.2022.908045/full#supplementary-material

REFERENCES

Abdel-Hady, H., Nasef, N., Shabaan, A. E., and Nour, I. (2015). Caffeine Therapy in Preterm Infants. *World J. Clin. Pediatr.* 4, 81–93. doi:10.5409/wjcp.v4.i4.81

Almeida, T. D. A. L., Santos, M. V., Da Silva Lopes, L., Goel, G., Leonardo De Freitas, R., De Medeiros, P., et al. (2019). Intraperitoneal Cannabidiol Attenuates Neonatal Germinal Matrix Hemorrhage-Induced Neuroinflamation and Perilesional Apoptosis. *Neurol. Res.* 41, 980–990. doi:10.1080/01616412.2019.1651487

Alexander, M., Smith, A., Rosenkrantz, T., and Fitch, R. (2013). Therapeutic Effect of Caffeine Treatment Immediately Following Neonatal Hypoxic-Ischemic Injury on Spatial Memory in Male Rats. *Brain Sci.* 3, 177–190. doi:10.3390/brainsci3010177

Alexander, M., Garbus, H., Smith, A. L., Rosenkrantz, T. S., and Fitch, R. H. (2014). Behavioral and Histological Outcomes Following Neonatal HI Injury in a Preterm (P3) and Term (P7) Rodent Model. *Behav. Brain Res.* 259, 85–96. doi:10.1016/j.bbr.2013.10.038

Atienza-Navarro, I., Alves-Martinez, P., Lubian-Lopez, S., and Garcia-Alloza, M. (2020). Germinal Matrix-Intraventricular Hemorrhage of the Preterm Newborn and Preclinical Models: Inflammatory Considerations. *Int. J. Mol. Sci.* 21, 8343. doi:10.3390/ijms21218343

Bolisetty, S., Dhawan, A., Abdel-Latif, M., Bajuk, B., Stack, J., Oei, J.-L., et al. (2014). Intraventricular Hemorrhage and Neurodevelopmental Outcomes in Extreme Preterm Infants. *Pediatrics* 133, 55–62. doi:10.1542/peds.2013-0372

Borszewska-Kornacka, M. K., Hożejowski, R., Rutkowska, M., and Lauterbach, R. (2017). Shifting the Boundaries for Early Caffeine Initiation in Neonatal Practice: Results of a Prospective, Multicenter Study on Very Preterm Infants with Respiratory Distress Syndrome. *PLoS One* 12, e0189152. doi:10.1371/journal.pone.0189152

Cerisola, A., Baltar, F., Ferrán, C., and Turcatti, E. (2019). Mecanismos De Lesión Cerebral En Niños Prematuros. *Med. (Buenos Aires)* 79, 10–14.

Christian, E. A., Jin, D. L., Attenello, F., Wen, T., Cen, S., Mack, W. J., et al. (2016). Trends in Hospitalization of Preterm Infants with Intraventricular Hemorrhage and Hydrocephalus in the United States, 2000-2010. *J. Neurosurg. Pediatr.* 17, 260–269. doi:10.3171/2015.7.peds15140

Chung, E. H., Chou, J., and Brown, K. A. (2020). Neurodevelopmental Outcomes of Preterm Infants: A Recent Literature Review. *Transl. Pediatr.* 9, S3–S8. doi:10.21037/tp.2019.09.10

Colella, M., Zinni, M., Pansiot, J., Cassanello, M., Mairesse, J., Ramenghi, L., et al. (2018). Modulation of Microglial Activation by Adenosine A2a Receptor in Animal Models of Perinatal Brain Injury. *Front. Neurol.* 9, 605. doi:10.3389/fneur.2018.00605

da Silva, L. S., Ribeiro, G. E., Montovani, J. C., and Silva, D. P. C. d. (2018). The Effect of Peri-Intraventricular Hemorrhage on the Auditory Pathway of Infants. *Int. J. Pediatr. Otorhinolaryngol.* 112, 24–26. doi:10.1016/j.ijporl.2018.06.026

Deger, J., Goethe, E. A., LoPresti, M. A., and Lam, S. (2021). Intraventricular Hemorrhage in Premature Infants: A Historical Review. *World Neurosurg.* 153, 21–25. doi:10.1016/j.wneu.2021.06.043

Del Pozo, A., Villa, M., Vargas, C., Castejon, D., Fernandez-Valle, M. E., Gutierrez-Rodriguez, A., et al. (2022). Intraventricular Hemorrhage Induces Inflammatory Brain Damage with Blood-Brain Barrier Dysfunction in Immature Rats. *Pediatr. Res.* [online ahead of print] doi:10.1038/s41390-022-02062-3

Dere, E., Huston, J. P., and De Souza Silva, M. A. (2005). Episodic-like Memory in Mice: Simultaneous Assessment of Object, Place and Temporal Order Memory. *Brain Res. Protoc.* 16, 10–19. doi:10.1016/j.brainresprot.2005.08.001

Desestret, V., Brisset, J.-C., Moucharrafie, S., Devillard, E., Nataf, S., Honnorat, J., et al. (2009). Early-Stage Investigations of Ultrasmall Superparamagnetic Iron Oxide-Induced Signal Change after Permanent Middle Cerebral Artery Occlusion in Mice. *Stroke* 40, 1834–1841. doi:10.1161/strokeaha.108.531269

Di Martino, E., Bocchetta, E., Tsuji, S., Mukai, T., Harris, R. A., Blomgren, K., et al. (2020). Defining a Time Window for Neuroprotection and Glia Modulation by Caffeine after Neonatal Hypoxia-Ischaemia. *Mol. Neurobiol.* 57, 2194–2205. doi:10.1007/s12035-020-01867-9

Doyle, L. W., Cheong, J., Hunt, R. W., Lee, K. J., Thompson, D. K., Davis, P. G., et al. (2010). Caffeine and Brain Development in Very Preterm Infants. *Ann. Neurol.* 68, 734–742. doi:10.1002/ana.22098

Doyle, L. W., Schmidt, B., Anderson, P. J., Davis, P. G., Moddemann, D., Grunau, R. E., et al. (2014). Reduction in Developmental Coordination Disorder with Neonatal Caffeine Therapy. *J. Pediatr.* 165, 356–359. doi:10.1016/j.jpeds.2014.04.016

Dukhovny, D., Lorch, S. A., Schmidt, B., Doyle, L. W., Kok, J. H., Roberts, R. S., et al. (2011). Economic Evaluation of Caffeine for Apnea of Prematurity. *Pediatrics* 127, e146–e155. doi:10.1542/peds.2010-1014

Endesfelder, S., Weichelt, U., Schiller, C., Sifringer, M., Bendix, I., and Bührer, C. (2017). Caffeine Protects against Anticonvulsant-Induced Neurotoxicity in the Developing Rat Brain. *Neurotox. Res.* 32, 460–472. doi:10.1007/s12640-017-9768-z

Endesfelder, S., Weichelt, U., Strauss, E., Schlör, A., Sifringer, M., Scheuer, T., et al. (2017). Neuroprotection by Caffeine in Hyperoxia-Induced Neonatal Brain Injury. *Int. J. Mol. Sci.* 18, 187. doi:10.3390/ijms18010187

Fan, X., Heijnen, C. J., van der Kooij, M. A., Groenendaal, F., and van Bel, F. (2011). Beneficial Effect of Erythropoietin on Sensorimotor Function and White Matter after Hypoxia-Ischemia in Neonatal Mice. *Pediatr. Res.* 69, 56–61. doi:10.1203/pdr.0b013e3181fcbef3

Fusch, C., Ozdoba, C., Kuhn, P., Dürig, P., Remonda, L., Müller, C., et al. (1997). Perinatal Ultrasonography and Magnetic Resonance Imaging Findings in Congenital Hydrocephalus Associated with Fetal Intraventricular Hemorrhage. *Am. J. Obstetrics Gynecol.* 177, 512–518. doi:10.1016/s0002-9378(97)70138-8

Goeral, K., Schwarz, H., Hammerl, M., Brugger, J., Wagner, M., Klebermass-Schrehof, K., et al. (2021). Longitudinal Reference Values for Cerebral Ventricular Size in Preterm Infants Born at 23-27 Weeks of Gestation. *J. Pediatr.* 238, 110–117. doi:10.1016/j.jpeds.2021.06.065

Harkin, P., Marttila, R., Pokka, T., Saarela, T., and Hallman, M. (2019). Survival Analysis of a Cohort of Extremely Preterm Infants Born in Finland during

2005-2013. *J. Matern. Fetal Neonatal Med.* 34, 1–7. doi:10.1080/14767058.2019.1668925

He, L., Zhou, W., Zhao, X., Liu, X., Rong, X., and Song, Y. (2019). Development and Validation of a Novel Scoring System to Predict Severe Intraventricular Hemorrhage in Very Low Birth Weight Infants. *Brain Dev.* 41, 671–677. doi:10.1016/j.braindev.2019.04.013

Helwich, E., Rutkowska, M., Bokiniec, R., Gulczyńska, E., and Hożejowski, R. (2017). Intraventricular Hemorrhage in Premature Infants with Respiratory Distress Syndrome Treated with Surfactant: Incidence and Risk Factors in the Prospective Cohort Study. *Dev. Period Med.* 21, 328–335. doi:10.34763/devperiodmed.20172104.328335

Hierro-Bujalance, C., Del Marco, A., José Ramos-Rodríguez, J., Infante-Garcia, C., Bella Gomez-Santos, S., Herrera, M., et al. (2020). Cell Proliferation and Neurogenesis Alterations in Alzheimer's Disease and Diabetes Mellitus Mixed Murine Models. *J. Neurochem.* 154, 673–692. doi:10.1111/jnc.14987

Hierro-Bujalance, C., Infante-Garcia, C., Sanchez-Sotano, D., Del Marco, A., Casado-Revuelta, A., Mengual-Gonzalez, C. M., et al. (2020). Erythropoietin Improves Atrophy, Bleeding and Cognition in the Newborn Intraventricular Hemorrhage. *Front. Cell Dev. Biol.* 8, 571258. doi:10.3389/fcell.2020.571258

Hochgräfe, K., Sydow, A., and Mandelkow, E.-M. (2013). Regulatable Transgenic Mouse Models of Alzheimer Disease: Onset, Reversibility and Spreading of Tau Pathology. *FEBS J.* 280, 4371–4381. doi:10.1111/febs.12250

Holwerda, J. C., Van Braeckel, K. N. J. A., Roze, E., Hoving, E. W., Maathuis, C. G. B., Brouwer, O. F., et al. (2016). Functional Outcome at School Age of Neonatal Post-hemorrhagic Ventricular Dilatation. *Early Hum. Dev.* 96, 15–20. doi:10.1016/j.earlhumdev.2016.02.005

Houghton, V., Du Preez, A., Lefèvre-Arbogast, S., de Lucia, C., Low, D. Y., Urpi-Sarda, M., et al. (2020). Caffeine Compromises Proliferation of Human Hippocampal Progenitor Cells. *Front. Cell Dev. Biol.* 8, 806. doi:10.3389/fcell.2020.00806

Infante-Garcia, C., Ramos-Rodriguez, J. J., Galindo-Gonzalez, L., and Garcia-Alloza, M. (2016). Long-term Central Pathology and Cognitive Impairment Are Exacerbated in a Mixed Model of Alzheimer's Disease and Type 2 Diabetes. *Psychoneuroendocrinology* 65, 15–25. doi:10.1016/j.psyneuen.2015.12.001

Infante-Garcia, C., Ramos-Rodriguez, J. J., Marin-Zambrana, Y., Teresa Fernandez-Ponce, M., Casas, L., Mantell, C., et al. (2017). Mango Leaf Extract Improves Central Pathology and Cognitive Impairment in a Type 2 Diabetes Mouse Model. *Brain Pathol.* 27, 499–507. doi:10.1111/bpa.12433

Infante-Garcia, C., Ramos-Rodriguez, J. J., Delgado-Olmos, I., Gamero-Carrasco, C., Fernandez-Ponce, M. T., Casas, L., et al. (2017). Long-Term Mangiferin Extract Treatment Improves Central Pathology and Cognitive Deficits in APP/PS1 Mice. *Mol. Neurobiol.* 54, 4696–4704. doi:10.1007/s12035-016-0015-z

Infante-Garcia, C., Ramos-Rodriguez, J. J., Hierro-Bujalance, C., Ortegon, E., Pickett, E., Jackson, R., et al. (2018). Antidiabetic Polypill Improves Central Pathology and Cognitive Impairment in a Mixed Model of Alzheimer's Disease and Type 2 Diabetes. *Mol. Neurobiol.* 55, 6130–6144. doi:10.1007/s12035-017-0825-7

Iyer, K. K., Roberts, J. A., Hellström-Westas, L., Wikström, S., Hansen Pupp, I., Ley, D., et al. (2015). Early Detection of Preterm Intraventricular Hemorrhage from Clinical Electroencephalography. *Crit. care Med.* 43, 2219–2227. doi:10.1097/ccm.0000000000001190

Jinnai, M., Koning, G., Singh-Mallah, G., Jonsdotter, A., Leverin, A.-L., Svedin, P., et al. (2020). A Model of Germinal Matrix Hemorrhage in Preterm Rat Pups. *Front. Cell. Neurosci.* 14, 535320. doi:10.3389/fncel.2020.535320

Johnson, G. V. W., and Stoothoff, W. H. (2004). Tau Phosphorylation in Neuronal Cell Function and Dysfunction. *J. Cell Sci.* 117, 5721–5729. doi:10.1242/jcs.01558

Kaindl, A. M., Sifringer, M., Koppelstaetter, A., Genz, K., Loeber, R., Boerner, C., et al. (2008). Erythropoietin Protects the Developing Brain from Hyperoxia-Induced Cell Death and Proteome Changes. *Ann. Neurol.* 64, 523–534. doi:10.1002/ana.21471

Kang, C.-H., Jayasooriya, R. G. P. T., Dilshara, M. G., Choi, Y. H., Jeong, Y.-K., Kim, N. D., et al. (2012). Caffeine Suppresses Lipopolysaccharide-Stimulated BV2 Microglial Cells by Suppressing Akt-Mediated NF-κB Activation and ERK Phosphorylation. *Food Chem. Toxicol.* 50, 4270–4276. doi:10.1016/j.fct.2012.08.041

Katheria, A. C., Sauberan, J. B., Akotia, D., Rich, W., Durham, J., and Finer, N. N. (2015). A Pilot Randomized Controlled Trial of Early versus Routine Caffeine in Extremely Premature Infants. *Am. J. Perinatol.* 32, 879–886. doi:10.1055/s-0034-1543981

Khanafer-Larocque, I., Soraisham, A., Stritzke, A., Al Awad, E., Thomas, S., Murthy, P., et al. (2019). Intraventricular Hemorrhage: Risk Factors and Association with Patent Ductus Arteriosus Treatment in Extremely Preterm Neonates. *Front. Pediatr.* 7, 408. doi:10.3389/fped.2019.00408

Ko, H. R., Ahn, S. Y., Chang, Y. S., Hwang, I., Yun, T., Sung, D. K., et al. (2018). Human UCB-MSCs Treatment upon Intraventricular Hemorrhage Contributes to Attenuate Hippocampal Neuron Loss and Circuit Damage through BDNF-CREB Signaling. *Stem Cell Res. Ther.* 9, 326. doi:10.1186/s13287-018-1052-5

Kumral, A., Yesilirmak, D. C., Aykan, S., Genc, S., Tugyan, K., Cilaker, S., et al. (2010). Protective Effects of Methylxanthines on Hypoxia-Induced Apoptotic Neurodegeneration and Long-Term Cognitive Functions in the Developing Rat Brain. *Neonatology* 98, 128–136. doi:10.1159/000278840

Lampe, R., Rieger-Fackeldey, E., Sidorenko, I., Turova, V., Botkin, N., Eckardt, L., et al. (2020). Assessing Key Clinical Parameters before and after Intraventricular Hemorrhage in Very Preterm Infants. *Eur. J. Pediatr.* 179, 929. doi:10.1007/s00431-020-03585-9

Laurent, C., Burnouf, S., Ferry, B., Batalha, V. L., Coelho, J. E., Baqi, Y., et al. (2016). A2A Adenosine Receptor Deletion is Protective in a Mouse Model of Tauopathy. *Mol. Psychiatry* 21, 97–107. doi:10.1038/mp.2014.151

Lekic, T., Klebe, D., McBride, D. W., Manaenko, A., Rolland, W. B., Flores, J. J., et al. (2015). Protease-activated Receptor 1 and 4 Signal Inhibition Reduces Preterm Neonatal Hemorrhagic Brain Injury. *Stroke* 46, 1710–1713. doi:10.1161/strokeaha.114.007889

Li, Q., Ding, Y., Krafft, P., Wan, W., Yan, F., Wu, G., et al. (2018). Targeting Germinal Matrix Hemorrhage-Induced Overexpression of Sodium-Coupled Bicarbonate Exchanger Reduces Posthemorrhagic Hydrocephalus Formation in Neonatal Rats. *J. Am. Heart Assoc.* 7, e007192. doi:10.1161/JAHA.117.007192

Li, H.-L., Zaghloul, N., Ahmed, I., Omelchenko, A., Firestein, B. L., Huang, H., et al. (2019). Caffeine Inhibits Hypoxia-Induced Nuclear Accumulation in HIF-1α and Promotes Neonatal Neuronal Survival. *Exp. Neurol.* 317, 66–77. doi:10.1016/j.expneurol.2019.01.014

Liu, S., Zhang, X., Liu, Y., Yuan, X., Yang, L., Zhang, R., et al. (2020). Early Application of Caffeine Improves White Matter Development in Very Preterm Infants. *Respir. Physiol. Neurobiol.* 281, 103495. doi:10.1016/j.resp.2020.103495

Long, J.-Y., Guo, H.-L., He, X., Hu, Y.-H., Xia, Y., Cheng, R., et al. (2021). Caffeine for the Pharmacological Treatment of Apnea of Prematurity in the NICU: Dose Selection Conundrum, Therapeutic Drug Monitoring and Genetic Factors. *Front. Pharmacol.* 12, 681842. doi:10.3389/fphar.2021.681842

Luan, Y., Ren, X., Zheng, W., Zeng, Z., Guo, Y., Hou, Z., et al. (2018). Chronic Caffeine Treatment Protects against α-Synucleinopathy by Reestablishing Autophagy Activity in the Mouse Striatum. *Front. Neurosci.* 12, 301. doi:10.3389/fnins.2018.00301

Maitre, N. L., Chan, J., Stark, A. R., Lambert, W. E., Aschner, J. L., and Key, A. P. (2015). Effects of Caffeine Treatment for Apnea of Prematurity on Cortical Speech-Sound Differentiation in Preterm Infants. *J. Child. Neurol.* 30, 307–313. doi:10.1177/0883073814538500

Mao, Z. F., Ouyang, S. H., Zhang, Q. Y., Wu, Y. P., Wang, G. E., Tu, L. F., et al. (2020). New Insights into the Effects of Caffeine on Adult Hippocampal Neurogenesis in Stressed Mice: Inhibition of CORT-induced Microglia Activation. *FASEB J.* 34, 10998–11014. doi:10.1096/fj.202000146rr

Matijevic, V., Barbaric, B., Kraljevic, M., Milas, I., and Kolak, J. (2019). Gender Differences in Neurodevelopmental Outcomes Among Full-Term Infants with Intraventricular Hemorrhage. *Acta Clin. Croat.* 58, 107–112. doi:10.20471/acc.2019.58.01.14

McPherson, C., Neil, J. J., Tjoeng, T. H., Pineda, R., and Inder, T. E. (2015). A Pilot Randomized Trial of High-Dose Caffeine Therapy in Preterm Infants. *Pediatr. Res.* 78, 198–204. doi:10.1038/pr.2015.72

Meyer-Luehmann, M., Spires-Jones, T. L., Prada, C., Garcia-Alloza, M., de Calignon, A., Rozkalne, A., et al. (2008). Rapid Appearance and Local Toxicity of Amyloid-β Plaques in a Mouse Model of Alzheimer's Disease. *Nature* 451, 720–724. doi:10.1038/nature06616

Mizutani, R., Saiga, R., Yamamoto, Y., Uesugi, M., Takeuchi, A., Uesugi, K., et al. (2021). Structural Diverseness of Neurons between Brain Areas and between Cases. *Transl. Psychiatry* 11, 49. doi:10.1038/s41398-020-01173-x

Moon, J.-H., Lee, J.-H., Park, J.-Y., Kim, S.-W., Lee, Y.-J., Kang, S.-J., et al. (2014). Caffeine Prevents Human Prion Protein-Mediated Neurotoxicity through the Induction of Autophagy. *Int. J. Mol. Med.* 34, 553–558. doi:10.3892/ijmm.2014.1814

Morita, T., Morimoto, M., Yamada, K., Hasegawa, T., Morioka, S., Kidowaki, S., et al. (2015). Low-grade Intraventricular Hemorrhage Disrupts Cerebellar White Matter in Preterm Infants: Evidence from Diffusion Tensor Imaging. *Neuroradiology* 57, 507–514. doi:10.1007/s00234-015-1487-7

Mukerji, A., Shah, V., and Shah, P. S. (2015). Periventricular/Intraventricular Hemorrhage and Neurodevelopmental Outcomes: A Meta-Analysis. *Pediatrics* 136, 1132–1143. doi:10.1542/peds.2015-0944

Mürner-Lavanchy, I. M., Doyle, L. W., Schmidt, B., Roberts, R. S., Asztalos, E. V., Costantini, L., et al. (2018). Neurobehavioral Outcomes 11 Years after Neonatal Caffeine Therapy for Apnea of Prematurity. *Pediatrics* 141, e20174047. doi:10.1542/peds.2017-4047

Potter, M., Rosenkrantz, T., and Fitch, R. H. (2018). Behavioral and Neuroanatomical Outcomes in a Rat Model of Preterm Hypoxic-ischemic Brain Injury: Effects of Caffeine and Hypothermia. *Int. J. Dev. Neurosci.* 70, 46–55. doi:10.1016/j.ijdevneu.2018.02.001

Radic, J. A. E., Vincer, M., and McNeely, P. D. (2015). Temporal Trends of Intraventricular Hemorrhage of Prematurity in Nova Scotia from 1993 to 2012. *J. Neurosurg. Pediatr.* 15, 573–579. doi:10.3171/2014.11.peds14363

Radic, J. A. E., Vincer, M., and McNeely, P. D. (2015). Outcomes of Intraventricular Hemorrhage and Posthemorrhagic Hydrocephalus in a Population-Based Cohort of Very Preterm Infants Born to Residents of Nova Scotia from 1993 to 2010. *J. Neurosurg. Pediatr.* 15, 580–588. doi:10.3171/2014.11.peds14364

Ramos-Rodriguez, J. J., Molina-Gil, S., Ortiz-Barajas, O., Jimenez-Palomares, M., Perdomo, G., Cozar-Castellano, I., et al. (2014). Central Proliferation and Neurogenesis is Impaired in Type 2 Diabetes and Prediabetes Animal Models. *PLoS One* 9, e89229. doi:10.1371/journal.pone.0089229

Ramos-Rodriguez, J. J., Spires-Jones, T., Pooler, A. M., Lechuga-Sancho, A. M., Bacskai, B. J., and Garcia-Alloza, M. (2017). Progressive Neuronal Pathology and Synaptic Loss Induced by Prediabetes and Type 2 Diabetes in a Mouse Model of Alzheimer's Disease. *Mol. Neurobiol.* 54, 3428–3438. doi:10.1007/s12035-016-9921-3

Rellan Rodríguez, S., García de Ribera, C., and Aragón García, M. (2008). El Recién Nacido Prematuro. *Protocolos Diágnosticos Terapeúticos de La AEP: Neonatología* 8, 68–77.

Saroha, V., and Patel, R. M. (2020). Caffeine for Preterm Infants: Fixed Standard Dose, Adjustments for Age or High Dose? *Seminars Fetal Neonatal Med.* 25, 101178. doi:10.1016/j.siny.2020.101178

Scheuer, T., Sharkovska, Y., Tarabykin, V., Marggraf, K., Brockmöller, V., Bührer, C., et al. (2018). Neonatal Hyperoxia Perturbs Neuronal Development in the Cerebellum. *Mol. Neurobiol.* 55, 3901–3915. doi:10.1007/s12035-017-0612-5

Schmidt, B., Roberts, R. S., Davis, P., Doyle, L. W., Barrington, K. J., Ohlsson, A., et al. (2007). Long-Term Effects of Caffeine Therapy for Apnea of Prematurity. *N. Engl. J. Med.* 357, 1893–1902. doi:10.1056/nejmoa073679

Schmidt, B., Anderson, P. J., Doyle, L. W., Dewey, D., Grunau, R. E., Asztalos, E. V., et al. (2012). Survival without Disability to Age 5 Years after Neonatal Caffeine Therapy for Apnea of Prematurity. *JAMA* 307, 275–282. doi:10.1001/jama.2011.2024

Schmidt, B., Roberts, R. S., Anderson, P. J., Asztalos, E. V., Costantini, L., Davis, P. G., et al. (2017). Caffeine for Apnea of Prematurity Trial, Academic Performance, Motor Function, and Behavior 11 Years after Neonatal Caffeine Citrate Therapy for Apnea of Prematurity: An 11-Year Follow-Up of the CAP Randomized Clinical Trial. *JAMA Pediatr.* 171, 564–572. doi:10.1001/jamapediatrics.2017.0238

Segado-Arenas, A., Infante-Garcia, C., Benavente-Fernandez, I., Sanchez-Sotano, D., Ramos-Rodriguez, J. J., Alonso-Ojembarrena, A., et al. (2017). Cognitive Impairment and Brain and Peripheral Alterations in a Murine Model of Intraventricular Hemorrhage in the Preterm Newborn. *Mol. Neurobiol.* 55, 4896–4910. doi:10.1007/s12035-017-0693-1

Semple, B. D., Blomgren, K., Gimlin, K., Ferriero, D. M., and Noble-Haeusslein, L. J. (2013). Brain Development in Rodents and Humans: Identifying Benchmarks of Maturation and Vulnerability to Injury across Species. *Prog. Neurobiol.* 106-107, 1–16. doi:10.1016/j.pneurobio.2013.04.001

Serrano-Pozo, A., William, C. M., Ferrer, I., Uro-Coste, E., Delisle, M.-B., Maurage, C.-A., et al. (2010). Beneficial Effect of Human Anti-amyloid-β Active Immunization on Neurite Morphology and Tau Pathology. *Brain* 133, 1312–1327. doi:10.1093/brain/awq056

Soontarapornchai, K., Cai, C. L., Ahmad, T., Aranda, J. V., Hand, I., and Beharry, K. D. (2021). Pharmacodynamic Effects of Standard versus High Caffeine Doses in the Developing Brain of Neonatal Rats Exposed to Intermittent Hypoxia. *Int. J. Mol. Sci.* 22, 3473. doi:10.3390/ijms22073473

Stazi, M., Lehmann, S., Sakib, M. S., Pena-Centeno, T., Büschgens, L., Fischer, A., et al. (2021). Long-term Caffeine Treatment of Alzheimer Mouse Models Ameliorates Behavioural Deficits and Neuron Loss and Promotes Cellular and Molecular Markers of Neurogenesis. *Cell. Mol. Life Sci.* 79, 55. doi:10.1007/s00018-021-04062-8

Stern, E. A., Bacskai, B. J., Hickey, G. A., Attenello, F. J., Lombardo, J. A., and Hyman, B. T. (2004). Cortical Synaptic Integration *In Vivo* is Disrupted by Amyloid- Plaques. *J. Neurosci.* 24, 4535–4540. doi:10.1523/jneurosci.0462-04.2004

Stoll, B. J., Hansen, N. I., Bell, E. F., Shankaran, S., Laptook, A. R., Walsh, M. C., et al. (2010). Neonatal Outcomes of Extremely Preterm Infants from the NICHD Neonatal Research Network. *Pediatrics* 126, 443–456. doi:10.1542/peds.2009-2959

Szentimrey, Z., de Ribaupierre, S., Fenster, A., and Ukwatta, E. (2022). Automated 3D U-net Based Segmentation of Neonatal Cerebral Ventricles from 3D Ultrasound Images. *Med. Phys.* 49, 1034–1046. doi:10.1002/mp.15432

Szpecht, D., Szymankiewicz, M., Nowak, I., and Gadzinowski, J. (2016). Intraventricular Hemorrhage in Neonates Born before 32 Weeks of Gestation-Retrospective Analysis of Risk Factors. *Childs Nerv. Syst.* 32, 1399–1404. doi:10.1007/s00381-016-3127-x

Tang, J., Miao, H., Jiang, B., Chen, Q., Tan, L., Tao, Y., et al. (2017). A Selective CB2R Agonist (JWH133) Restores Neuronal Circuit after Germinal Matrix Hemorrhage in the Preterm via CX3CR1+ Microglia. *Neuropharmacology* 119, 157–169. doi:10.1016/j.neuropharm.2017.01.027

Trushina, N. I., Bakota, L., Mulkidjanian, A. Y., and Brandt, R. (2019). The Evolution of Tau Phosphorylation and Interactions. *Front. Aging Neurosci.* 11, 256. doi:10.3389/fnagi.2019.00256

Valdez Sandoval, P., Hernández Rosales, P., Quiñones Hernández, D. G., Chavana Naranjo, E. A., and García Navarro, V. (2019). Intraventricular Hemorrhage and Posthemorrhagic Hydrocephalus in Preterm Infants: Diagnosis, Classification, and Treatment Options. *Childs Nerv. Syst.* 35, 917–927. doi:10.1007/s00381-019-04127-x

Vesoulis, Z. A., McPherson, C., Neil, J. J., Mathur, A. M., and Inder, T. E. (2016). Early High-Dose Caffeine Increases Seizure Burden in Extremely Preterm Neonates: A Preliminary Study. *J. Caffeine Res.* 6, 101–107. doi:10.1089/jcr.2016.0012

Vohr, B. R. (2022). Neurodevelopmental Outcomes of Premature Infants with Intraventricular Hemorrhage across a Lifespan. *Seminars Perinatol.* 28, 151594. doi:10.1016/j.semperi.2022.151594

Walani, S. R. (2020). Global Burden of Preterm Birth. *Int. J. Gynecol. Obstet.* 150, 31–33. doi:10.1002/ijgo.13195

Xie, G., Huang, X., Li, H., Wang, P., and Huang, P. (2021). Caffeine-related Effects on Cognitive Performance: Roles of Apoptosis in Rat hippocampus Following Sleep Deprivation. *Biochem. Biophys. Res. Commun.* 534, 632–638. doi:10.1016/j.bbrc.2020.11.029

Yang, L., Yu, X., Zhang, Y., Liu, N., Xue, X., and Fu, J. (2021). Encephalopathy in Preterm Infants: Advances in Neuroprotection with Caffeine. *Front. Pediatr.* 9, 724161. doi:10.3389/fped.2021.724161

Yang, L., Yu, X., Zhang, Y., Liu, N., Xue, X., and Fu, J. (2022). Caffeine Treatment Started before Injury Reduces Hypoxic-Ischemic White-Matter Damage in Neonatal Rats by Regulating Phenotypic Microglia Polarization. *Pediatr. Res.* doi:10.1038/s41390-021-01924-6

You, J., Shamsi, B. H., Hao, M.-c., Cao, C.-H., and Yang, W.-Y. (2019). A Study on the Neurodevelopment Outcomes of Late Preterm Infants. *BMC Neurol.* 19, 108. doi:10.1186/s12883-019-1336-0

Zhao, Z.-A., Zhao, Y., Ning, Y.-L., Yang, N., Peng, Y., Li, P., et al. (2017). Adenosine A2A Receptor Inactivation Alleviates Early-Onset Cognitive Dysfunction after Traumatic Brain Injury Involving an Inhibition of Tau Hyperphosphorylation. *Transl. Psychiatry* 7, e1123. doi:10.1038/tp.2017.98

Conflict of Interest: The authors declare that the research was conducted in the absence of any commercial or financial relationships that could be construed as a potential conflict of interest.

Publisher's Note: All claims expressed in this article are solely those of the authors and do not necessarily represent those of their affiliated organizations, or those of the publisher, the editors, and the reviewers. Any product that may be evaluated in this article, or claim that may be made by its manufacturer, is not guaranteed or endorsed by the publisher.

Advantages of publishing in Frontiers

OPEN ACCESS
Articles are free to read for greatest visibility and readership

FAST PUBLICATION
Around 90 days from submission to decision

HIGH QUALITY PEER-REVIEW
Rigorous, collaborative, and constructive peer-review

TRANSPARENT PEER-REVIEW
Editors and reviewers acknowledged by name on published articles

Frontiers
Avenue du Tribunal-Fédéral 34
1005 Lausanne | Switzerland

Visit us: www.frontiersin.org
Contact us: frontiersin.org/about/contact

REPRODUCIBILITY OF RESEARCH
Support open data and methods to enhance research reproducibility

DIGITAL PUBLISHING
Articles designed for optimal readership across devices

FOLLOW US
@frontiersin

IMPACT METRICS
Advanced article metrics track visibility across digital media

EXTENSIVE PROMOTION
Marketing and promotion of impactful research

LOOP RESEARCH NETWORK
Our network increases your article's readership